

# Guided Wave Optics Laboratory

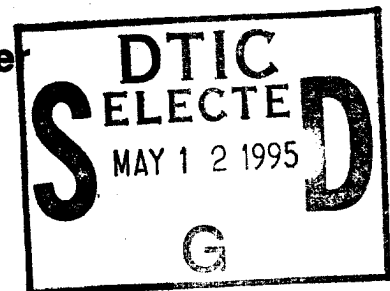
Report No. 68

Optical Properties of Lithium  
Niobate Waveguides, and Prism Coupling  
for Optimizing Waveguide Fabrication

Stephen Lawrence Kwiatkowski

## Department of Electrical and Computer Engineering

University of Colorado at Boulder  
Boulder, Colorado



### DISTRIBUTION STATEMENT A

Approved for public release;  
Distribution Unlimited

DTIC QUALITY INSPECTED 8



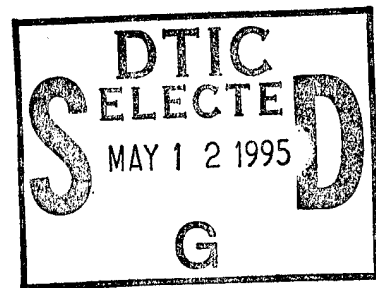
Report No. 68

**Optical Properties of Lithium  
Niobate Waveguides, and Prism Coupling  
for Optimizing Waveguide Fabrication**

Stephen Lawrence Kwiatkowski

April 25, 1995

**Guided Wave Optics Laboratory  
Department of Electrical and Computer Engineering  
University of Colorado at Boulder  
Boulder, Colorado 80309-0425**



**DISTRIBUTION STATEMENT A**

**Approved for public release;  
Distribution Unlimited**

19950511 058

This work was supported by the National Science Foundation under Contract #ECS-9015752, the Office of Naval Research under Contract #N00014-92-J-1190, and the Army Research Office under Contract #DAAL-03-92-G-0289.

REPORT DOCUMENTATION PAGE				Form Approved OMB No. 0704-0188	
1a. REPORT SECURITY CLASSIFICATION <div style="text-align: center;">unclassified</div>		1b. RESTRICTIVE MARKINGS <div style="text-align: center;">none</div>			
2a. SECURITY CLASSIFICATION AUTHORITY <div style="text-align: center;">DISCASS</div>		3. DISTRIBUTION/AVAILABILITY OF REPORT <div style="text-align: center;">unrestricted</div>			
2b. DECLASSIFICATION/DOWNGRADING SCHEDULE <div style="text-align: center;">N/A</div>					
4. PERFORMING ORGANIZATION REPORT NUMBER(S) <div style="text-align: center;">ECE/GWOL/ 68</div>		5. MONITORING ORGANIZATION REPORT NUMBER(S) <div style="text-align: center;">DOD-ONRN00014-92-J-1190</div>			
6a. NAME OF PERFORMING ORGANIZATION University of Colorado		6b. OFFICE SYMBOL (if applicable)	7a. NAME OF MONITORING ORGANIZATION Office of Naval Research Attn: Dr. Arthur Jordan, Code 1114 SE		
6c. ADDRESS (City, State, and ZIP Code) Electrical & Computer Engineering Dept. Boulder, CO 80309-0425		7b. ADDRESS (City, State, and ZIP Code) 800 N. Quincy Avenue Arlington, VA 22217-5000			
8a. NAME OF FUNDING/SPONSORING ORGANIZATION Office of Naval Research		8b. OFFICE SYMBOL (if applicable)	9. PROCUREMENT INSTRUMENT IDENTIFICATION NUMBER		
8c. ADDRESS (City, State, and ZIP Code) 800 N. Quincy Avenue Arlington, VA 22217-5000		10. SOURCE OF FUNDING NUMBERS			
		PROGRAM ELEMENT NO.	PROJECT NO.	TASK NO.	WORK UNIT ACCESSION NO.
11. TITLE (Include Security Classification) (u) Optical Properties of Lithium Niobate Waveguides, and Prism Coupling for Optimizing Waveguide Fabrication					
12. PERSONAL AUTHOR(S) Stephen L. Kwiatkowski					
13a. TYPE OF REPORT technical		13b. TIME COVERED FROM 1992 TO 1995		14. DATE OF REPORT (Year, Month, Day) 95,04,25	
15. PAGE COUNT 182					
16. SUPPLEMENTARY NOTATION					
17. COSATI CODES			18. SUBJECT TERMS (Continue on reverse if necessary and identify by block number)		
FIELD      GROUP      SUB-GROUP					
19. ABSTRACT (Continue on reverse if necessary and identify by block number)					
<p>I investigated the accuracy and precision of effective index of refraction measurements using prism coupling. I found that the coupling gap's geometry is critical to predicting the accuracy and resolution of measurements. I provide experimental evidence that there are advantages to using high coupling pressures that yield long coupling lengths. I present and evaluate an experimental technique aimed at reducing the effects of perturbation and find that it may not be applicable to all situations. I extend a previous model of prism coupling to include a finite coupling length. Also, I introduce an alternative model of prism coupling based upon a local normal-mode expansion and present its preliminary numerical results.</p> <p>I have observed more extraordinary polarized guide modes near cut-off in TI in-diffused lithium niobate planar waveguides than are predicted by Ti in-diffusion models. I also observe these nearly cut-off modes in lithium niobate specimens fabricated without Ti under a variety of diffusion atmospheres. Values of the effective index of these nearly cut-off modes found do not agree with those calculated.</p>					
20. DISTRIBUTION/AVAILABILITY OF ABSTRACT <input checked="" type="checkbox"/> UNCLASSIFIED/UNLIMITED <input type="checkbox"/> SAME AS RPT. <input type="checkbox"/> DTIC USERS			21. ABSTRACT SECURITY CLASSIFICATION <div style="text-align: center;">unclassified</div>		
22a. NAME OF RESPONSIBLE INDIVIDUAL Alan R. Mickelson		22b. TELEPHONE (Include Area Code) 303/492-7539		22c. OFFICE SYMBOL	

OPTICAL PROPERTIES OF LITHIUM NIOBATE  
WAVEGUIDES, AND PRISM COUPLING FOR  
OPTIMIZING WAVEGUIDE FABRICATION.

by

Stephen Lawrence Kwiatkowski

B.S. Physics, University of Michigan-Dearborn, 1979

M.S. Optics, University of Rochester, 1985

A thesis submitted to the  
Faculty of the Graduate School of the  
University of Colorado in partial fulfillment  
of the requirements for the degree of  
Doctor of Philosophy

Department of Electrical and Computer Engineering

1995

Accession For	
NTIS	CRA&I <input checked="" type="checkbox"/>
DTIC	TAB <input type="checkbox"/>
Unannounced	<input type="checkbox"/>
Justification _____	
By _____	
Distribution / _____	
Availability Codes	
Dist	Avail and/or Special
A-1	

This thesis for the Doctor of Philosophy degree by  
Stephen Lawrence Kwiatkowski  
has been approved for the  
Department of  
Electrical and Computer Engineering  
by

---

Alan R. Mickelson

---

Matt Young

Date \_\_\_\_\_

Kwiatkowski, Stephen Lawrence (Ph.D., Electrical Engineering)

Optical properties of lithium niobate waveguides, and prism coupling for optimizing waveguide fabrication.

Thesis directed by Associate Professor Alan R. Mickelson

I investigated the accuracy and precision of effective index of refraction measurements using prism coupling. I found that the coupling gap's geometry is critical to predicting the accuracy and resolution of measurements. I provide experimental evidence that there are advantages to using high coupling pressures that yield long coupling lengths. I present and evaluate an experimental technique aimed at reducing the effects of perturbation and find that it may not be applicable to all situations. I extend a previous model of prism coupling to include a finite coupling length. Also, I introduce an alternative model of prism coupling based upon a local normal-mode expansion and present its preliminary numerical results.

I have observed more extraordinary polarized guided modes near cut-off in titanium in-diffused lithium niobate planar waveguides than are predicted by titanium in-diffusion models. I also observe these nearly cut-off modes in lithium niobate specimens fabricated without titanium under a variety of diffusion atmospheres. Values of the effective index of these nearly cut-off modes found in plain lithium niobate planar waveguides do not agree with those calculated using the lithium out-diffusion model for either vacuum-diffused or oxygen-diffused lithium niobate waveguides. I found good agreement between measured values of the effective mode index in specimens fabricated in either dry oxygen or air and calculated values found using an empirical diffusion model of a step index profile whose depth increases as the square root of diffusion time.

I report on polarization coupling from x-propagating TE-polarized waveguide modes to TM-polarized radiation modes in y-cut titanium in-diffused lithium niobate slab waveguides. The polarization coupling is linear with respect to the TE-polarized input power and depends on the titanium diffusion time. Furthermore, the polarization coupling was not affected by white light flooding the waveguide. I observe no turn-on delay greater than 1 s between the excitation of the TE waveguide mode and the observation of the TM radiation. Intentional amplitude modulations of the TE-polarized waveguide mode were registered as equivalent amplitude modulations by the TM-polarized radiation modes.

Foremost to my wife Lillian Pia Zamora Gacusan, and to our first child

Alexander Tibay.

## ACKNOWLEDGEMENTS

We acknowledge the support of the National Science Foundation under grant number ECS-9015752, the United States Army Research Office under grant number DAAL-03-92-G-0289 and the Office of Naval Research under grant number DOD ONR 14-92-J-1190.

## CONTENTS

### CHAPTER

1	INTRODUCTION . . . . .	1
1.1	Statement of Purpose . . . . .	1
1.2	Original Contributions . . . . .	2
1.3	Format and Outline . . . . .	2
2	EFFECTIVE INDEX OF REFRACTION MEASUREMENTS USING PRISM COUPLING . . . . .	3
2.1	Prism Coupling . . . . .	3
2.2	First-Order Analysis of Prism Coupling . . . . .	6
2.2.1	Analysis of the Effective Index Measurement . . . . .	7
2.2.2	Analysis of the M-Line's Profile . . . . .	8
2.3	Previous Models of Perturbation Effects . . . . .	13
2.4	Effective Index Measurement . . . . .	17
2.4.1	Experimental Setup . . . . .	17
2.4.2	Relative Effective Index Measurements . . . . .	19
2.4.3	Measurement Uncertainty Analysis . . . . .	21
2.4.4	Example M-Line Profiles and Effective Index Case History	22
2.5	Effective Index Perturbations . . . . .	25
2.5.1	Coupling Gap Geometry . . . . .	25
2.5.2	M-Line's Radiation Angle and Profile Perturbations . . .	26
2.5.3	Perturbation of the Substrate's Effective index . . . . .	28
2.6	A Local-Normal Mode Model of Prism Coupling . . . . .	29

2.6.1	Local normal mode algorithm . . . . .	30
2.6.2	Model Results . . . . .	32
2.7	Discussion . . . . .	33
3	NEARLY CUT-OFF MODES IN LITHIUM NIOBATE SLAB WAVE- GUIDES . . . . .	66
3.1	Introduction . . . . .	66
3.2	Background . . . . .	69
3.3	Waveguide Fabrication and Metrology . . . . .	73
3.3.1	Fabrication . . . . .	73
3.3.2	Metrology . . . . .	75
3.4	Experimental Results . . . . .	77
3.4.1	Titanium in-diffused $\text{LiNbO}_3$ waveguides . . . . .	77
3.4.2	Plain $\text{LiNbO}_3$ waveguides . . . . .	78
3.5	Diffusion Models . . . . .	80
3.5.1	Titanium in-diffusion model . . . . .	80
3.5.2	Lithium out-diffusion model . . . . .	82
3.5.3	Step-index model . . . . .	82
3.6	Discussion . . . . .	83
4	DIFFUSION PROCESSES IN LITHIUM NIOBATE . . . . .	97
4.1	SIMS Analysis of Plain $\text{LiNbO}_3$ Specimens . . . . .	97
4.2	SIMS Analysis of $\text{Ti:LiNbO}_3$ Specimens . . . . .	101
4.2.1	Titanium In-Diffusion . . . . .	101
4.2.2	SIMS of Y-Cut $\text{Ti:LiNbO}_3$ Specimens . . . . .	102
4.2.3	SIMS of X-Cut $\text{Ti:LiNbO}_3$ Specimens . . . . .	104
4.3	SIMS Analysis of $\text{TIPE:LiNbO}_3$ Specimen 33A . . . . .	106

4.4	Waveguide Attenuation . . . . .	106
4.5	Conclusions . . . . .	107
5	ON-AXIS POLARIZATION COUPLING IN Y-CUT TITANIUM IN- DIFFUSED LITHIUM NIOBATE SLAB WAVEGUIDES . . . . .	127
5.1	Introduction . . . . .	127
5.2	Waveguide Fabrication . . . . .	130
5.3	Waveguide Characterization . . . . .	132
5.4	Experimental Results . . . . .	136
5.5	Discussion . . . . .	139
5.5.1	Polarization coupling through rotation of the principal di- electric axes . . . . .	140
5.6	Summary . . . . .	148
5.7	Acknowledgments . . . . .	148
6	CONCLUDING STATEMENTS . . . . .	159
	BIBLIOGRAPHY . . . . .	160
	APPENDIX	
A	QUANTIFICATION OF SECONDARY ION MASS SPECTROSCOPY DATA FROM LITHIUM NIOBATE SPECIMENS . . . . .	168
A.1	Introduction to SIMS . . . . .	168
A.2	SIMS Calibration Procedures . . . . .	169
A.2.1	Depth Calibration . . . . .	170
A.2.2	Atom Density Calibration . . . . .	170
A.2.3	Stoichiometry of Lithium Niobate . . . . .	172
A.2.4	Calibration of Titanium Concentration . . . . .	174

## TABLES

### TABLE

2.1	Index of refraction for congruent lithium niobate [35] and rutile [36] at $\lambda = 0.6328 \mu\text{m}$ and $\lambda = 0.829 \mu\text{m}$ . . . . .	37
2.2	Set 1. Effective index versus coupling pressure for waveguide specimen 56 at $\lambda = 0.6328 \mu\text{m}$ . The relationship between the coupling pressures is $P_1^{(1)} < P_2^{(1)}$ . . . . .	37
2.3	Set 2. Effective index versus coupling pressure for waveguide specimen 56 at $\lambda = 0.6328 \mu\text{m}$ . The relationship between the pressures is $P_1^{(2)} < P_2^{(2)} < P_6^{(2)}$ . . . . .	38
3.1	The fabrication parameters for the $\text{LiNbO}_3$ specimens discussed in this Chapter. . . . .	86
3.2	Diffusion time is 2 h. Measured values of $\Delta N_{eff}$ for the fundamental TE waveguide mode are given for specimens fabricated using different diffusion atmospheres. The number of TE modes supported by each waveguide is also indicated. The entries for the lithium out-diffusion specimen were calculated using the lithium out-diffusion model described in Appendix 3.5.2 . . . . .	87

3.3	Diffusion time is 8 h. Measured values of $\Delta N_{eff}$ for the fundamental TE waveguide mode are given for specimens fabricated using different diffusion atmospheres. The number of TE modes supported by each waveguide is also indicated. The entries for the lithium out-diffusion specimen were calculated using the lithium out-diffusion model described in Appendix 3.5.2 . . . . .	87
3.4	Diffusion time is 21 h. Measured values of $\Delta N_{eff}$ for the fundamental TE waveguide mode are given for specimens fabricated using different diffusion atmospheres. The number of TE modes supported by each waveguide is also indicated. The entries for the lithium out-diffusion specimen were calculated using the lithium out-diffusion model described in Appendix 3.5.2 . . . . .	88
4.1	Area-densities of out-diffused lithium and in-diffused titanium. The negative value for specimen 100 indicates an abundance of lithium in comparison to the uniform concentration of an ideal congruent specimen. The thickness of evaporated titanium was 24.3 nm for specimen 42, 28.0 nm for specimen 56, and 25.0 nm for specimens X2, X3, X4, and X5. The lithium out-diffusion model is from [30] .	109
4.2	Effective indices of TE modes in specimens 42 and 56. Values represent the increment above the substrate index. The wavelength is $\lambda = 0.6328\mu\text{m}$ . . . . .	110
4.3	Effective indices of the $TE_0$ mode in x-cut specimens X2, X3, X4 and X5. Values represent the increment above the substrate index. The wavelength is $\lambda = 0.6328\mu\text{m}$ . . . . .	110

4.4	Waveguide attenuation measurements. Measured attenuation of the fundamental TE mode. The wavelength is $\lambda = 0.6328\mu\text{m}$ . . . . .	111
5.1	The difference between the TE mode effective index and the substrate extraordinary index ( $n_e = 2.2028$ ) are tabulated for the LiNbO <sub>3</sub> slab waveguides. Effective index measurements were made using prism out-coupling. Also listed are the phase-matching angles $\phi$ calculated using equation (5.4) and the substrate ordinary index $n_o = 2.2865$ . The effective mode index N was found by adding the substrate extraordinary index $n_e = 2.2028$ to the value of $\Delta N_{eff}$ . The values for $n_e$ and $n_o$ are from [35] . . . . .	149
5.2	Measured TE-TM coupling characteristics for the LiNbO <sub>3</sub> slab waveguides. . . . .	150
A.1	The variability of the averaged normalized lithium intensity. The average is taken over measurement cycles representative of the unperturbed lithium niobate substrate. . . . .	178

## FIGURES

### FIGURE

- |   |           |
|---|-----------|
| <p>2.1 Relevant features of the output prism-coupler. Effective index measurements reported in this dissertation were made using this prism-coupling arrangement. . . . .</p>   | <p>39</p> |
| <p>2.2 Construction in k-space illustrating the relationship between the radiation angle and the mode's effective index. The prism with index of refraction <math>n_p</math> occupies the upper half-space while the waveguide substrate with index of refraction <math>n_s &lt; n_p</math> occupies the lower half-space. Only one radiation direction in the prism space satisfies the phase-matching condition. In contrast, no directions in the substrate space satisfy the phase-matching condition. Thus, the m-line radiates only at the angle <math>\theta_m</math>. . . . .</p> | <p>40</p> |
| <p>2.3 Relationship between field amplitudes in Tien's [9] model describing output prism-coupling. The waveguide mode's initial field amplitude is <math>b_1(0)</math>. This field couples with the m-line field amplitude <math>b_3</math>. . . .</p>  | <p>41</p> |
| <p>2.4 Sketch of <math>b_3</math> in the rotated coordinate system <math>(x_r, z_r)</math>. Also shown is the field truncation resulting from finite coupling length <math>L_c</math>. . . . .</p>  | <p>42</p> |
| <p>2.5 Input prism-coupling for effective index measurement using dark m-line characteristics. . . . .</p>  | <p>42</p> |

- 2.6 Effective index perturbation  $\delta N$  versus effective index  $N$  and gap height  $s$  (in micrometers) for the prism-waveguide structure in Figure 2 of [7]. The range of  $s$  includes strong coupling ( $s < 0.2 \mu\text{m}$ ) to beyond the weak-coupling condition ( $s > 0.2 \mu\text{m}$ ). The boundary between weak and strong coupling is specific to the waveguide structure in Figure 2 of [7]. The black shaded region of this plot indicates that  $\delta N$  is positive whereas the white shaded region indicates  $\delta N$  is negative. . . . . 43
- 2.7 Effective index perturbation  $\delta N$  versus effective index  $N$  with gap height  $S = 0.2 \mu\text{m}$  for the prism-waveguide structure in Figure 2 of [7]. The sign of  $\delta N$  is negative for  $N$  less than 2.14 and positive elsewhere. . . . . 44
- 2.8 Experimental setup for effective index measurements using output prism coupling. . . . . 45
- 2.9 Geometric construction for determining the m-line radiation angle in the stage coordinate system  $\theta'_{m,s}$ . The CCD array is translations  $\Delta x_s$  and  $\Delta y_s$  form a right triangle. The radiation angle is found from this triangle using  $\theta'_{m,s} = \arctan(\Delta x_s / \Delta y_s)$ . . . . . 46
- 2.10 Measuring the misalignment between the translation stages and the prism output face. Inset shows the relationship between the stage's coordinate system  $(x_s, y_s)$  and the prism's coordinate system  $(x_p, y_p)$ . The rotation angle between these two coordinate systems is  $\gamma$ . . . 47

2.11	Exciting the substrate radiation mode by positioning the input fiber. Inset illustrates the phase-matching condition Equation (2.1) for the substrate radiation mode. We use the substrate effective index for $N_{sub}$ to reduce systematic uncertainties when measuring mode effective index. . . . .	48
2.12	Mode TE-0 m-line irradiance profiles of a titanium in-diffused slab waveguide ( $\lambda = 0.6328 \mu\text{m}$ ) versus position along the CCD array. The solid curve corresponds to the far propagation distance while the dashed curve corresponds to the near propagation distance. The difference between propagation distances is 50.00 mm. These irradiance profiles have been normalized to 1 and shifted so that their maximum values coincide. . . . .	49
2.13	Displacement of m-line maximum irradiance from far-field propagation direction versus propagation distance. . . . .	50
2.14	Increment above the substrate index of refraction for mode effective index versus diffusion time. The fundamental mode's effective index is TM-0 and that of the first higher order mode is TM-1. Theoretical curves are fitted to measured data points using the parameters in Equation (2.27). . . . .	51
2.15	Titanium concentration versus substrate depth for 2 h diffusion (specimen 42). SIMS data are the short-dash curve. The solid curve is a Gaussian fit using $D = 0.245 \mu\text{m}^2/\text{h}$ . The long-dash curve is a Gaussian fit using $D = 0.2 \mu\text{m}^2/\text{h}$ . . . . .	52
2.16	Schematic cross section of prism coupling region at initial contact between prism and waveguide. . . . .	53

2.17 Schematic cross section of prism coupling region for high pressure applied to prism and waveguide. . . . .	54
2.18 Comparing Set 1 TE-0 m-line profiles for low $P_1^{(1)}$ and high $P_2^{(1)}$ coupling pressures. . . . .	55
2.19 Comparing Set 1 TE-3 m-line profiles for low $P_1^{(1)}$ and high $P_2^{(1)}$ coupling pressures. . . . .	56
2.20 Comparing Set 1 TE-0 m-line profile to the TE-3 m-line profile when the coupling pressure is low $P_1^{(1)}$ . . . . .	57
2.21 Comparing Set 1 TE-0 m-line profile to the TE-3 m-line profile when the coupling pressure is high $P_2^{(1)}$ . . . . .	58
2.22 Measurements of m-line's irradiance profile full-width at half-maximum at various coupling pressures of Set 2. The coupling pressures increases from $P_1^{(2)}$ to $P_7^{(2)}$ . . . . .	59
2.23 Measuring the TE substrate mode effective index versus angle of incidence $\theta_i$ at $\lambda = 0.829 \mu\text{m}$ . The open circles represent measurement set A while the filled circles represent measurement set B. The continuous line is a fit to the measured data for $\theta_i < 87.5^\circ$ using the first-order model which ignores the prism-waveguide perturbation. This fit yields an effective index of 2.1712 at $\theta_i = 90^\circ$ . The filled square represents the highest order TE guided mode effective index. We have widened the uncertainty bars of data set B as a graphical visualization aid. . . . .	60
2.24 Geometry of composite waveguide for the local normal mode model for prism coupling. The segmented prism and unperturbed waveguide form composite waveguides. . . . .	61

2.25 Comparison between the $TE_0$ mode of the unperturbed waveguide and the excited modes of the composite waveguide. . . . .	62
2.26 Evolution of the composite waveguide modes under the prism. . .	63
2.27 Irradiance distribution within the prism showing the evolution of the m-line. . . . .	64
2.28 Near-field M-line irradiance profile calculated using the local normal mode model of output prism-coupling. . . . .	65
3.1 The waveguide orientation and mode propagation direction relative to the $LiNbO_3$ crystal's axes. The extraordinary index is $n_e =$ 2.2028 and the ordinary index is $n_o = 2.2865$ at the wavelength $\lambda = 0.6328 \mu m$ [35] . . . . .	89
3.2 Schematic diagram of the diffusion furnace (not drawn to proportion) illustrating the flow of gas into the furnace chamber. . . . .	90
3.3 Prism out-coupler setup used to measure the effective index of the modes in the planar $LiNbO_3$ waveguides. . . . .	91

- 3.4 TE waveguide mode dispersion curves for titanium in-diffused lithium niobate planar waveguide specimens 41, 42, 43, and 48. Experimentally measured values of  $\Delta N$  are represented by discrete symbols with error bars. The fundamental TE mode was confidently identified in each specimen and its value of  $\Delta N$  is indicated by empty circle symbols. The order number for the higher-order modes could not be determined with the same confidence so values of  $\Delta N$  for all these modes are indicated using filled circle symbols. Calculated results from the titanium diffusion model yield three guided modes. These modes are shown as continuous lines:  $TE_0$ , solid line style;  $TE_1$ , dashed line style;  $TE_2$ , dash-dot line style . . . . . 92
- 3.5 TM waveguide mode dispersion curves for titanium in-diffused lithium niobate planar waveguide specimens 41, 42, 43, and 48. Experimentally measured values of  $\Delta N$  are represented by discrete symbols with error bars. Experimental observations confidently identified both the fundamental and the first higher-order modes. These modes are indicated by different plot symbols:  $TM_0$ , empty circles;  $TM_1$ , filled circles. Calculated results from the titanium diffusion model yield two guided modes. These modes are shown as continuous lines:  $TM_0$ , solid line style;  $TM_1$ , dashed line style. . . . . 93

- 3.6 Comparison between measured  $\Delta N$  from waveguide specimens diffused in air and calculated  $\Delta N$  from lithium out-diffusion and step-index models. Measured values of  $\Delta N$  for the fundamental mode in specimens diffused in air are represented by plus signs. Calculated values of  $\Delta N$  for the fundamental mode of a lithium out-diffused waveguide (calculated using the lithium out-diffusion model discussed in Appendix 3.5.2 ) are represented by square symbols. Calculated values of  $\Delta N$  for the fundamental mode of a step-index waveguide (calculated using the step index waveguide model discussed in Appendix 3.5.3 ) are represented by triangles. The number of guided modes found in each type of waveguide is indicated by the numbers adjacent to each plot symbol. . . . . 94
- 3.7 Comparison between measured  $\Delta N$  from waveguide specimens diffused in dry-oxygen and calculated  $\Delta N$  from lithium out-diffusion and step-index models. Measured values of  $\Delta N$  for the fundamental mode in specimens diffused in dry-oxygen are represented by empty circles. Calculated values of  $\Delta N$  for the fundamental mode of a lithium out-diffused waveguide (calculated using the lithium out-diffusion model discussed in Appendix 3.5.2 ) are represented by square symbols. Calculated values of  $\Delta N$  for the fundamental mode of a step-index waveguide (calculated using the step index waveguide model discussed in Appendix 3.5.3 ) are represented by triangles. The number of guided modes found in each type of waveguide is indicated by the numbers adjacent to each plot symbol. . . . . 95

3.8	Comparison between measured $\Delta N$ from waveguide specimens diffused in wet-oxygen and calculated $\Delta N$ from a lithium out-diffusion model. Measured values of $\Delta N$ for the fundamental mode in specimens diffused in wet-oxygen are represented by filled circles. Calculated values of $\Delta N$ for the fundamental mode of a lithium out-diffused waveguide (calculated using the lithium out-diffusion model discussed in Appendix 3.5.2 ) are represented by square symbols. The number of guided modes found in each type of waveguide is indicated by the numbers adjacent to each plot symbol. Results from the step-index waveguide model did not agree with $\Delta N$ measurements from the wet-oxygen diffused waveguides. . . . .	96
4.1	Lithium concentration for plain waveguide specimens 50B, 51, and 53. Diffusion time is 2 h and diffusion temperature is 1000 °C . Also shown is the lithium concentration from untreated $\text{LiNbO}_3$ specimen 100. This data was processed by Evans East. . . . .	112
4.2	Hydrogen concentration for plain waveguide specimens 50B, 51, and 53. Diffusion time is 2 h and diffusion temperature is 1000 °C . This data was processed by Evans East. . . . .	113
4.3	Lithium and hydrogen concentration profiles for specimen 50A (21 h diffusion in air without titanium). This SIMS data was processed by Evans East. . . . .	114

- 4.4 Lithium concentration for plain waveguide specimens 53 and 54. Diffusion time is 2 h for specimen 53 and 21 h for specimen 54. The diffusion temperature for these specimens was 1000 °C and the diffusion atmosphere was flowing oxygen bubbled through water. This data was processed by Evans East. . . . . 115
- 4.5 Hydrogen concentration for plain waveguide specimens 50A, 52, and 54, and untreated specimen 100. The diffusion time is 21 h and the diffusion temperature is 1000 °C for the waveguide specimens. This data was processed by Evans East. . . . . 116
- 4.6 Lithium concentrations from waveguide specimens 42 and 56. The diffusion atmosphere was oxygen bubbled through water for specimen 42 and argon bubbled through water for specimen 56. The diffusion time is 2 h and the diffusion temperature is 1000 °C for both waveguide specimens. I processed this SIMS data. . . . . 117
- 4.7 Normalized lithium concentrations in  $\text{Ti:LiNbO}_3$  specimens 42 and 56, and plain specimens 51 and 53. The diffusion atmosphere was oxygen bubbled through water for specimens 42 and 53, and argon bubbled through water for specimens 51 and 56. The diffusion time is 2 h and the diffusion temperature is 1000 °C for all of these specimens. . . . . 118
- 4.8 Titanium concentrations from waveguide specimens 42 and 56. The diffusion atmosphere was oxygen bubbled through water for specimen 42 and argon bubbled through water for specimen 56. The diffusion time is 2 h and the diffusion temperature is 1000 °C for both waveguide specimens. I processed this SIMS data. . . . . 119

- 4.9 Lithium concentration in x-cut  $\text{Ti:LiNbO}_3$  specimens. The diffusion time is 1 h for specimen X2, 2 h for specimen X3, 4 h for specimen X4, and 2 h for specimen X5. The diffusion temperature was 950 °C for specimens X2, X3, and X4, and 1050 °C for specimen X5. The diffusion atmosphere was ambient air and the titanium thickness was 25 nm for all of these specimens. These x-cut specimens were fabricated by Ms. Milica Popovic, and I processed this SIMS data according to Appendix A . . . . . 120
- 4.10 Detailed view of the lithium concentration in x-cut  $\text{Ti:LiNbO}_3$  specimens. The diffusion time is 1 h for specimen X2, 2 h for specimen X3, 4 h for specimen X4, and 2 h for specimen X5. The diffusion temperature was 950 °C for specimens X2, X3, and X4, and 1050 °C for specimen X5. The diffusion atmosphere was ambient air and the titanium thickness was 25 nm for all of these specimens. These x-cut specimens were fabricated by Ms. Milica Popovic, and I processed this SIMS data according to Appendix A . . . . . 121
- 4.11 Titanium concentration in x-cut  $\text{Ti:LiNbO}_3$  specimens plotted using a logarithmic scale. The diffusion time is 1 h for specimen X2, 2 h for specimen X3, 4 h for specimen X4, and 2 h for specimen X5. The diffusion temperature was 950 °C for specimens X2, X3, and X4, and 1050 °C for specimen X5. The diffusion atmosphere was ambient air and the titanium thickness was 25 nm for all of these specimens. These x-cut specimens were fabricated by Ms. Milica Popovic, and I processed this SIMS data according to Appendix A . . . . . 122

4.12	Details of titanium concentration in x-cut Ti:LiNbO <sub>3</sub> specimens. The diffusion time is 1 h for specimen X2, 2 h for specimen X3, 4 h for specimen X4, and 2 h for specimen X5. The diffusion temperature was 950 °C for specimens X2, X3, and X4, and 1050 °C for specimen X5. The diffusion atmosphere was ambient air and the titanium thickness was 25 nm for all of these specimens. These x-cut specimens were fabricated by Ms. Milica Popovic, and I processed this SIMS data according to Appendix A . . . . .	123
4.13	Atomic concentrations in TIPE:LiNbO <sub>3</sub> specimen 33A. This SIMS data was processed by Evans East (file 94171_52). . . . .	124
4.14	Effective index of the fundamental TE mode in TIPE:LiNbO <sub>3</sub> specimens. Effective index is plotted as a function of exchange time and annealing time. . . . .	125
4.15	Titanium concentration in y-cut specimen 42 and x-cut specimens x3 and x5. The diffusion time for all of these specimens is 2 h. . . .	126
5.1	The waveguide orientation and mode propagation direction relative to the LiNbO <sub>3</sub> crystal's axes. The extraordinary index is $n_e = 2.2028$ and the ordinary index is $n_o = 2.2865$ at the wavelength $\lambda = 0.6328 \mu\text{m}$ [35] . . . . .	151
5.2	The experimental setup used to observe the intensity patterns emerging from the waveguide specimens. The polarization of the emerging radiation is determined using the polarizing analyzer. . . . .	152
5.3	Illustration of phase matching between the TE polarized waveguide and the TM radiation mode. The TE mode propagates with effective index $N$ while the TM mode propagates with refractive index $n_o$ . . .	153

5.4	Depth dependence of titanium concentration and absolute value of strain within specimen 42 after diffusion. Measured titanium concentration is compared to the Gaussian solution to the diffusion equation. The Gaussian profile was fitted with the following parameter values: the surface concentration $C_{Ti}(0)$ is $2.31 \times 10^{21}$ atoms/cm <sup>3</sup> and the 1/e diffusion depth is 1.4 $\mu$ m. The strain along the crystal's y-axis $S_y$ is calculated using the Gaussian titanium concentration profile and the linear relationship between strain and titanium concentration calculated from the data in [62] . . . . .	154
5.5	Intensity pattern emerging from specimen 41 as seen on the viewing screen. The central region is TE polarized while both the upper and lower regions are TM polarized. . . . .	155
5.6	Detailed view of branch A radiation from specimen 53. The on-axis intensity minimum is indicated by the arrow. . . . .	156
5.7	Detailed view of branch A radiation from specimen 41. . . . .	156
5.8	Temperature dependence of $S_2/C_s(Ti)$ from [62] where $S_2$ is the strain along the y-axis and $C_s(Ti)$ is the surface concentration of titanium in atoms/cm <sup>3</sup> . . . . .	157

5.9	Depth dependence of the change in principal refractive index $\Delta n$ and the principal axes rotation angles $\alpha$ within specimen 42 after diffusion. The change in refractive index between the principal axes $x$ and $x'$ is $\Delta n_x$ , between principal axes $y$ and $y'$ is $\Delta n_y$ and between principal axes $z$ and $z'$ is $\Delta n_z$ . The rotation angles are found by taking the vector dot product between corresponding principal dielectric axes. The angle between $x$ and $x'$ is $\alpha_x$ , the angle between $y$ and $y'$ is $\alpha_y$ and the angle between $z$ and $z'$ is $\alpha_z$ . . . . .	158
A.1	Raw intensity data from SIMS measurements of the implanted titanium standard. Data is from Evans East file 41785.10. . . . .	179
A.2	Raw titanium intensity $I_{Ti}$ from SIMS measurements of x-cut titanium in-diffused lithium niobate specimens. The in-diffusion time was 1 h for specimen x2, 2 h for specimen x3, and 4 h for x4. The in-diffusion temperature was 950 °C . . . . .	180
A.3	Titanium densities for the x-cut specimens calibrated using my procedure discussed in Section A.2.4 . The in-diffusion time was 1 h for specimen x2, 2 h for specimen x3, and 4 h for x4. The in-diffusion temperature was 950 °C . . . . .	181
A.4	Titanium densities for the x-cut specimens calibrated by Evans East. The in-diffusion time was 1 h for specimen x2, 2 h for specimen x3, and 4 h for x4. The in-diffusion temperature was 950 °C . . . . .	182

## CHAPTER 1

### INTRODUCTION

#### 1.1 Statement of Purpose

This dissertation presents my research of the prism coupler, and optical waveguides in lithium niobate.

I have studied prism coupling to determine its capabilities and limitations as a means to measure the effective index of refraction (to be known as "effective index" and denoted by  $N$ ) of a waveguide mode. Important questions regarding the accuracy and precision of this measurement remain unanswered. Resolving these issues is important because the effective index is a critical waveguide characteristic. Often, the effective index is used as a parameter for evaluating waveguide materials, fabrication procedures and waveguide designs. Furthermore, the effective index is used as a calibration parameter for waveguide computer aided design (CAD) algorithms. Thus, accurate and precise measurement of the effective index is prerequisite to realizing cost effective and high performance waveguide devices.

The planar waveguide is the simplest waveguide geometry. Measuring the optical characteristics of planar waveguides can provide information on the properties of the material forming the waveguide. This information is used to evaluate materials according to their ability to form high performance waveguides. I evaluated both titanium in-diffused and plain lithium niobate planar waveguides and found that the current models do not explain all of their observed optical properties. Only after accurate models are found can high performance integrated

optical devices be fabricated in lithium niobate.

## 1.2 Original Contributions

My work resulted in original contributions to the fields of lithium niobate integrated optics, and waveguide metrology. These contributions are:

- The discovery and characterization of polarization coupling in titanium in-diffused lithium niobate planar waveguides.
- The discovery and characterization of nearly cut-off modes in lithium niobate.
- The experimental verification and modeling of effective index perturbations due to prism coupling.

This work has produced one published paper [1], and two additional manuscripts have been submitted [2, 3] and are currently in the review process.

## 1.3 Format and Outline

Chapter 2 discusses the prism coupler. Chapter 3 discusses nearly cut-off modes in lithium niobate optical waveguides. Chapter 4 continues the work in Chapter 3 by discussing secondary ion mass spectroscopy measurements of lithium niobate waveguides. Chapter 5 presents measurements of polarization coupling in  $\text{Ti:LiNbO}_3$  planar waveguides. Appendix A explores calibration and data processing issues related to this analytical measurement.

Chapters 2, 3, and 5 are essentially self contained manuscripts. By this I mean these chapters begin with an introduction that presents relevant background material and places this work in the context of related works, and ends with a discussion of the results and their implications.

## CHAPTER 2

### EFFECTIVE INDEX OF REFRACTION MEASUREMENTS USING PRISM COUPLING

We investigate the accuracy and precision of effective index of refraction measurements using prism coupling. The coupling gap's geometry is critical to predicting the accuracy and resolution of measurements. We provide experimental evidence that there are advantages to using high coupling pressures that yield long coupling lengths. Furthermore, effective index perturbations vary with mode number in some cases. We present and evaluate an experimental technique aimed at reducing the effects of perturbation and find that it may not be applicable to all situations. We extend a previous model of prism coupling to include a finite coupling length. This allows us to explain some of our experimental observations of m-line characteristics. Comparing other previous models yields some disagreements in regard to predicting effective index perturbations. Also, we introduce an alternative model of prism coupling based upon a local normal-mode expansion and present its preliminary numerical results. Finally, our results indicate that using prism coupling to measure effective index beyond the fourth decimal place will require additional experimental and numerical techniques.

#### 2.1 Prism Coupling

The prism coupler couples modes of optical waveguides with the radiation modes of free space. The prism coupler can, for example, inject light into waveguides from optical sources and remove light from waveguides for detection,

and is used in waveguide metrology. This chapter deals with the issues of prism out-coupling as they relate to waveguide metrology, more specifically, the measurement of a mode's effective index of refraction (or, just "effective index")  $N$ .

According to [4] the first experimental results of prism-coupling light into and out of waveguides was reported in 1964 [5]. Since then, prism coupling became an area of active research with many articles describing its theory [6, 7, 8, 9, 10, 11, 12, 13, 14], numerical calculations of its operation [15, 16, 17, 18], and its application to effective index measurements [19, 20, 21, 22].

However, one aspect of prism coupling has been analyzed only for special cases and is lacking experimental investigation. This is the perturbation of the effective index by the presence of the prism. The prism locally affects the boundary conditions of the waveguide and changes the properties of the effective index. This introduces an uncertainty that prevents accurate measurement of the mode effective indexes. Understanding the concept of this perturbation in prism coupling is aided by the quantum mechanical axiom which states that the act of measuring affects the outcome of the measurement.

The usual way to minimize this perturbation uncertainty is to reduce the coupling strength and therefore the coupling efficiency, to the point where m-lines are just visible enough for measurement. Theoretical investigations have been made into the conditions leading to this weak coupling but not experimental investigations. This is probably because weak coupling is often used. In fact, the weak coupling condition, to be obtained by reducing coupling pressure, is explicitly cited as part of the experimental procedure for measuring  $N$  [23, 20]. What is needed are experimental procedures to obtain and verify weak coupling, or better, quantify and compensate for the perturbation regardless of the coupling

strength.

The need for accurate and precise measurements of effective index become especially important when these effective indices are used to calibrate optical CAD algorithms, construct index of refraction profiles [24], or to design integrated optical components such as directional couplers and waveguide lenses [25]. Calibrating waveguide fabrication parameters is one example where accurate effective index measurements are important. Usually, measuring effective indices of all the modes propagating in a waveguide is necessary to calibrate the associated fabrication process. Otherwise, overlooking some modes will result in obtaining incorrect fabrication parameters. Our experimental observations indicate that strong (not weak) coupling is needed to resolve and measure modes whose effective indices are closely spaced.

In contrast to accuracy, precision determines how exactly we measure. Measuring  $N$  within 0.01% is a typical precision requirement. For example, an uncertainty of 0.015% in effective index causes a power-coupling loss of 3 dB when designing waveguide lenses to couple light into channel waveguides.

The accuracy and precision requirements will become more strict with increasing demand for high-performance and cost-effective guided wave optical components. This is the motivation for our investigation of prism coupling. The goals of this investigation are to determine experimental procedures and theoretical models for recovering the unperturbed effective index. This includes modeling the prism-waveguide interaction, predicting the dependency of m-line characteristics such as profile and propagation direction on coupling geometry, determining the optimal set of experimental parameters, and finally, encouraging others to make additional contributions regarding perturbation effects on effective index

measurements.

The organization of this chapter is the following. The next section presents a first-order analysis of prism coupling. Section 2.3 follows with a discussion of previous models of prism coupling which consider perturbation effects. Section 2.4 describes the experimental setup and the experimental procedure used throughout this dissertation for effective index measurements. Section 2.5 presents experimental results from investigations into perturbation effects. The final section discusses these experimental results and model predictions and compares them to other published results.

## 2.2 First-Order Analysis of Prism Coupling

Figure 2.1 schematically illustrates the relevant features and parameters of output prism coupling. This is the prism coupling set-up used to make the effective index measurements reported throughout this dissertation. Pressing a prism onto the surface of a waveguide forms the prism-coupler. A requirement for successful prism coupling is that the prism's index of refraction must be greater than the waveguide mode's effective index. The coupling between the prism and waveguide mode extends over the length  $L_c$ . We estimate from experimental observations that the coupling length is several hundred micrometers. The height of the gap determines the coupling strength between the prism and waveguide. In some cases, spacers are used to engineer the gap's geometry [13]. Other times dust particles and surface irregularities determine the gap's geometry. The height of the gap should be a fraction of a wavelength to efficiently couple light from the waveguide. However, the gap should be as large as possible during effective index measurements to minimize perturbation effects. The out-coupled radiation forms irradiance patterns called m-lines. Each m-line is associated with a particular

waveguide mode. Furthermore, the gap geometry and the mode's effective index determine the characteristics of each m-line.

Next, we present a first-order analysis describing the measurement of the effective index using m-lines. This analysis is for weak coupling and assumes the prism and waveguide are composed of loss-less dielectric materials. In addition, we assume a uniform gap of infinite length. Afterwards, in Section 2.2.2 we discuss the m-line's irradiance distribution, or profile.

**2.2.1 Analysis of the Effective Index Measurement** The following description of out-coupling a waveguide mode through a prism uses coupled-mode theory [23, 26, 27]. This description applies to weak coupling where the presence of the prism does not alter the mode's effective index. The waveguide mode propagates along the waveguide until it reaches the region of the prism. Here, the waveguide mode's evanescent tail interacts with the prism's higher index of refraction. This interaction causes the waveguide modes to couple with a prism radiation mode. The radiation mode propagates in a particular direction determined by satisfying the phase-matching condition. The phase-matching condition is given by

$$N_m = n_p \sin \theta_m, \quad (2.1)$$

where  $n_p$  is the prism's index of refraction, and  $\theta_m$  is the radiation angle internal to the prism that is determined by a particular effective index  $N_m$ . Figure 2.2 is a k-space construction illustrating the relationship between the radiation angle and the mode's effective index. The idea behind the selectivity of the phase-matching condition is that only the radiation mode satisfying Equation (2.1) will constructively couple with the waveguide mode over distances greater than a few wavelengths. All other radiation modes will be out of phase with the waveguide

mode and therefore never reach an appreciable field strength.

The radiation mode continues to propagate away from the waveguide at the angle  $\theta_m$  until exiting the prism. There, it refracts into the radiation angle  $\theta'_m$  according to Snell's law. The optical irradiance distribution associated with this radiated mode appears as a distinct line at distances greater than about 1 m from the prism. This pattern of light is called a bright m-line or just an m-line. Measuring the m-line's radiation angle  $\theta'_m$  determines the effective index according to [23]

$$N_m = n_p \sin \left[ \phi_p + \arcsin \left( \frac{n_c}{n_p} \sin \theta'_m \right) \right], \quad (2.2)$$

where  $\phi_p$  is the prism's angle, and  $n_c = 1$  is the index of air. Furthermore, the m-line associated with each mode will radiate at a different angle because every mode has a different effective index.

**2.2.2 Analysis of the M-Line's Profile** This section presents an analysis describing the m-line's profile by combining the first-order coupled-mode model with an extension of the analysis by Tien [9]. This analysis expands Tien's work to include a finite coupling length and extends his analysis to predict the m-line's far-field irradiance distribution using the radiation angle of Section 2.2.1. First, we summarize the analysis by Tien.

Tien uses the concept of optical tunneling to describe the penetration of optical power across the gap's refractive index barrier. Figure 2.3 shows a diagram of output prism coupling illustrating the concepts used in Tien's analysis. A waveguide mode has initial amplitude  $b_1(z = 0)$  at positions  $z \leq 0$ . This mode begins to interact with the prism at  $z = 0$ , where it couples to the radiation mode of amplitude  $b_3(z)$ . The coupling continues for all  $z \geq 0$ . This coupling depletes

the field amplitude of the waveguide mode according to

$$\frac{db_1(z)}{dz} = -S b_1(z), \text{ for } 0 \leq z \leq L_c, \quad (2.3)$$

where  $S$  is the coupling strength. The coupling strength is constant for all  $z \geq 0$ .

The solution to Equation (2.3) is

$$b_1(z) = \begin{cases} b_1(0) & \text{for } z < 0 \\ b_1(0) \exp(-S z) & \text{for } z \geq 0 \end{cases} \quad (2.4)$$

The power lost by the waveguide mode at any position  $z \geq 0$  is proportional to  $b_1(z) b_1^*(z)$ . This power reappears in the prism as the radiation mode  $b_3$ . According to Tien, the  $z$ -dependence of the radiation mode's field amplitude is

$$b_3(z) = \begin{cases} 0 & \text{for } z < 0, \\ b_3(0) \exp(-S z) & \text{for } z \geq 0. \end{cases} \quad (2.5)$$

Equation (2.5) is the relevant result of Tien's analysis. This result shows that the radiation mode's (or m-line's) initial field distribution is a decaying exponential along the  $z$ -axis.

We can extend Tien's result by combining the field distribution in Equation (2.5) with a propagation direction. This will allow us to calculate the m-line's far-field irradiance distribution. The m-line's propagation direction was given by the phase-matching condition in Equation (2.1). Furthermore, we can truncate the initial field distribution by introducing a finite coupling length  $L_c$ . Thus, using the phase-matching angle and the finite coupling length, we write the m-line's complete initial field distribution (omitting the harmonic time dependence) as

$$b_3(x, z) = \begin{cases} 0 & \text{for } z < 0, \\ b_3(0) \exp(-S z) \exp[i n_p k (x \cos \theta_m + z \sin \theta_m)] & \text{for } 0 \leq z \leq L_c, \\ 0 & \text{for } z > L_c, \end{cases} \quad (2.6)$$

where  $k = 2\pi/\lambda$  and  $\lambda$  is the wavelength of free space. In addition, we express  $b_3(z)$  in a rotated coordinate system  $(x_r, z_r)$  such that the m-line's propagation direction is only along  $x_r$ :

$$b_3(x_r, z_r) = \begin{cases} 0 & \text{for } z_r < 0, \\ b_3(0) \exp(i n_p k x_r - S z_r \sec \theta_m) & \text{for } 0 \leq z_r \leq L_c \cos \theta_m, \\ 0 & \text{for } z_r > L_c \cos \theta_m, \end{cases} \quad (2.7)$$

where we have used the coordinate substitutions

$$\begin{aligned} x_r &= x \cos \theta_m \\ z_r &= z \cos \theta_m \end{aligned} \quad (2.8)$$

Equation (2.7) describes the m-line's initial field distribution, which we will propagate into the far field. Figure 2.4 sketches the form of  $b_3(x_r, z_r)$  illustrating the rotated coordinates  $x_r$  and  $z_r$ . The field distribution in Equation (2.7) is similar to the result of the analysis based on leaky modes found on pages 102-103 of [23]. Those results differ from Equation (2.7) by omitting the effects of a finite coupling length. Next, we calculate the m-line's far-field irradiance distribution.

Consider Equation (2.7) as describing the field in a coordinate system  $z_r$ . We define a new coordinate system  $z'_r$  which is a distance  $x_r$  from  $z_r$ . We would like to find the field distribution  $b'_3$  in the  $z'_r$  coordinate system. We will ignore prism boundaries and assume the m-line propagates in a half-space of refractive index  $n_p$ . If  $x_r$  satisfies the Fraunhofer, or far-field, requirements [28] then  $b'_3$  is found using

$$b'_3(x_r, \nu) \propto \int_{-\infty}^{\infty} b_3(x_r, z_r) \exp(i 2\pi n_p \nu z_r) dz_r, \quad (2.9)$$

where

$$\nu \equiv \frac{z'_r}{\lambda x_r}. \quad (2.10)$$

Substituting Equation (2.7) into Equation (2.9) yields

$$b'_3(x_r, \nu) \propto \int_0^{L_c \cos \theta_m} \exp[(i 2\pi n_p \nu - S \sec \theta_m) z_r] dz_r \exp(in_p k x_r). \quad (2.11)$$

Evaluating the integral in Equation (2.11) yields

$$\begin{aligned} b'_3(x_r, \nu) &\propto \frac{\exp[(i 2\pi n_p \nu - S \sec \theta_m) z_r] \Big|_0^{L_c \cos \theta_m}}{i 2\pi n_p \nu - S \sec \theta_m} \exp(in_p k x_r) \\ &\propto \frac{\exp[(i 2\pi n_p \cos \theta_m \nu - S) L_c] - 1}{i 2\pi n_p \nu - S} \exp(in_p k x_r). \end{aligned} \quad (2.12)$$

The far-field irradiance distribution  $I'_3$  is proportional to  $(b'_3)(b'_3)^*$  yielding

$$I'_3(x_r, \nu) \propto \frac{1 + \exp(-S L_c) [\exp(-S L_c) - 2 \cos(2\pi n_p \cos \theta_m \nu L_c)]}{S^2 + (2\pi n_p \nu)^2}. \quad (2.13)$$

$I'_3(x_r, \nu)$  depends on  $z'_r$  by way of  $\nu \equiv z'_r / \lambda x_r$ .

Equation (2.13) predicts the far-field characteristics of the m-line's irradiance distribution within the frame work of the first-order analysis for weak coupling and uniform gap height. One other simplifying approximation was the omission of the prism boundary. Thus, Equation (2.13) neglects the refraction of the m-line at the prism-air interface. One straightforward way to include refraction, that remains within the confines of the first-order model, is to assume that the m-line has a planar phase front when it reaches the index boundary. Then we can apply Snell's law and use another appropriately rotated coordinate system in which to express the far-field distribution. This planar phase-front assumption is implied in the development of Equation (2.2).

A higher-order correction for refraction at the prism boundary can be made to Equation (2.13). For example, we could regard the index boundary as being in the near-field or Fresnel zone of the initial field distribution. Thus, we would propagate the field  $b_3$  in Equation (2.7) to the index boundary using

Fresnel approximations [28]. There, we could incorporate Snell's law and finish the propagation to the far field.

Even without making this modification we can still use Equation (2.13) qualitatively to identify certain m-line characteristics that will aid in effective index measurements. Equation (2.13) predicts a maximum value for  $I'_3$  at  $z'_r = 0$ . We determine this by evaluating the first and second partial derivatives with respect to  $\nu$  of  $I'_3$ . This means that the irradiance maximum propagates at the radiation angle  $\theta'_m$ . We can use this m-line characteristic to measure the radiation angle  $\theta'_m$  and thus determine  $N_m$ . We can accomplish this by first determining the radiation angle from a geometric construction that is formed by tracking the position of the irradiance maximum for two different values of  $x_R$ . Then, we can calculate  $N_m$  using Equation (2.2).

Another m-line characteristic given by Equation (2.13) is the dependence of the irradiance distribution on coupling length  $L_c$ . For a given weak coupling strength (small  $S$ ) the irradiance distribution will be broader for short  $L_c$ , and conversely, narrower for long  $L_c$ . This characteristic will have consequences regarding the resolving power of the prism coupler.

One consequence of coupled-mode theory is that energy couples from the first mode to the second, and then back to the first mode. Even though this back-and-forth coupling results from the mathematics, there is neither the experimental evidence nor any aspect of the physical model for prism coupling to support this result. One possible way to resolve this point is to consider that the necessary coupling length for the return coupling is longer than  $L_c$ .

While this first-order model does not predict perturbations on the effective index, it provides a qualitative description of the m-line's far-field irradiance

distribution. The next Section discusses higher-order models which calculate the effective index perturbation for the weak coupling.

### 2.3 Previous Models of Perturbation Effects

The first-order model falls short in addressing an important issue related to the accuracy of effective index measurements. It does not determine the perturbation to the effective index due to the prism. Previous models address effective index perturbations, but they do so in the context of input prism coupling. As a consequence, these models often emphasize input coupling efficiency. The approaches taken by these previous models include transverse resonance [23], ray optics [14], a combination of ray and wave optics [6], optical tunneling [9], plane-wave expansion [7, 8], and the matrix method [15, 16, 17, 18].

This Section looks at some of these previous models and discusses their results regarding the perturbation of effective index. But first, we provide a brief introduction to input prism coupling.

A prism can couple light into a waveguide as well as couple light out of a waveguide. We can visualize input prism coupling by reversing the ray directions in Figure 2.1. This is also used as another technique to measure effective index. It is called the dark m-line measurement and is shown in Figure 2.5. Here, light is incident upon the prism at the angle  $\theta_i$ . This incident light undergoes total internal reflection at the prism base and creates an evanescent field. This evanescent field couples with waveguide modes at certain values of  $\theta_{i,m}$  that satisfy the phase-matching condition, Equation (2.1). These waveguide modes suffer effective index perturbations just as in the case of input prism coupling. The reflected irradiance, however, is a minimum at these phase-matching angles of incidence. Thus, monitoring the reflected light  $R(\theta_i)$  and noting the angle of incidence where  $R(\theta_i)$  is

a minimum (dark) determines the effective index. The output prism-coupler can also measure effective index by using bright m-lines. These bright m-lines are a result of the waveguide mode, which was excited by input-coupling, subsequently out-coupling through the same prism. Thus, the appearance of this bright m-line will signal a phase-matching angle of incidence.

Ulrich [7] analyzes input prism coupling using a plane-wave expansion with emphasis on coupling efficiency. However, he provides numerical results and analytical expressions for the perturbation of effective index. Ulrich analyzes the following prism-waveguide structure at  $\lambda = 0.6328 \mu\text{m}$ . The substrate's index of refraction is 1.52, the waveguide's index of refraction is 2.35, the gap's index of refraction is 1.0, the prism's index of refraction is 2.87, the waveguide's height is  $0.5 \mu\text{m}$ , and the prism-waveguide gap's height is  $s$ . This waveguide supports three TE modes whose effective index ranges from 1.7 to 2.3.

For strong coupling ( $s < 0.2 \mu\text{m}$ ), Ulrich plots numerical results (in his Figure 3) showing the change in effective index with different gap heights. These calculations show that the effective index of all the waveguide modes decreases as the gap height decreases (coupling strength increases). Others [14, 15, 17] report the same relationship between effective index and coupling strength in the strong coupling regime. While another group [18] reports the opposite relationship between increasing effective index and coupling strength. In [18] numerical calculations show that effective index increases with increasing coupling strength over both weak- and strong-coupling regimes.

In addition to numerical results, Ulrich develops an expression [his Equation (36)] for the effective index perturbation  $\delta N$  for weak coupling ( $s \geq 0.2 \mu\text{m}$ ).

Ulrich's analytical expressions for effective index perturbations results from a series of approximations valid for weak coupling. In Figure 2.6 we plot  $\delta N$  versus gap height  $s$  and unperturbed effective index  $N$  using Ulrich's Equation (36). The range of  $s$  for the calculations in Figure 2.6 includes both the strong-coupling ( $S < 0.2$ ) and the weak-coupling ( $S > 0.2$ ) regimes. The boundary between weak and strong coupling is given in [7] and is specific to the waveguide under study. Also, we plot  $\delta N$  versus unperturbed effective index for  $s = 0.2 \mu\text{m}$  in Figure 2.7.

We see from Figures 2.6 and 2.7 that  $\delta N$  changes sign. For weak coupling,  $\delta N$  changes sign when  $N = 2.14$ . This means that the perturbation of waveguide modes whose effective index is less than 2.14 will be of opposite sign from the perturbation of those waveguide modes with effective index greater than 2.14. However, this is in contrast to the strong coupling case in Ulrich's Figure 3, where it appears that  $\delta N$  is negative for all modes supported by the waveguide. In addition, Ulrich derives that the prism can increase, decrease, or leave unchanged the effective index, according to

$$\delta N \propto \cos(2\phi_{32}), \quad (2.14)$$

where

$$\phi_{32} = \arctan \left[ \frac{n_2^2 - N_m^2}{i(n_3^2 - N_m^2)} \right]^{1/2}, \quad (2.15)$$

and  $n_2$  is the refractive index of the gap,  $n_3$  is the refractive index of the prism, and  $N_m$  is the unperturbed effective index. Equations (2.14) and 2.15 shows that the sign and magnitude of  $\delta N$  depends only on the unperturbed effective index and the refractive indices of the prism and the gap. Furthermore, the prism has no effect on the effective index ( $\delta N = 0$ ) if  $\phi_{32} = \pi/4$ . This occurs when the fundamental mode has effective index 2.28, the prism has index 3.07, and  $n_2 = 1$ .

Unfortunately, we must know the unperturbed mode indices in addition

to the gap height in order to calculate  $\delta N$  when using Ulrich's analysis. This requirement prohibits using Ulrich's analysis to recover unperturbed effective indices from their measured values unless the perturbation is assumed to be so small that the measured effective index could be used in his Equation (36).

In summary, Ulrich's results for weak coupling predicts that  $\delta N$  can vary in magnitude and sign for each waveguide mode, and the existence of a particular prism refractive index which yields  $\delta N = 0$  for a particular effective index. However, his analysis does not apply to the strong-coupling case. Furthermore, he does not address the effects of coupling strength on the m-line's irradiance profile since he is analyzing input prism coupling.

Next, we apply Ulrich's analytical expressions to another case reporting numerical results for effective index perturbations. This case is from Walpita [17], who reports effective index decreasing as coupling strength increases. The prism-waveguide structure that Walpita analyzes has prism index of refraction 1.788, waveguide index of refraction 1.7, substrate index of refraction 1.45, gap index of refraction 1, waveguide thickness  $0.2 \mu\text{m}$ , and wavelength  $0.633 \mu\text{m}$ . We calculate that the unperturbed waveguide supports one TE mode with effective index 1.5188. His plot of effective index versus gap height (his Figure 10) clearly shows that the effective index decreases with increasing coupling strength. The range of gap heights in his Figure 10 spans from strong coupling to weak coupling. However, we find the opposite relationship between gap height and effective index for this prism-waveguide structure and range of gap heights using Ulrich's analytical expressions.

## 2.4 Effective Index Measurement

In this section we show how we measure effective index and why we use this method.

We base our measurement on the concepts and relationships in the first-order model of Section 2.2. Our method includes a procedure to yield relative rather than absolute effective index. We resort to measuring the effective index relative to the substrate index in order to reduce the influence of the prism perturbation and other residual systematic uncertainties. This procedure uses an m-line which is associated with a substrate radiation mode. The advantage of using this procedure is that we do not require a model to predict prism perturbation effects, nor do we need to determine the gap's geometry. However, a disadvantage of reporting relative effective index is that the measurement uncertainty increases due to adding the uncertainty in measuring the mode's m-line to the uncertainty in measuring the substrate's m-line.

The following section describes our experimental setup for measuring the effective index. Section 2.4.2 describes the relative measurement procedure and is followed by Section 2.4.3 describing uncertainty analysis.

**2.4.1 Experimental Setup** Figure 2.8 illustrates the experimental setup we use to measure effective index. Laser light at wavelengths  $\lambda = 0.6328 \mu\text{m}$  or  $\lambda = 0.829 \mu\text{m}$  is butt-coupled into the slab waveguide using a single-mode polarization-maintaining fiber. The extinction ratio between the two orthogonally polarized modes of the fiber was greater than 400:1. A rutile prism with its optic axis parallel to the waveguide's optic axis is pressed against the waveguide to couple light out from the waveguide. The prism's index of refraction at our operating wavelengths can be found in Table 2.1. At the output face of the prism,

the m-line is refracted into air (index of refraction of air is  $n_c = 1.0003$ ) at the radiation angle  $\theta'_m$ . The relationship between a mode's effective index  $N_m$  and  $\theta'_m$  was presented in Equation (2.2) and is repeated here for convenience

$$N_m = n_p \sin \left[ \phi_p + \arcsin \left( \frac{n_c}{n_p} \sin \theta'_m \right) \right], \quad (2.16)$$

where  $\phi_p = 60.59 \pm 0.02^\circ$  is the prism's angle (see Figure 2.1).

In order to measure  $\theta'_m$ , we aligned two translation stages, one with travel parallel to the prism output face and one with travel perpendicular to the prism output face. A charge-coupled device (CCD array) is affixed to these stages at a distance of approximately 1 m from the prism output face. We use a Pulnix model TM-745 camera with a windowless CCD array. The m-line illuminates the CCD array, and a profile of the m-line is viewed on a digital oscilloscope while a TV monitor displays the entire CCD field. We measure the m-line's radiation angle  $\theta'_{m,s}$  in the translation stages' coordinate system  $(x_s, y_s)$  using triangulation. A right triangle is formed by translating the CCD array a distance  $\Delta y_s$  and a perpendicular distance  $\Delta x_s$ ; see Figure 2.9. For a particular translation  $\Delta y_s = 50.00$  mm, the translation  $\Delta x_s$  is determined by repositioning the m-line at the same location on the CCD array. Now, we can calculate the mode angle using the equation

$$\tan \theta'_{m,s} = \frac{x_s}{y_s}. \quad (2.17)$$

Note however, that Equation (2.16) requires we know the m-line's radiation angle  $\theta'_m$  in the prism coordinate system  $(x_p, y_p)$ . Thus, we must determine the alignment between the prism's coordinate system and the stages coordinates system. We determine this alignment using a dial indicator gauge mounted on the translation stage assembly. We position its indicator tip to be under pressure

contact with the prism's output face (see Figure 2.10). The dial registers the displacement along  $y_s$  necessary to maintain contact between the tip and the prism's output face as the dial indicator translates along  $x_s$ . Recording the translations  $\Delta x_s$  and  $\Delta y_s$  allow us to calculate the rotation angle  $\gamma$  between the two coordinate systems using

$$\gamma = \arctan \left( \frac{\Delta y_s}{\Delta x_s} \right). \quad (2.18)$$

Once  $\gamma$  is known then the radiation angle in the prism's coordinate system can be found using

$$\theta'_m = \theta'_{m,s} - \gamma. \quad (2.19)$$

The inset of Figure 2.10 illustrates these angular relationships (all of the angles for this particular case are negative).

The measurement of  $\theta'_m$  has several sources of systematic uncertainty which affect the calculation of  $N_m$ . These sources include the uncertainty in both the prism angle and the prism index, the uncertainty of both the alignment and travel of the stages, and the perturbation due to waveguide-prism coupling. The next section describes our procedure which reduces the influence of these sources of uncertainty.

**2.4.2 Relative Effective Index Measurements** The procedure for making relative effective index measurements uses the substrate radiation mode. The substrate radiation mode propagates with a value of effective index  $N_{sub}$  that lies between 0 and the substrate index of refraction  $n_{sub}$ :

$$0 \leq N_{sub} \leq n_{sub}. \quad (2.20)$$

This substrate radiation mode is excited by positioning the input fiber a distance  $d$  perpendicular to the plane of the waveguide; see Figure 2.11. As  $d \rightarrow 0$ ,

the value of  $\theta'_m$  for the radiation mode approaches the value of the substrate angle  $\theta'_{sub}$ . This follows from the phase-matching condition [Equation (2.1)] illustrated in the inset of Figure 2.11. The substrate m-line distinguishes itself from the m-lines of guided modes as its position moves on the CCD array as the input fiber position changes ( $d$  changes). In addition to moving with  $d$ , the maximum irradiance of the substrate m-line decreases as  $d \rightarrow 0$ . Thus, we equate  $\theta'_m \equiv \theta'_{sub}$  when  $d$  is near 0 and the irradiance of the substrate m-line is still far enough above the noise to make a confident measurement of the radiation angle.

The movement of the substrate m-line appears continuous, not in discrete steps, as the fiber position changes. The appearance of continuous movement is reasonable even though, strictly speaking, the substrate forms a step index waveguide supporting a discrete set of guided modes. In this waveguide, the lowest order modes have effective index  $N \approx n_{sub}$  and the difference between the effective index for consecutive lowest order modes is  $\Delta N \approx 10^{-6}$ . This effective index spacing is approximately two orders of magnitude below the resolution of our experimental setup for measuring m-lines.

The substrate effective index  $N_{sub}$  is calculated from  $\theta'_{sub}$  using Equation (2.16). A value of  $N_{sub}$  is obtained for each effective index measurement and is subtracted from the value of  $N_m$  for the guided mode. This relative value  $\Delta N_m = N_m - N_{sub}$  yields the increment by which the effective index exceeds the substrate index. We reduce the influence of systematic uncertainties, including the influence of the prism's perturbation effects, by taking this difference and assuming that the prism's perturbation is the same for both the guided modes and the substrate mode.

**2.4.3 Measurement Uncertainty Analysis** Uncertainty with the measured values of  $\Delta N_m$  due to the random uncertainty of repositioning the m-line on the CCD array remains. The uncertainty bars displayed in the plots of  $\Delta N$  presented throughout this dissertation represent this measurement uncertainty. We determine this component of the measurement uncertainty as follows. First, we determine the uncertainty of measuring the radiation angle  $\theta'$  using the differential of Equation (2.17)

$$\begin{aligned} d\theta'_m &= \left| \frac{\partial \theta'_m}{\partial x_s} dx_s - \frac{\partial \theta'_m}{\partial y_s} dy_s \right| \\ &= \left| \frac{\frac{1}{y_s} dx_s - \frac{x_s}{y_s^2} dy_s}{1 + \left(\frac{x_s}{y_s}\right)^2} \right|. \end{aligned} \quad (2.21)$$

Typical values of the parameters in Equation (2.21) for the waveguide mode under study here are  $y_s = 50.00 \pm 0.01$  mm and  $x_s \approx y_s/2 \pm 0.01$  mm. Our experimental apparatus limits the measurement uncertainty  $dy_s$  while m-line characteristics determine the measurement uncertainty  $dx_s$  as we reposition the m-line on the CCD array. These experimental measurement uncertainties yield a maximum uncertainty in the radiation angle

$$\begin{aligned} d\theta'_m &= 2 \times 10^{-4} \text{ rad} \\ &= 0.01^\circ \end{aligned} \quad (2.22)$$

when using opposite signs for  $dx_s$  and  $dy_s$ . There are instances when the m-line characteristic allows the uncertainty in  $x_s$  to be as small as  $\pm 0.005$  mm or as large as  $\pm 0.03$  mm. Thus, each measurement carries along its own uncertainty.

Next, we determine the uncertainty in  $\Delta N_m$  to be

$$d\Delta N_m = \frac{\partial N_m}{\partial \theta'_m} d\theta'_m + \frac{\partial N_{sub}}{\partial \theta'_{sub}} d\theta'_{sub}. \quad (2.23)$$

using the differential once again. We use a plus sign in Equation (2.23) so that we calculate the largest uncertainty in  $d\Delta N_m$ . Values of the partial differentials in Equation (2.23) lie between 0.008 and 0.01 using typical parameters for the our waveguides at both wavelengths. Taking the larger value and using Equation (2.22) yields the measurement uncertainty

$$d\Delta N_m = \pm 2 \times 10^{-4} \quad (2.24)$$

The next section presents some example m-line irradiance profiles and a case history for a particular set of effective index measurements. This case history includes using the effective index measurements to determine waveguide fabrication parameters and comparing these parameters to analytical measurements.

**2.4.4 Example M-Line Profiles and Effective Index Case History** M-line irradiance profiles at  $\lambda = 0.6328 \mu\text{m}$  for the fundamental mode of a titanium in-diffused planar waveguide are shown in Figure 2.12. These two profiles correspond to the two propagation distances forming the right triangle in Figure 2.9. The far propagation distance is 1.24 m and the difference between propagation distances is 50.00 mm. The m-line profile propagating furthest is slightly wider, as expected. However, we find different divergence angles for these profiles using

$$\theta_d = \arctan\left(\frac{\text{FWHM}}{2D}\right), \quad (2.25)$$

where  $D$  is the propagation distance. We calculate  $\theta_d = 0.522 \pm 0.005$  mrad for the near profile while  $\theta_d = 0.549 \pm 0.005$  mrad for the far profile. The divergence angles should be the same if these profiles are in the far-field of the m-line's source (the prism-waveguide gap). Also notice the slight asymmetry in these irradiance profiles. The profiles from a uniform gap should be symmetric according the first-order model in Section 2.2.2 (Equation (2.13)). This asymmetry and the unequal

divergence angles could indicate that these profiles are not in the far-field of the gap.

We investigate the effects of propagating only into the Fresnel zone on our measurement. We use coupling length  $L_c = 1$  mm, coupling strength  $S_c = 0.00035 \mu\text{m}^{-1}$  and  $\lambda = 0.6328 \mu\text{m}$  to calculate the m-line's irradiance profile using the Fresnel propagating equations. We find that the maximum irradiance does not occur at  $z_r = 0$  but is offset along  $+z_r$ . We plot this perpendicular displacement from the far-field propagation direction versus propagation distance in Figure 2.13. We see that the displacement become nearly constant after propagating 30 cm. Thus, the position of the m-line's maximum irradiance follows a path nearly parallel to the  $x_r$  axis. We calculate an additional uncertainty of  $\pm 1 \times 10^{-6}$  in  $\Delta N$  using our method after a propagation distance of only 30 cm. We consider this uncertainty negligible since it is two orders of magnitude less than the uncertainty already accounted for in the previous section.

Next, we use the methods outlined in the previous section to measure effective index in a set of titanium in-diffused, lithium niobate slab waveguides. The waveguides are formed on y-cut wafers, and the waveguide modes propagate parallel to the crystal's x-axis. The input light is polarized along the crystal's y-axis to excite TM-polarized guided modes. These modes will guide because of the increase in lithium niobate's ordinary index of refraction due to titanium in-diffusion [29]. The TM-polarization was chosen over TE-polarization to avoid confusion arising from other coincident diffusion processes affecting lithium niobate's extraordinary index of refraction [30, 1].

The diffusion time  $t$ , the titanium thickness  $\tau$ , the diffusion coefficient

$D(T)$ , and the diffusion temperature  $T$  are the parameters for titanium concentration  $C(y, t; D(T), \tau)$  after diffusion [54]. Converting titanium concentration to a change of index of refraction  $\Delta n(y, t)$  introduces two more parameters [32]. These are  $\eta$  and  $K$ , where

$$\Delta n(y, t) = (K C(y, t; D(T), \tau))^\eta. \quad (2.26)$$

We would like to determine  $D(T)$ ,  $\eta$ , and  $K$ . We accomplish this by fabricating four waveguide specimens using the same parameters except for diffusion time. The common parameters are  $T = 1000^\circ\text{C}$  and  $\tau = 25$  nm. The diffusion times are  $t = 1, 2, 4, 8$  h. Then we measure the effective index  $\Delta N$  of the modes in these waveguides. Finally, we compare these measured mode effective indices to those calculated using the index profile given by Equation (2.26). This comparison is shown in Figure 2.14, where we plot effective index versus diffusion time. The parameter values used to fit the theoretical curves to the measured data are

$$\begin{aligned} K &= \frac{0.033}{C_0}, \\ \eta &= 0.62, \\ D &= 0.2 \mu\text{m}^2/\text{h}. \end{aligned} \quad (2.27)$$

There is good agreement between the measurements and fitted curves for both effective index and number of guided modes.

We use  $D = 0.2 \mu\text{m}^2/\text{h}$  to calculate the titanium concentration profile for diffusion time  $t = 2$  h using the approximate Gaussian solution to the diffusion equation [33]. Then we compare this calculated profile to that which was measured in specimen 42 (2 h diffusion) using secondary ion mass spectroscopy (SIMS). Figure 2.15 shows this comparison. We find better agreement between the

calculated and measured titanium concentration profiles using  $D = 0.245 \mu\text{m}^2/\text{h}$ .

## 2.5 Effective Index Perturbations

The previous sections illustrate the theoretical impact of the prism-waveguide perturbation on effective index measurements. In this section we discuss our experimental observations regarding measurement perturbations starting with coupling gap geometry.

**2.5.1 Coupling Gap Geometry** We have pointed out the importance of the gap height  $s$  and the coupling length  $L_c$  on effective index measurements. Our experimental observations indicate the gap is nonuniform over the contact region, contrary to the illustration in Figure 2.1. In fact, Newton's rings are visible when the gap is viewed through the waveguide's substrate. These nearly concentric interference fringes delineate regions of equal gap height. Both the spacing and distribution of these fringes change as the pressure changes. To see this, consider the prism as a rigid body while the waveguide is an elastic body undergoing pure bending without compression or extension. Figure 2.16 illustrates the initial contact between waveguide and prism for low coupling pressure. Here, the planar waveguide contacts the prism at three points determined by surface inhomogeneities. At this pressure there is a minimum gap height  $s_{min}$  and a coupling length  $L_c$  (actually the coupling occurs over an area) over which the gap height is less than some critical height. The critical gap height  $s_c$  is defined to be the height at which the interaction between prism and waveguide becomes insignificant. Nearly parallel and equally spaced interference fringes are seen at this initial contact. Increasing the coupling pressure causes the waveguide to bend (Figure 2.17). This can decrease  $s_{min}$  and also move the positions of both  $s_{min}$  and  $s_c$ . Thus, higher pressure can result in both a different coupling strength and

a different coupling length. The coupling length increases in this case. The interference fringes become more concentric and unevenly spaced at higher pressures. Later, we will show how these effects can change the characteristics of m-lines and therefore, affect the measurement of  $N$ .

We cannot associate a stronger coupling pressure with a smaller gap height or a longer coupling length since we are unable to accurately quantify the gap's geometry. In fact, we cannot rule out that  $s$  could be unchanged by increasing the coupling pressure.

Next, we present experimental results regarding the perturbation effects on both the m-line's radiation angle and its irradiance profile.

**2.5.2 M-Line's Radiation Angle and Profile Perturbations** We report two data sets (Set 1 and Set 2) measuring the variation of effective index with applied coupling pressure on waveguide specimen 56. Waveguide specimen 56 is a titanium in-diffused, lithium niobate slab waveguide. The fabrication parameters for specimen 56 are, 25 nm of titanium evaporated on y-cut lithium niobate, and a 2 h diffusion at 1000°C in flowing argon. The waveguide modes propagate parallel to the crystal's x-axis. The input light is polarized along the crystal's z-axis (TE-polarized). We cannot compare coupling pressures between the data sets because the specimen was removed and then remounted for each data set. Furthermore, we do not use the substrate m-line in these measurements because we want see the influence of the perturbation. Thus, we report absolute effective index here.

Table 2.2 shows Set 1 effective index measurements at  $\lambda = 0.6328 \mu\text{m}$  for two different coupling pressures  $P_1^{(1)}$  and  $P_2^{(1)}$ , where  $P_1^{(1)} < P_2^{(1)}$  (the parenthetic superscript 1 denotes Set 1). The fundamental mode TE-0 shows an effective

index decrease of 0.0022 as the coupling pressure increases. However, the effective index of the lowest order mode TE-3 shows an increase of 0.0005 with the same increase in coupling pressure.

Figure 2.18 compares the m-line irradiance profiles of the TE-0 mode at coupling pressures  $P_1^{(1)}$ ,  $P_2^{(1)}$ . We see that the m-line profile's full width at half maximum FWHM decreases as the coupling pressure increases. Likewise, Figure 2.19 compares the TE-3 mode m-line profiles at these two pressures. A similar decrease of FWHM with increasing coupling pressure is seen in the TE-3 mode m-line. Also in Figure 2.19, there is poor separation between the TE-2 and TE-3 modes at pressure  $P_1^{(1)}$ , while the resolution between these modes improves at the higher pressure  $P_2^{(1)}$ . Furthermore, the m-line profiles at the higher pressure  $P_2^{(1)}$  are nearly symmetric while the profiles at the lower pressure  $P_1^{(1)}$  are asymmetric.

We make further comparisons between the m-line profiles in Figures 2.20 and 2.21. Figure 2.20 compares the TE-0 and TE-3 m-line profiles at low coupling pressure  $P_1^{(1)}$  while Figure 2.21 makes the same comparison but at high coupling pressure  $P_2^{(1)}$ . The m-line profiles of the two modes have similar shapes at each coupling pressure. Furthermore, the FWHM of modes TE-0 and TE-3 are nearly identical at  $P_1^{(1)}$  while the FWHM of TE-0 is larger than the FWHM of TE-3 at  $P_2^{(1)}$ .

In each of the Figures 2.18 through 2.21 we normalized the maximum irradiance to 1 and shifted the profiles so that the maximum is at far-field angle  $\theta_f = 0$ . The far-field angle is calculated using

$$\theta_f \equiv \frac{z'_r}{x_r}, \quad (2.28)$$

where  $z'_r$  is the position along the CCD array and  $x_r = 1.17 \pm 0.02$  m is the

propagation distance.

Table 2.3 shows Set 2 of effective index measurements at  $\lambda = 0.6328 \mu\text{m}$  for three different coupling pressures  $P_1^{(2)}$ ,  $P_2^{(2)}$  and  $P_6^{(2)}$  where  $P_1^{(2)} < P_2^{(2)} < P_6^{(2)}$ . The changes in effective index are smaller here in Set 2 than they are in Set 1. In fact, most of the changes here are within the measurement uncertainty. An important observation from Table 2.3 is the appearance of mode TE-4 at coupling pressures  $P_2^{(2)}$  and  $P_6^{(2)}$ . This mode was not seen in Set 1 nor at coupling pressure  $P_1^{(2)}$ .

The FWHM of various modes at coupling pressures  $P_1^{(2)}$  through  $P_7^{(2)}$  are shown in Figure 2.22. The coupling pressure increases from  $P_1^{(2)}$  to  $P_7^{(2)}$ . The FWHM of mode TE-0 increases with each increase in coupling pressure. The FWHM of mode TE-4 also increases from pressure  $P_6^{(2)}$  to  $P_7^{(2)}$ . In contrast, the FWHM's of modes TE-1 and TE-2 decrease with increasing coupling pressure. In comparison, the difference in FWHM between modes TE-0 and TE-3 of Set 1 is 0.5 in the same units as Figure 2.22.

In the next section we present results of measuring the substrate effective index in the presence of the prism perturbation.

**2.5.3 Perturbation of the Substrate's Effective index** We use the substrate's effective index in our effective index measurements (Section 2.4) to remove the effects of the prism perturbation. In this section we report how the substrate effective index deviates from the predictions of the phase-matching condition for the unperturbed interaction.

The substrate effective index (Section 2.4.2) should vary sinusoidally with angle of incidence according to the phase-matching condition, Equation (2.1) and Figure 2.11. Two measurement sets were made of  $N_{sub}$  versus angle of incidence

$\theta_i$  at  $\lambda = 0.829 \mu\text{m}$ . First Set A was measured and then Set B. Figure 2.23 illustrates these data sets. Each plot symbol in Figure 2.23 represents at least 3 repeated measurements. The measurements of Set A yields wide variations in  $N_{sub}$  at angle of incidence between  $87.5^\circ$  and  $90^\circ$ . While the variation in  $N_{sub}$  of Set B are smaller. Comparing the measurements of these two data sets at  $\theta_i = 89.5^\circ$  yields the result that the Set B measurement of  $N_{sub}$  is greater than the Set A measurement of  $N_{sub}$ . However, the opposite relationship is found at  $\theta_i = 89.8^\circ$ . Furthermore, the measurements of Set B and Set A nearly coincide at  $\theta_i = 89.8^\circ$  and at  $\theta_i = 85.5^\circ$ . We cannot explain these inconsistencies.

We are able to measure the substrate effective index at angles up to  $\theta_i = 89.76^\circ$  where the substrate m-line begins to interfere with the m-line from the highest order guided mode. The Set B measurement at this angle of incidence yields  $N_{sub} = 2.1721$ . The square plot symbol in Figure 2.23 represents the measurement of the highest order guided mode's effective index  $N = 2.1726$ . We subtract this substrate's effective index from the guided mode's effective index to yield the relative effective index  $\Delta N$  described in Section 2.4.2.

The solid curve in Figure 2.23 represents calculations of substrate effective index fit to the measurements for  $\theta_i \leq 87.5^\circ$  using the phase-matching condition. The substrate index  $n_{sub,f}$  is the fitting parameter and has value  $n_{sub,f} = 2.1712$ .

## 2.6 A Local-Normal Mode Model of Prism Coupling

This section introduces a numerical approach to determine the m-line characteristics in output prism coupling. This model describes the propagation of waveguide mode in the presence of an output coupling prism. The basis for this

model is a local-normal mode expansion [26] using the modes of composite waveguides. This composite waveguide is formed using the prism and waveguide. This model uses a straight forward algorithm to describe the generation and propagation of the m-line. The algorithm is essentially the repetitive sequence of mode propagation followed by mode coupling at an interface. This model has several advantages including the capability for arbitrary gap geometry and coupling strength, does not use a computational grid with spacing on the order of a wavelength, and is not limited by paraxial approximations.

**2.6.1 Local normal mode algorithm** Figure 2.24 illustrates the geometry of output prism coupling used by the model. The prism is segmented into regions  $r = 1, 2 \dots n$ . The position of each region relative to the waveguide defines the coupling gap geometry. The gap geometry shown in Figure 2.24 is a constant height. Additionally, the waveguide could also be segmented to represent bending and other perturbations due to the coupling pressure.

The model generates a m-line from a waveguide mode as follows. First, a waveguide mode propagates without perturbation in the waveguide according to

$$\Psi_{wg} = \psi_{wg} \cos \beta z, \quad (2.29)$$

where  $\beta = \frac{2\pi}{\lambda} N$  is the mode propagation constant,  $N$  is the mode effective index, and the  $x$  dependence of  $\psi$  is implicit. We have omitted the negative harmonic time dependence. This modes propagate along the waveguide until it reaches the first prism segment at  $z = 0$ .

This first prism segment and the waveguide form a composite waveguide that supports a discrete set of guided modes and a continuum of radiation modes. We only consider the guided modes here. The guided modes of this first composite

waveguide are

$$\Psi^{(1)} = \sum_{i=1}^{m_1} a_i^{(1)} \psi_i^{(1)} \cos \beta_i^{(1)} z. \quad (2.30)$$

where  $a_i^{(1)}$  is the amplitude of the  $i$  th mode of the first composite waveguide.

Next, we must satisfy the boundary conditions at this interface between the waveguide mode and the modes of the composite waveguide. We can approximately satisfy the boundary condition if we ignore the radiation modes of both the waveguide and the composite waveguide, and also ignore any reflected waves at each segment interface. Ignoring the reflected waves is a reasonable approximation. This can be seen to be the case if we use the Fresnel formula [34] to calculate the magnitude of the normal incident reflection coefficient  $|R|$  for the waveguide mode. We substitute effective index of refraction  $N$  for the index of refraction to obtain

$$|R| = \frac{\Delta N}{N + N_i^{(1)}} \quad (2.31)$$

for the amplitude reflection coefficient. Later calculations show that the largest difference of effective index between modes with an appreciable coupling is  $\Delta N = 0.005$ . Thus, we calculate

$$|R| \approx 0.001 \quad (2.32)$$

where we have used  $N \approx N_i^{(1)} = 2.2$  for a Ti:LiNbO<sub>3</sub> waveguide.

Thus, we can approximately satisfy the boundary conditions by equating Equation (2.29) to Equation (2.30)

$$\psi_{wg} = \sum_{i=1}^{m_1} a_i^{(1)} \psi_i^{(1)}, \quad (2.33)$$

where we have taken  $z = 0$ . We find the amplitude coefficients  $a_i^{(1)}$  by successively multiplying both sides of Equation (2.33) by the conjugate of the composite waveguide mode  $(\psi_i^{(1)})^*$  and integrating from  $x = \pm\infty$ . The range of integration over

$x$  is effectively reduced to the range over which the fields have significant value. This range can be as small as a few micrometers for the waveguide mode, or as large as several millimeters for modes in the composite waveguide.

We find that our approximate boundary conditions are reasonable because nearly 0.97% of the power is coupled at the interface from the waveguide mode into the set of composite waveguide modes.

The next step in the algorithm is the propagation of each composite waveguide mode  $\psi_i^{(1)}$  along the  $z$ -axis according to Equation (2.30). These modes start out in phase. However, a phase difference accumulates between these modes because each mode propagates with a different effective index. This accumulation of phase is responsible for the appearance of the m-line within the prism and the apparent decrease in waveguide mode amplitude under the prism.

The composite modes of segment 1 propagate without loss until they reach the next prism segment at  $z = z_{1,2}$ . There, the boundary conditions are again approximately satisfied by equating the fields on each side of the interface according to

$$\sum_{i=1}^{m_1} a_i^{(1)} \psi_i^{(1)} \cos \beta_i^{(1)} z_{1,2} = \sum_{i=1}^{m_2} a_i^{(2)} \psi_i^{(2)} \cos \beta_i^{(2)} z_{1,2}. \quad (2.34)$$

This sequence of steps, mode propagation- mode coupling at an interface, is repeated until the last prism segment is reached.

**2.6.2 Model Results** This section presents results of the model applied to a simplified prism geometry. For this simplified model we represent the prism using only one segment. This means that the prism is essentially a block of material placed on top of the waveguide.

The following parameters apply to the upcoming results. The wavelength is  $0.6328\mu\text{m}$ . The waveguide supports two TE modes of effective index  $N = 2.2055$

and  $N = 2.2182$ . The prism extends from  $0 < x < 800\mu\text{m}$  and has index of refraction 2.8666. The coupling gap is uniform with height  $S = 0$ .

Figure 2.25 compares the fundamental TE waveguide mode to the sum of the composite waveguide modes  $\Psi^{(1)}$  at  $z = 0$ . We see there is good agreement between the fields of the waveguide mode and the composite waveguide modes. The simplified prism geometry is located at the top of Figure 2.25. The shaded region of this schematic drawing indicates the portion of the model represented by the accompanying graph.

Figure 2.26 shows the perturbation on the electric fields of the two waveguide modes due to the presence of the prism. The fundamental waveguide mode  $\text{TE}_0$  decays with a slower rate than the higher order mode  $\text{TE}_1$ . This makes sense because the fundamental mode is more confined to the waveguide region than the higher order mode and is less influenced by the prism.

Figure 2.27 shows the irradiance distribution within the prism region. The irradiance distribution represents the m-line propagating away from the prism-waveguide coupling gap.

Figure 2.28 shows the m-line's irradiance profile at  $x_r = 450\mu\text{m}$ . Notice the exponential decay of the m-line's profile in Figure 2.28. This is also predicted by the first-order model of Section 2.2.

## 2.7 Discussion

We have attempted to reduce perturbation effects on effective index measurements by recording relative rather than absolute measurements. This technique assumes that the perturbation is the same for all waveguide modes. However, our observations of effective index perturbation include cases where the

effective index perturbation varies measurably with each waveguide mode (Table 2.2) and cases where it does not (Table 2.3). We attribute this variability in effective index perturbations to the geometrical details of the coupling gap. Consequently, our relative measurements aimed at reducing the perturbation effects on effective index may not be applicable to all cases. Unfortunately, we know of no other experimental techniques which can reduce the effective index perturbations without also sacrificing resolution.

In addition to affecting the m-line's radiation angle, the gap geometry also affects the m-line's irradiance profile. Figures 2.18 and 2.19 illustrate that m-lines can narrow with increasing coupling pressure. This narrowing provides better resolution for closely spaced m-lines. In fact, we have also seen what at first appears to be one m-line split into two m-lines representing two very closely spaced modes as the coupling pressure increases. Thus, we see advantages to using high coupling pressures. This is at odds with the recommendations that effective index measurements should only be made at low coupling pressures to avoid perturbations [23, 15]. However, if we use high coupling pressures, then we must be prepared to recover the unperturbed effective index. Otherwise, we are not taking full advantage of the additional resolution and we are just trading resolution enhancements for a reduction in measurement precision.

We also present evidence in Figure 2.22 that m-lines broaden with increasing coupling pressure. We can reconcile these observations with those in Figures 2.18 and 2.19 if we do not always correlate coupling pressure with coupling strength. For example, we can imagine in one case that increasing the coupling pressure causes a longer coupling length while the coupling strength remains constant (or, equivalently gap height remains constant), whereas in another case,

increasing the coupling pressure increases the coupling strength while leaving the coupling length unchanged. Using the first-order model, we find in the first case that the m-line profiles narrow with increasing coupling pressure if the product  $S_c L_c \approx 1$  but remains unchanged if  $S_c L_c \gg 1$ . In contrast, the second case will result in the m-line's profile broadening as coupling pressure increases. This was probably the situation when others observed m-line broadening with increasing coupling strength [19, 20].

Our measurements of substrate effective index produce more interesting results. For example, the measurements of  $N_{sub}$  at angle  $\theta_i \leq 87.5^\circ$  in Figure 2.23 can be fitted to the unperturbed phase-matching condition using a substrate index of refraction  $n_{sub,f} = 2.1712$ . We are not surprised to find that  $n_{sub,f}$  differs from the unperturbed substrate index of refraction  $n_{sub} = 2.1728$  [35]. However, we find it interesting that the measurements of  $N_{sub}$  at angle of incidence  $\theta_i \geq 87.5^\circ$  yield values that deviate from the fitted curve and approach the unperturbed index of refraction. The fiber displacement is  $d = 10 \mu\text{m}$  (see Figure 2.11) at the largest angle of incidence ( $\theta_i = 89.76^\circ$ ) that we can measure  $N_{sub}$ . This places the fiber's input coupling point within the substrate, below the region of titanium indiffusion. Thus, light from the fiber should propagate with the substrate's index of refraction even at this extreme angle of incidence.

Our observations of m-line characteristics show that there are two important parameters of the coupling gap. These are the gap height, which determines how significant are the effective index perturbations, and the coupling length, which influences inter-modal resolution. The coupling pressure does not always correlate with either of these gap characteristics in a consistent manner, probably due to the details surrounding the formation of the gap. Furthermore, waveguide

material properties could be as important to gap geometry as coupling pressure in determining m-line characteristics. For example, the waveguide could flow instead of bend under the coupling pressure. Thus, m-lines originating from polymer waveguides may well respond differently to the same coupling pressure applied to crystalline or glass waveguides.

Developing an experimental procedure to characterize the coupling gap for each measurement may not be simple. Even if we completely determine the coupling gap geometry, there are situations where we cannot use the previous models to recover the unperturbed effective index. For example, the analytical treatment in [7] applies only to cases of weak coupling, uniform gap, and infinite coupling length. Numerical techniques remove one of these limitations and allow cases of strong coupling. We attempted to address these limitations by introducing a numerical model of prism coupling based upon a local normal mode expansion. Preliminary results from our model agree qualitatively with the first-order model of Section 2.2.

We hope the results presented in this chapter provide additional insights into effective index measurements using the prism coupler. Furthermore, these results indicate that to accurately measure effective index beyond the fourth decimal place using prism coupling will require additional experimental methods and theoretical models.

Table 2.1. Index of refraction for congruent lithium niobate [35] and rutile [36] at  $\lambda = 0.6328 \mu\text{m}$  and  $\lambda = 0.829 \mu\text{m}$ .

Wave-length [ $\mu\text{m}$ ]	Lithium Niobate		Rutile	
	Extra-ordinary Index of Refraction	Ordinary Index of Refraction	Extra-ordinary Index of Refraction	Ordinary Index of Refraction
$\lambda=0.6328$	2.2028	2.2865	2.8666	2.5821
$\lambda=0.829$	2.1728	2.2517	2.7789	2.5142

Table 2.2. Set 1. Effective index versus coupling pressure for waveguide specimen 56 at  $\lambda = 0.6328 \mu\text{m}$ . The relationship between the coupling pressures is  $P_1^{(1)} < P_2^{(1)}$ .

Mode #	Low Coupling Pressure $P_1$	High Coupling Pressure $P_2$
TE 0	$2.2186 \pm 1.4 \times 10^{-4}$	$2.2164 \pm 1.4 \times 10^{-4}$
TE 3	$2.2039 \pm 1.8 \times 10^{-4}$	$2.2044 \pm 1.3 \times 10^{-4}$

Table 2.3. Set 2. Effective index versus coupling pressure for waveguide specimen 56 at  $\lambda = 0.6328 \mu\text{m}$ . The relationship between the pressures is  $P_1^{(2)} < P_2^{(2)} < P_6^{(2)}$ .

Mode #	Low Coupling Pressure $P_1$	Intermediate Coupling Pressure $P_2$ ( $P_1 < P_2 < P_6$ )	High Coupling Pressure $P_6$
TE 0	2.2168 $\pm 0.0002$	2.2167 $\pm 0.0002$	2.2165 $\pm 0.0002$
TE 1	2.2063 $\pm 0.0002$	2.2066 $\pm 0.0002$	2.2065 $\pm 0.0002$
TE 2	2.2045 $\pm 0.0002$	2.2053 $\pm 0.0002$	2.2048 $\pm 0.0002$
TE 3	2.2034 $\pm 0.0002$	2.2038 $\pm 0.0002$	2.2036 $\pm 0.0002$
TE 4		2.2034 $\pm 0.0002$	2.2031 $\pm 0.0002$

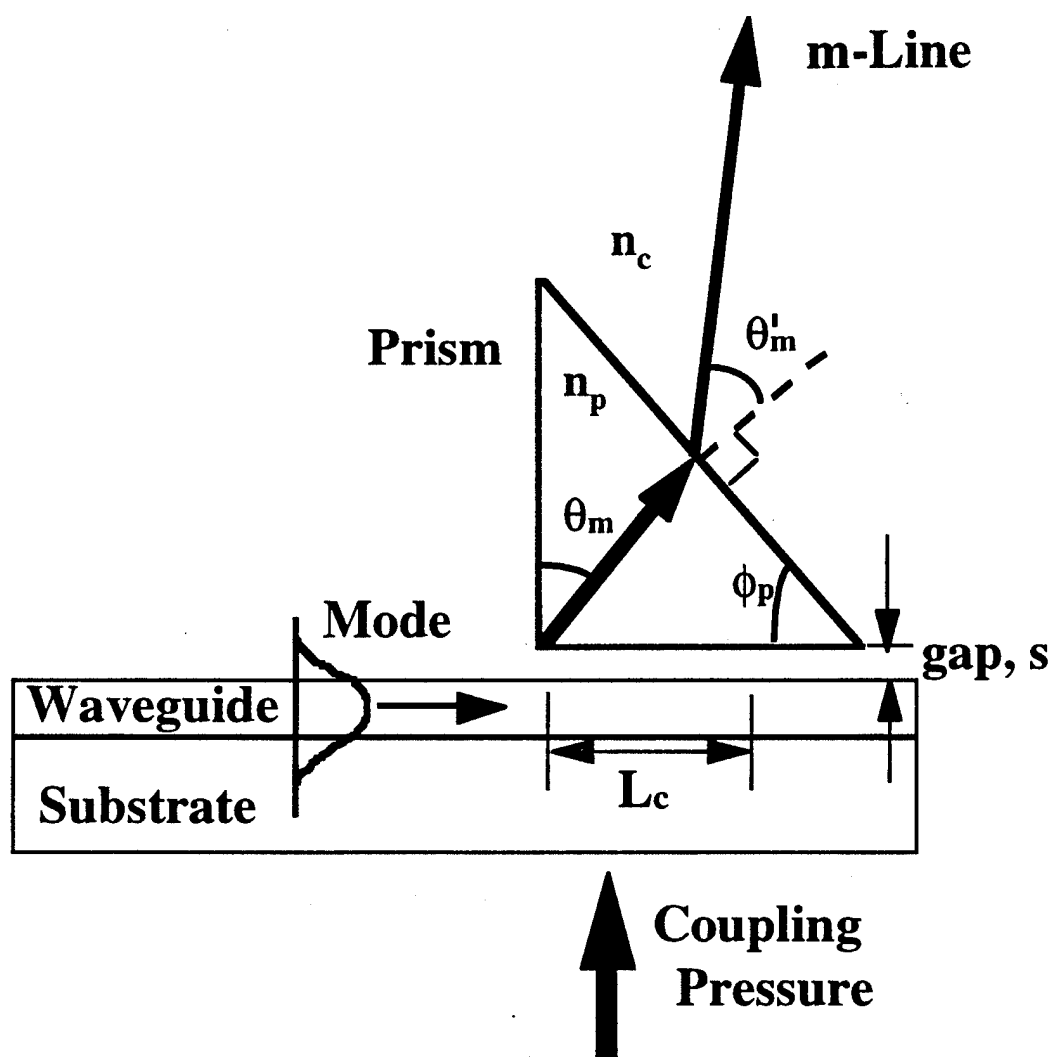


Figure 2.1. Relevant features of the output prism-coupler. Effective index measurements reported in this dissertation were made using this prism-coupling arrangement.

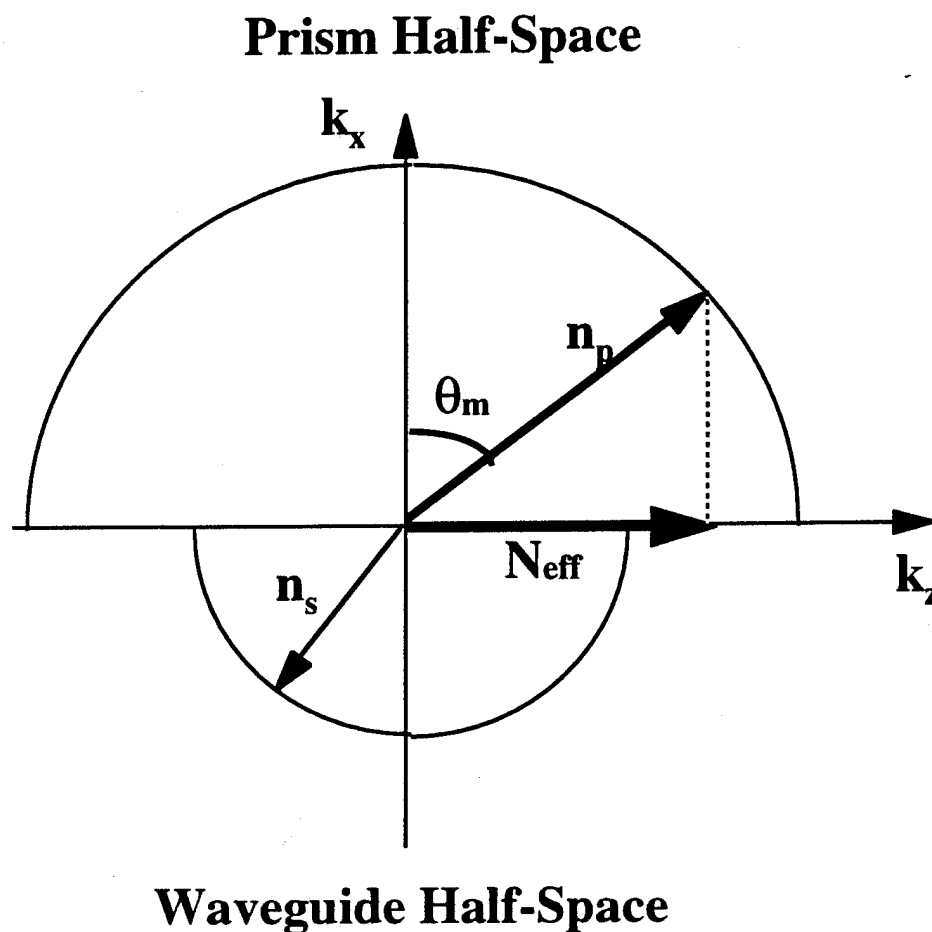


Figure 2.2. Construction in  $k$ -space illustrating the relationship between the radiation angle and the mode's effective index. The prism with index of refraction  $n_p$  occupies the upper half-space while the waveguide substrate with index of refraction  $n_s < n_p$  occupies the lower half-space. Only one radiation direction in the prism space satisfies the phase-matching condition. In contrast, no directions in the substrate space satisfy the phase-matching condition. Thus, the  $m$ -line radiates only at the angle  $\theta_m$ .

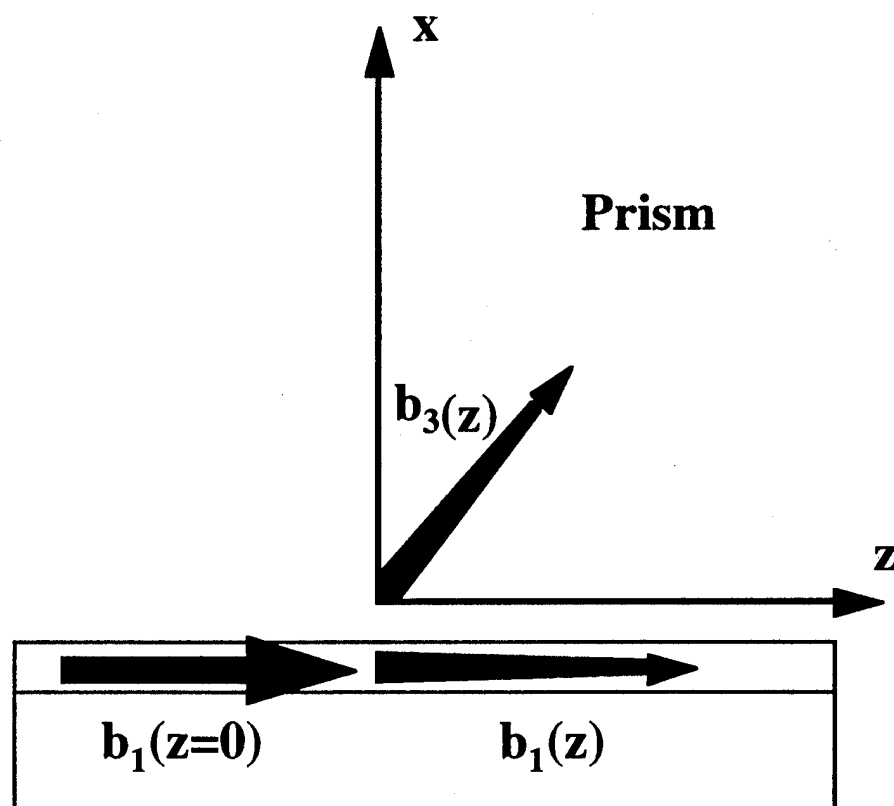


Figure 2.3. Relationship between field amplitudes in Tien's [9] model describing output prism-coupling. The waveguide mode's initial field amplitude is  $b_1(0)$ . This field couples with the m-line field amplitude  $b_3$ .

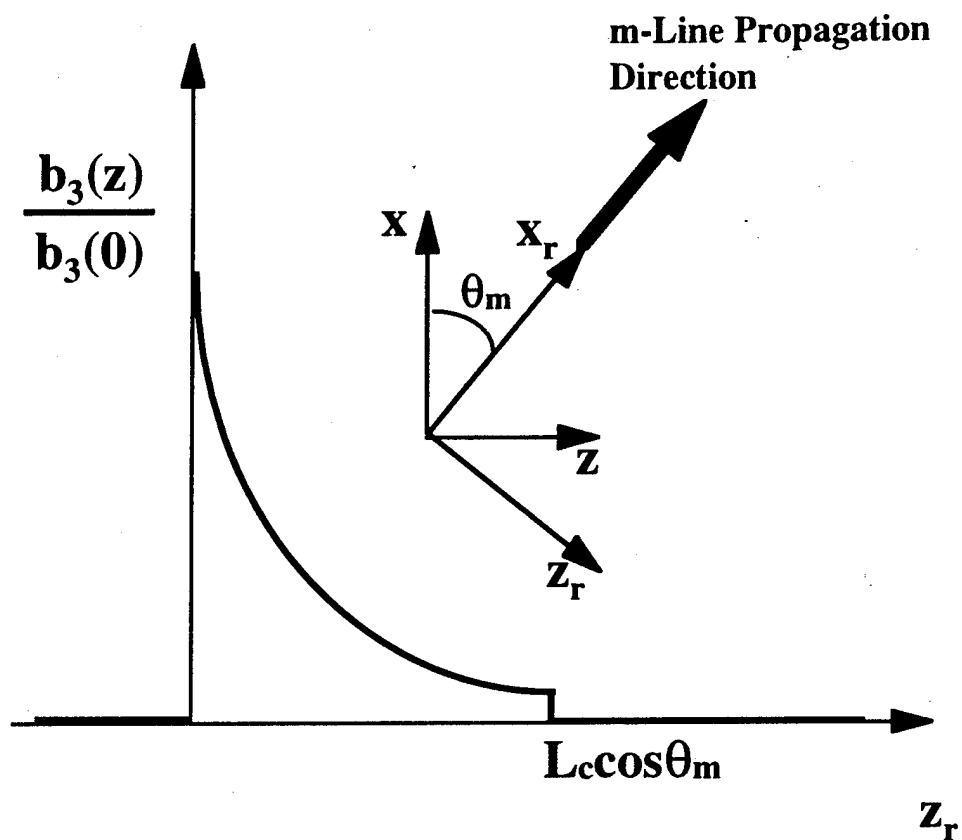


Figure 2.4. Sketch of  $b_3$  in the rotated coordinate system  $(x_r, z_r)$ . Also shown is the field truncation resulting from finite coupling length  $L_c$ .

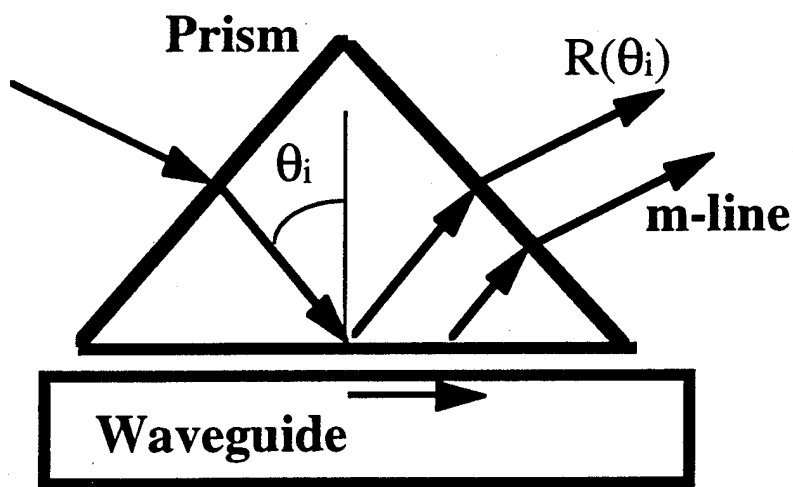


Figure 2.5. Input prism-coupling for effective index measurement using dark m-line characteristics.

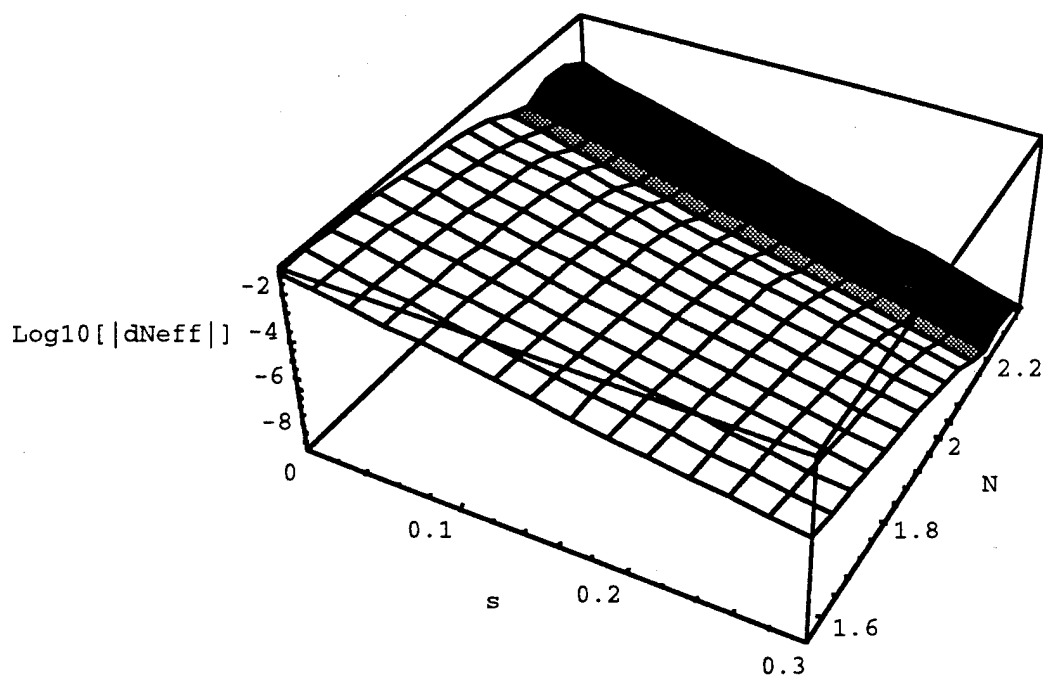


Figure 2.6. Effective index perturbation  $\delta N$  versus effective index  $N$  and gap height  $s$  (in micrometers) for the prism-waveguide structure in Figure 2 of [7]. The range of  $s$  includes strong coupling ( $s < 0.2 \mu\text{m}$ ) to beyond the weak-coupling condition ( $s > 0.2 \mu\text{m}$ ). The boundary between weak and strong coupling is specific to the waveguide structure in Figure 2 of [7]. The black shaded region of this plot indicates that  $\delta N$  is positive whereas the white shaded region indicates  $\delta N$  is negative.

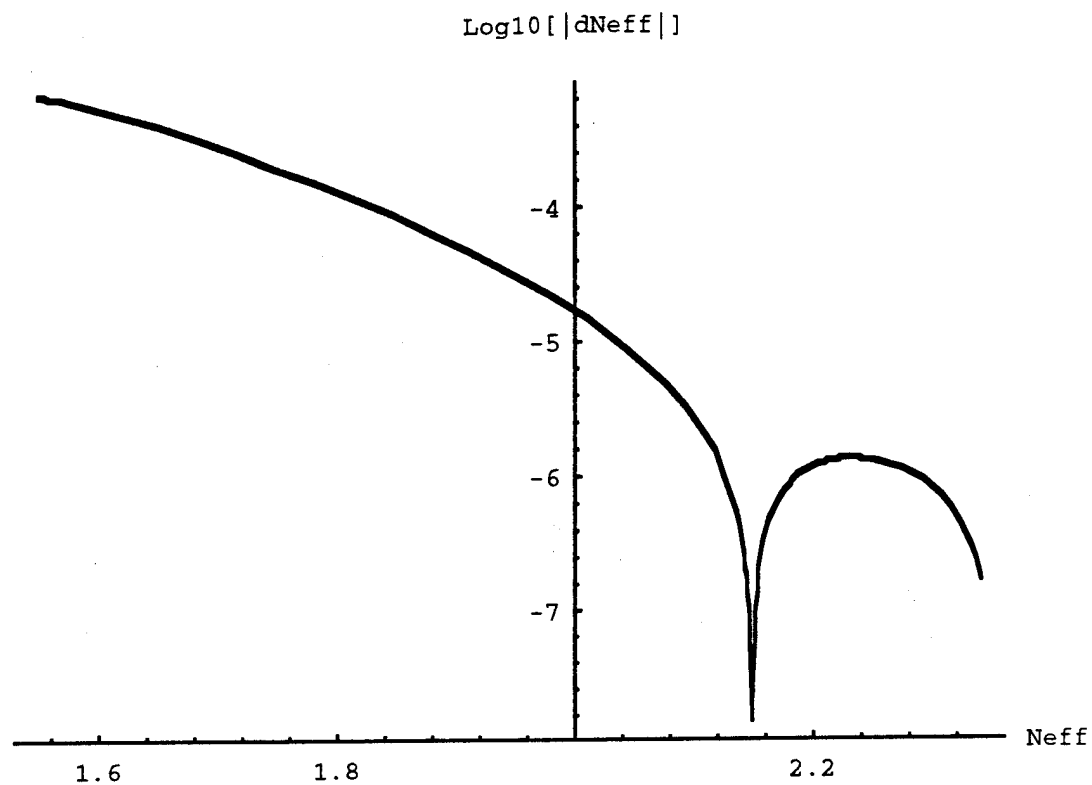


Figure 2.7. Effective index perturbation  $\delta N$  versus effective index  $N$  with gap height  $S = 0.2 \mu\text{m}$  for the prism-waveguide structure in Figure 2 of [7]. The sign of  $\delta N$  is negative for  $N$  less than 2.14 and positive elsewhere.

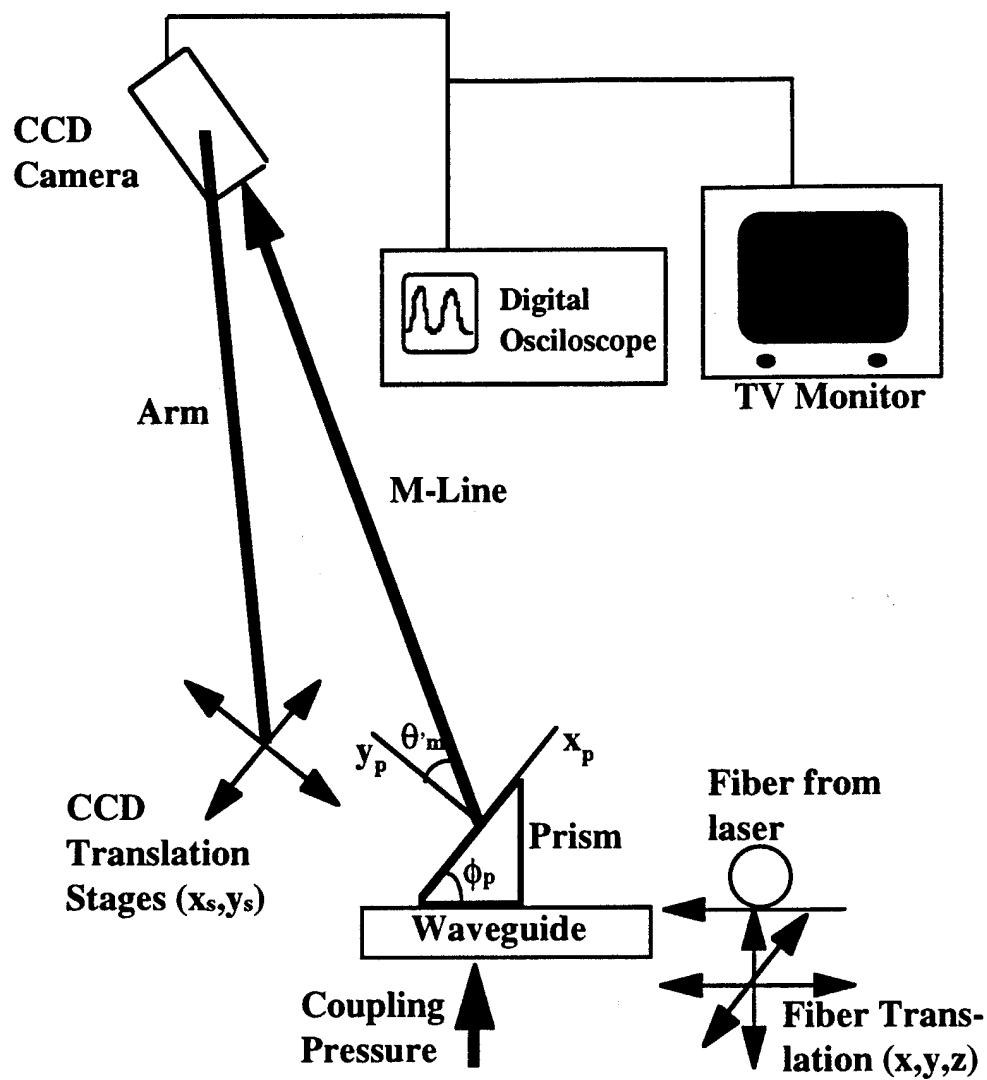


Figure 2.8. Experimental setup for effective index measurements using output prism coupling.

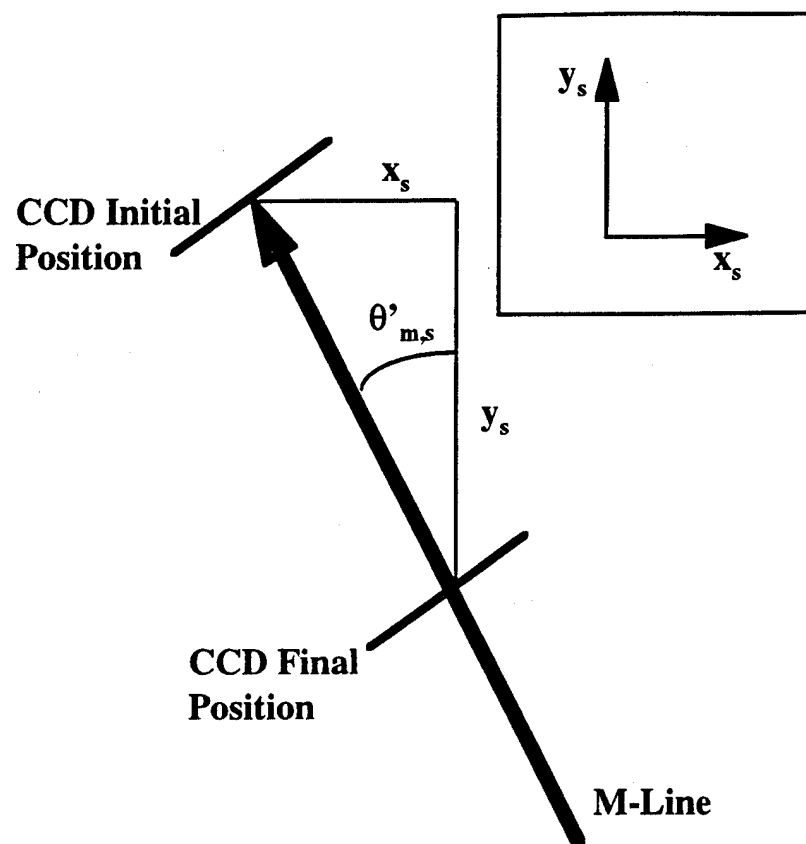


Figure 2.9. Geometric construction for determining the m-line radiation angle in the stage coordinate system  $\theta'_{m,s}$ . The CCD array is translations  $\Delta x_s$  and  $\Delta y_s$  form a right triangle. The radiation angle is found from this triangle using  $\theta'_{m,s} = \arctan(\Delta x_s / \Delta y_s)$ .

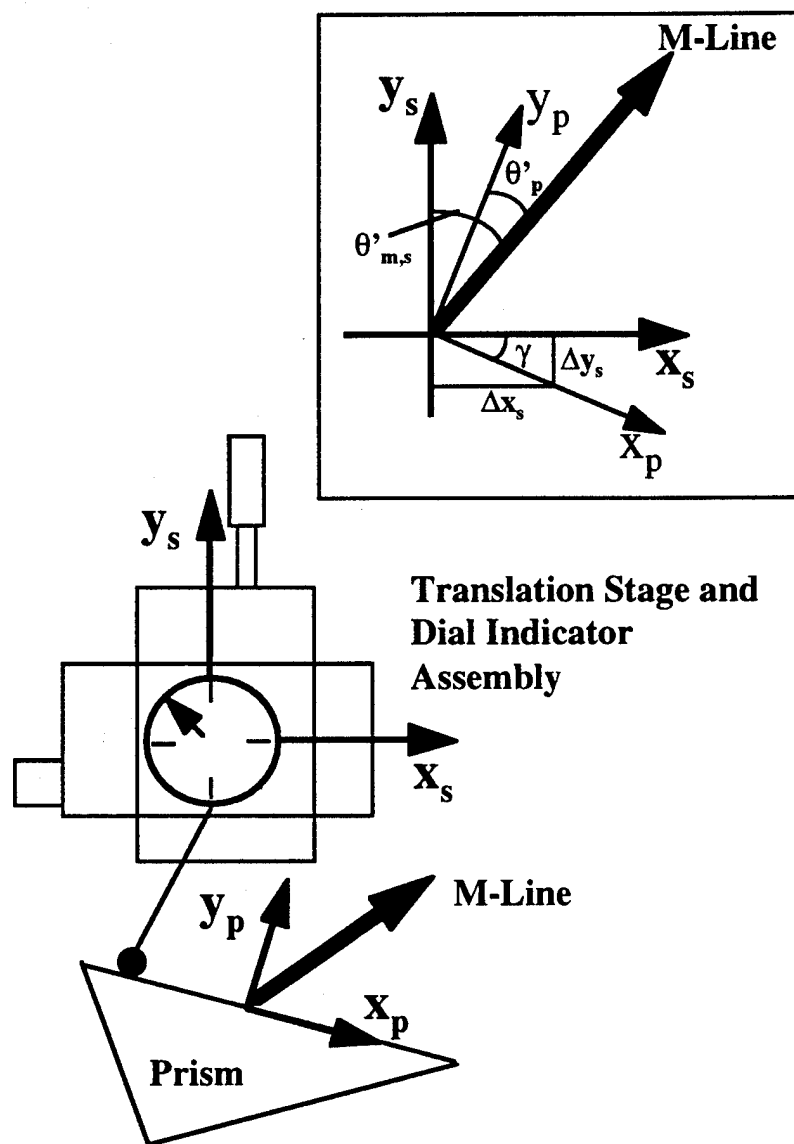


Figure 2.10. Measuring the misalignment between the translation stages and the prism output face. Inset shows the relationship between the stage's coordinate system  $(x_s, y_s)$  and the prism's coordinate system  $(x_p, y_p)$ . The rotation angle between these two coordinate systems is  $\gamma$ .

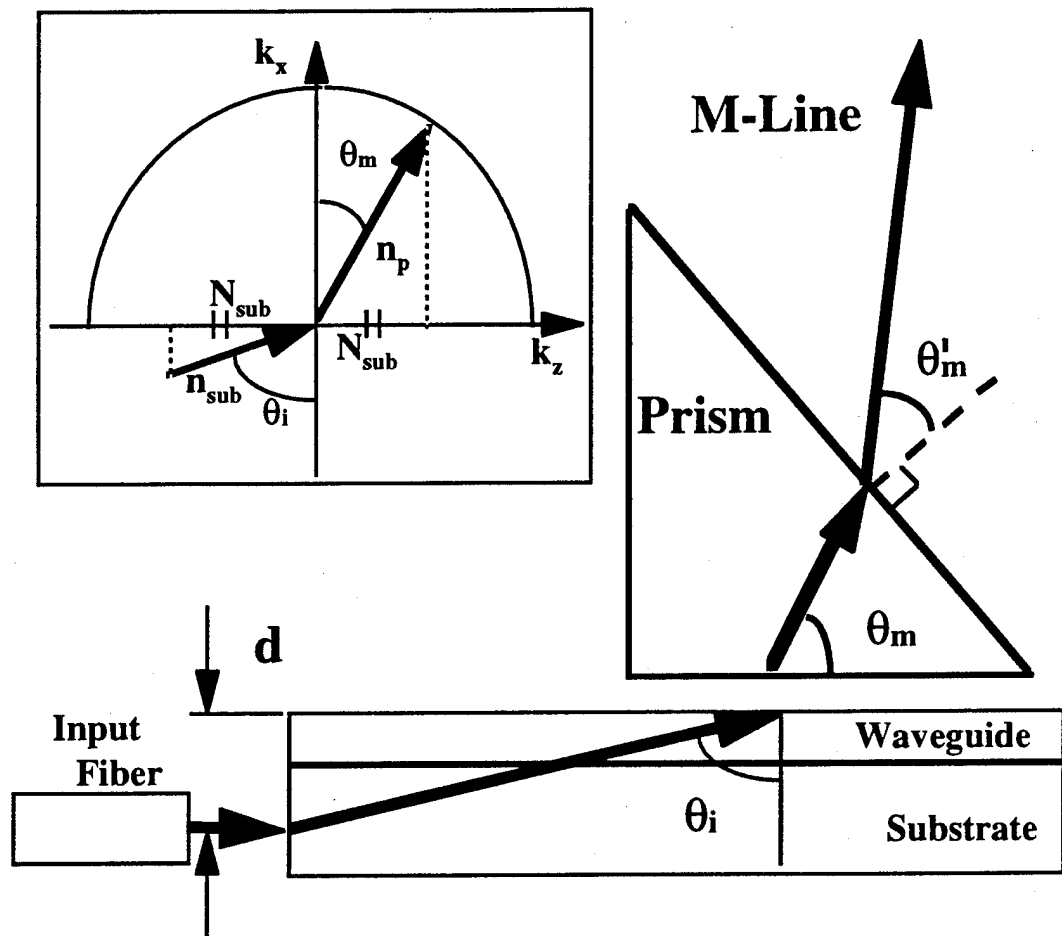


Figure 2.11. Exciting the substrate radiation mode by positioning the input fiber. Inset illustrates the phase-matching condition Equation (2.1) for the substrate radiation mode. We use the substrate effective index for  $N_{sub}$  to reduce systematic uncertainties when measuring mode effective index.

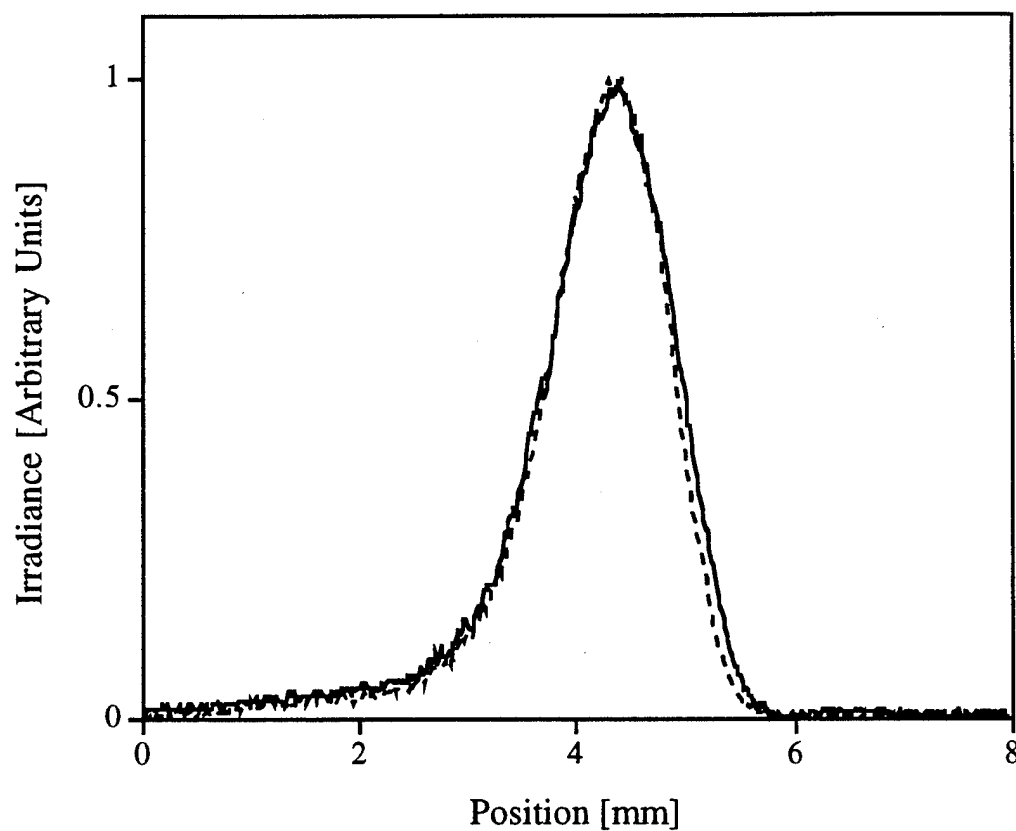


Figure 2.12. Mode TE-0 m-line irradiance profiles of a titanium in-diffused slab waveguide ( $\lambda = 0.6328 \mu\text{m}$ ) versus position along the CCD array. The solid curve corresponds to the far propagation distance while the dashed curve corresponds to the near propagation distance. The difference between propagation distances is 50.00 mm. These irradiance profiles have been normalized to 1 and shifted so that their maximum values coincide.

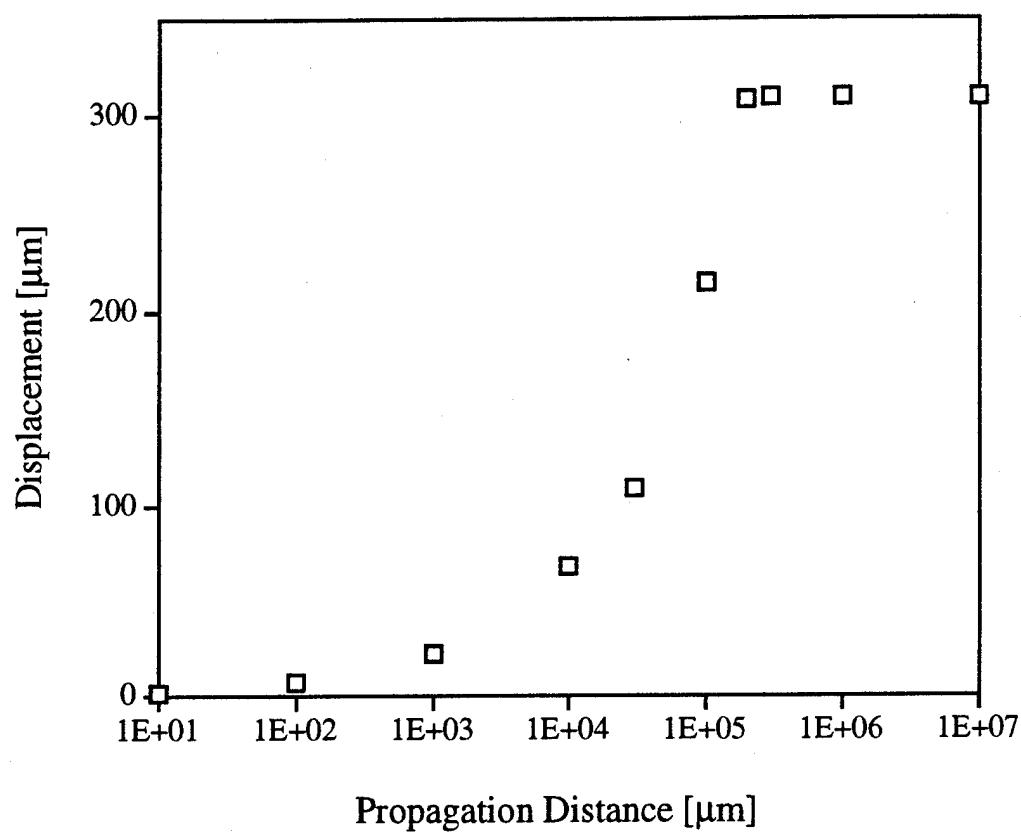


Figure 2.13. Displacement of m-line maximum irradiance from far-field propagation direction versus propagation distance.

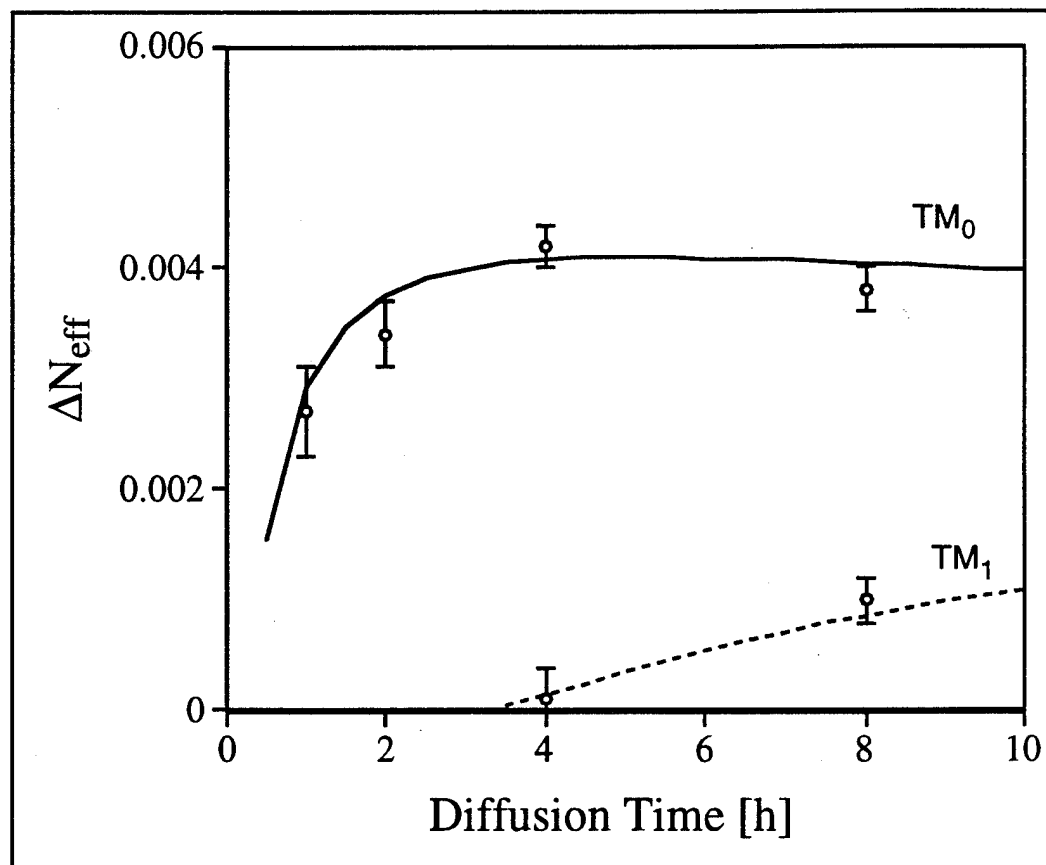


Figure 2.14. Increment above the substrate index of refraction for mode effective index versus diffusion time. The fundamental mode's effective index is TM-0 and that of the first higher order mode is TM-1. Theoretical curves are fitted to measured data points using the parameters in Equation (2.27).

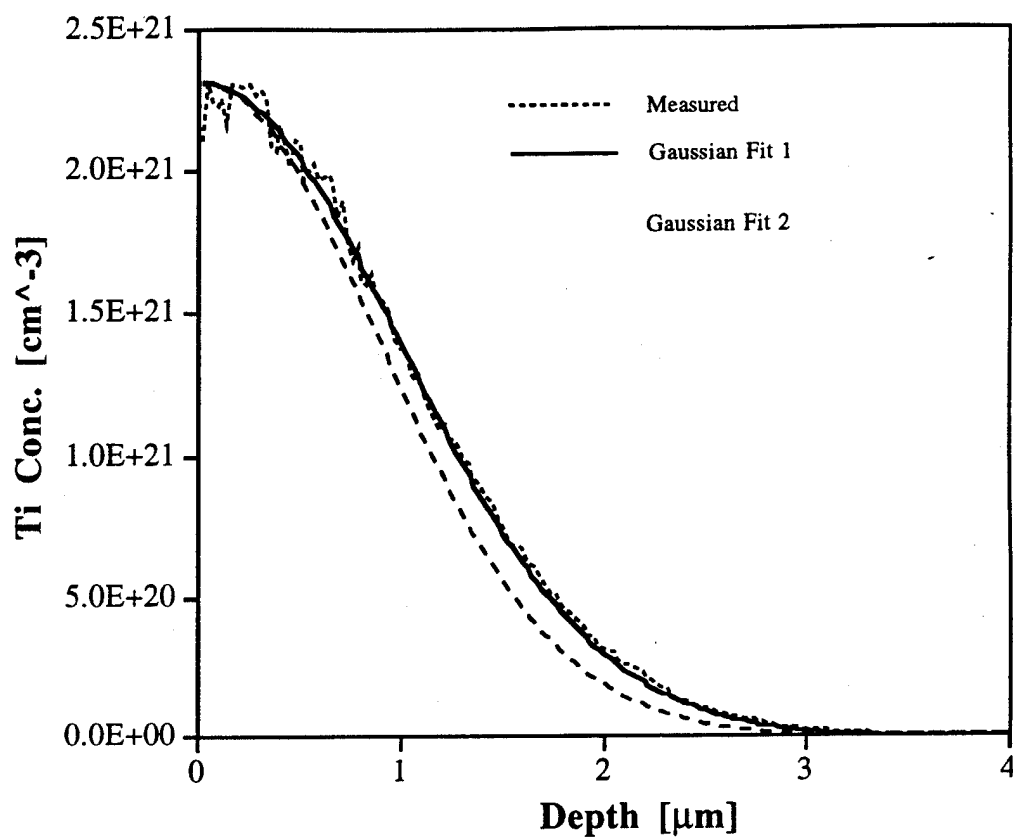


Figure 2.15. Titanium concentration versus substrate depth for 2 h diffusion (specimen 42). SIMS data are the short-dash curve. The solid curve is a Gaussian fit using  $D = 0.245 \mu\text{m}^2/\text{h}$ . The long-dash curve is a Gaussian fit using  $D = 0.2 \mu\text{m}^2/\text{h}$ .

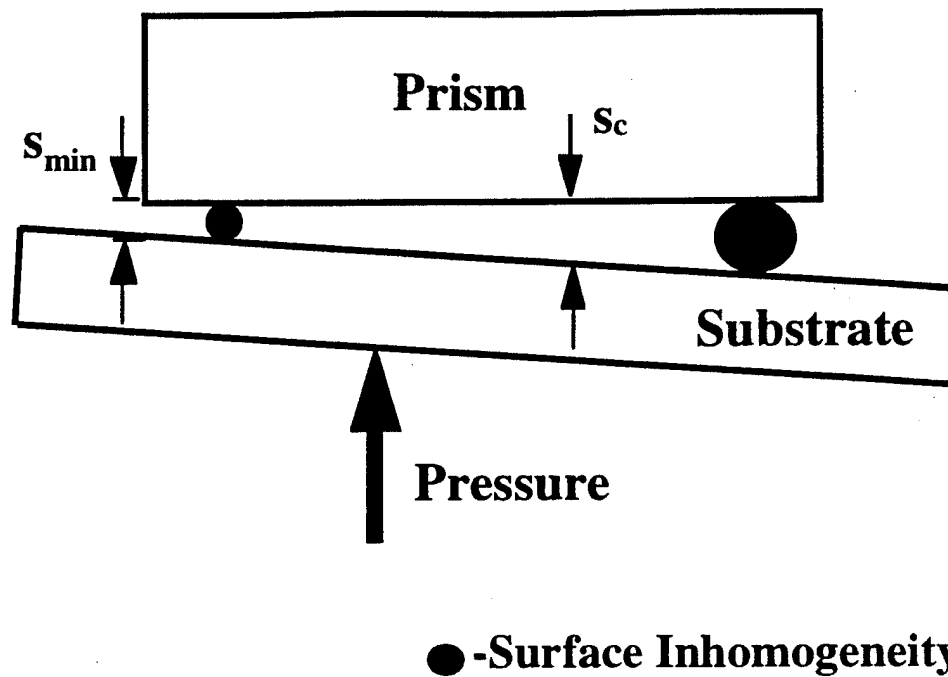


Figure 2.16. Schematic cross section of prism coupling region at initial contact between prism and waveguide.

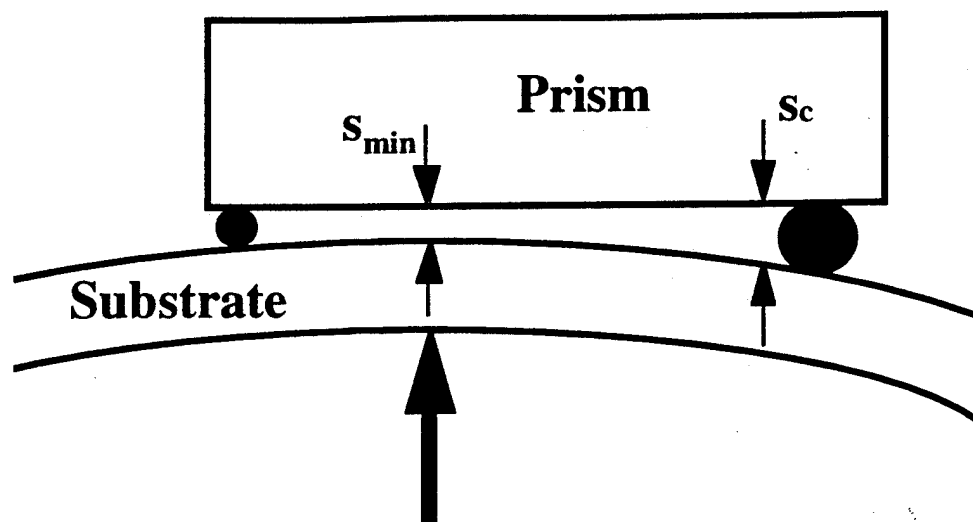


Figure 2.17. Schematic cross section of prism coupling region for high pressure applied to prism and waveguide.

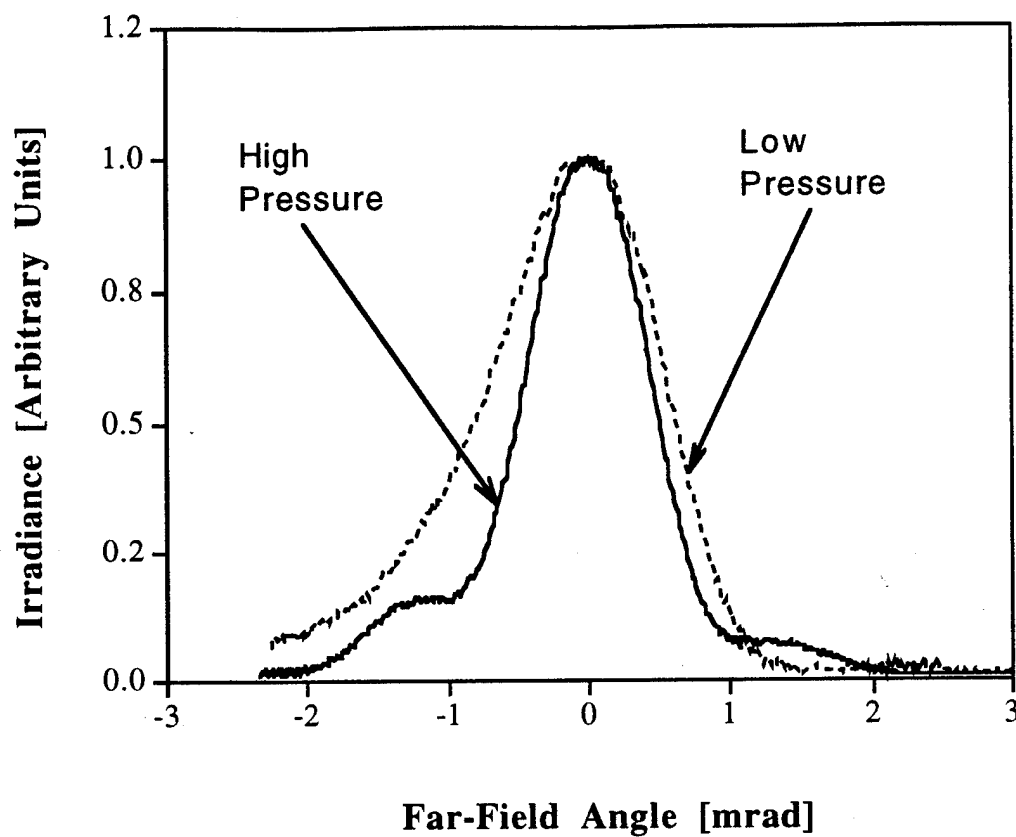


Figure 2.18. Comparing Set 1 TE-0 m-line profiles for low  $P_1^{(1)}$  and high  $P_2^{(1)}$  coupling pressures.

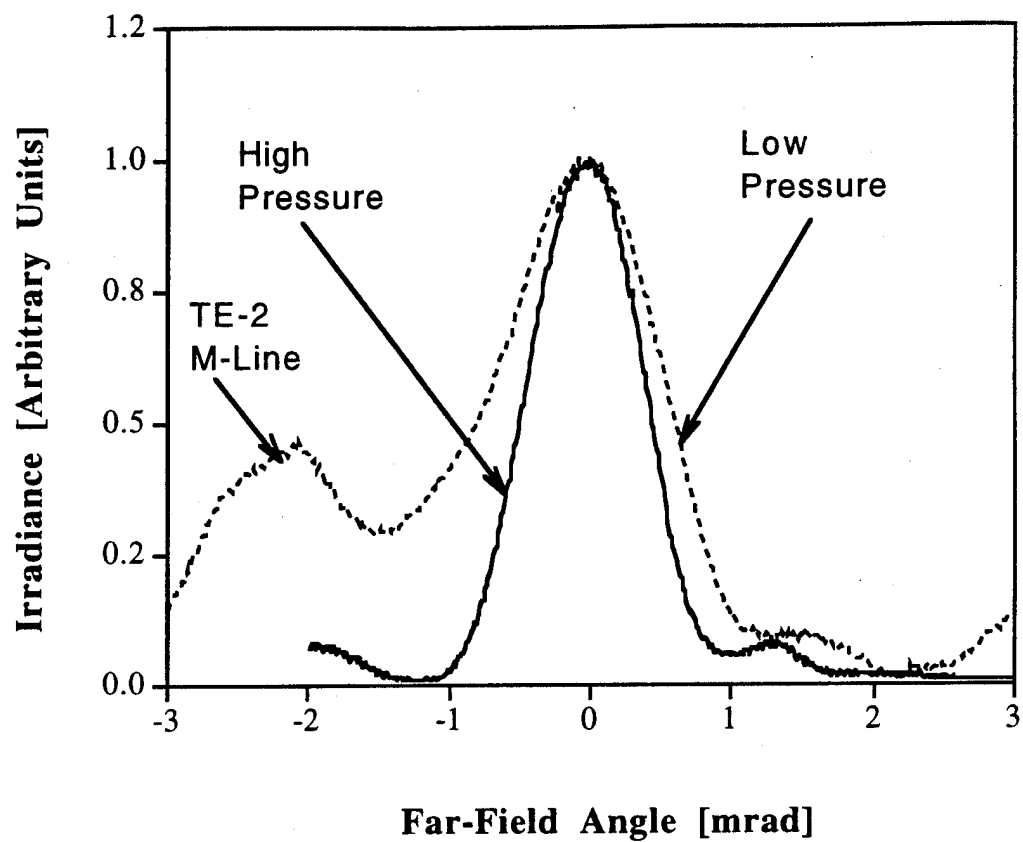


Figure 2.19. Comparing Set 1 TE-3 m-line profiles for low  $P_1^{(1)}$  and high  $P_2^{(1)}$  coupling pressures.

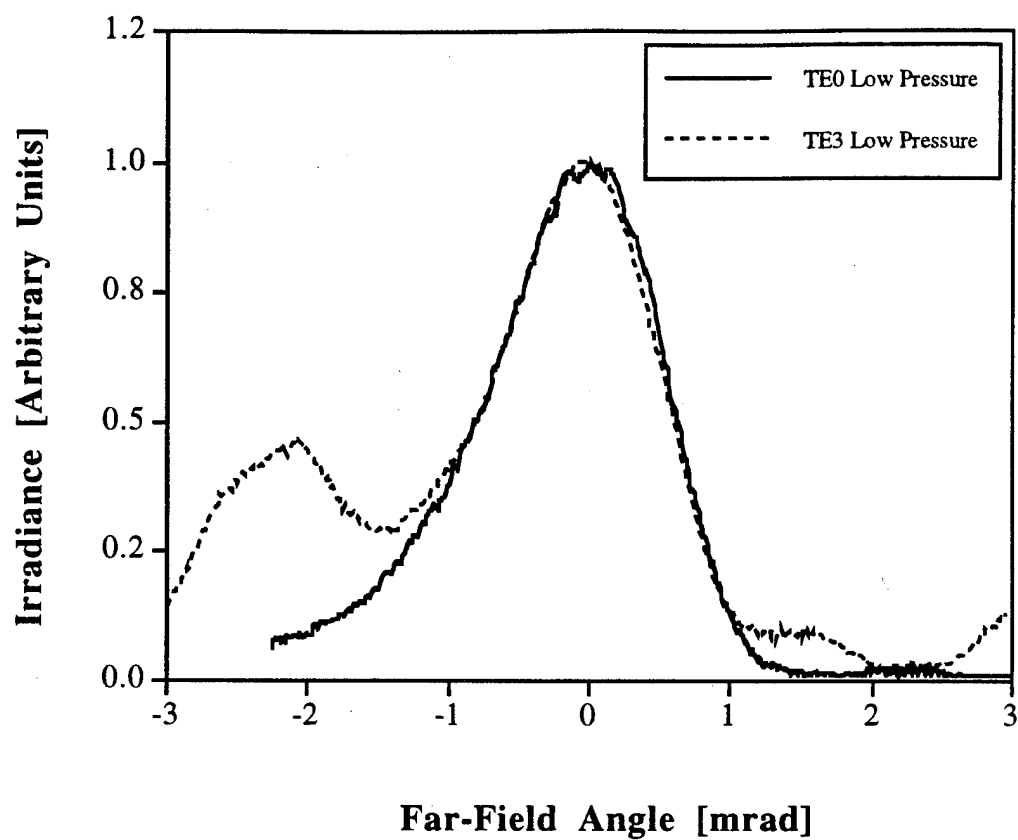


Figure 2.20. Comparing Set 1 TE-0 m-line profile to the TE-3 m-line profile when the coupling pressure is low  $P_1^{(1)}$ .

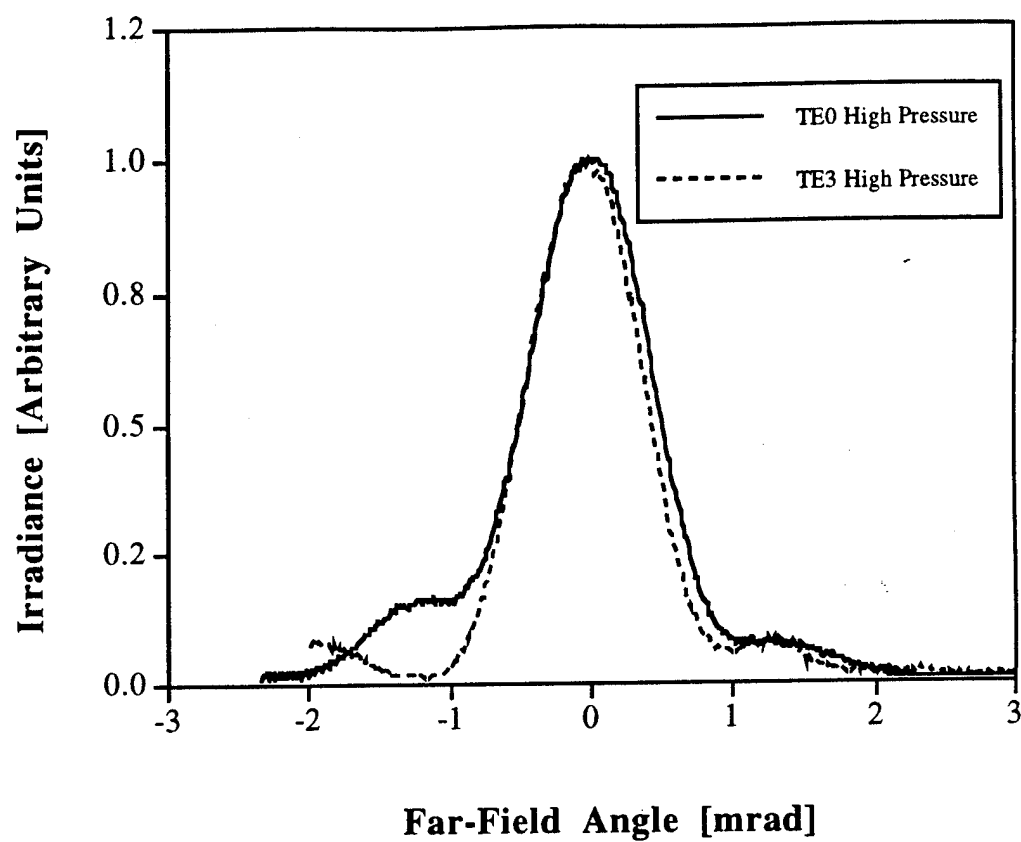


Figure 2.21. Comparing Set 1 TE-0 m-line profile to the TE-3 m-line profile when the coupling pressure is high  $P_2^{(1)}$ .

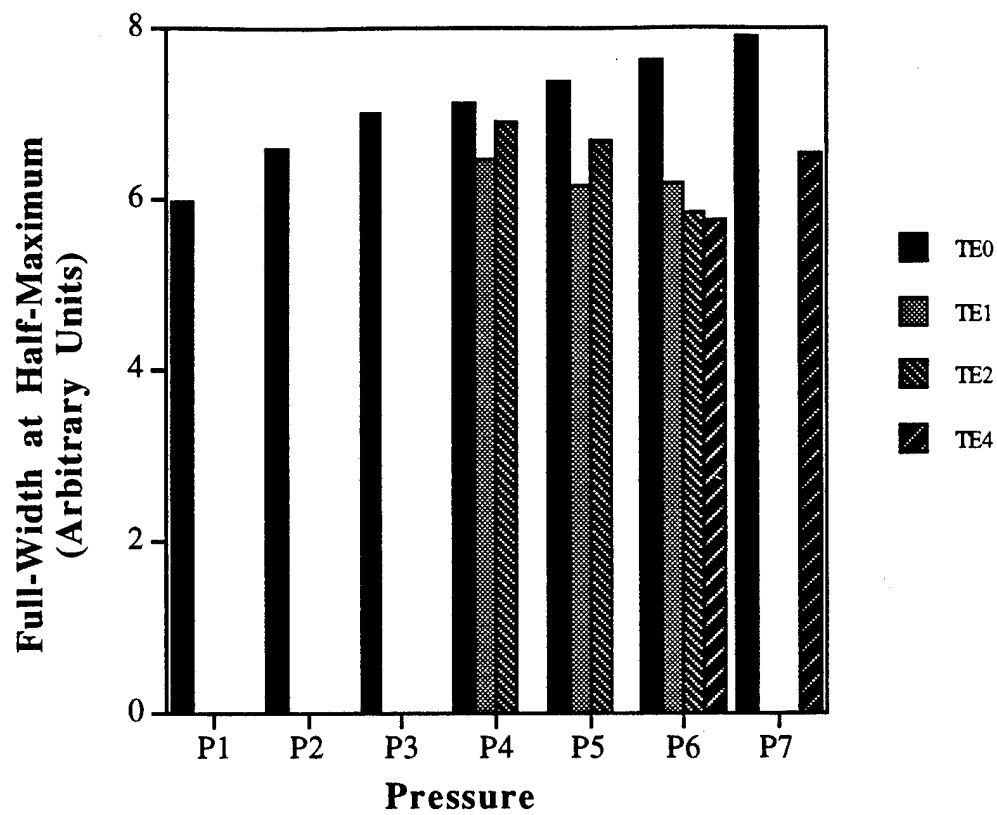


Figure 2.22. Measurements of m-line's irradiance profile full-width at half-maximum at various coupling pressures of Set 2. The coupling pressures increases from  $P_1^{(2)}$  to  $P_7^{(2)}$ .

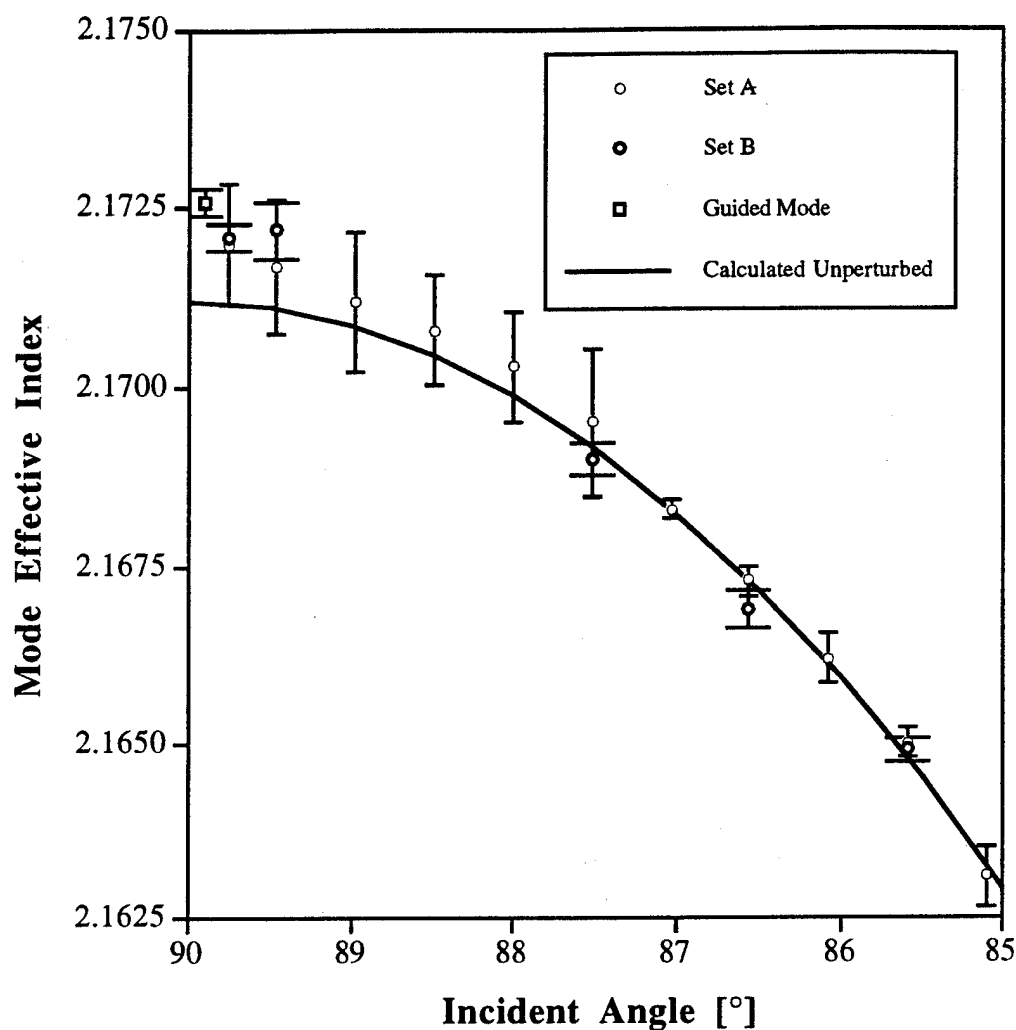


Figure 2.23. Measuring the TE substrate mode effective index versus angle of incidence  $\theta_i$  at  $\lambda = 0.829 \mu\text{m}$ . The open circles represent measurement set A while the filled circles represent measurement set B. The continuous line is a fit to the measured data for  $\theta_i < 87.5^\circ$  using the first-order model which ignores the prism-waveguide perturbation. This fit yields an effective index of 2.1712 at  $\theta_i = 90^\circ$ . The filled square represents the highest order TE guided mode effective index. We have widened the uncertainty bars of data set B as a graphical visualization aid.

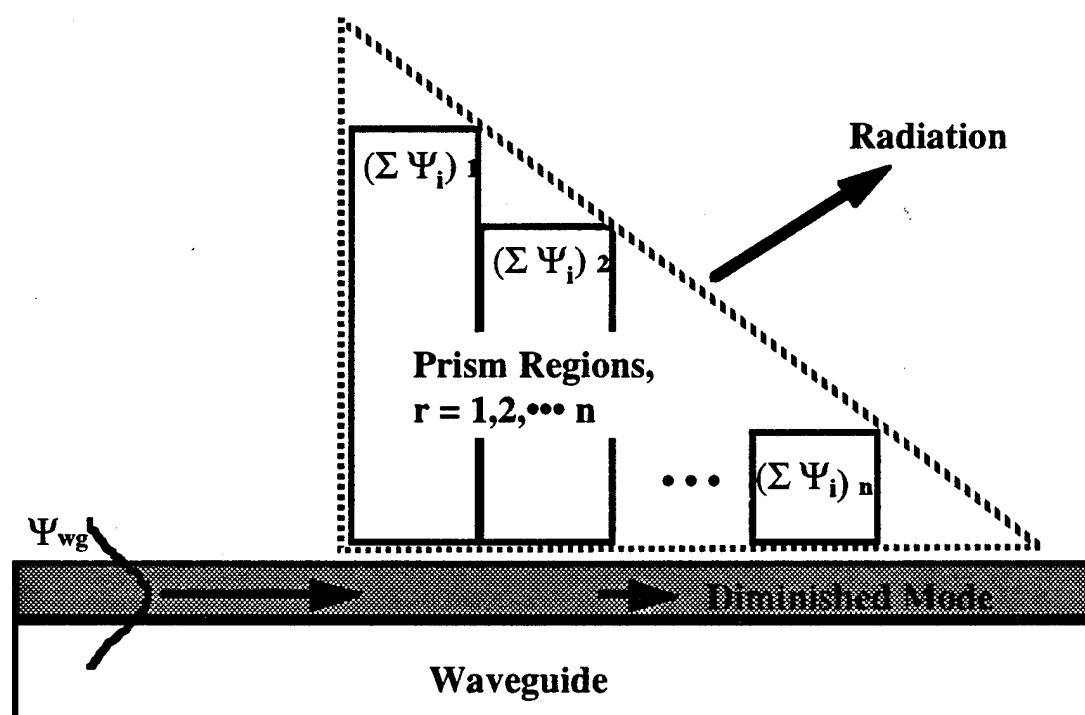


Figure 2.24. Geometry of composite waveguide for the local normal mode model for prism coupling. The segmented prism and unperturbed waveguide form composite waveguides.

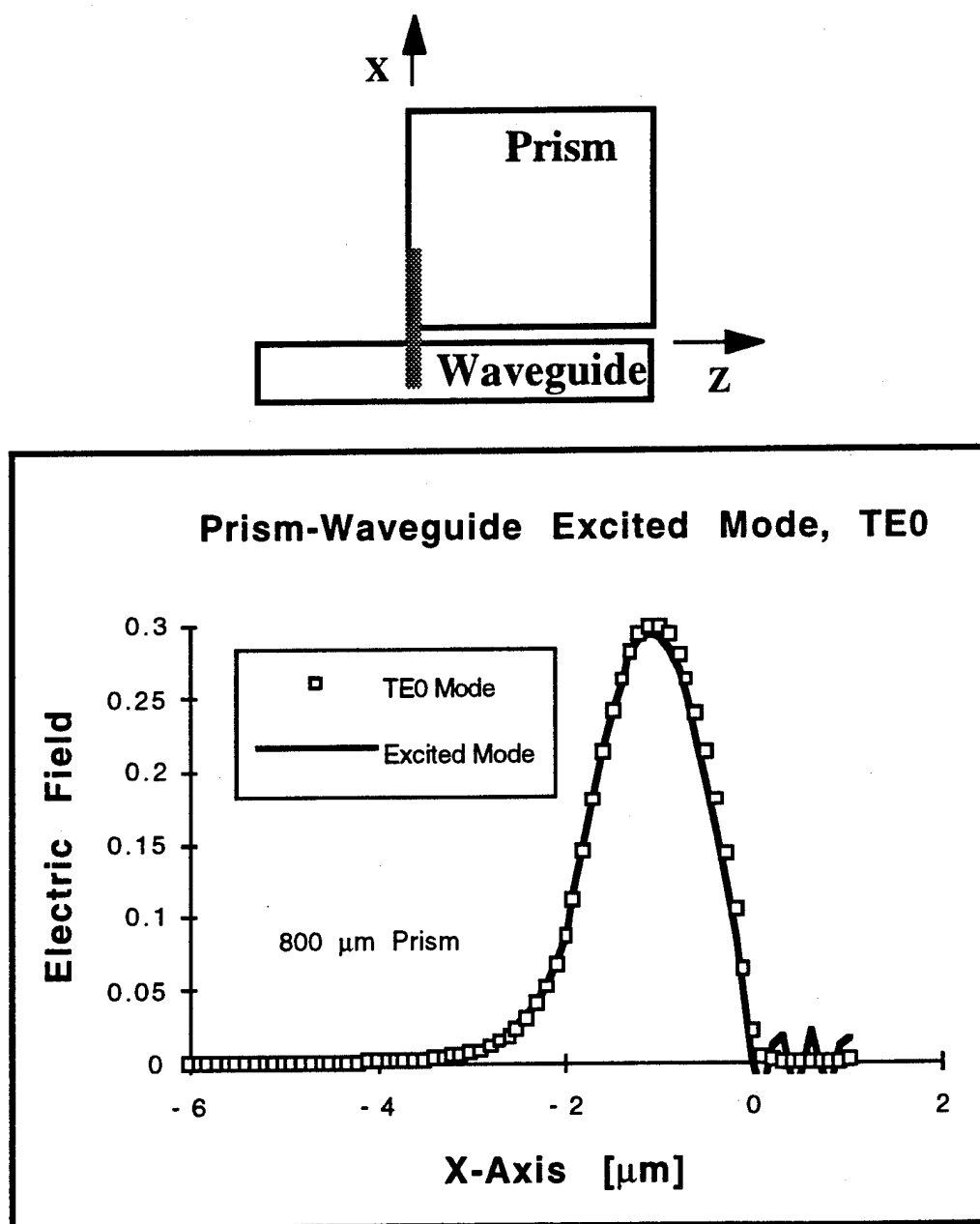


Figure 2.25. Comparison between the  $\text{TE}_0$  mode of the unperturbed waveguide and the excited modes of the composite waveguide.

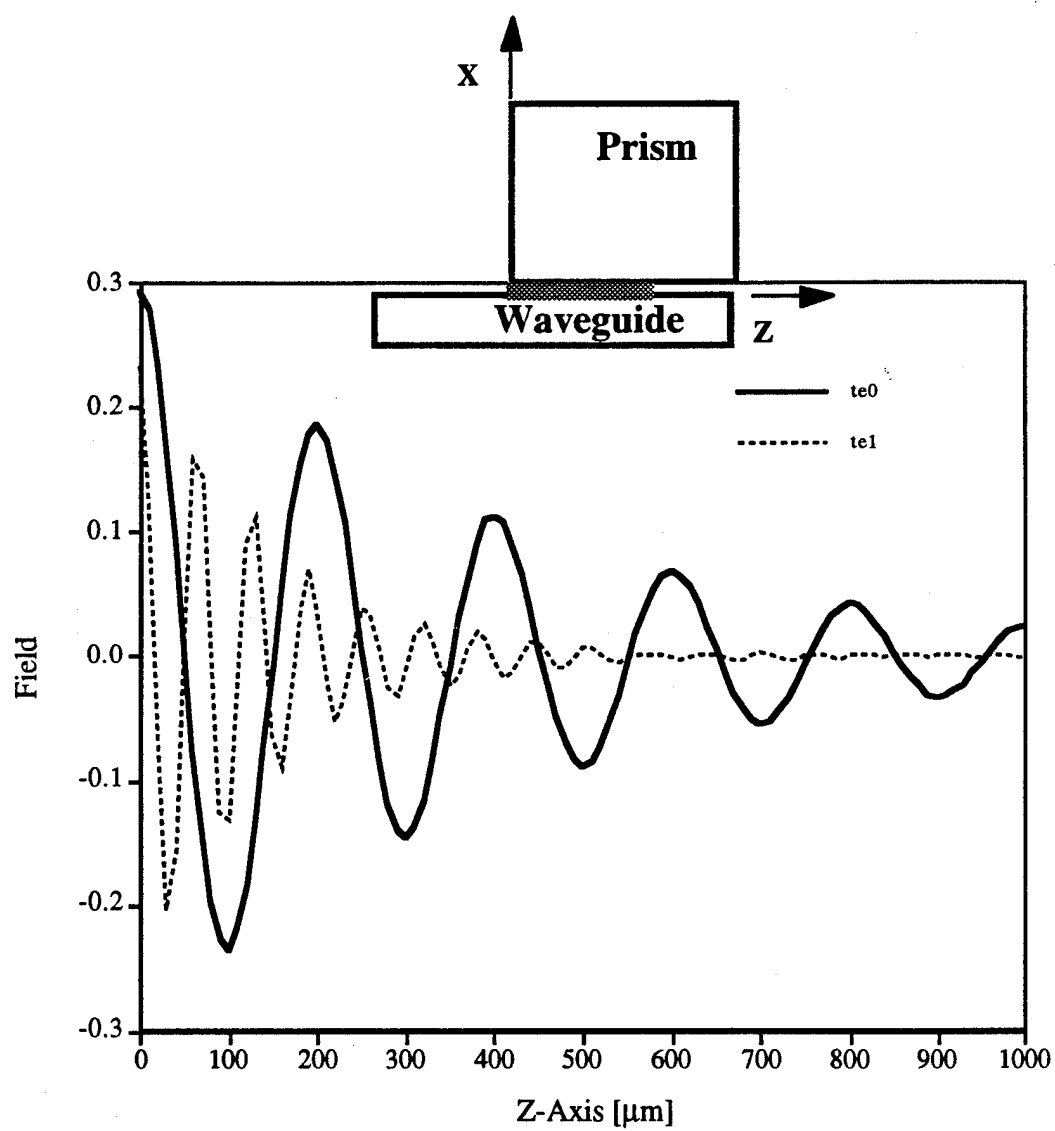


Figure 2.26: Evolution of the composite waveguide modes under the prism.

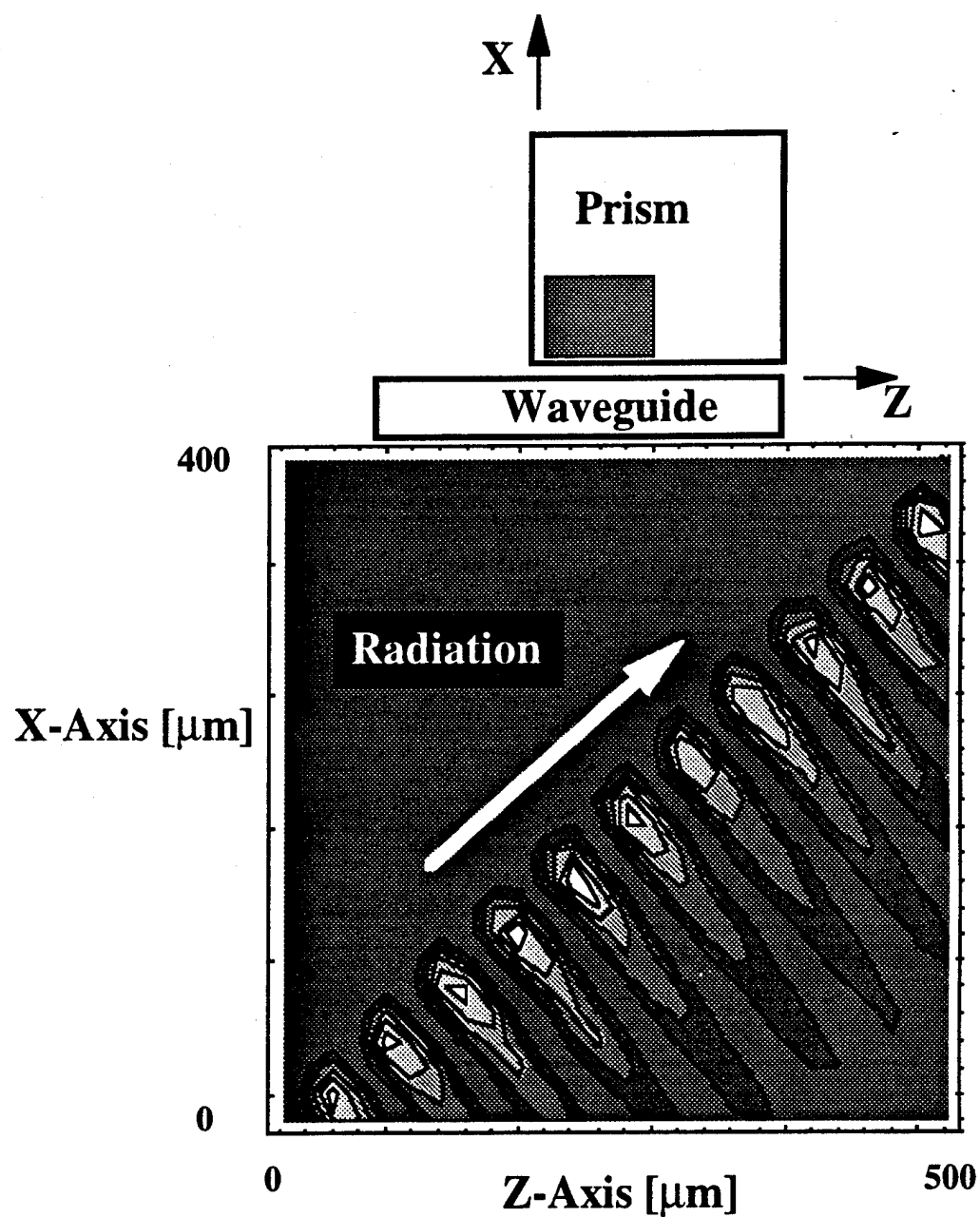


Figure 2.27. Irradiance distribution within the prism showing the evolution of the m-line.

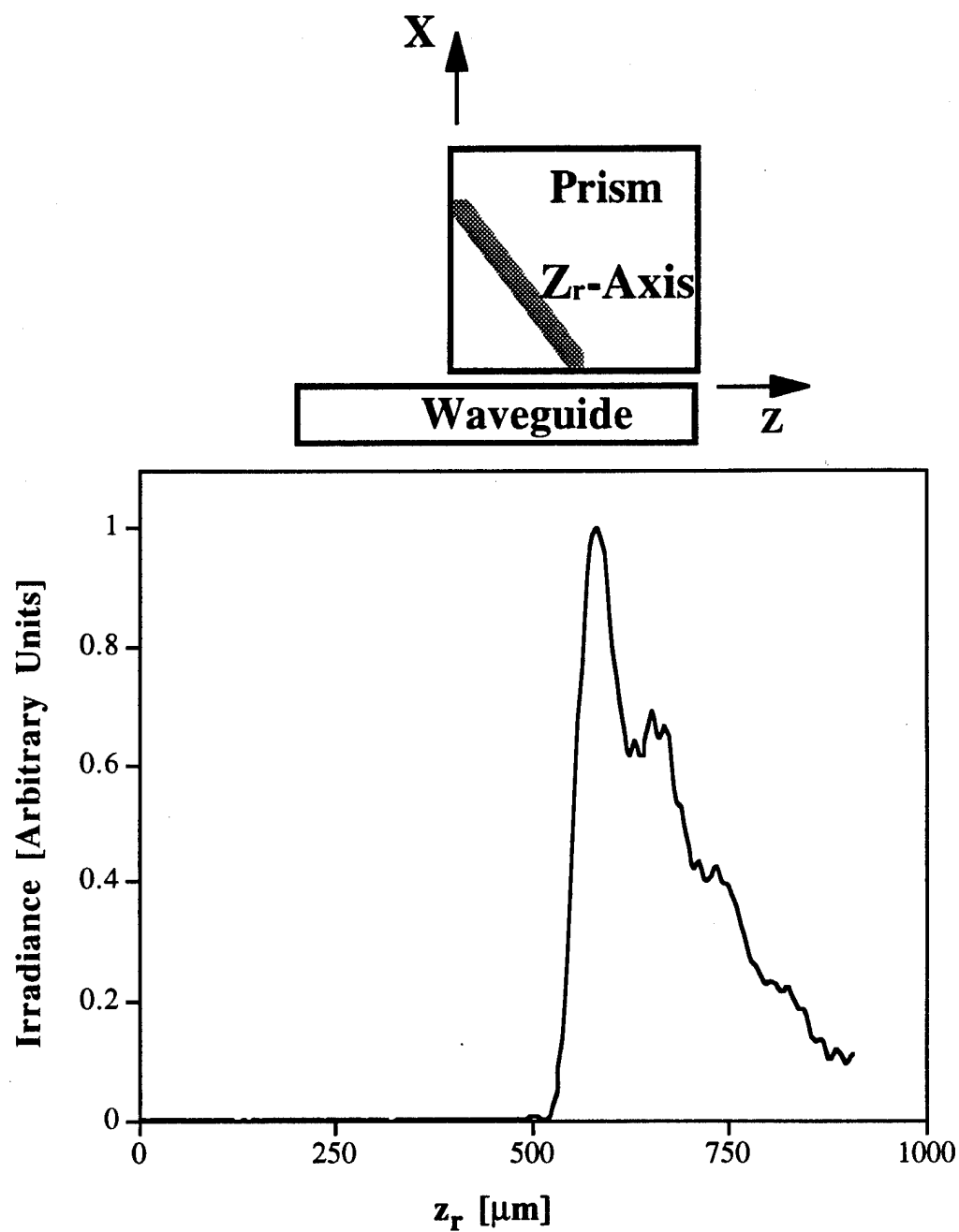


Figure 2.28. Near-field M-line irradiance profile calculated using the local normal mode model of output prism-coupling.

## CHAPTER 3

### NEARLY CUT-OFF MODES IN LITHIUM NIOBATE SLAB WAVEGUIDES

I have observed more extraordinary polarized guided modes near cut-off in titanium in-diffused lithium niobate planar waveguides than are predicted by titanium in-diffusion models. I also observe these nearly cut-off modes in lithium niobate specimens fabricated without titanium under a variety of diffusion atmospheres. I found more guided modes, with higher effective index in these plain lithium niobate specimens fabricated in wet oxygen than in specimens fabricated in either air, dry oxygen, dry argon, or wet argon. Values of the effective index of these nearly cut-off modes found in plain lithium niobate planar waveguides do not agree with those calculated using the lithium out-diffusion model for either vacuum-diffused or oxygen-diffused lithium niobate waveguides. I found good agreement between measured values of the effective mode index in specimens fabricated in either dry oxygen or air and calculated values found using an empirical diffusion model of a step index profile whose depth increases as the square root of diffusion time.

#### 3.1 Introduction

I have observed more extraordinary polarized (TE) x-propagating modes near cut-off in y-cut, titanium in-diffused lithium niobate planar waveguides than are predicted using a titanium in-diffusion model. However, both the number and effective index of the ordinary polarized (TM) x-propagating modes in these waveguides are in good agreement with the titanium in-diffusion model. I also

observed nearly cut-off TE modes in plain lithium niobate specimens fabricated under similar conditions in diffusion atmospheres containing air, dry oxygen, wet oxygen, dry argon, or wet argon.

The unexpected presence of these nearly cut-off modes signals the presence of processes, in addition to titanium in-diffusion affecting the refractive index profile in the waveguide. Accurate knowledge of the refractive index profile forming the waveguide is necessary to develop models predicting the number of guided modes, their field distribution, and their effective index of refraction. These models will become part of a waveguide computer aided design tool. The accuracy of the model is important because it directly affects the performance of optical components designed using this CAD tool.

Consider the design and fabrication of planar waveguides and integrated planar waveguide lenses of titanium in-diffused lithium niobate[29] ( $\text{Ti}:\text{LiNbO}_3$ ). These waveguide components form the optical system of an integrated acousto-optical device. From a device performance point of view, the ideal planar waveguide would support only one guided mode whose effective index could be accurately predicted. The value of the mode's effective index directly affects the focal length of the waveguide lens which is an important device design parameter. A single-mode waveguide is preferred because light coupled from the fundamental guided mode into higher-order guided modes can result in noise or cross-talk, thereby degrading device performance. Mechanisms that cause higher-order mode coupling include imperfect mode coupling at device input, abrupt waveguide-lens transitions, the acousto-optic interaction, and mode scattering from material inhomogeneities.

Each of these mechanisms is a source of power loss from the fundamental

guided mode. In a single-mode waveguide this lost power would radiate away from the fundamental mode, never again to interact with the fundamental mode. However, power radiated from the fundamental mode can couple into higher-order guided modes of a multimode waveguide. These higher-order modes will propagate along with the fundamental mode to the device output. The presence of multiple modes at the device output will degrade signal fidelity since the arrival time of each mode will differ because of mode dispersion. Additionally, if the relative path difference between the guided modes is less than a coherence length, then these modes will interact coherently causing further degradation of the signal.

It would be most desirable to find fabrication techniques that eliminate the processes producing these nearly cut-off modes. However, as will be shown in this Chapter, I have not been able to completely eliminate the formation of nearly cut-off modes in lithium niobate planar waveguides. Thus, in order to accurately model  $\text{Ti:LiNbO}_3$  planar waveguides I must determine both the origin and characteristics of these near cut-off modes including any interdependency with titanium in-diffusion.

I have begun to solve this problem by separating titanium in-diffusion from other diffusion processes. I have done this by examining the diffusion processes in plain  $\text{LiNbO}_3$  specimens. Also, I have fabricated planar as opposed to channel waveguide specimens to avoid confusion between the elimination of and inefficient coupling into nearly cut-off modes.

In this Chapter I report values of effective index for modes in y-cut lithium niobate planar waveguides formed by thermal diffusion. I show that nearly cut-off modes persist in waveguides fabricated under various conditions reported to suppress modes due to lithium out-diffusion. I also compare these measurements

of effective index to values calculated using various diffusion models presented in the literature and to an empirical model deduced from my data.

The outline of this Chapter follows. Section 3.2 discusses previous work analyzing near cut-off modes in lithium niobate and fabrication methods reported to eliminate these modes. Section 3.3 presents details of the waveguide fabrication and characterization procedures. Experimental results are presented in Section 3.4. Section 3.6 concludes this Chapter first by summarizing our results and then comparing our results to previous work related to diffusion processes in lithium niobate. In Appendix 3.5 I describe diffusion models used to generate calculated values of effective mode index for comparison to our measured values.

### 3.2 Background

Several groups have observed unwanted modes near cut-off in  $\text{Ti:LiNbO}_3$  waveguides [37, 38, 39]. The near cut-off modes are attributed to lithium out-diffusion taking place concurrently with titanium in-diffusion. Titanium in-diffused waveguides are formed by diffusing titanium metal into a lithium niobate substrate at elevated temperature [29]. During this period of high temperature, lithium also diffuses from the lithium niobate substrate [40]. Titanium in-diffusion produces an increase of both ordinary and extraordinary refractive indices. Lithium out-diffusion, by contrast, produces a relatively small increase in extraordinary refractive index, but it extends deep into the lithium niobate substrate. The combination of both lithium out-diffusion and titanium in-diffusion yields a composite index profile. The contribution to the index profile from lithium out-diffusion is suspected to allow extraordinary polarized guided modes near cut-off.

Secondary-ion mass spectrometry (SIMS) has been used by other groups

to verify a lithium-depleted region near the surface of Ti:LiNbO<sub>3</sub> waveguide specimens [38, 41]. However, their SIMS measurements reveal that the titanium in-diffusion depth and lithium out-diffusion depth are approximately equal. In addition, it appears that the distribution of lithium does not follow the functional form for lithium out-diffusion found previously [30]. This is an interesting result since reported values of the diffusion coefficient for titanium in-diffusion are two orders of magnitude smaller than the diffusion coefficient for lithium out-diffusion. This could indicate an interdependence between the two diffusion processes. Also, neither of these SIMS measurements reported the distribution of hydrogen in the LiNbO<sub>3</sub> specimen. The presence of hydrogen could be important because hydrogen increases the extraordinary refractive index in LiNbO<sub>3</sub>[42].

Various methods to suppress near cut-off modes in Ti:LiNbO<sub>3</sub> waveguides due to lithium out-diffusion have been reviewed by Jackel [43]. These methods include flowing argon and oxygen gases (sometimes bubbled through a column of water) into the furnace during diffusion and placing lithium powder within the furnace to control the partial pressure of lithium. These methods have not always yielded the same results when implemented by different groups. Possible explanations for these inconsistent results include variations in furnace type, grade and stoichiometry of LiNbO<sub>3</sub>, waveguide geometry, and evaluation techniques employed to determine the presence of lithium out-diffusion. These experimental variations make comparison of results from different research groups difficult. Even an unintentional difference such as ambient humidity is suspected to influence the outcome of waveguide fabrication [43].

For example, planar waveguides attributed to lithium out-diffusion were

formed in plain  $\text{LiNbO}_3$  specimens heated to  $1000^\circ\text{C}$  for 1-16 h in both flowing oxygen or flowing oxygen bubbled through water [44]. The effects of water vapor on  $\text{Ti:LiNbO}_3$  planar waveguides was also studied by Forouhar et al. [39]. Forouhar et al. reported that a diffusion atmosphere of flowing oxygen bubbled through water eliminated lithium out-diffusion in  $\text{Ti:LiNbO}_3$  (acoustic grade  $\text{LiNbO}_3$ ) planar waveguides for both shorter diffusion times and lower diffusion temperatures. They also reported that  $\text{Ti:LiNbO}_3$  waveguides diffused in  $\text{LiNbO}_3$  powder were free from lithium out-diffusion in all cases. However, they commented that many of their waveguides supported modes near cut-off. Furthermore, the characteristics of these nearly cut-off modes were not quantified.

Elimination of lithium out-diffusion was reported for  $\text{Ti:LiNbO}_3$  channel waveguides (acoustic grade  $\text{LiNbO}_3$ ) [45] and (unspecified  $\text{LiNbO}_3$  grade) [46] diffused in an atmosphere of flowing argon bubbled through water. Near-field images of channel waveguide endfaces were evaluated to determine whether there had been lithium out-diffusion. If light was guided only by the channel waveguide and not by the surface waveguide associated with lithium out-diffusion, then the fabrication method was deemed successful at eliminating lithium out-diffusion. However, Noda and Fukuma [47] showed that this evaluation method may be a better measure of the coupling efficiency between the light source and the channel waveguide than it is a measure of the presence of a multi-mode waveguide.

The orientation of our waveguide specimens is illustrated in Figure 3.1. The electric field of the TE modes is parallel to the axis of extraordinary refractive index  $n_e$  while the electric field of the TM modes is parallel to the axes of ordinary refractive index  $n_o$ . Since the characteristics of TE modes do not agree with diffusion models, I look toward mechanisms that affect the extraordinary refractive

index. In particular, I am looking for processes which could take place during the fabrication of titanium in-diffused waveguides and increase  $n_e$  while leaving  $n_o$  unchanged or slightly decreased. I know of two such processes in lithium niobate; they are lithium out-diffusion and proton exchange. In the remainder of this section, I present background information on both lithium out-diffusion and proton exchange in  $\text{LiNbO}_3$ .

Lithium out-diffusion from a lithium niobate substrate in vacuum was first reported as a means of forming optical waveguides [40]. Experimental results revealed a region with higher extraordinary refractive index at the surface of the lithium niobate substrate after exposure to elevated temperature in vacuum. The mechanism causing the change in index was identified from analysis of diffusion kinetics as the out-diffusion of lithium and oxygen ions [30]. The functional form of the lithium out-diffused index profile was obtained from theoretical considerations to be the integral of the complementary error function. This index profile was experimentally verified [30] using an interference microscope [40]. The dependence of crystal stoichiometry on lithium out-diffusion was studied [48] for  $\text{LiNbO}_3$  specimens out-diffused in flowing oxygen. These results show a general agreement with Carruthers et al. [30] for both the diffusion coefficient and increase in surface refractive index for diffusion at  $1080^\circ\text{C}$ . Two consequences of the form of the lithium out-diffusion index profile are that both the surface index and the diffusion depth increase proportionally to the square root of out-diffusion time. Thus, as the diffusion time increases, both the number of guided modes and the effective mode index will increase. Typical values for the index profile in a specimen held at  $1000^\circ\text{C}$  for 21 h in vacuum are: surface extraordinary index increase is 0.0013 and the diffusion depth is  $140\ \mu\text{m}$ .

Proton exchange in lithium niobate [42] is another process that increases the surface extraordinary refractive index of a lithium niobate substrate. Proton exchange in lithium niobate is usually carried out by placing a lithium niobate specimen in a bath of molten benzoic acid at temperatures less than 249 °C for several hours. It is thought that lithium ions within the  $\text{LiNbO}_3$  specimen are exchanged for protons within the acid melt. This ion exchange process results in a step-like increase in the extraordinary refractive index at the surface [42, 49]. A proton exchange for 1 h at 249 °C yields a step-like index layer that is 2  $\mu\text{m}$  deep with extraordinary refractive index increased by 0.12 above the substrate refractive index [42].

Proton exchange in 100% benzoic acid for long times is known to etch the y-face of y-cut  $\text{LiNbO}_3$  specimens [42, 50], rendering the specimen unsuitable for optical waveguides. However, proton exchange either in dilute benzoic acid [51] or, for short exchange times, in 100% benzoic acid [52] result in waveguides free from surface damage but with a relatively smaller increase in extraordinary refractive index.

### 3.3 Waveguide Fabrication and Metrology

**3.3.1 Fabrication** Waveguide specimens discussed in this Chapter were fabricated on substrates cut from 1 mm thick optical grade y-cut  $\text{LiNbO}_3$  wafers. According to the manufacturer, these lithium niobate wafers originate from a crystalline boule that is grown using the Czochralski crystal growth technique. The crystalline boule is drawn from a congruent melt of high purity  $\text{Nb}_2\text{O}_5$  and  $\text{LiCO}_3$  powders (less than 2 ppm of each transition metal, including iron). The congruent composition value of the melt is  $48.38 \pm 0.015$  mole-%  $\text{Li}_2\text{O}$ . The resultant crystalline boule has compositional uniformity that is less than  $\pm 0.005$

mole-%  $\text{Li}_2\text{O}$ . Wafers are cut from this boule, then polished. The final surface quality of the wafer is 10/5 scratch-dig for the -y face and 60/30 scratch-dig for the +y face.

Waveguides are formed on the -y face of the  $\text{LiNbO}_3$  substrates. Waveguide modes propagate along the direction of the crystal's x-axis. Typical dimensions of the rectangular waveguide substrates are 1 cm along the z-axis and 1 to 3 cm along the x-axis. Waveguides were formed on two different types of substrates: those with evaporated titanium and those without evaporated titanium (plain substrates). Substrates with titanium were prepared as follows. Titanium metal was evaporated onto an entire  $\text{LiNbO}_3$  wafer in order to insure titanium thickness uniformity for each waveguide specimen. The titanium metal was evaporated to a thickness of 25nm by resistive heating in a vacuum of  $5 \cdot 10^{-4}$  Pa. The titanium thickness was determined by a quartz crystal oscillator. Individual specimens were cut from this metalized wafer and then placed in a high temperature diffusion furnace. Afterwards, the specimen's endfaces were polished to optical quality for efficient input and output optical coupling.

Substrates without titanium were prepared in the same manner but with the following differences: the metalization step was omitted, and the polishing of the sample endfaces preceded the high temperature diffusion. A schematic diagram of the diffusion furnace is shown in Figure 3.2. The composition of the furnace liner is not precisely known to us. However, after consultation with a furnace liner manufacturer, I concluded that the liner in our furnace is most likely composed of  $\text{Al}_2\text{O}_3$  and  $\text{SiO}_2$ . The temperature schedule for the diffusion begins at room temperature and reaches the diffusion temperature,  $T=1000^\circ\text{C}$ , after a 2h ramp-up time. The substrates are maintained at the diffusion temperature for

a time  $t$ . Afterwards, the samples cool to room temperature within 2h.

The diffusion atmosphere surrounding some specimens was created by flowing various gases inside the diffusion furnace. The flowing gases included both oxygen and argon. In some cases the gases flowed through a 17 cm column of room-temperature de-ionized water before reaching the diffusion furnace; this diffusion atmosphere will be identified as wet. When the diffusion gases did not bubble through de-ionized water, the process is identified as dry. Some specimens were diffused without flowing gases into the diffusion furnace. These cases are referred to as air. The specimens diffused in wet or dry argon were cooled to room temperature in flowing oxygen to reoxidize the specimen and prevent discoloration.

After fabrication all specimens appeared to be free from surface defects and yielded good quality waveguides. The fabrication parameters for  $\text{LiNbO}_3$  waveguide specimens are listed in Table 3.1.

**3.3.2 Metrology** The effective index  $N$  of a waveguide mode is measured using the prism out-coupling technique [9]. Figure 3.3 illustrates the effective index measurement experimental setup. Light from a HeNe laser at wavelength  $\lambda = 0.6328\mu\text{m}$  is butt-coupled into the slab waveguide using a single-mode polarization-maintaining fiber. The extinction ratio between the two orthogonally polarized modes of the fiber was greater than 400:1. A rutile prism with its optic axis parallel to the waveguide's optic axis is pressed against the waveguide to couple light out from the waveguide. At the output face of the prism the out-coupled light, or  $m$ -line, is refracted into air at the mode angle  $\theta'_m$ . The mode's effective index is related to the mode angle by [23]

$$N = n_p \sin \left( \theta_p + \arcsin \left( \frac{n_c}{n_p} \sin (\theta'_m) \right) \right), \quad (3.1)$$

where  $n_p = 2.8666$  [36] is the prism's extraordinary index,  $\theta_p = 60.59 \pm 0.02^\circ$  is the prism's angle, and  $n_c = 1.0003$  is the index of air.

In order to measure  $\theta'_m$ , I aligned two translation stages; one with travel parallel to the prism output face and one with travel perpendicular to the prism output face. A charge coupled device (ccd array) is affixed to these stages at a distance of 1 m from the prism output face. The  $m$ -line illuminates the ccd array, and a profile of the  $m$ -line is viewed on a digital oscilloscope. The angle  $\theta'_m$  is determined using inverse triangulation. A right triangle is formed by translating the ccd array a distance and a perpendicular distance; see Figure 3.3. For a particular stage translation  $\Delta x$ , the translation  $\Delta y$  is determined by repositioning the  $m$ -line at the location on the ccd array. Now, the mode angle can be calculated using the equation

$$\tan(\theta'_m) = \frac{\Delta x}{\Delta y}. \quad (3.2)$$

The measurement of  $\theta'_m$  has several sources of systematic uncertainty which affect the calculation of  $N$ . These sources include the uncertainty in both the prism angle and the prism index, uncertainty of both the alignment and travel of the stages, and variations in the waveguide-to-prism coupling. Our technique includes a procedure which reduces the influence of these uncertainties at the expense of yielding a relative, rather than absolute values of the effective index. This procedure uses an  $m$ -line which is associated with a substrate radiation mode. This substrate radiation mode is excited by positioning the input fiber a distance  $d$  from the waveguide surface perpendicular to the plane of the waveguide; see Figure 3.3. As the value of  $d \rightarrow 0$ , the value of  $\theta'_m$  for the radiation mode approaches the value of the substrate angle  $\theta'_{sub}$ . A value of the substrate index  $n_{sub}$  is calculated from  $\theta'_{sub}$  using Eq. 3.1. A value of  $n_{sub}$  is obtained for each

effective index measurement and is subtracted from the value of  $N$  for the guided mode. This relative value  $\Delta N = N - n_{sub}$  yields the increment by which the effective index exceeds the substrate index.

Uncertainty with the measured values of  $\Delta N$  due to the random uncertainty of repositioning the  $m$ -line on the ccd array remains. The error bars displayed in the plots of  $\Delta N$  presented in this Chapter represent this measurement uncertainty. The minimum value of the random measurement uncertainty yields an uncertainty of  $\Delta N = \pm 2 \cdot 10^{-4}$ .

### 3.4 Experimental Results

**3.4.1 Titanium in-diffused LiNbO<sub>3</sub> waveguides** Measured effective index values for specimens 41, 42, 43, and 48 are plotted versus diffusion time for TE modes in Figure 3.4 and for TM modes in Figure 3.5. These waveguide specimens were diffused at 1000°C in flowing O<sub>2</sub>+H<sub>2</sub>O. Measured values are represented by discrete symbols with error bars. Values of  $\Delta N$  predicted from a titanium in-diffusion model are represented by continuous lines. This titanium in-diffusion model is described in Appendix 3.5.1. In Figure 3.4 we see moderate agreement between the measured and predicted values for the fundamental waveguide mode. Furthermore, Figure 3.4 shows more TE modes near cut-off are measured than predicted by the model. For example, in specimen diffused for 4 h I measured five TE modes and the model predicts only two TE modes.

When the titanium in-diffusion model is applied to the calculation of the effective index of the TM mode, I find better agreement with measured results. This is illustrated in Figure 3.5, where we see good agreement between both the number of modes and  $\Delta N$ .

**3.4.2 Plain LiNbO<sub>3</sub> waveguides** Measured values of the fundamental waveguide mode effective index in plain LiNbO<sub>3</sub> planar waveguide specimens are shown in Tables 3.2–3.4. Only effective index values for the fundamental waveguide mode are reported because the higher order modes were closely spaced and thus could not be resolved by *m*-line measurements. The diffusion temperature was 1000°C for all the specimens. Another consequence of the close spacing between the *m*-lines is the uncertainty of the total number of guided modes in a waveguide specimen. In each of Tables 3.2–3.4 I have displayed the best estimate of the total number of modes supported in each waveguide. Tables 3.2–3.4 include the calculated values of both the fundamental mode effective index and the total number of modes in a lithium out-diffused waveguide using the lithium out-diffusion model described in Appendix 3.5.2.

Table 3.2 shows measured values of effective index for waveguide specimens 50A, 50B, 51, 52, and 53. These specimens have been processed for 2 h in the following atmospheres: air, wet argon, dry argon, wet oxygen, and dry oxygen. Each of these diffusion atmospheres resulted in the formation of guided modes. The measurement uncertainty makes comparisons of both  $\Delta N$  and mode number difficult between specimens diffused for 2 h. However, diffusion in wet-argon yields the lowest value of  $\Delta N$  and possibly the fewest number of modes. In Table 3.2, the calculated value of  $\Delta N$  for lithium out-diffusion is lower than each of the measured values of  $\Delta N$ . Also, the calculated number of lithium out-diffused modes is slightly greater than the number of modes measured in each of the waveguide specimens.

The results for plain LiNbO<sub>3</sub> specimens 50A, 52, and 54 processed for 8 h are shown in Table 3.3. After an 8 h diffusion we begin to see a distinction

between  $\Delta N$  for specimens diffused in a wet-oxygen atmosphere and for specimens diffused in both air or dry-oxygen atmospheres. Specimen 54 (diffused in wet oxygen) has a larger value of  $\Delta N$  than either specimen 50A (diffused in air) or specimen 52 (diffused in dry oxygen). While the differences in both  $\Delta N$  and the number of modes between specimens 50A and 52 remain indistinguishable due to measurement uncertainty. There is a greater distinction between the measured values of both  $\Delta N$  and the number of modes, and those values calculated using the lithium out-diffusion model after an 8 h diffusion (Table 3.3) than after a 2 h diffusion (Table 3.2).

The results for plain  $\text{LiNbO}_3$  specimens 50A, 52, and 54 processed for 21 h are shown in Table 3.4. After 21 h there is a clear distinction between the value of  $\Delta N$  for specimen 54 (diffused in wet-oxygen) and  $\Delta N$  for both specimen 50A (diffused in air) and specimen 52 (diffused in dry-oxygen). The value of  $\Delta N$  for specimen 54 is approximately twice the value of  $\Delta N$  for both specimen 50A and specimen 52. The numbers of modes observed in the specimens diffused in dry oxygen and wet oxygen are approximately equal and greater than the number observed in the specimen diffused in air. Once again, the calculated value of  $\Delta N$  for lithium out-diffusion is lower than all of the measured values. Also, the calculated number of modes for the lithium out-diffused waveguide is much larger than the measured number of modes. However, the calculated value of  $\Delta N$  using the lithium out-diffusion model is closer to the measured values of  $\Delta N$  for both specimens 50A (diffused in air) and 52 (diffused in dry oxygen) after a 21 h diffusion than after an 8 h diffusion.

Measured values of  $\Delta N$  for the fundamental mode for specimens diffused in a particular atmosphere are plotted versus diffusion time in figures 3.6–3.8.

These measured values are compared to calculated values of  $\Delta N$  for the fundamental mode in a lithium out-diffused waveguide [30]. Figure 3.6 and Figure 3.7 also show plots of calculated values of  $\Delta N$  for the modes of a step index waveguide whose high index layer increases in depth proportionally to the square root of diffusion time. Results for specimens diffused in air are plotted in Figure 3.6, for specimens diffused in dry oxygen in Figure 3.7, and for specimens diffused in wet oxygen in Figure 3.8.

### 3.5 Diffusion Models

This Section presents three models used to generate calculated values of effective index presented in this Chapter. Each model addresses a different type of refractive index profile. These refractive index profiles result from: titanium in-diffusion, lithium out-diffusion or an as yet unidentified diffusion process which results in a step-like index profile. Each model is comprised of two parts: the first part determines the refractive index profile forming the waveguide and the second part, common to each model, solves for the waveguide's effective mode indices. This second part uses a multilayer approximation to the graded-index profiles and solves Maxwell's equations subject to the guided-mode boundary conditions [53].

In the next three sections I discuss the basis for the algorithms used to determine the refractive index profile for the each model.

**3.5.1 Titanium in-diffusion model** This section describes the refractive index profile caused by titanium in-diffusion in lithium niobate. First, I describe the concentration profile  $C(y)$  of titanium within the  $\text{LiNbO}_3$  substrate; then I relate the titanium concentration to an increase in refractive index. The concepts of particle diffusion are applied to finding  $C(y)$ . The diffusion problem I solve here is one-dimensional diffusion of a finite source of material (evaporated

titanium metal) into an infinite half-space (lithium niobate substrate). The concentration profile resulting from this diffusion problem is [54]

$$C(y, t) = \frac{1}{2} C_0 \left\{ \operatorname{erf} \left( \frac{\tau - y}{2\sqrt{Dt}} \right) + \operatorname{erf} \left( \frac{\tau + y}{2\sqrt{Dt}} \right) \right\}, \quad (3.3)$$

where  $C_0$  is the initial titanium concentration of the evaporated layer,  $\operatorname{erf}()$  is the error function,  $y$  is the depth measured from the surface of the  $\text{LiNbO}_3$  substrate,  $\tau$  is the thickness of evaporated titanium,  $D$  is the diffusion coefficient, and  $t$  is the diffusion time. The diffusion depth is defined as  $b = 2\sqrt{Dt}$ .

I used the following relationship for the change in refractive index ( $\Delta n(y)$ ) due to the titanium concentration [32]:

$$\Delta n(y, t) = (K C(y, t; D))^\eta \quad (3.4)$$

where  $K$ ,  $\eta$  and  $D$  are treated as fitting parameters. The values of the fitting parameters are:

$$\begin{aligned} K &= \frac{0.73}{C_0}, \\ \eta &= 0.88, \end{aligned} \quad (3.5)$$

$$D = 0.2 \mu\text{m}^2/h$$

for the extraordinary refractive index profile used to calculate  $\Delta N$  in Figure 3.4, and

$$\begin{aligned} K &= \frac{0.033}{C_0}, \\ \eta &= 0.62, \end{aligned} \quad (3.6)$$

$$D = 0.2 \mu\text{m}^2/h$$

for the ordinary refractive index profile used to calculate  $\Delta N$  in Figure 3.5. Please note that Equations (3.3), (3.6), and (3.7) are wrong in [1].

**3.5.2 Lithium out-diffusion model** This section describes the change in refractive index profile caused by lithium out-diffusion from a lithium niobate substrate in vacuum. The diffusion problem to be solved here is the one-dimensional out-diffusion of material ( $\text{Li}_2\text{O}$ ) from one medium ( $\text{LiNbO}_3$  substrate) into another medium (vacuum). A boundary condition is imposed across the  $\text{LiNbO}_3$ -vacuum interface to make the vaporization flux  $J_v$  a constant, where

$$J_v = D \frac{\partial C(y=0, t)}{\partial y}. \quad (3.7)$$

The solution to this diffusion problem is [55]

$$C(y, t) = 2J_v \left(\frac{t}{D}\right)^{\frac{1}{2}} \text{ierfc}\left(\frac{y}{2\sqrt{Dt}}\right), \quad (3.8)$$

where  $C(y, t)$   $\text{g/cm}^3$  is the density deficit of  $\text{Li}_2\text{O}$ ,  $\text{ierfc}()$  is the integral of the error function complement,  $y$  is the depth measured from the surface of the lithium niobate substrate,  $D$  is the diffusion coefficient, and  $t$  is the diffusion time. The change in extraordinary refractive index due to the out-diffusion of  $\text{Li}_2\text{O}$  is

$$\Delta n(y, t) = K C(y, t). \quad (3.9)$$

Values of  $J_v$ ,  $D$  and  $K$  for diffusion temperature of  $1000^\circ\text{C}$  are [30]:

$$\begin{aligned} J_v &= 6.04 \cdot 10^{-11} \text{ g/cm}^2\text{-s}, \\ D &= 6.5 \cdot 10^{-10} \text{ cm}^2/\text{s}, \\ K &= 1.75 \text{ cm}^3/\text{g}. \end{aligned} \quad (3.10)$$

**3.5.3 Step-index model** This section describes the step-index model used to calculate  $\Delta N$  for comparison to measured values of  $\Delta N$  in plain  $\text{LiNbO}_3$  specimens. This model is an empirical model whose parameters are deduced from our experimental data. I assume the process causing the increase in refractive

index is by thermal diffusion. However, I have not determined the diffusion mechanism, which could be either out-diffusion or in-diffusion, or a combination of both. Our data suggest that the increase in  $\Delta N$  reaches a saturation value within a short time while the diffusion depth is proportional to the square root of diffusion time. This process would result in a step-like index profile

$$\Delta n(y, t) = \begin{cases} \Delta n(0, t) & \text{if } 0 \leq y \leq b, \\ 0 & \text{otherwise,} \end{cases} \quad (3.11)$$

for the extraordinary refractive index, where the thickness of the high index layer is  $b = 2\sqrt{Dt}$  and  $D$  is the diffusion coefficient. Values for  $D$  and  $\Delta n(0, t)$  used to calculate  $\Delta N$  in Figure 3.6 and Figure 3.7 are:

$$\begin{aligned} \Delta n(0, t) &= 0.002, \\ D &= 5 \mu\text{m}^2/\text{h}. \end{aligned} \quad (3.12)$$

### 3.6 Discussion

I have presented measured values of the effective mode index for both titanium in-diffused  $\text{LiNbO}_3$  planar waveguides diffused in flowing wet oxygen and plain  $\text{LiNbO}_3$  diffused in a variety of atmospheres. Our measurements characterizing  $\text{Ti}:\text{LiNbO}_3$  planar waveguides revealed more TE modes than predicted using a titanium in-diffusion model, but the number of TM modes agreed with the model. I also observed near cut-off TE modes in plain  $\text{LiNbO}_3$  specimens diffused in the following atmospheres: air, dry oxygen, wet oxygen, dry argon, and wet argon. A plain  $\text{LiNbO}_3$  specimen diffused for 2 h in wet argon produced the fewest modes with the lowest effective index of all the other diffusion atmospheres. However, these near cut-off modes were not eliminated by any of the atmospheres. Furthermore, I did not observe TM modes in any of the plain  $\text{LiNbO}_3$  specimens.

Our results showing more guided modes in plain specimens diffused in flowing wet oxygen than in specimens diffused in air or dry oxygen (see Table 3.4) are directly opposite of the result by Goldberg [56]. Goldberg shows that the change in surface index of refraction becomes smaller as more water vapor is added into the diffusion chamber. Our results indicate that adding water increases the surface index of refraction.

In [44], planar waveguides were observed in plain  $\text{LiNbO}_3$  specimens diffused at 1000 °C in both wet or dry oxygen. The grade of  $\text{LiNbO}_3$  used by Canali et al. [44] was not specified. Their results show  $\Delta N$  decreasing with diffusion time for y-cut specimens diffused in dry oxygen. In fact, after 7 h diffusion, the fundamental mode is at cut-off. This is contrary to our results for dry-oxygen diffusion; see Figure 3.7. In [57] calculations of index profiles using the inverse WKB technique reveal a step-like increase in extraordinary refractive index profiles for y-cut  $\text{Ti:LiNbO}_3$  specimens diffused in wet-oxygen. However, no step-like refractive index features were observed in specimens diffused in an atmosphere of dry oxygen.

These results indicate that a process other than titanium in-diffusion is increasing the extraordinary refractive index in  $\text{Ti:LiNbO}_3$  specimens. This same process (or processes) may be responsible for the formation of TE guided modes in plain lithium niobate specimens. It is important to identify and understand all the processes affecting the extraordinary refractive index profile. Only then will it be possible to accurately model both the number of waveguide modes and the effective indices of the modes. I cannot identify with certainty the process which increases the extraordinary index in plain lithium niobate specimens resulting in nearly cut-off TE modes. However, from our experiments I have determined some

characteristics of the process or the processes:

- (a) The process is present in plain  $\text{LiNbO}_3$  specimens diffused under conditions usual for titanium in-diffusion.
- (b) The process is polarization dependent; it increases the extraordinary index.
- (c) The addition of water to the diffusion atmosphere increases the effects of the process.
- (d) In plain  $\text{LiNbO}_3$  specimens diffused in air or dry oxygen, longer diffusion times result in more guided modes, but the value of fundamental mode's effective index appears to saturate.
- (e) For plain  $\text{LiNbO}_3$  specimens diffused in air or dry oxygen, the process yields waveguide properties that are in general agreement with those from a step-like index profile whose depth increases as the square root of diffusion time.
- (f) The process does not follow lithium out-diffusion models.

The next Chapter continues this investigation into the origin of these near cut-off modes by making SIMS measurements on the lithium niobate specimens.

%

Table 3.1. The fabrication parameters for the  $\text{LiNbO}_3$  specimens discussed in this Chapter.

Specimen	Titanium Thickness, Å	Diffusion Temp., °C	Diffusion Time, h	Diffusion Gas	Gas Flow Rate, l/h
41	253	1000	1	wet oxygen	300
42	253	1000	2	wet oxygen	300
43	253	1000	4	wet oxygen	300
48	253	1000	8	wet oxygen	300
50A	0	1000	2	air	static
50A	0	1000	8	air	static
50A	0	1000	21	air	static
50B	0	1000	2	dry argon	300
				(dry oxygen during cool-down)	
51	0	1000	2	wet argon	300
				(wet oxygen during cool-down)	
52	0	1000	2	dry oxygen	330
52	0	1000	8	dry oxygen	330
52	0	1000	21	dry oxygen	330
53	0	1000	2	wet oxygen	300
54	0	1000	4	wet oxygen	300
54	0	1000	8	wet oxygen	300
54	0	1000	21.1	wet oxygen	330

Table 3.2. Diffusion time is 2 h. Measured values of  $\Delta N$  for the fundamental TE waveguide mode are given for specimens fabricated using different diffusion atmospheres. The number of TE modes supported by each waveguide is also indicated. The entries for the lithium out-diffusion specimen were calculated using the lithium out-diffusion model described in Appendix 3.5.2.

Specimen	Diffusion Atmosphere	$\Delta N$ for TE <sub>0</sub> Waveguide Mode	Number of TE Waveguide Modes
50A	Air	$1.5 \cdot 10^{-3} \pm 4 \cdot 10^{-4}$	2-3
52	dry-oxygen	$1.7 \cdot 10^{-3} \pm 7 \cdot 10^{-4}$	2-3
53	wet-oxygen	$2.1 \cdot 10^{-3} \pm 6 \cdot 10^{-4}$	3
50B	dry-argon	$1.4 \cdot 10^{-3} \pm 2 \cdot 10^{-4}$	2-3
51	wet-argon	$7 \cdot 10^{-4} \pm 2 \cdot 10^{-4}$	1-2
Lithium Out-Diffusion	vacuum	$2.0 \cdot 10^{-4}$	4

Table 3.3. Diffusion time is 8 h. Measured values of  $\Delta N$  for the fundamental TE waveguide mode are given for specimens fabricated using different diffusion atmospheres. The number of TE modes supported by each waveguide is also indicated. The entries for the lithium out-diffusion specimen were calculated using the lithium out-diffusion model described in Appendix 3.5.2.

Specimen	Diffusion Atmosphere	$\Delta N$ for TE <sub>0</sub> Waveguide Mode	Number of TE Waveguide Modes
50A	Air	$1.8 \cdot 10^{-3} \pm 4 \cdot 10^{-4}$	3-4
52	dry-oxygen	$1.7 \cdot 10^{-3} \pm 4 \cdot 10^{-4}$	3-5
54	wet-oxygen	$3.4 \cdot 10^{-3} \pm 9 \cdot 10^{-4}$	4-7
Lithium Out-Diffusion	vacuum	$6.0 \cdot 10^{-4}$	12

Table 3.4. Diffusion time is 21 h. Measured values of  $\Delta N$  for the fundamental TE waveguide mode are given for specimens fabricated using different diffusion atmospheres. The number of TE modes supported by each waveguide is also indicated. The entries for the lithium out-diffusion specimen were calculated using the lithium out-diffusion model described in Appendix 3.5.2.

Specimen	Diffusion Atmosphere	$\Delta N$ for Waveguide Mode TE <sub>0</sub>	Number of TE Waveguide Modes
50A	Air	$1.7 \cdot 10^{-3} \pm 4 \cdot 10^{-4}$	5-6
52	dry-oxygen	$2.0 \cdot 10^{-3} \pm 5 \cdot 10^{-4}$	6-8
54	wet-oxygen	$4.7 \cdot 10^{-3} \pm 7 \cdot 10^{-4}$	7-9
Lithium Out- Diffusion	vacuum	$2.0 \cdot 10^{-4}$	21

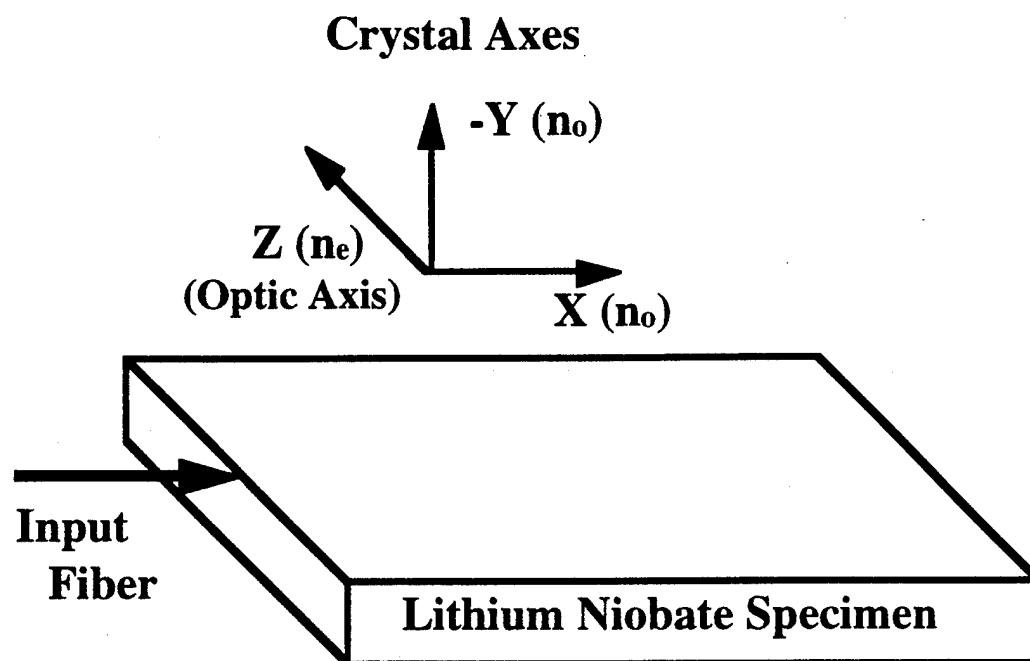


Figure 3.1. The waveguide orientation and mode propagation direction relative to the LiNbO<sub>3</sub> crystal's axes. The extraordinary index is  $n_e = 2.2028$  and the ordinary index is  $n_o = 2.2865$  at the wavelength  $\lambda = 0.6328 \mu\text{m}$  [35].

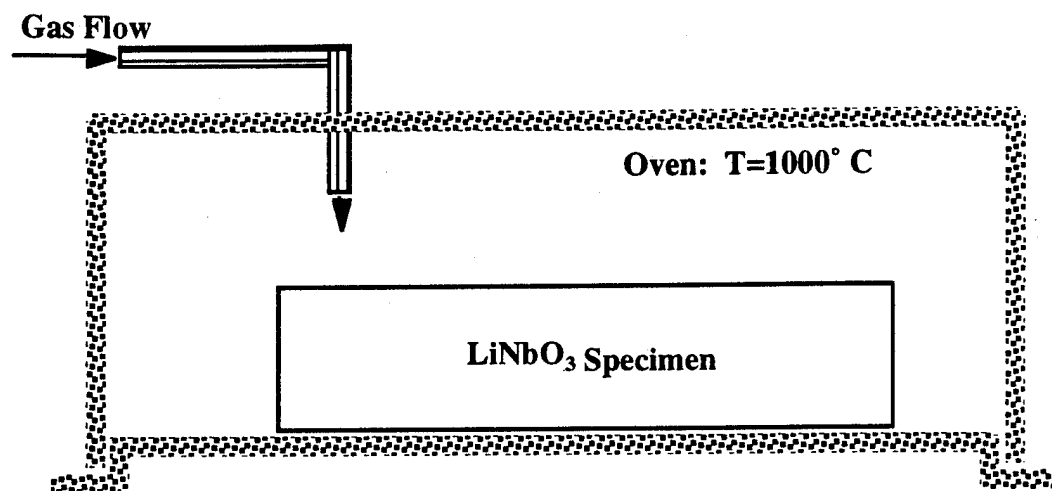


Figure 3.2. Schematic diagram of the diffusion furnace (not drawn to proportion) illustrating the flow of gas into the furnace chamber.

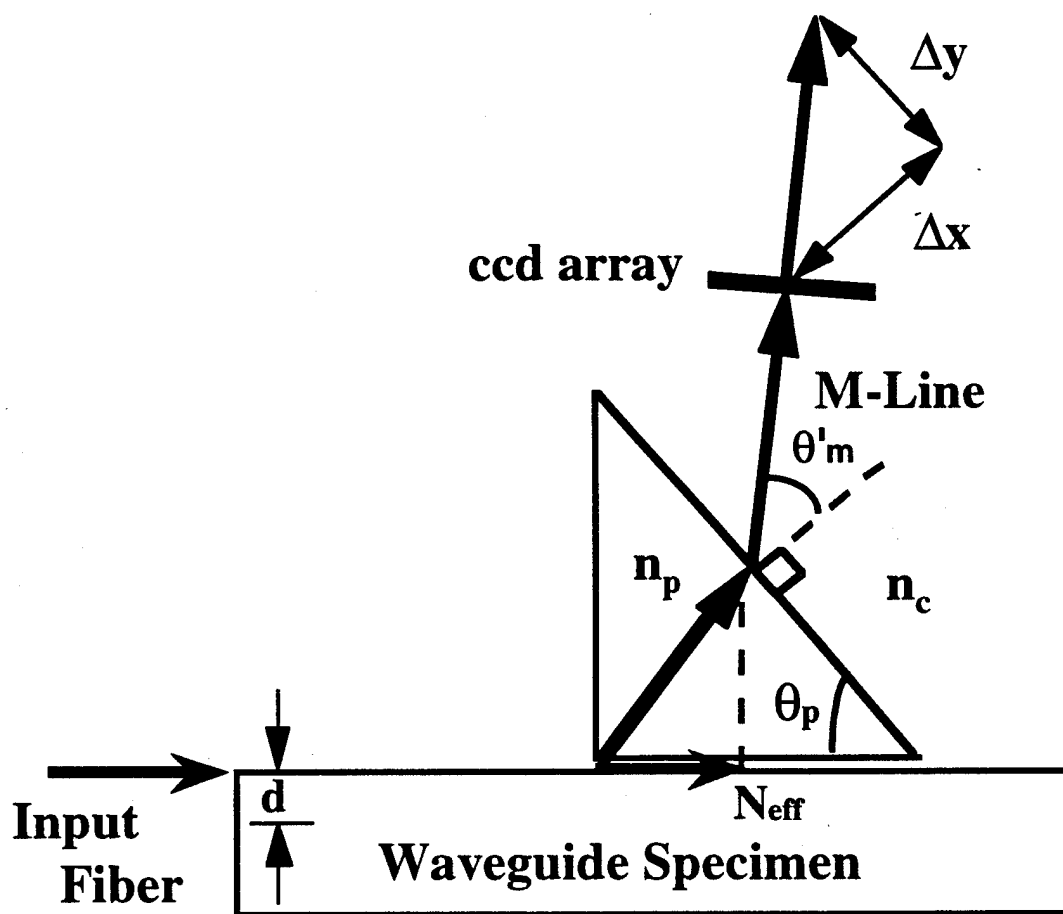


Figure 3.3. Prism out-coupler setup used to measure the effective index of the modes in the planar  $\text{LiNbO}_3$  waveguides.

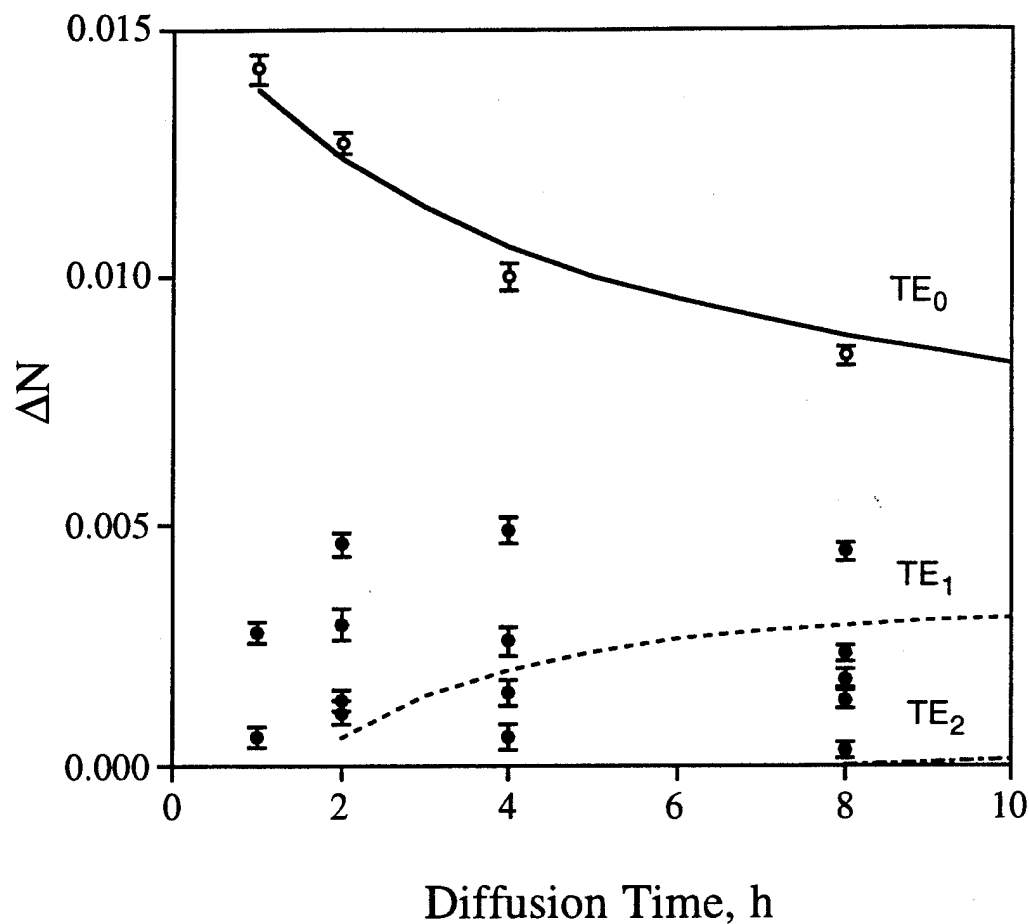


Figure 3.4. TE waveguide mode dispersion curves for titanium in-diffused lithium niobate planar waveguide specimens 41, 42, 43, and 48. Experimentally measured values of  $\Delta N$  are represented by discrete symbols with error bars. The fundamental TE mode was confidently identified in each specimen and its value of  $\Delta N$  is indicated by empty circle symbols. The order number for the higher-order modes could not be determined with the same confidence so values of  $\Delta N$  for all these modes are indicated using filled circle symbols. Calculated results from the titanium diffusion model yield three guided modes. These modes are shown as continuous lines:  $TE_0$ , solid line style;  $TE_1$ , dashed line style;  $TE_2$ , dash-dot line style

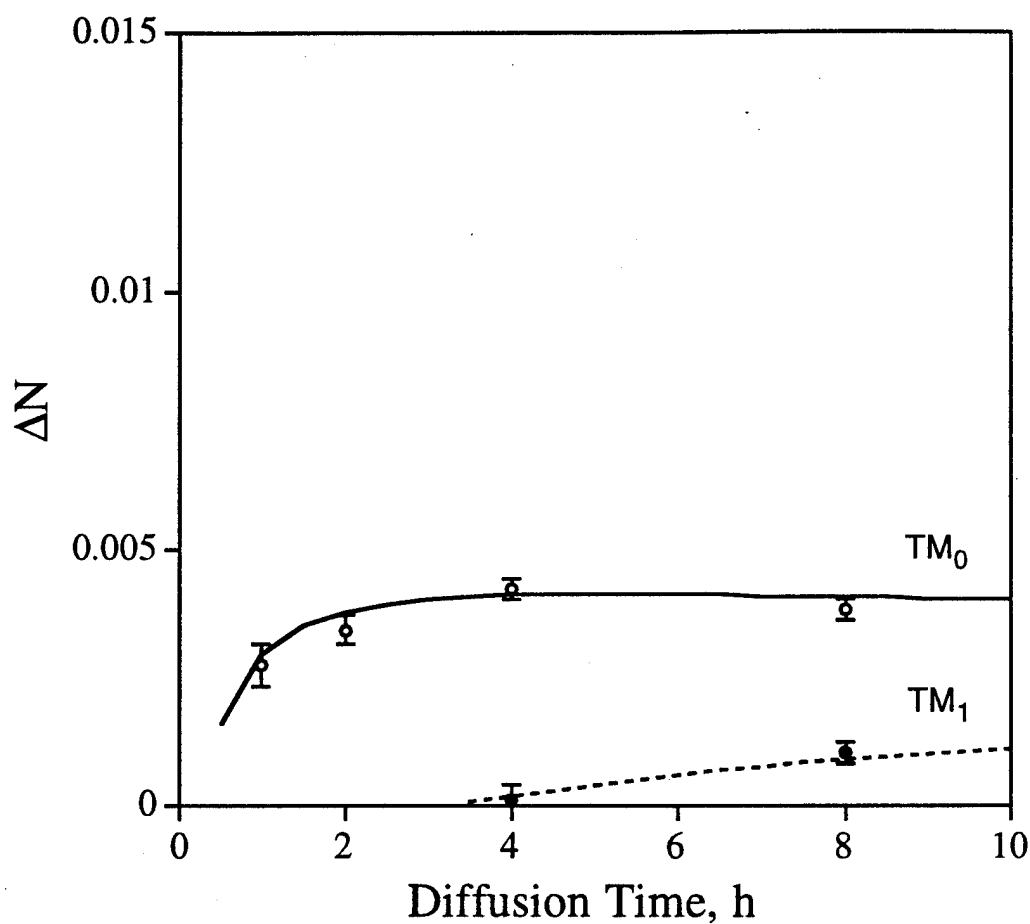


Figure 3.5. TM waveguide mode dispersion curves for titanium in-diffused lithium niobate planar waveguide specimens 41, 42, 43, and 48. Experimentally measured values of  $\Delta N$  are represented by discrete symbols with error bars. Experimental observations confidently identified both the fundamental and the first higher-order modes. These modes are indicated by different plot symbols:  $TM_0$ , empty circles;  $TM_1$ , filled circles. Calculated results from the titanium diffusion model yield two guided modes. These modes are shown as continuous lines:  $TM_0$ , solid line style;  $TM_1$ , dashed line style.

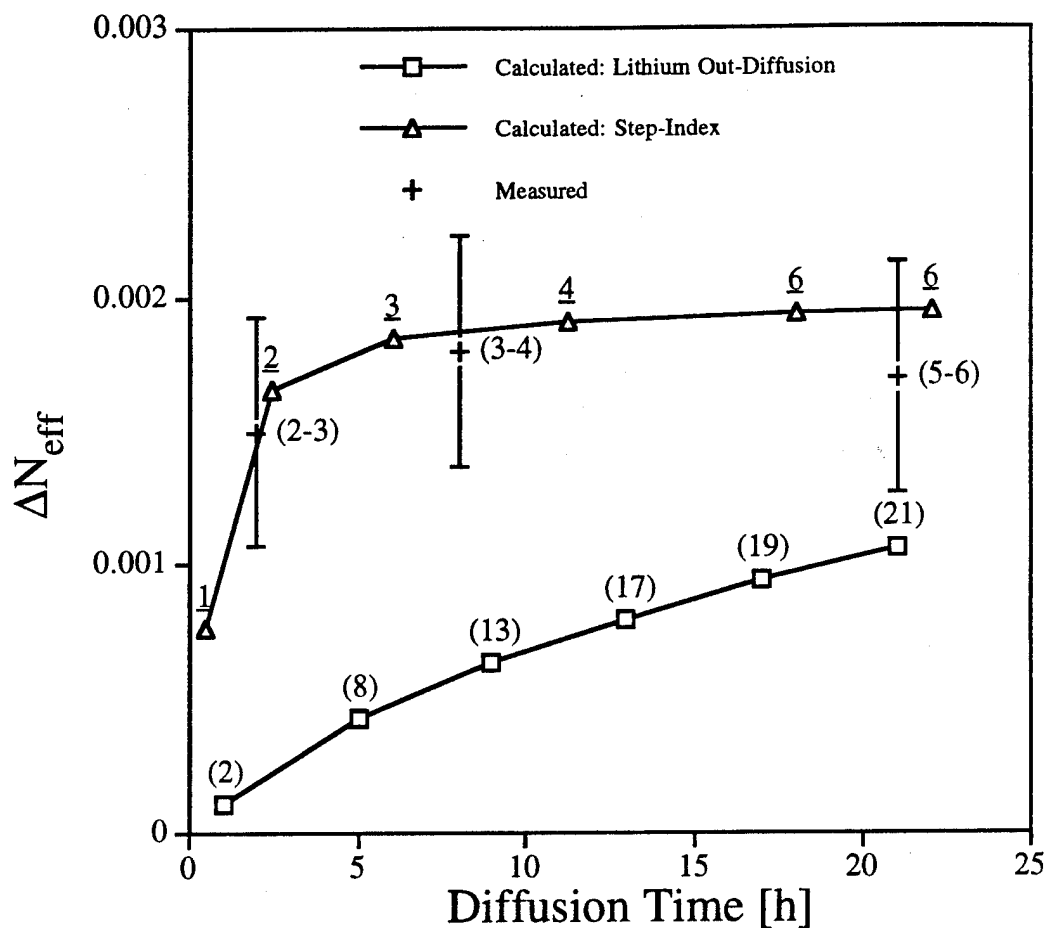


Figure 3.6. Comparison between measured  $\Delta N$  from waveguide specimens diffused in air and calculated  $\Delta N$  from lithium out-diffusion and step-index models. Measured values of  $\Delta N$  for the fundamental mode in specimens diffused in air are represented by plus signs. Calculated values of  $\Delta N$  for the fundamental mode of a lithium out-diffused waveguide (calculated using the lithium out-diffusion model discussed in Appendix 3.5.2) are represented by square symbols. Calculated values of  $\Delta N$  for the fundamental mode of a step-index waveguide (calculated using the step index waveguide model discussed in Appendix 3.5.3) are represented by triangles. The number of guided modes found in each type of waveguide is indicated by the numbers adjacent to each plot symbol.

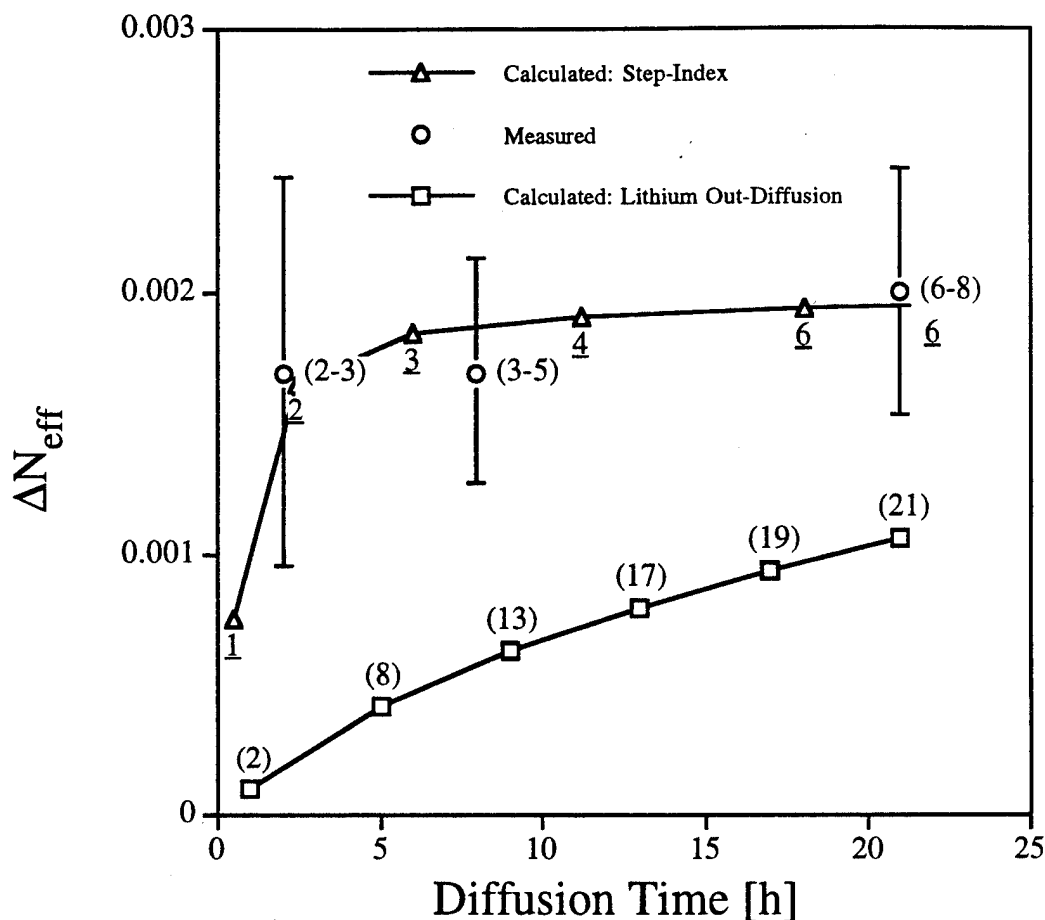


Figure 3.7. Comparison between measured  $\Delta N$  from waveguide specimens diffused in dry-oxygen and calculated  $\Delta N$  from lithium out-diffusion and step-index models. Measured values of  $\Delta N$  for the fundamental mode in specimens diffused in dry-oxygen are represented by empty circles. Calculated values of  $\Delta N$  for the fundamental mode of a lithium out-diffused waveguide (calculated using the lithium out-diffusion model discussed in Appendix 3.5.2) are represented by square symbols. Calculated values of  $\Delta N$  for the fundamental mode of a step-index waveguide (calculated using the step index waveguide model discussed in Appendix 3.5.3) are represented by triangles. The number of guided modes found in each type of waveguide is indicated by the numbers adjacent to each plot symbol.

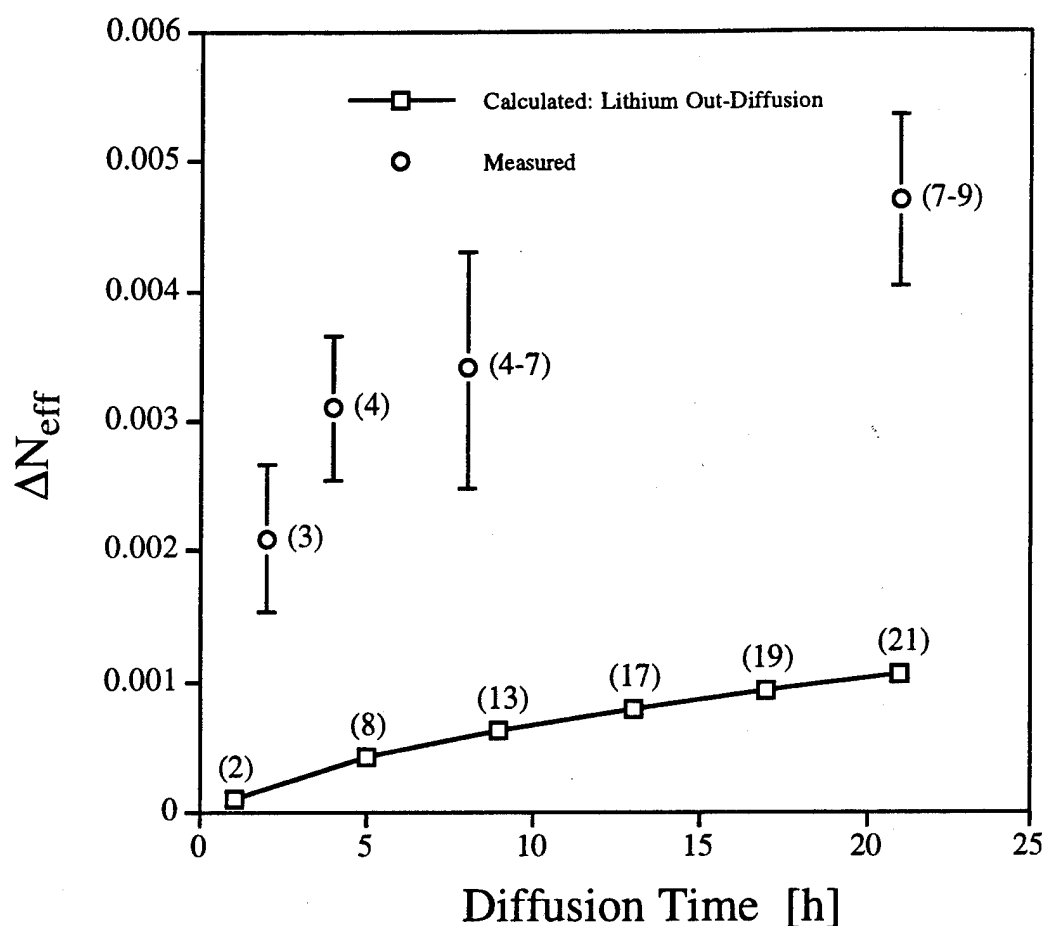


Figure 3.8. Comparison between measured  $\Delta N$  from waveguide specimens diffused in wet-oxygen and calculated  $\Delta N$  from a lithium out-diffusion model. Measured values of  $\Delta N$  for the fundamental mode in specimens diffused in wet-oxygen are represented by filled circles. Calculated values of  $\Delta N$  for the fundamental mode of a lithium out-diffused waveguide (calculated using the lithium out-diffusion model discussed in Appendix 3.5.2) are represented by square symbols. The number of guided modes found in each type of waveguide is indicated by the numbers adjacent to each plot symbol. Results from the step-index waveguide model did not agree with  $\Delta N$  measurements from the wet-oxygen diffused waveguides.

## CHAPTER 4

### DIFFUSION PROCESSES IN LITHIUM NIOBATE

This Chapter is a compilation of secondary ion mass spectroscopy (SIMS) data of lithium niobate waveguide specimens. This work was motivated by the results of Chapter 3 which showed the existence of unexpected, higher-order modes in titanium in-diffused waveguides. Those results demonstrate that the fabrication parameters required for single mode titanium in-diffused planar waveguides are unknown, and the diffusion model is incomplete.

Several lithium niobate specimens were sent to Evans East, Inc. for SIMS analysis. The objectives of the SIMS measurements were to measure the dependence of diffusion atmosphere on lithium out-diffusion, titanium in-diffusion, and hydrogen in-diffusion. The following sections present the results of these measurements and discusses them within the context of diffusion models.

Appendix A should be consulted for information regarding SIMS data processing and calibration methods.

#### 4.1 SIMS Analysis of Plain $\text{LiNbO}_3$ Specimens

Lithium and hydrogen concentrations in specimens 50B, 51, and 53 were measured using SIMS. These are plain specimens as they do not contain a layer of evaporated titanium. The diffusion temperature was 1000 °C and the diffusion time was 2 h for these specimens. Refer to Table 3.2 for other fabrication parameters and the waveguide characteristics of these specimens. Figure 4.1 shows the lithium concentration profiles for specimens 50B, 51, and 53. Also shown is

the lithium concentration profile from untreated specimen 100. This data was processed by Evans East.

We will discuss several characteristics of these curves. The first is the pronounced build-up of lithium  $2\text{ }\mu\text{m}$  below the surface of untreated specimen 100. This build-up is also observed in each of the processed specimens, but it is located closer to the specimen's surface. I only found one other example of a subsurface lithium build-up [58]. There, elastic recoil detection measured a region of elevated lithium concentration in He-implanted  $\text{LiNbO}_3$  specimens. However, this lithium build-up was not detected in their unprocessed specimens.

The second characteristic is that the two specimens (50B and 51) processed in Ar have nearly the same lithium concentration profile. Specimen 50B was processed in dry Ar while specimen 51 was processed in Ar bubbled through water. While specimen 53, processed in  $\text{O}_2$  bubbled through water, has a lower surface lithium concentration. Also, the build-up of lithium is closest to the surface in specimen 53.

I calculate the amount of lithium that was out-diffused by first scaling the unperturbed region to equal the congruent lithium concentration. Then I subtract the measured lithium concentration from a uniform (ideal) congruent concentration. Finally, I integrate the difference with respect to depth to yield an area-density  $\text{atoms/cm}^2$  representing the amount lithium lost from the specimen. Results of this calculation are shown in Table 4.1 for plain specimens 50B, 51 and 53, and untreated specimen 100. The negative value for specimen 100 indicates an abundance of lithium in comparison to the uniform concentration of an ideal congruent specimen.

It is difficult to draw a correlation between the lithium concentration

profiles and optical properties of specimens 50B, 51, and 53. Table 3.2 shows that specimen 53 supports the largest number of modes and has the  $TE_0$  mode with the highest effective index. In contrast, specimen 51 supports the fewest modes and its  $TE_0$  mode has the lowest effective index. Surprisingly, each of these specimens have lost equal amounts of lithium. However, their lithium profiles are noticeably different. Furthermore, measurement uncertainty creates a low level of confidence for any correlation drawn from these results.

Hydrogen concentration profile for specimens 50B, 51, and 53 are shown in Figure 4.2. This data was processed by Evans East and the hydrogen concentration was calibrated using a hydrogen implanted standard [59]. Here, specimen 53 has a hydrogen concentration above that in either specimen 50B or 51. However, the hydrogen profile from specimen 53 does not show a distinct transition between the surface concentration and the unperturbed substrate concentration, even though the measurement extends to 12  $\mu\text{m}$ . Recall that the transition for lithium was at a depth less than 3  $\mu\text{m}$  for these specimens. In fact, the transition for hydrogen is so gradual that it suggests the cause could instrument drift, or some other artifact. In addition, if we accept the hydrogen profile for specimen 53 as indicating the hydrogen concentration of the unperturbed substrate to be at a depth of 12  $\mu\text{m}$  then we must reconcile the lower hydrogen concentrations for specimens 50B and 51.

One other interpretation of the hydrogen profiles in Figure 4.2 is that they do accurately represent the specimen's hydrogen content. This would imply the transition occurs at a depth below 12  $\mu\text{m}$ . Since the presence of hydrogen increases the index of refraction of  $\text{LiNbO}_3$  [43, 59] we attempt to correlate the hydrogen profiles with the specimen's optical properties. We find that specimen

53 has the highest hydrogen concentration, supports the largest number of modes, and has the fundamental TE mode with the highest effective index. However, the hydrogen concentration of specimen 53 is approximately 2000 times lower than that in a proton exchanged  $\text{LiNbO}_3$  specimen [59]. Since the change in index of refraction of a proton exchanged specimen is approximately  $\Delta n \approx 0.1$ , we could estimate that the increase in index of refraction in specimen 53 is  $\Delta n \approx 5 \cdot 10^{-5}$ . This estimate assumes a linear relationship between hydrogen concentration and index of refraction. This increase in index of refraction is below the effective index of the fundamental TE modes found in Table 3.2. Thus, if hydrogen is contributing to the waveguide properties of these specimens, then the contribution is small compared to some other affect.

Plain specimens 50A, 52, and 54 with 21 h diffusion time were also analyzed using SIMS. However, these measurements are less conclusive than those just presented. These specimens were also prepared using a diffusion temperature of  $1000^\circ\text{C}$  in various atmospheres (see Table 3.4 for waveguide characteristics). The lithium concentration profile for specimen 50A is shown in Figure 4.3. This SIMS data was also processed by Evans East. The SIMS measurement was made to a depth of nearly  $6\text{ }\mu\text{m}$ . We anticipated seeing a more pronounced transition from the lowered lithium concentration at the surface, to the higher lithium concentration in the unperturbed substrate. However, the lithium concentration appears nearly constant over the measurement depth. The lithium concentration profile from specimens 52 and 54 show the same nearly constant lithium concentration profile.

The lithium concentration for these specimens was arbitrarily scaled to equal the lithium concentration in unperturbed stoichiometric  $\text{LiNbO}_3$ . This was

done because of the absence of a definite transition to the substrate concentration which could be used for calibration.

Figure 4.4 compares the lithium concentrations from specimen 53 and 54. These specimens were prepared in flowing oxygen bubbled through water. The diffusion time for specimen 53 is 2 h while the diffusion time for specimen 54 is 21 h.

The hydrogen concentration profile for specimen 50A is also shown in Figure 4.3. Again, these SIMS results were also inconclusive. The hydrogen signals from specimens 50A, 52, and 54 were indistinguishable from the background hydrogen signal of an unprocessed specimen of  $\text{LiNbO}_3$  as is shown in Figure 4.5. Therefore, if hydrogen is present in these specimens, it is at a level below the sensitivity of the SIMS measurement. The background hydrogen concentration is higher in Figure 4.5 than in Figure 4.2 because the specimens in Figure 4.2 were measured using different instrument settings.

## 4.2 SIMS Analysis of $\text{Ti:LiNbO}_3$ Specimens

Before we discuss the SIMS analysis of  $\text{Ti:LiNbO}_3$  specimens, we will present some background information on titanium in-diffusion.

**4.2.1 Titanium In-Diffusion** Titanium (atomic symbol is Ti) is a group IVB transition metal with specific gravity 4.54, atomic number 22 and atomic weight 47.90 u. The oxidation states of titanium are  $\text{Ti}^{2+,3+,4+}$ , where the 2+ state is less common. The atomic radius of Ti is 132 pm while the ionic radii are 90 pm for  $\text{Ti}^{2+}$  and 76 pm for  $\text{Ti}^{3+}$ . The melting point of Ti is 1675 °C and its boiling point is 3260 °C. The density of 99.5 % pure Ti is 4.51 g/cm<sup>3</sup> [60].

Titanium in-diffusion increases both the extraordinary and the ordinary index of lithium niobate by different amounts [29]. The maximum increase in the

extraordinary index is  $\Delta n_e \approx 0.01$  and this is approximately a factor of 2 larger than the increase of the ordinary index [32, 61].

Arguments presented in [62] (and the references therein) support the idea that titanium ions diffuse substitutionally into the lithium niobate substrate. Furthermore, there is evidence that titanium ions are incorporated into lithium niobate in two distinct, concentration dependent phases. X-ray absorption spectra indicates titanium sites are less ordered at titanium concentrations above  $5 \cdot 10^{20} \text{ cm}^{-3}$  ) than at lower concentrations [63]. It is suggested these two phases explain the non-linear relationship between the change in ordinary index of refraction and titanium concentration.

For which of the atomic species in  $\text{LiNbO}_3$  the titanium substitutes remains an active research topic. Arguments have been made which favor either a titanium-for-lithium substitution [64] or a titanium-for-niobium substitution [62].

We will look for relationships between titanium and lithium concentrations, and fabrication conditions using SIMS of  $\text{Ti:LiNbO}_3$  specimens.

**4.2.2 SIMS of Y-Cut  $\text{Ti:LiNbO}_3$  Specimens** Continuing with our analysis of lithium niobate waveguides, we present SIMS measurements of y-cut  $\text{Ti:LiNbO}_3$  waveguide specimens 42 and 56. The thickness of evaporated titanium was 24.3 nm on specimen 42 and 28.0 nm on specimen 56. The diffusion atmosphere consisted of oxygen bubbled through water for specimen 42 and argon bubbled through water for specimen 56. The diffusion time is 2 h and the diffusion temperature is 1000 °C for both waveguide specimens.

I processed the SIMS data for the following elemental concentration curves. The procedures I followed are outlined in Appendix A.

The lithium concentrations from specimens 42 and 56 are shown in Figure 4.6. The lithium concentrations in the unperturbed substrate were scaled to equal the concentration in congruent  $\text{LiNbO}_3$  ( $1.78 \cdot 10^{22}$  atoms/cm<sup>3</sup>). We see that specimen 56 has lost more lithium than specimen 42. I find  $3.7 \cdot 10^{17}$  lithium-atoms/cm<sup>2</sup> have left specimen 42, while  $1.0 \cdot 10^{18}$  lithium-atoms/cm<sup>2</sup> have left specimen 56. These lithium-atom area densities are listed in Table 4.1 along with the in-diffused titanium area-densities.

Normalized lithium concentrations are shown in Figure 4.7 for Ti:LiNbO<sub>3</sub> specimens 42 and 56, and plain specimens 51 and 53.

The titanium concentration in specimens 42 and 56 is shown in Figure 4.8. Each waveguide supports several TE modes. The effective indices for these modes at  $\lambda = 0.6328\mu\text{m}$  are shown in Table 4.2.

We can find some correlations between material and optical properties in these y-cut Ti:LiNbO<sub>3</sub> specimens. Table 4.2 shows us that the effective index of the fundamental TE mode is higher in specimen 56 than in specimen 42. This agrees with the higher titanium concentration in specimen 56. However, we also notice that specimen 56 supports fewer higher-order modes than does specimen 42, and they have lower effective index. This is interesting because specimen 56 has lost more lithium than specimen 42 (see Figure 4.7). We would expect specimen 56 to support more modes of higher effective index if only the titanium and lithium concentrations contribute to the index of refraction profile. We might conclude then, that there are other, yet unidentified processes contributing to the index of refraction profile.

**4.2.3 SIMS of X-Cut Ti:LiNbO<sub>3</sub> Specimens** We investigated the dependence of diffusion temperature and diffusion time on the optical properties of y-propagating, x-cut Ti:LiNbO<sub>3</sub> waveguide specimens. Our goal was to find a set of fabrication parameters that yield a planar waveguide which support a single TE mode. The results from four of these specimens, X2, X3, X4, and X5 are reported here. The diffusion time is 1 h for specimen X2, 2 h for specimen X3, 4 h for specimen X4, and 2 h for specimen X5. The diffusion temperature was 950 °C for specimens X2, X3, and X4, and 1050 °C for specimen X5. The diffusion atmosphere was ambient air and the titanium thickness was 25 nm for each of these specimens.

Specimens X2, X3, and X4 each supported only one TE mode. This is a very encouraging result in view of the difficulty in obtaining a single TE mode in the waveguide specimens discussed in Chapter 3. In comparison, specimen X5 supported between two to four TE modes. The effective index of the TE<sub>0</sub> mode in specimens X2, X3, X4, and X5 is shown in Table 4.3.

Lithium concentration profiles from these x-cut Ti:LiNbO<sub>3</sub> specimens are shown in Figure 4.9. Figure 4.10 better reveals the details of the lithium concentrations in these specimens.

The amount of lithium lost from these specimens is tabulated in Table 4.1. It is interesting that the x-cut specimens have lost more lithium than any of the multi-mode, y-cut specimens. We see that x-cut specimen X3 has lost approximately 20 times more lithium than y-cut specimen 42. This is the case even though the diffusion temperature was higher for specimen 42, while the diffusion time and titanium thickness were nearly the same.

The titanium concentration in these x-cut specimens is shown in Figure 4.11, and a detailed view is shown in Figure 4.12. We make the following observations regarding the titanium concentration. Notice the surface layer with an elevated titanium concentration. I believe this surface layer to be a residual titanium compound due to the low diffusion temperature, not an artifact of the SIMS measurement. The titanium concentration in this surface layer decreases with diffusion time. In comparison, the titanium concentrations are nearly identical in Specimens X1, X2, and X3 in the region immediately below the surface layer.

We also see in Figure 4.12 that the surface layer is approximately 100 nm thick in specimen X2. This is four times the thickness of the evaporated titanium. Furthermore, the surface layer becomes thinner with increasing diffusion time. The depth increment between SIMS data points is 22 nm for specimens X2 and X4, and 12 nm for specimens X3 and X5. This can limit the depth resolution of the surface layer. The thickness of the surface layer in specimen X4 appears to approach this resolution limit.

I can not explain the small titanium build-up located just below the surface of specimen X5. Recall that the diffusion temperature was higher (1050 °C ) for specimen X5 than for the other three x-cut specimens (950 °C ).

The surface layer in specimen X2 was analyzed using x-ray photoelectron spectrometry (XPS). The results of this analysis indicate that the surface layer is composed of 15 % titanium, 15 % niobium, and 70 % oxygen [65]. It should be noted that XPS cannot detect the presence of lithium in these specimens.

Ms. Milica Popovic fabricated these x-cut specimens and measured their

mode's effective index. I processed this SIMS data without using a matrix normalization according to the procedures in Appendix A.

#### 4.3 SIMS Analysis of TIPE:LiNbO<sub>3</sub> Specimen 33A

Figure 4.13 shows the atomic concentrations in titanium in-diffused and proton exchanged lithium niobate (TIPE:LiNbO<sub>3</sub>) specimen 33A. This specimen was fabricated by first in-diffusing 24.3 nm of titanium for 2 h at a temperature of 1000 °C . Then, the specimen was placed in pure benzoic acid at 230 °C for 1.5 h.

The SIMS measurements show a discontinuity in the titanium intensity, with the titanium intensity lower on the side of high hydrogen intensity. Likewise, there is a similar discontinuity in the lithium intensity. In contrast, the titanium profiles are continuous in specimens which have only been subjected to titanium in-diffusion. There should be no additional titanium diffusion resulting from the proton exchange in a TIPE:LiNbO<sub>3</sub> specimen because the proton exchange temperature is much lower than the titanium in-diffusion temperature. Therefore, I believe that this discontinuity is a result of either using a uniform excavation rate to calculate the profile's depth, using only one RSF over the entire SIMS measurement, or using an inappropriate matrix signal for normalization.

Effective index of the fundamental TE mode as a function of exchange time and anneal time is shown in Figure 4.14. Annealing of these TIPE:LiNbO<sub>3</sub> specimens was done in air at a temperature of 360 °C .

#### 4.4 Waveguide Attenuation

Attenuation of the fundamental TE mode of several titanium in-diffused waveguides is shown in Table 4.4. The mode attenuation was determined imaging

onto a ccd array the radiation scattered from the mode. The image was processed to account for the beam divergence in the plane of the waveguide. The residual decrease in mode power with propagation distance was attributed to waveguide attenuation. Specimen 57 was fabricated identical to specimen 56, specimen 44 was fabricated identical to specimen 42. The diffusion time for specimen 46 was 8 h, while the remaining fabrication parameters were identical to those of specimen 42. The measurement uncertainty in Table 4.4 corresponds to a 95% confidence level.

#### 4.5 Conclusions

Clearly, the results indicate that the relationships between material properties and optical properties in  $\text{LiNbO}_3$  waveguides are complex. For example, consider y-cut specimen 42 and x-cut specimen x3. Their titanium concentration profiles are shown in Figure 4.15. Both of these specimens have diffusion times of 2 h and nearly the same titanium thickness but the diffusion temperature was 1000 °C for specimen 42 and 950 °C for specimen x3. The titanium concentrations of these two specimens are similar except for the high titanium concentration at the surface of specimen x3. However, the effective index of the fundamental TE mode in specimen 42 is about 5 times larger than in specimen x3. Furthermore, specimen 42 guides 5 TE modes while specimen x3 guides 1 TE mode (compare Tables 4.2 and 4.3).

These comparisons suggests that the surface layer in specimen x3 lowers the waveguide index of refraction, or that similar titanium concentrations produce significantly different changes in index of refraction in y-cut  $\text{LiNbO}_3$  than in x-cut  $\text{LiNbO}_3$ .

Also shown in Figure 4.15 is the titanium concentration in x-cut specimen

x5. The diffusion time for specimen x5 is also 2 h but the diffusion temperature is 1050 °C . We see that the higher diffusion temperature has lowered the surface titanium concentration and increased the diffusion depth, both are expected according to current diffusion model. However, the effective index of fundamental TE mode in specimen x5 is about 4 times larger than in specimen x3.

Final observations regard the surface layer in the x-cut specimens (see Figure 4.12). Others have reported a residual surface layer of titanium compound on titanium in-diffused specimens [38, 41, 66]. However, there is disagreement in the reported composition of the surface layer. Furthermore, this layer appears to be about 4 times the thickness of the evaporated titanium layer. If this surface layer is the source for the titanium diffusion then the parameters in the diffusion model should reflect this increase in thickness. This will be more important for short diffusion times than for long diffusion times.

One last comment regards the titanium concentration discontinuity between the surface layer and the region immediately below the surface layer (see Figure 4.12). This could be an indication of the finite solid solubility of titanium in lithium niobate.

Additional research is needed to identify and understand the relationships between material properties and optical properties of LiNbO<sub>3</sub> waveguides. Future work should include a critical evaluation of analytical methods for quantifying the elemental composition of LiNbO<sub>3</sub> waveguide specimens.

Table 4.1. Area-densities of out-diffused lithium and in-diffused titanium. The negative value for specimen 100 indicates an abundance of lithium in comparison to the uniform concentration of an ideal congruent specimen. The thickness of evaporated titanium was 24.3 nm for specimen 42, 28.0 nm for specimen 56, and 25.0 nm for specimens X2, X3, X4, and X5. The lithium out-diffusion model is from [30].

Specimen	Diffusion Time h	Diffusion Temperature °C	Diffusion Atmosphere	Out-Diffused Lithium atoms/cm <sup>2</sup>	In-Diffused Titanium atoms/cm <sup>2</sup>
100	2	1000	Untreated	$-1.4 \cdot 10^{17}$	--
50B	2	1000	Ar	$1.6 \cdot 10^{17}$	--
51	2	1000	Ar +H <sub>2</sub> O	$2.6 \cdot 10^{17}$	--
53	2	1000	O <sub>2</sub> +H <sub>2</sub> O	$2.6 \cdot 10^{17}$	--
42	2	1000	O <sub>2</sub> +H <sub>2</sub> O	$3.7 \cdot 10^{17}$	$1.4 \cdot 10^{17}$
56	2	1000	Ar +H <sub>2</sub> O	$1.0 \cdot 10^{18}$	$1.6 \cdot 10^{17}$
X2	1	950	Air	$5.9 \cdot 10^{18}$	$1.4 \cdot 10^{17}$
X3	2	950	Air	$6.3 \cdot 10^{18}$	$1.4 \cdot 10^{17}$
X4	4	950	Air	$9.1 \cdot 10^{18}$	$1.4 \cdot 10^{17}$
X5	2	1050	Air	$1.2 \cdot 10^{19}$	$1.4 \cdot 10^{17}$
Lithium Out- Diffusion Model	2	1000	vacuum	$1.8 \cdot 10^{16}$	--

Table 4.2. Effective indices of TE modes in specimens 42 and 56. Values represent the increment above the substrate index. The wavelength is  $\lambda = 0.6328\mu\text{m}$ .

Mode	$\Delta N_{\text{eff}} \pm 0.0002$	$\Delta N_{\text{eff}} \pm 0.0002$
	Specimen 42	Specimen 56
TE <sub>0</sub>	0.0127	0.0140
TE <sub>1</sub>	0.0046	0.0034
TE <sub>2</sub>	0.0030	0.0018
TE <sub>3</sub>	0.0014	0.0006
TE <sub>4</sub>	0.0010	--

Table 4.3. Effective indices of the TE<sub>0</sub> mode in x-cut specimens X2, X3, X4 and X5. Values represent the increment above the substrate index. The wavelength is  $\lambda = 0.6328\mu\text{m}$ .

Specimen	Diffusion Time h	Diffusion Temperature °C	Number of TE Modes Supported	TE <sub>0</sub> Effective Index $\Delta N_{\text{eff}}$
X2	1	950	1	$0.0009 \pm 0.0002$
X3	2	950	1	$0.0025 \pm 0.0001$
X4	4	950	1	$0.0040 \pm 0.0002$
X5	2	1050	2-4	$0.0097 \pm 0.001$

Table 4.4. Waveguide attenuation measurements. Measured attenuation of the fundamental TE mode. The wavelength is  $\lambda = 0.6328\mu\text{m}$ .

Specimen	Diffusion Temperature °C	Diffusion Time h	Diffusion Atmosphere	TE <sub>0</sub> Attenuation dB/cm
X2	950	1	Air	$5.1 \pm 0.5$
44	1000	2	O <sub>2</sub> +H <sub>2</sub> O	$1.7 \pm 0.3$
46	1000	8	O <sub>2</sub> +H <sub>2</sub> O	$0.6 \pm 0.7$
57	1000	2	Ar+H <sub>2</sub> O	$3.0 \pm 0.6$

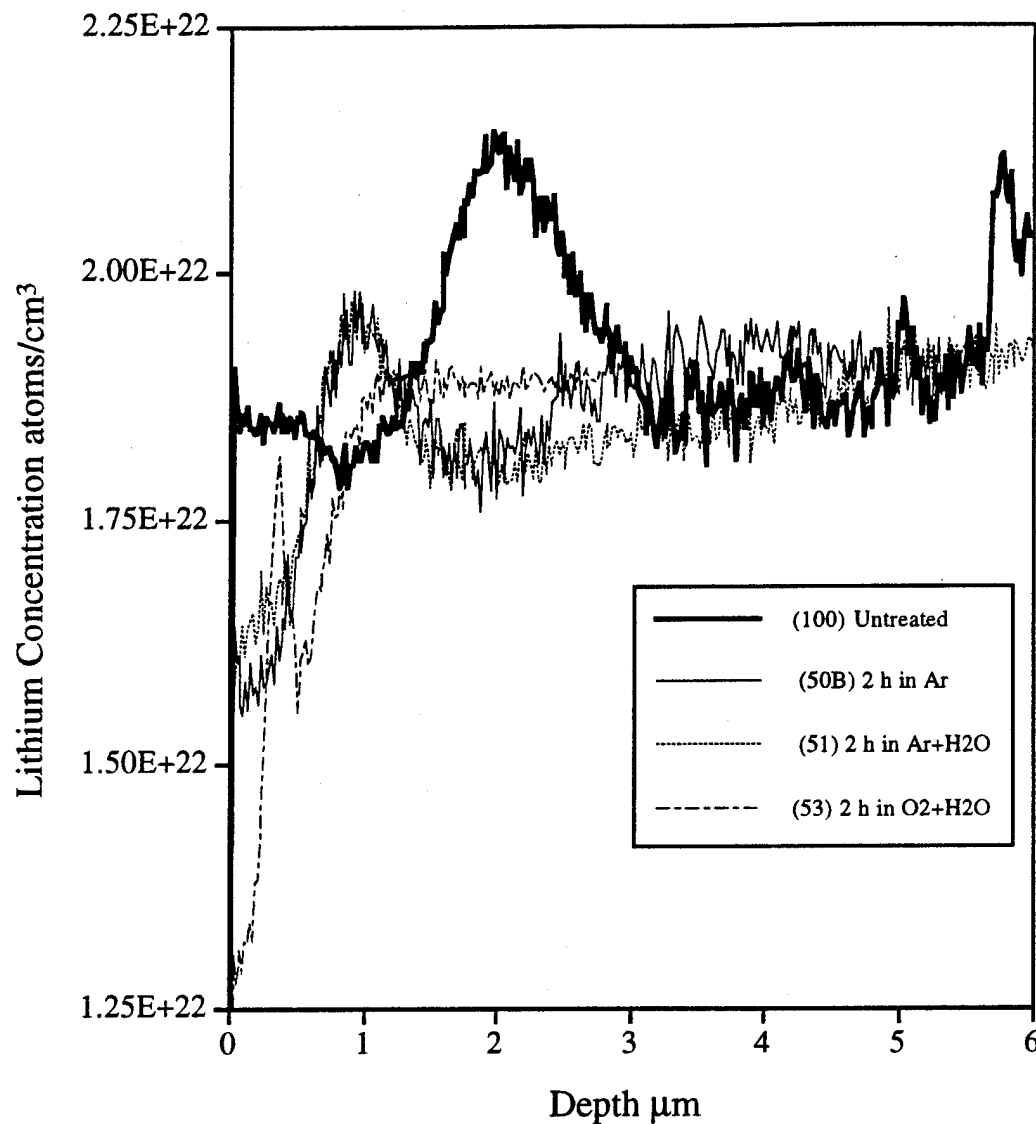


Figure 4.1. Lithium concentration for plain waveguide specimens 50B, 51, and 53. Diffusion time is 2 h and diffusion temperature is 1000 °C . Also shown is the lithium concentration from untreated  $\text{LiNbO}_3$  specimen 100. This data was processed by Evans East.

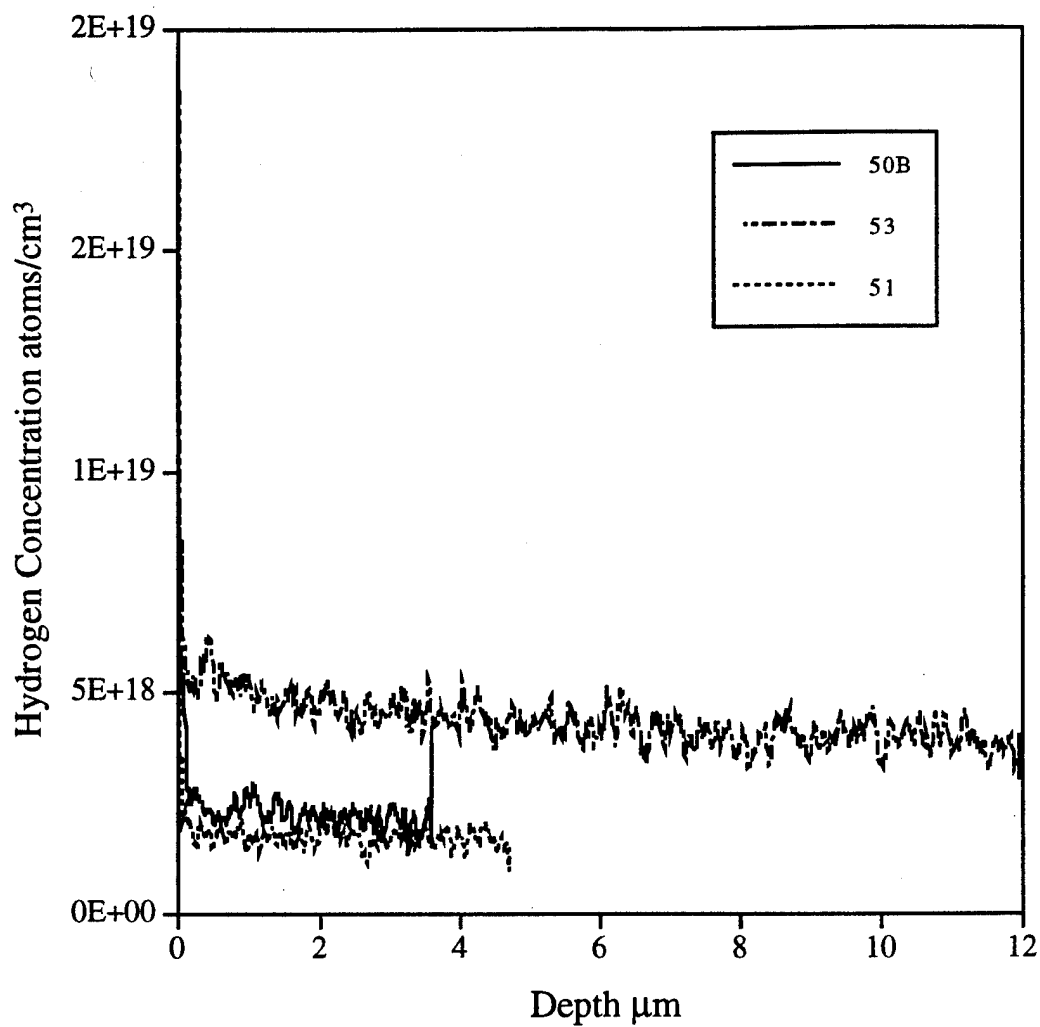


Figure 4.2. Hydrogen concentration for plain waveguide specimens 50B, 51, and 53. Diffusion time is 2 h and diffusion temperature is 1000 °C . This data was processed by Evans East.

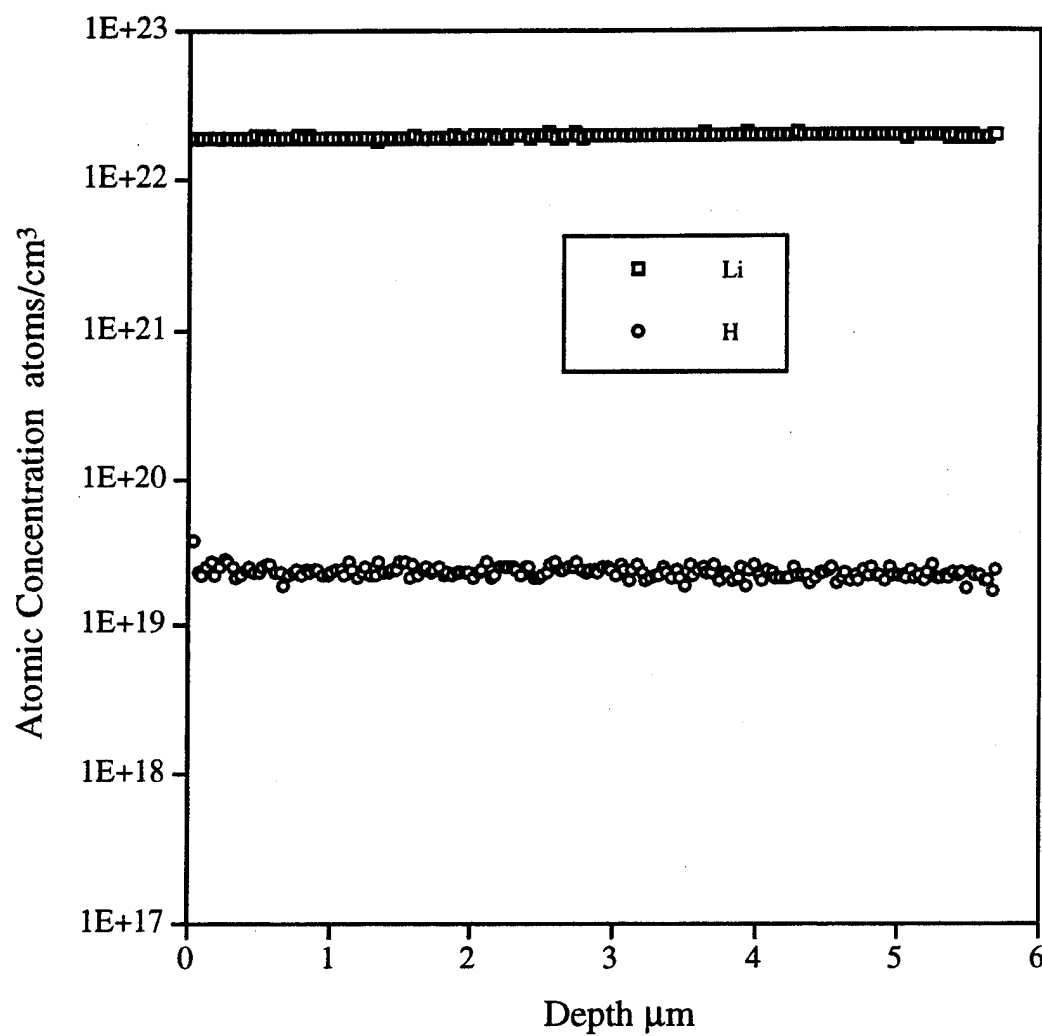


Figure 4.3. Lithium and hydrogen concentration profiles for specimen 50A (21 h diffusion in air without titanium). This SIMS data was processed by Evans East.

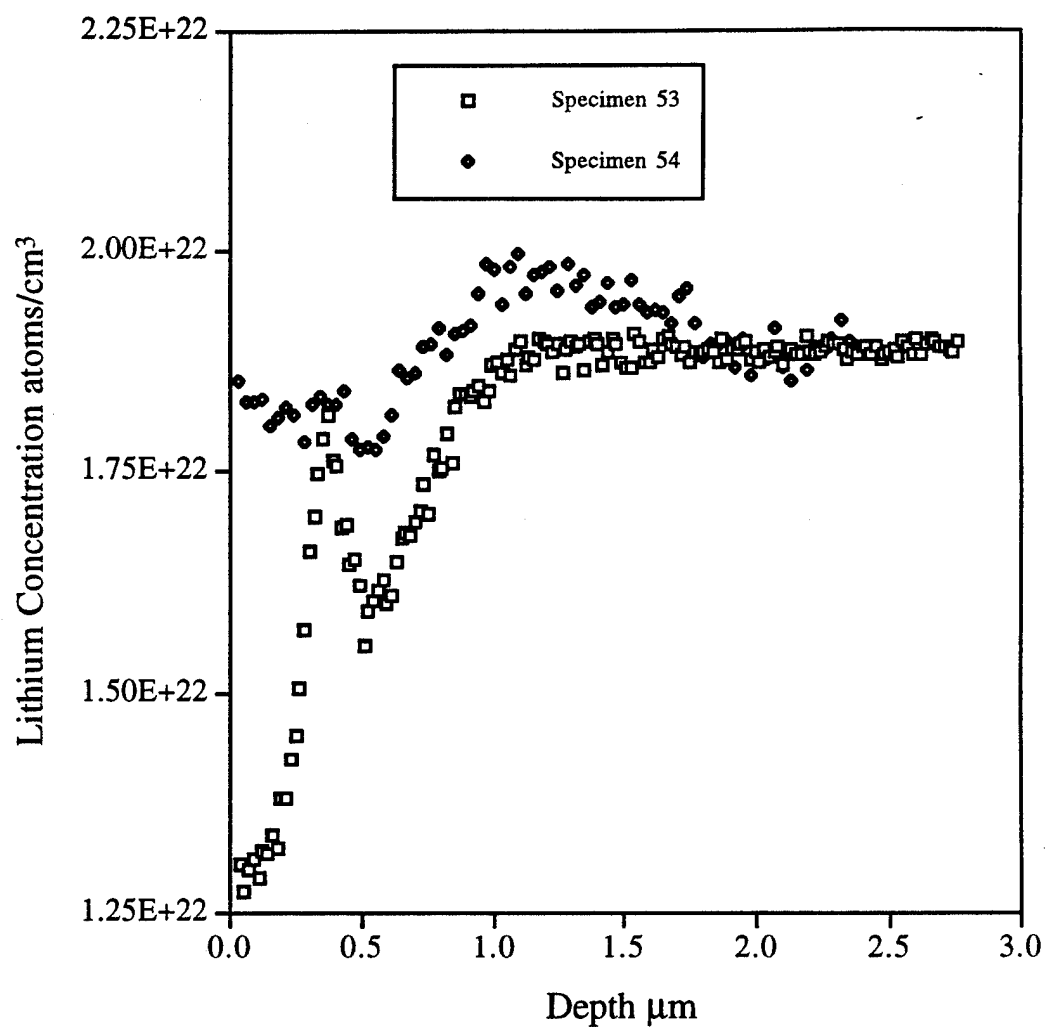


Figure 4.4. Lithium concentration for plain waveguide specimens 53 and 54. Diffusion time is 2 h for specimen 53 and 21 h for specimen 54. The diffusion temperature for these specimens was 1000 °C and the diffusion atmosphere was flowing oxygen bubbled through water. This data was processed by Evans East.

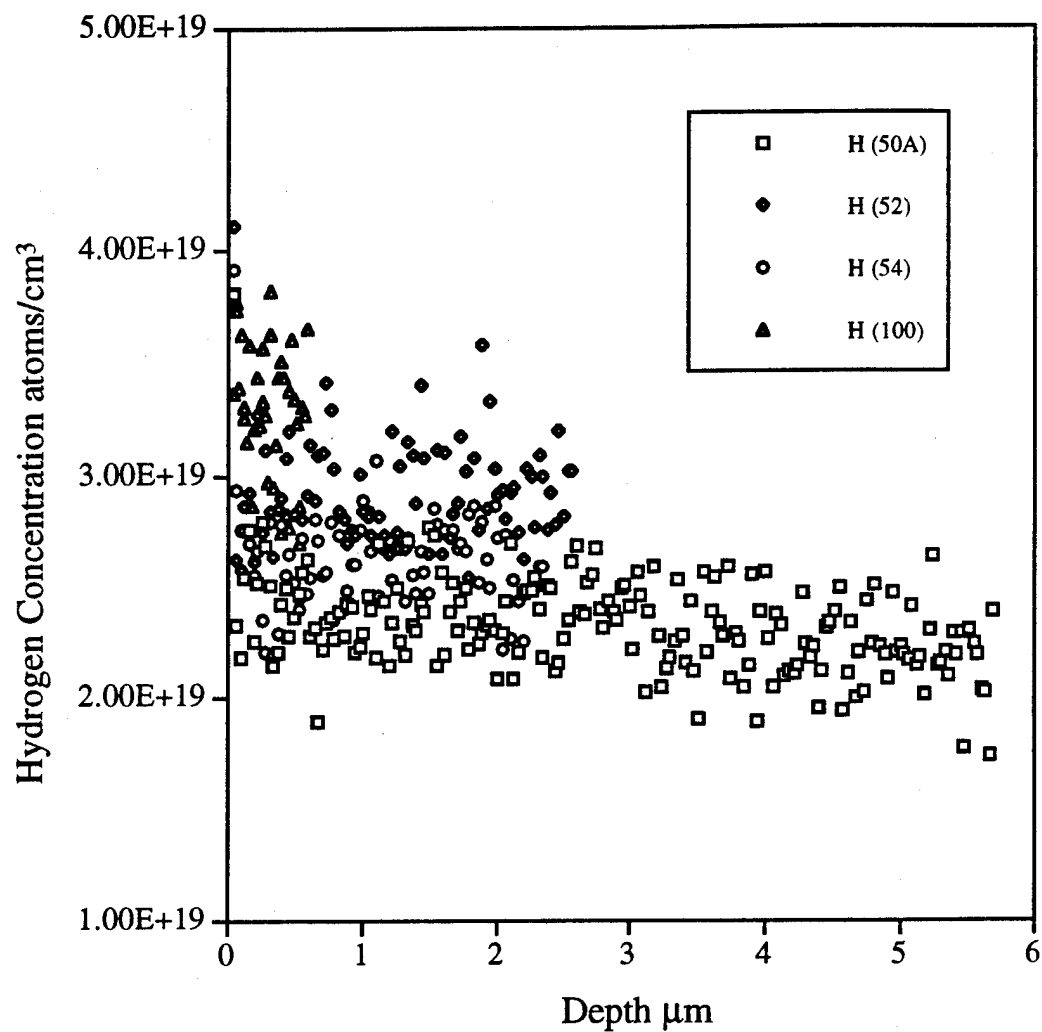


Figure 4.5. Hydrogen concentration for plain waveguide specimens 50A, 52, and 54, and untreated specimen 100. The diffusion time is 21 h and the diffusion temperature is 1000 °C for the waveguide specimens. This data was processed by Evans East.

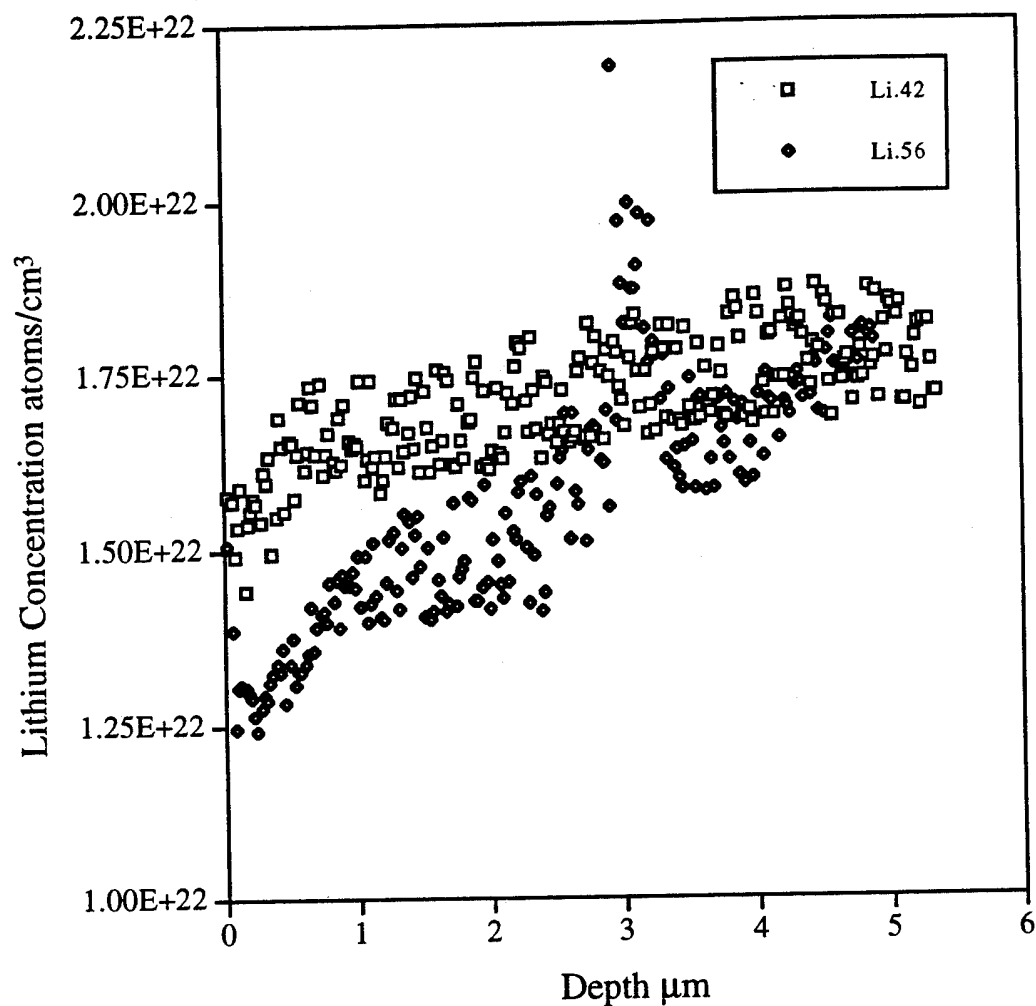


Figure 4.6. Lithium concentrations from waveguide specimens 42 and 56. The diffusion atmosphere was oxygen bubbled through water for specimen 42 and argon bubbled through water for specimen 56. The diffusion time is 2 h and the diffusion temperature is 1000 °C for both waveguide specimens. I processed this SIMS data.

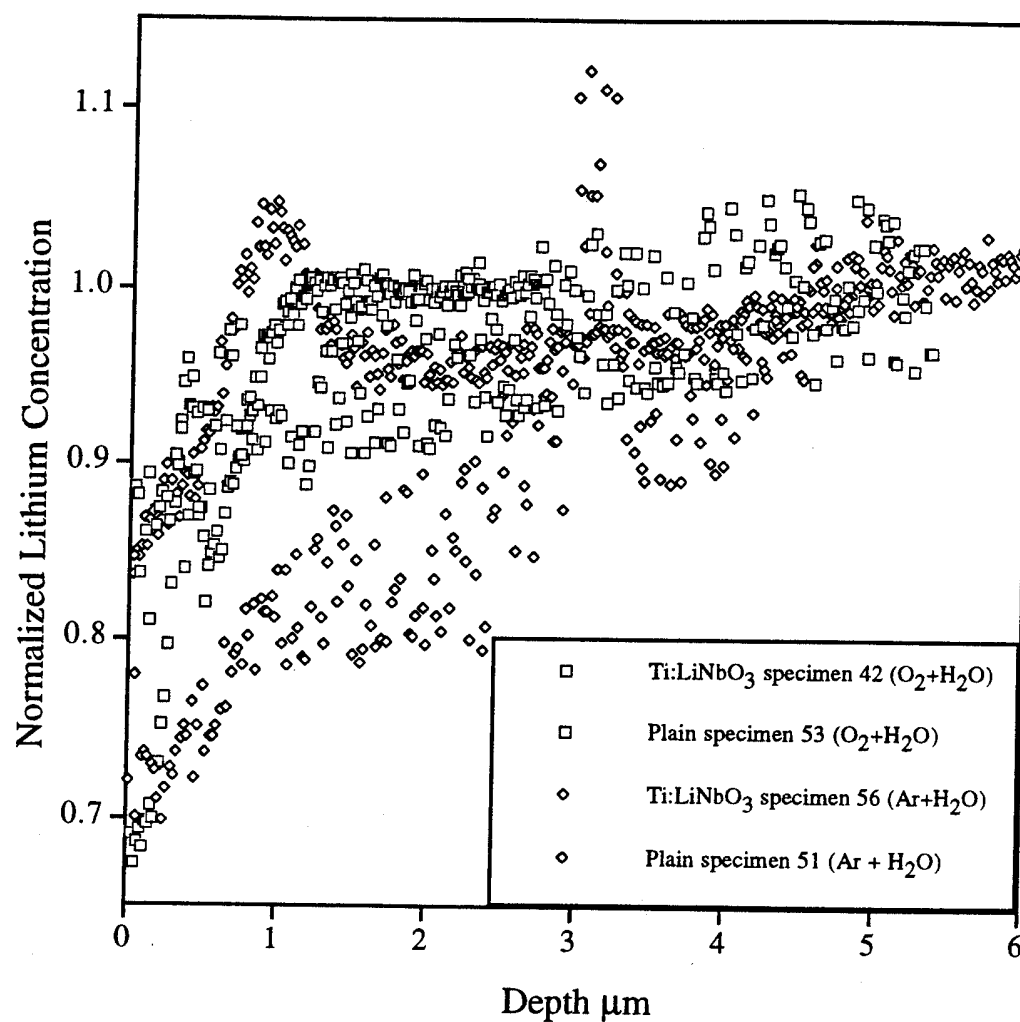


Figure 4.7. Normalized lithium concentrations in Ti:LiNbO<sub>3</sub> specimens 42 and 56, and plain specimens 51 and 53. The diffusion atmosphere was oxygen bubbled through water for specimens 42 and 53, and argon bubbled through water for specimens 51 and 56. The diffusion time is 2 h and the diffusion temperature is 1000 °C for all of these specimens.

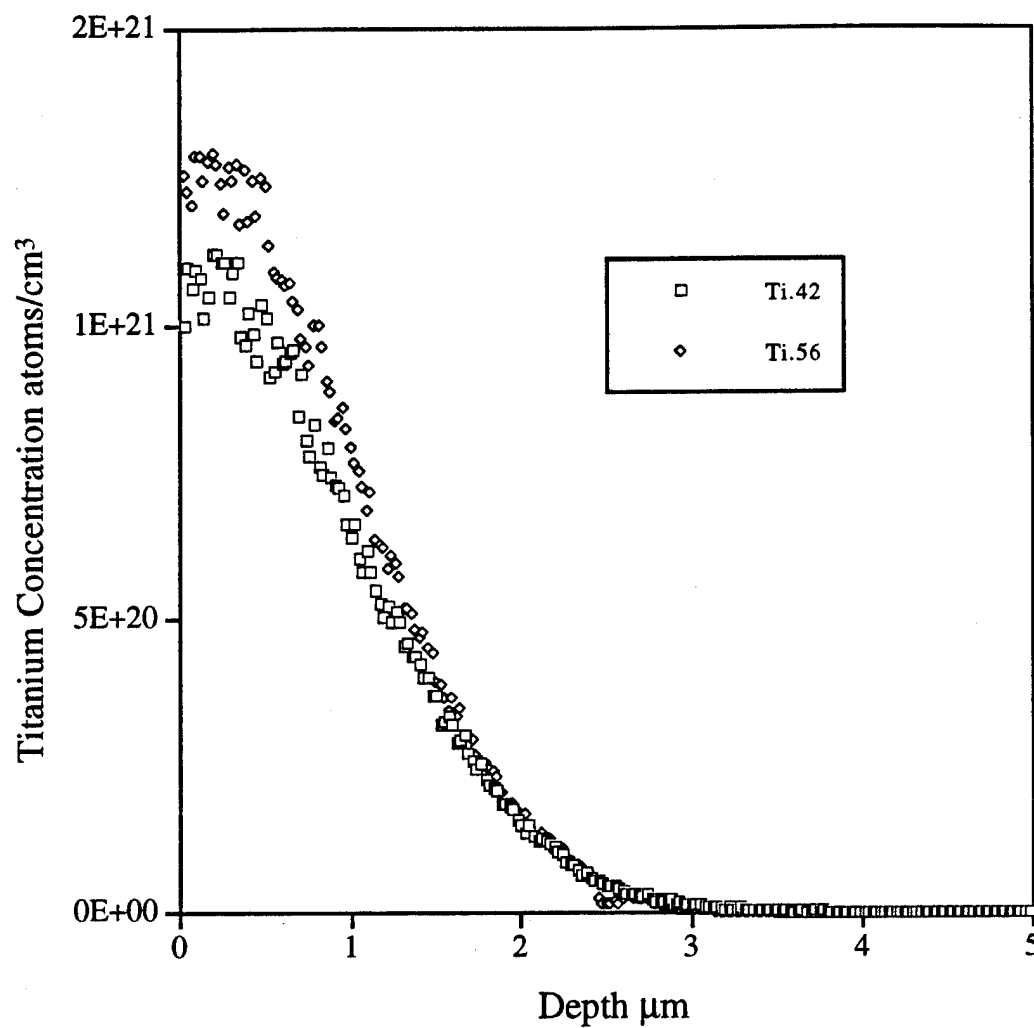


Figure 4.8. Titanium concentrations from waveguide specimens 42 and 56. The diffusion atmosphere was oxygen bubbled through water for specimen 42 and argon bubbled through water for specimen 56. The diffusion time is 2 h and the diffusion temperature is 1000 °C for both waveguide specimens. I processed this SIMS data.

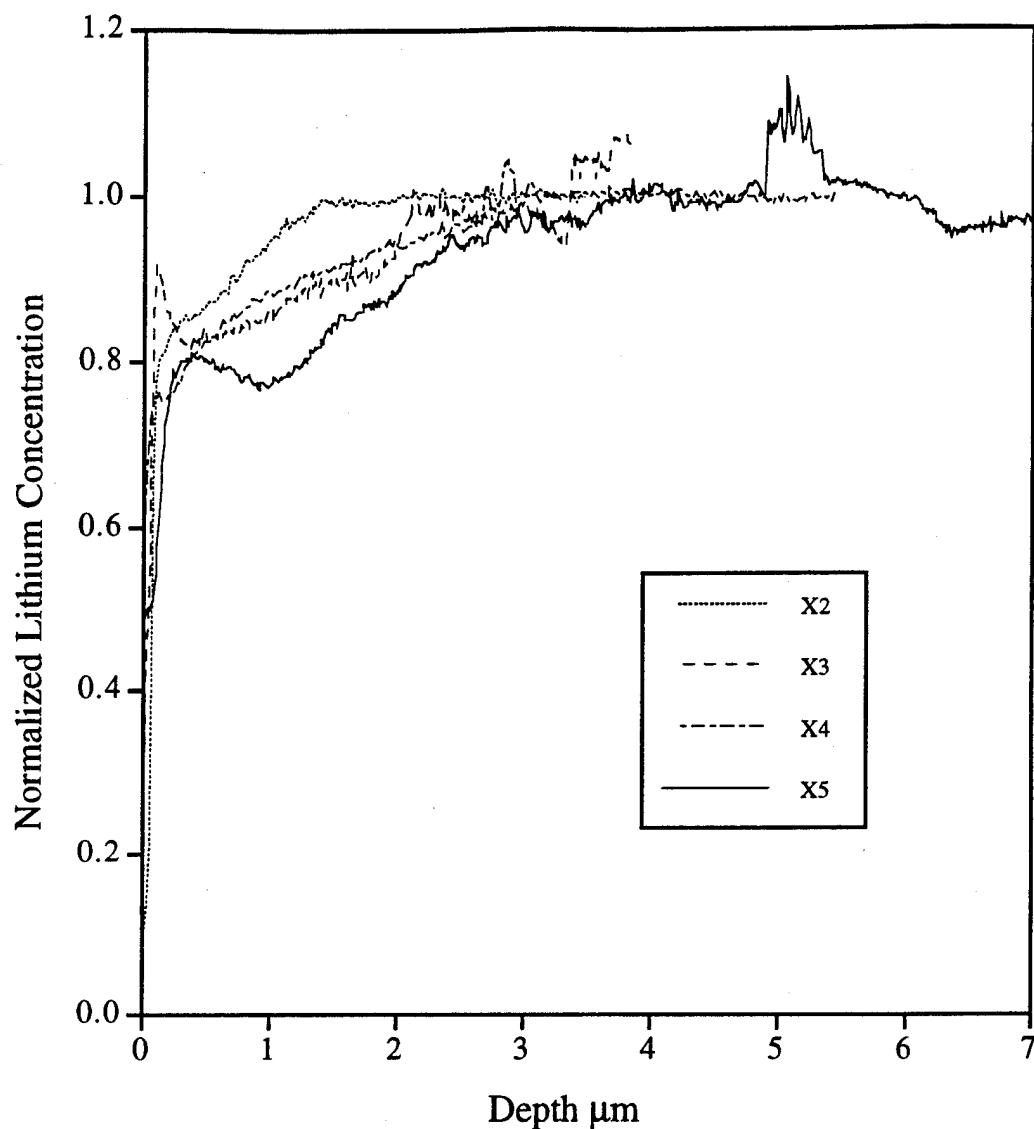


Figure 4.9. Lithium concentration in x-cut  $\text{Ti:LiNbO}_3$  specimens. The diffusion time is 1 h for specimen X2, 2 h for specimen X3, 4 h for specimen X4, and 2 h for specimen X5. The diffusion temperature was 950 °C for specimens X2, X3, and X4, and 1050 °C for specimen X5. The diffusion atmosphere was ambient air and the titanium thickness was 25 nm for all of these specimens. These x-cut specimens were fabricated by Ms. Milica Popovic, and I processed this SIMS data according to Appendix A.

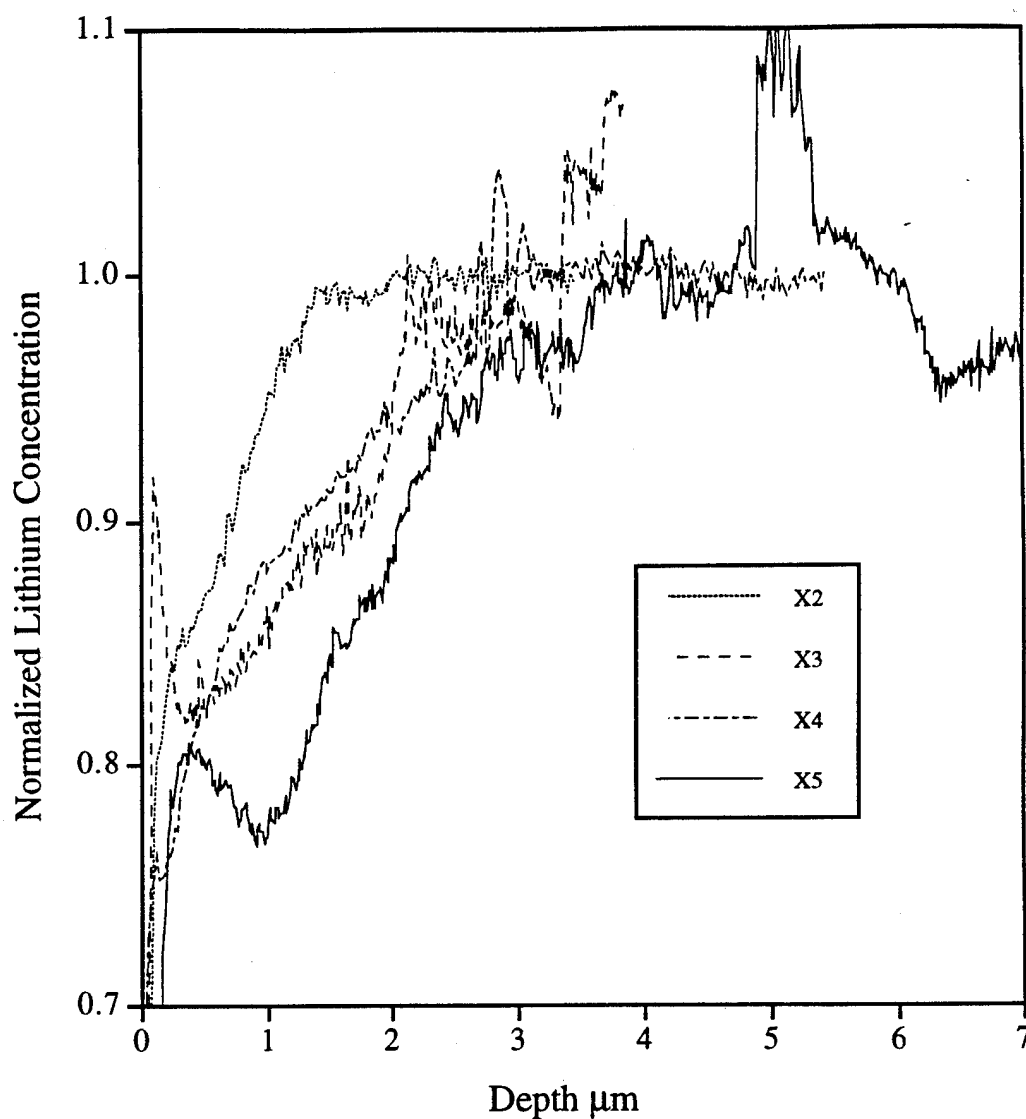


Figure 4.10. Detailed view of the lithium concentration in x-cut Ti:LiNbO<sub>3</sub> specimens. The diffusion time is 1 h for specimen X2, 2 h for specimen X3, 4 h for specimen X4, and 2 h for specimen X5. The diffusion temperature was 950 °C for specimens X2, X3, and X4, and 1050 °C for specimen X5. The diffusion atmosphere was ambient air and the titanium thickness was 25 nm for all of these specimens. These x-cut specimens were fabricated by Ms. Milica Popovic, and I processed this SIMS data according to Appendix A.

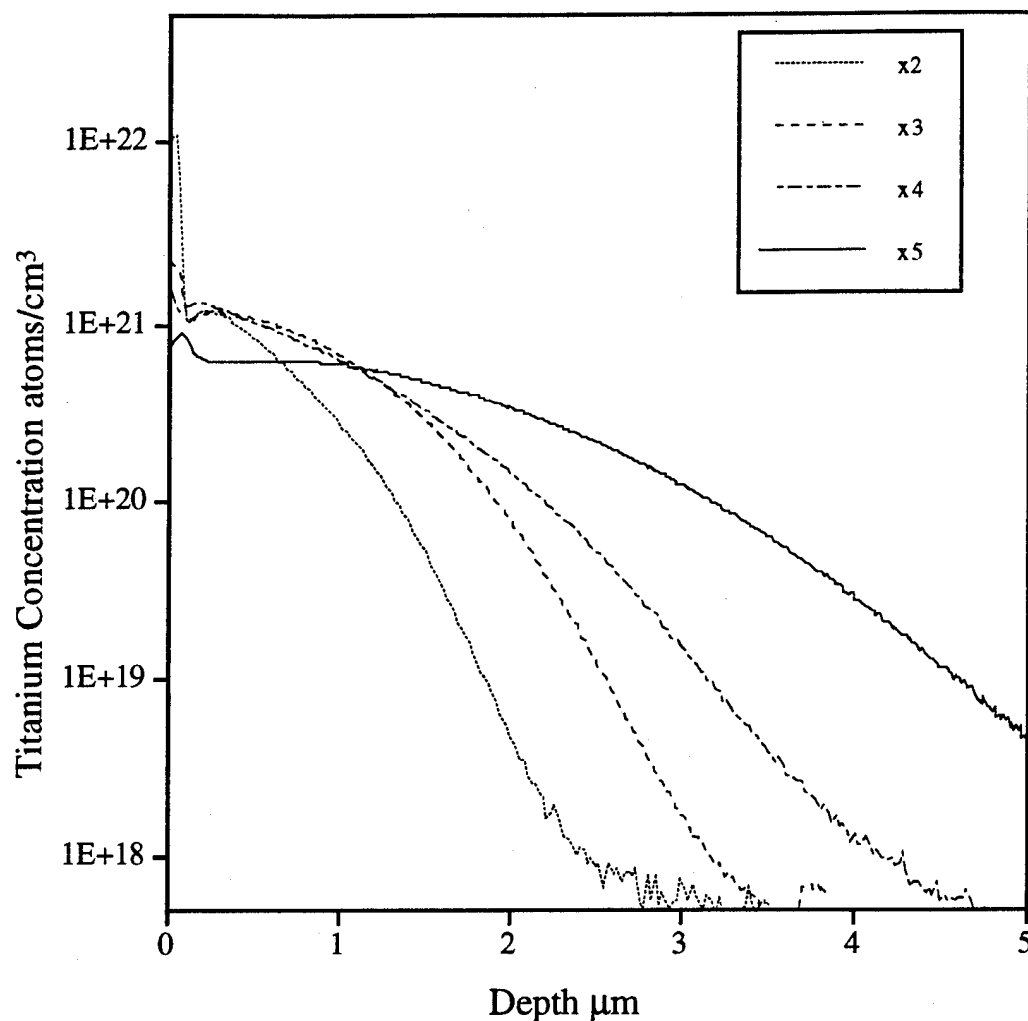


Figure 4.11. Titanium concentration in x-cut  $\text{Ti:LiNbO}_3$  specimens plotted using a logarithmic scale. The diffusion time is 1 h for specimen X2, 2 h for specimen X3, 4 h for specimen X4, and 2 h for specimen X5. The diffusion temperature was 950 °C for specimens X2, X3, and X4, and 1050 °C for specimen X5. The diffusion atmosphere was ambient air and the titanium thickness was 25 nm for all of these specimens. These x-cut specimens were fabricated by Ms. Milica Popovic, and I processed this SIMS data according to Appendix A.

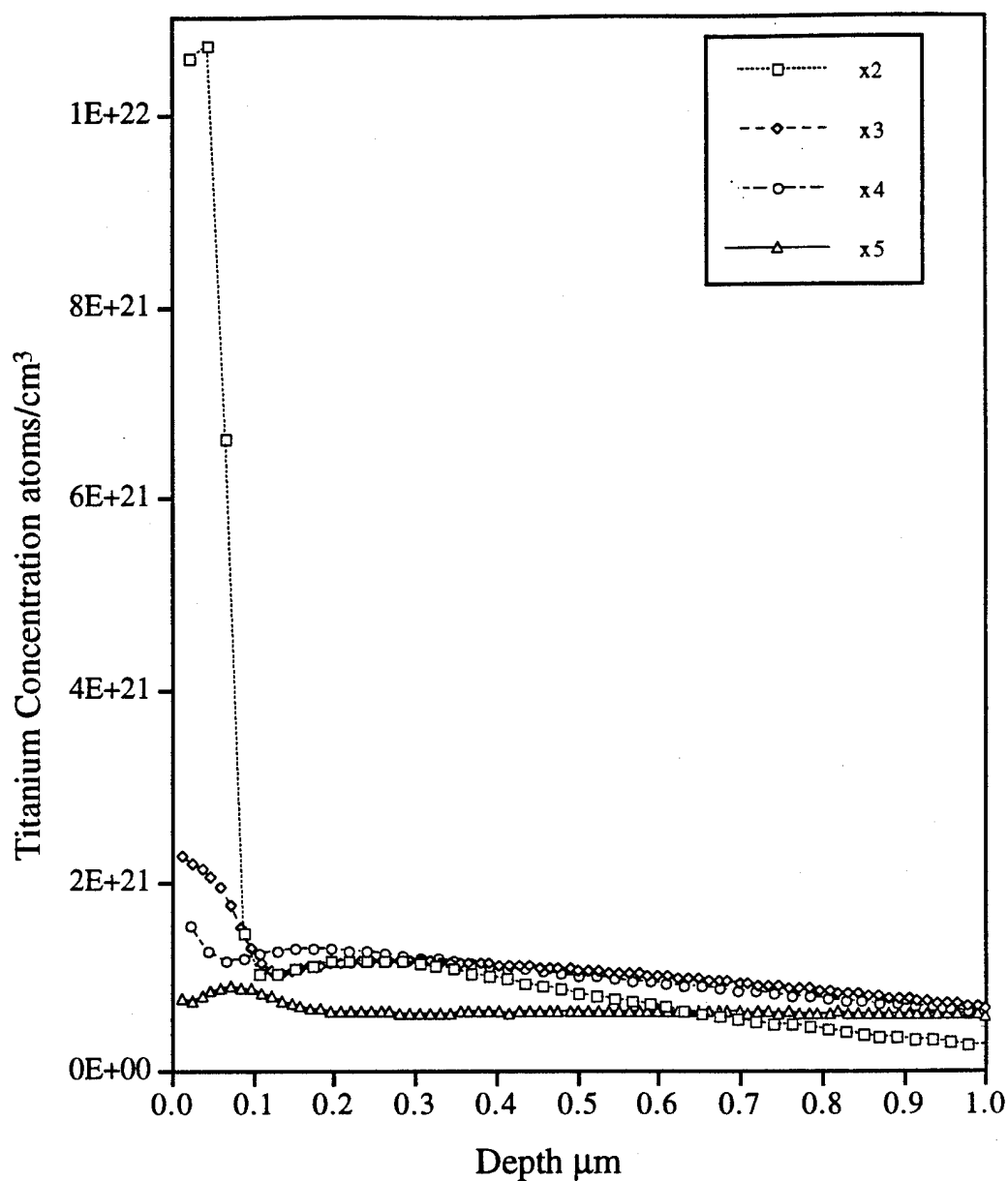


Figure 4.12. Details of titanium concentration in x-cut  $\text{Ti}:\text{LiNbO}_3$  specimens. The diffusion time is 1 h for specimen X2, 2 h for specimen X3, 4 h for specimen X4, and 2 h for specimen X5. The diffusion temperature was 950 °C for specimens X2, X3, and X4, and 1050 °C for specimen X5. The diffusion atmosphere was ambient air and the titanium thickness was 25 nm for all of these specimens. These x-cut specimens were fabricated by Ms. Milica Popovic, and I processed this SIMS data according to Appendix A.

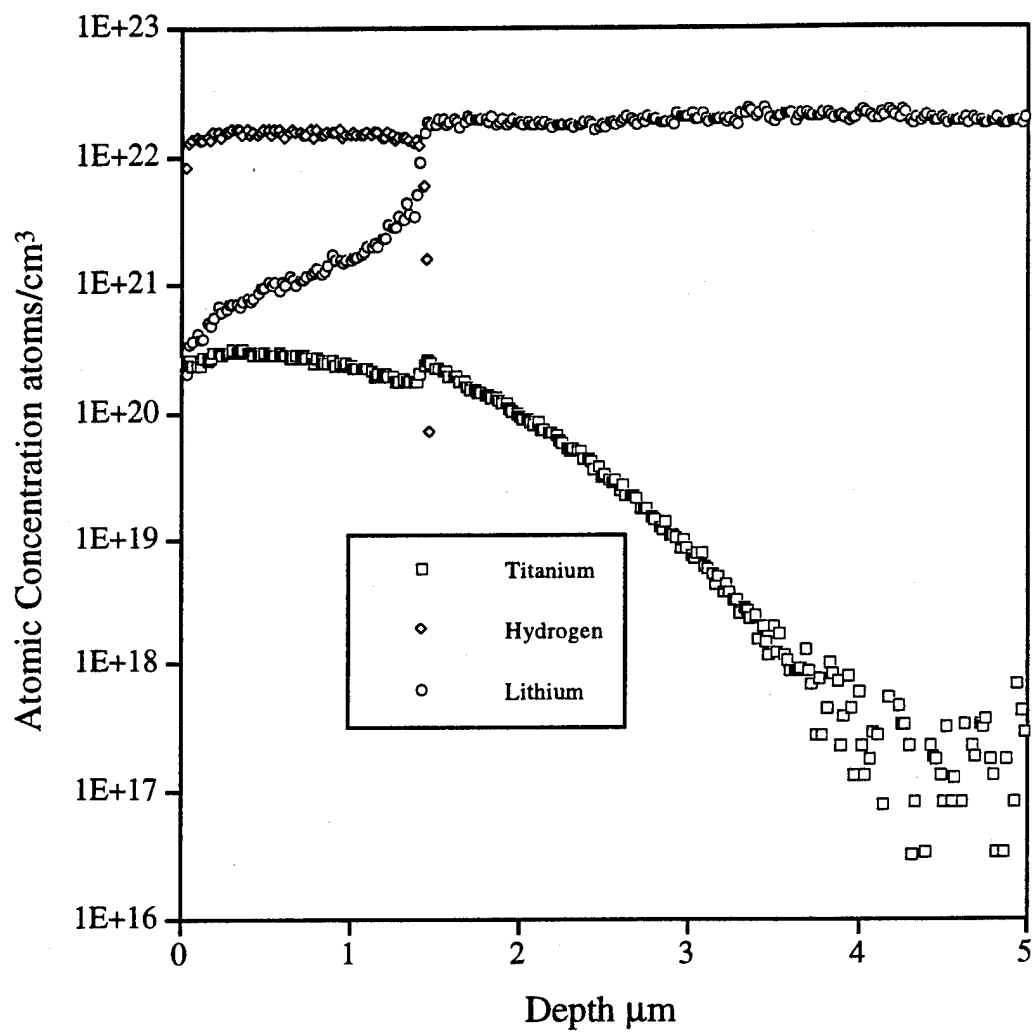


Figure 4.13. Atomic concentrations in TIPE:LiNbO<sub>3</sub> specimen 33A. This SIMS data was processed by Evans East (file 94171.52).

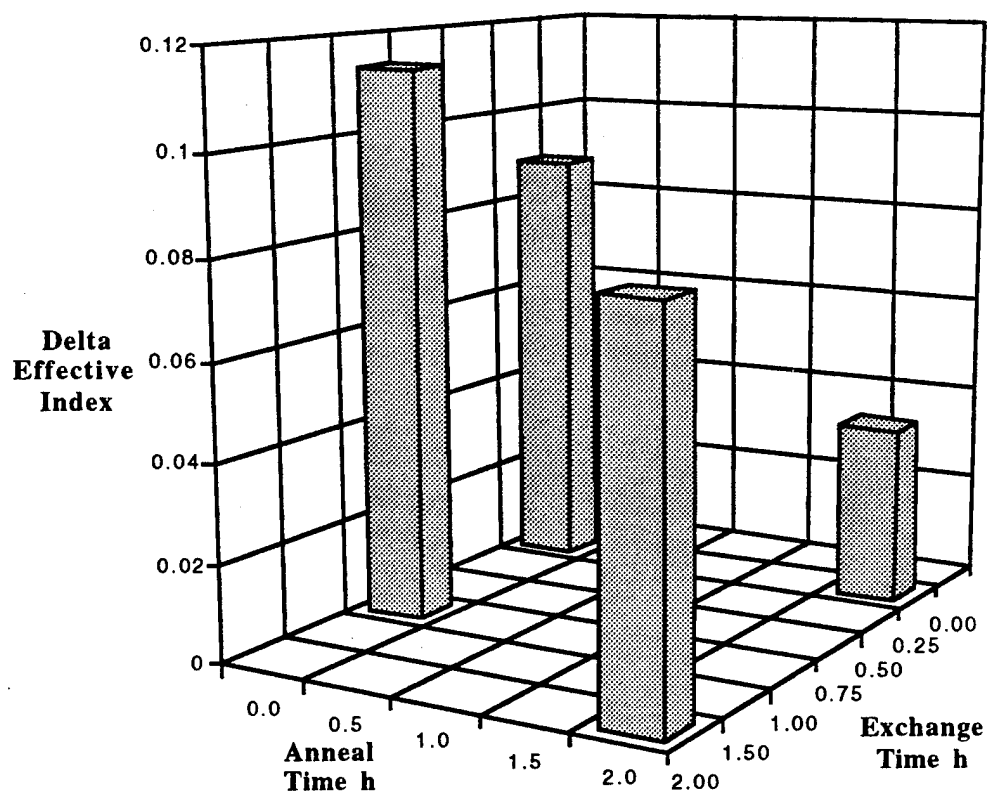


Figure 4.14. Effective index of the fundamental TE mode in  $\text{TIPE:LiNbO}_3$  specimens. Effective index is plotted as a function of exchange time and annealing time.

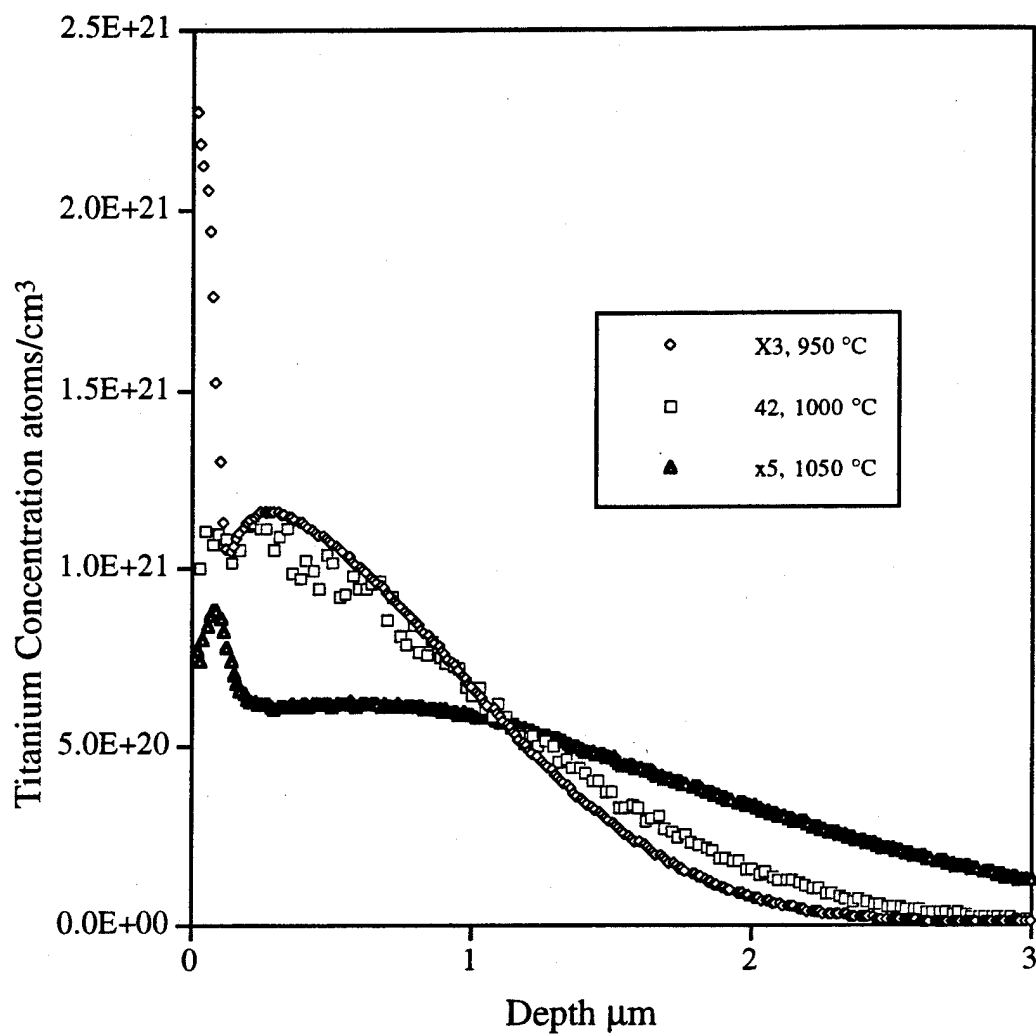


Figure 4.15. Titanium concentration in y-cut specimen 42 and x-cut specimens x3 and x5. The diffusion time for all of these specimens is 2 h.

## CHAPTER 5

### ON-AXIS POLARIZATION COUPLING IN Y-CUT TITANIUM IN-DIFFUSED LITHIUM NIOBATE SLAB WAVEGUIDES

We report on polarization coupling from x-propagating TE-polarized waveguide modes to TM-polarized radiation modes in y-cut titanium in-diffused lithium niobate slab waveguides. The polarization coupling is linear with respect to the TE-polarized input power and depends on the titanium diffusion time. Furthermore, the polarization coupling was not affected by white light flooding the waveguide. The maximum conversion from a TE-polarized waveguide mode to a TM-polarized radiation mode is 3.2 %/cm using a conservative estimate for the power initially in the TE waveguide mode. We observe no turn-on delay greater than 1 s between the excitation of the TE waveguide mode and the observation of the TM radiation. In addition, intentional amplitude modulations of the TE-polarized waveguide mode were registered as equivalent amplitude modulations by the TM-polarized radiation modes. We did not observe polarization coupling from x-propagating TM-polarized waveguide modes to TE-polarized radiation modes. This polarization coupling is a source of loss and potentially a source of noise for titanium in-diffused lithium niobate optical devices.

#### 5.1 Introduction

This work describes polarization coupling in titanium in-diffused lithium niobate slab waveguides: a source of polarization dependent loss and potentially a source of noise, in integrated-optical devices.

We are developing a methodology for the fabrication and testing of titanium in-diffused lithium niobate ( $\text{Ti:LiNbO}_3$ ) [29] slab waveguides. One unexpected result of this work has been the observation of polarization coupling in these slab waveguides. When we couple transverse electric field (TE) polarized light into waveguide modes, we observe transverse magnetic field (TM) radiation modes radiating from the waveguide. Since this polarization coupling occurs for propagation along the crystal axis, the observed TM radiation can be distinguished from the TM radiation that would result from leaky modes propagating off-axis in an anisotropic waveguide. When the polarization of the input was changed to TM-polarized, we did not observe polarization coupling into TE-polarized radiation modes.

There are previous reports of polarization coupling in y-cut  $\text{Ti:LiNbO}_3$  for on-axis propagation of TE waveguide modes. However, the properties of the TM radiation and the circumstances yielding the polarization coupling in these reports are different from those in our experiments. For example, Kazansky [67] reports a nonlinear coupling between TE and TM modes in x-propagating y-cut  $\text{Ti:LiNbO}_3$  channel waveguides. One of his results shows a nonlinear relationship between the power of the input TE light and the power of the TM radiation. Another measurement shows a delay of the order of tens of minutes between the input of the TE light and the onset of the TM radiation. Kazansky proposes that the mechanism for the polarization coupling is a grating caused by the nonlinear circular photovoltaic effect and directed perpendicular to the plane of the waveguide. This grating couples TE waveguide modes into TM radiation modes. Since we found neither the power nonlinearity nor the delay of onset, our observations are probably not the result of the same mechanism suggested by Kazansky.

Other observations of polarization coupling from TE waveguide modes to TM radiation modes in lithium niobate waveguides are those reported by Chen and Chang [68]. They report an anomalously large attenuation loss for x-propagating TE waveguide modes in waveguides formed by proton-exchange in y-cut lithium niobate. This attenuation was observed for TE modes whose effective index is less than the substrate's ordinary index. Furthermore, this attenuation is associated with polarization coupling into TM radiation modes. The TE waveguide modes with an effective index greater than the substrate's ordinary index experience neither polarization coupling nor increased propagation loss. Chen and Chang do not mention either a nonlinear power relationship between the TE or TM modes nor an onset delay between the TE-polarized and TM-polarized modes. The polarization coupling seen by Chen and Chang has a similar characteristic to the polarization coupling we see. We both observe polarization coupling from TE guided modes whose effective index is less than the TM substrate's index of refraction. Our observations come from waveguides formed by titanium indiffusion, not proton exchange. In their search for the mechanism causing this phase-matched polarization coupling, Chen and Chang ruled out scattering from surface defects, but otherwise stated that the mechanism is not well understood.

Another situation which yields TM-polarized light radiating from a predominantly TE-polarized waveguide mode is when modes propagate off-axis in anisotropic waveguides. Theoretical studies of these leaky modes in anisotropic slab waveguides has been extensively reported in the literature; see for example [69, 70, 71, 72, 73, 74, 75, 76]. Experimental verification of leaky modes in uniaxial waveguides have been reported for y-cut  $\text{Ti:LiNbO}_3$  [77, 78]. We also have observed leaky modes, but in lithium out-diffused y-cut  $\text{LiNbO}_3$  slab waveguides.

For propagation directions not along a crystal axis, these leaky modes exist with a hybrid polarization containing all six field components. For the specialized waveguide orientations which yield on-axis mode propagation, no leaky modes result, and these modes are characterized as uncoupled TE- and TM-guided modes.

This paper presents our measurements of TE to TM polarization coupling for propagation along the crystal's x-axis in y-cut  $\text{Ti:LiNbO}_3$  slab waveguides. Our observations differ from [67] in that we do not measure a nonlinear relationship between the power of the TM radiation and the power of the TE waveguide mode, nor do we observe a delay between the input time of the TE waveguide mode and the onset of the TM radiation. Furthermore, the polarization coupling that we observe occurs for mode propagation along the crystal axis and thus cannot be explained only by leaky mode theory, which describes off-axis mode propagation in anisotropic waveguides.

The outline of this paper is as follows. In the second section we describe our waveguide fabrication procedures. The third section contains the description of our experimental technique, and the fourth section presents the results of our measurements and observations. In the fifth and final section, we compare and contrast our results with other published observations of coupling between orthogonal polarizations and discuss the possible mechanisms which cause this polarization coupling.

## 5.2 Waveguide Fabrication

The slab waveguides discussed in this paper were fabricated on the minus face of optical grade y-cut lithium niobate wafers [79]. The orientation of the slab waveguide with respect to the substrate's crystal axes is shown in Fig. 5.1. The propagation of the guided modes is predominantly along the crystal's x-axis.

Typical dimensions for the rectangular waveguide specimens are 1 cm to 3 cm along the x-axis, 0.1 cm along the y-axis, and 1 cm along the z-axis.

According to the manufacturer, these lithium niobate wafers originate from a crystalline boule that is grown using the Czochralski technique. The crystalline boule is drawn from a congruent melt of high purity  $\text{Nb}_2\text{O}_5$  and  $\text{LiCO}_3$  powders (less than 2 ppm of each transition metal, including iron). The congruent composition value of the melt is  $48.38 \pm 0.015$  mole-%  $\text{Li}_2\text{O}$ . The resulting crystalline boule has compositional uniformity less than  $\pm 0.005$  mole-%  $\text{Li}_2\text{O}$ .

We fabricated two different types of slab waveguides on the  $\text{LiNbO}_3$  substrates. One type of waveguide was formed using titanium in-diffusion [29]. The fabrication procedure for these waveguides is as follows. Titanium metal was evaporated onto an entire wafer in order to insure uniformity of the titanium thickness for each waveguide specimen. The titanium metal was evaporated by resistive heating in a vacuum of  $5 \times 10^{-4}$  Pa to a thickness of 25 nm as determined by a quartz crystal oscillator. Individual specimens were cut from this metalized wafer and then placed in a high temperature oven for the desired diffusion time.

The temperature schedule for the diffusion begins at room temperature and reaches the diffusion temperature,  $T=1000^\circ\text{C}$ , after a 2 h ramp-up time. The diffusion temperature is maintained for a time  $t$ . Afterwards, the specimens cooled to room temperature within two hours. The diffusion was carried out in an atmosphere of wet oxygen which was created by bubbling medical grade oxygen through a 17 cm column of room-temperature de-ionized water. This wet oxygen flowed at a rate of 300 l/h, into the oven chamber. We began flowing the wet oxygen during the temperature ramp-up at  $345 \pm 50^\circ\text{C}$ , and the wet oxygen continued to flow until the ramp-down temperature of  $140 \pm 25^\circ\text{C}$ . The final

step consisted of polishing the specimen endfaces to optical quality use in input and output optical coupling. Specimen 41 was fabricated with a dwell time of 1 h while specimen 42 has a 2 h dwell time.

The second type of waveguide was fabricated without the titanium metallization. Our intention was to form lithium out-diffused waveguides [40, 30]. However, subsequent studies [1] indicate that waveguide formation in these specimens may involve other processes in addition to lithium out-diffusion.

Waveguides of the second type were fabricated in the same manner as the titanium in-diffused waveguides but with the following differences: the waveguide originated from a different yet similar  $\text{LiNbO}_3$  wafer, and the polishing of the specimen endfaces preceded the out-diffusion step. Specimen 53 is a waveguide of the second type with a 2 h dwell time.

### 5.3 Waveguide Characterization

The effective index  $N$  of a waveguide mode is measured using prism out-coupling [9]. Light from a HeNe laser at wavelength  $\lambda = 0.6328 \mu\text{m}$  is butt-coupled into the slab waveguide using a single-mode polarization-maintaining fiber. The extinction ratio between the two orthogonally polarized modes of the fiber was greater than 400:1. A rutile prism with its optic axis parallel to the substrate's optic axis is pressed against the waveguide to couple light out from the waveguide. At the output face of the prism the out-coupled light, or  $m$ -line, is refracted into air at the mode angle  $\theta'_m$ . The mode's effective index is related to the mode angle by [23]

$$N = n_p \sin \left[ \theta_p + \arcsin \left( \frac{n_c}{n_p} \sin (\theta'_m) \right) \right], \quad (5.1)$$

where  $n_p = 2.8666$  [36] is the prism's extraordinary index,  $\theta_p = 60.59 \pm 0.02^\circ$  is the prism's angle, and  $n_c = 1.0003$  is the index of air.

We determine the mode angle  $\theta'_m$  using two aligned translation stages, one with travel parallel to the prism output face and one with travel perpendicular to the prism output face. A charge-coupled device (ccd) array is affixed to these stages at a distance of 1 m from the prism output face. The  $m$ -line illuminates the ccd array, and a profile of the  $m$ -line is viewed on a digital oscilloscope. The angle  $\theta'_m$  is determined using inverse triangulation. A right triangle is formed by translating the ccd array a distance  $\Delta x$  and a perpendicular distance  $\Delta y$ . For a particular stage translation  $\Delta x$ , the translation  $\Delta y$  is determined by repositioning the  $m$ -line at the location on the ccd array. Now, the mode angle can be calculated using the equation

$$\tan(\theta'_m) = \frac{\Delta x}{\Delta y}. \quad (5.2)$$

In a similar manner, we determine the substrate effective index  $N_s$  by measuring mode angle associated with the substrate  $m$ -line. Then we calculate the increment  $\Delta N = N - N_s$  by which the effective index of the mode exceeds the substrate index. Using this technique, we eliminate the influences of systematic measurement errors at the expense of reporting relative, rather than absolute values for the effective index. Details of the measurement can be found in Ref. [1].

The experimental arrangement used for observing TM radiation is shown in Fig. 5.2. The same fiber-coupled light source used for the  $m$ -line measurements is used here to butt-couple into the waveguide. The maximum power output from the fiber is 230  $\mu\text{W}$ . A polarizer and viewing screen are positioned far enough from the waveguide output face that the polarization content of the radiation pattern can be investigated. The fiber source is oriented so that TE polarized light is coupled into a set of slab waveguide modes which will propagate in the plane

of the waveguide with an angular extent  $\pm\theta_b$  about the x-axis. This maximum divergence angle  $\theta_b$  was calculated by fitting a Gaussian profile to the fiber mode field and using the properties of Gaussian beam propagation in an isotropic and homogeneous medium [80]. The propagation angle is calculated from the equation

$$\theta_b = \arctan\left(\frac{\lambda}{\pi\omega_0 N}\right), \quad (5.3)$$

where  $\omega_0$  is the beam radius where the intensity is reduced from the peak value by a factor of  $e^{-2}$ . Using the values  $\omega_0 = 1.5\mu\text{m}$  from a near-field measurement,  $\lambda = 0.6328\mu\text{m}$ , and  $N = 2.22$ , we calculate that the waveguide modes propagate within the angular range of  $\pm\theta_b = 3.5^\circ$  to the crystal's x-axis.

Any TM radiation modes which are phase-matched to the TE waveguide modes will propagate at the phase-matching angle  $\pm\phi$  with respect to the plane of the waveguide; see Fig. 5.3. The phase-matching condition is given by

$$\cos(\phi) = \frac{N}{n_o}, \quad (5.4)$$

where  $N$  is the effective mode index and  $n_o$  is the substrate's ordinary index. This TM radiation undergoes total internal reflection at both air-LiNbO<sub>3</sub> interfaces and then emerges from the specimen at the waveguide endface in two branches, labeled A and B. These two branches of TM radiation emerge the sample with angles  $\pm\phi'$  which are related to the phase matching angle  $\phi$  through Snell's law,

$$\sin(\phi') = n_o \sin(\phi). \quad (5.5)$$

A two-dimensional ccd array was positioned in the path of branch A to record the detailed structure of the TM radiation pattern. The angular extent of the TM radiation pattern captured by the ccd array corresponds to a propagation angle of  $\theta = \pm 3^\circ$  about the crystal's x-axis.

We quantified the polarization coupling by measuring the power ratio  $\rho$  per unit propagation length of TM-polarized radiation to the TE-polarized input. To determine the value of  $\rho$ , a cylindrical lens, a power meter, and a polarizer were positioned at the output face of the waveguide so as to measure the TM radiation power in branch A. The TE input power to the waveguide was determined by measuring the output power of the fiber with the same power meter and polarizer combination. The measured TE input power should be multiplied by a factor of 2 to account for the loss in the polarizer in order to estimate the TE input power present at the waveguide.

Since only one branch of the TM radiation was collected by the power meter, the measured value of the TM power was multiplied by a compensating factor  $\Gamma$  to obtain the total TM power. The compensation factor is determined by calculating the relative powers expected in each TM radiation branch. In general, the TM power in each branch will not be equal; see Fig. 5.3. The relative power in each branch depends on the geometrical properties of the particular sample, for example, the length of the waveguide and the thickness of the substrate. As Fig. 5.3 shows, more of the waveguide length contributes to the TM radiation in branch B than to branch A. For the case illustrated in Fig. 5.3, the total TM power radiated by the waveguide would be equal to the power measured in branch A multiplied by the compensation factor  $\Gamma = 3$ . The calculated values of  $\rho$  using this method will underestimate the amount of polarization coupling because (1) the calculation assumes complete power transfer from the input fiber to the TE waveguide modes and (2) the calculation excludes the possibility of TM radiation coupling back into the TE waveguide mode.

The degree of linearity between the TM radiation power and the input

TE power was measured using the same experimental setup as that used for determining  $\rho$ . The power linearity was measured by varying the input TE power while measuring the TM power in branch A. The TE input power was varied by adjusting the laser power coupled into the polarization maintaining fiber.

We illuminate the specimen with a 250 W quartz halogen lamp to test for the presence of a photorefractive grating within the waveguide. An optical fiber bundle delivers the whitelight to the waveguide.

#### 5.4 Experimental Results

Measured values of  $\Delta N$  are shown in Table 5.1 for the TE modes in the titanium in-diffused waveguide specimens 41 and 42, and for the TE modes in the plain  $\text{LiNbO}_3$  specimen, 53. Specimens 41 and 42 also supported TM-guided modes, whereas we did not observe any TM waveguide modes in specimen 53. The values of  $\Delta N$  were determined from regions of the m-lines that correspond to the propagation direction of the waveguide mode along the crystal's x-axis. Also listed in Table 5.1 are the calculated phase-matching angles  $\phi$  for each mode.

Figure 5.4 displays the titanium concentration of specimen 42 after diffusion. Titanium concentration was measured using secondary ion mass spectroscopy (SIMS) [81]. The evaporated titanium layer appears to be fully diffused into the  $\text{LiNbO}_3$  substrate with no residual surface titanium layer. The measurements of titanium concentration agree well with the Gaussian solution to the diffusion equation with source layer thickness much less than the diffusion depth [31].

The intensity radiation pattern for each specimen was studied using the experimental setup in Fig. 5.2. The branches of TM radiation emerged from the specimen endface with a divergence angle much less than the divergence angle

of the TE radiation. This observation is consistent with a larger beam aperture for the TM radiation. The beam aperture for the TM radiation is determined by the phase-matching angle and the substrate thickness whereas the aperture for the TE radiation is determined by the TE mode profile. The TM radiation forms lines of intensity on the screen which are analogous to the m-lines created by prism out-coupling. Distinct TM radiation lines are observed on the screen for each waveguide mode, since each mode propagates with a different effective index and yields a different radiation angle  $\phi'$ . Another noticeable feature of the TM radiation is a slight curvature of the radiation line.

The radiation pattern from specimen 41 is shown in Fig. 5.5. This intensity pattern was recorded by imaging the viewing screen in Fig. 5.2 onto a ccd camera. A polarizer determines that the two horizontal strips of light positioned above and below the centrally located bright spot are TM-polarized, while the central bright spot is TE-polarized. The top TM radiation line corresponds to branch A while the bottom TM radiation line corresponds to branch B (refer to Fig. 5.3). Note in Fig. 5.5 the unequal power in the two branches of the TM radiation. It is possible to preferentially excite the fundamental waveguide mode or excite all the remaining higher-order waveguide modes of specimen 41. The radiation pattern shown in Fig. 5.5 is a result of exciting the fundamental waveguide mode.

Figures 5.6 and 5.7 provide a detailed view of the TM radiation pattern in branch A from two waveguide specimens; Figure 5.6 shows the TM radiation from specimen 53, while Fig. 5.7 shows the TM radiation pattern from specimen 41 (the titanium in-diffused waveguide). Note the intensity minimum in Fig. 5.6, which corresponds to the on-axis TE propagation in specimen 53. This intensity

minimum is not present in any of the modes in the titanium in-diffused specimens as illustrated in Fig. 5.7. Another feature in Fig. 5.7 is the two groups of TM radiation lines within branch A from specimen 41. These two horizontal stripes are a result of simultaneously exciting both the lowest-order mode and the higher-order modes of specimen 41. The bottom stripe in Fig. 5.7 corresponds to the lowest-order mode while the top stripe corresponds to higher-order modes.

The angle  $\phi'$  at which the TM radiation line emerges from the waveguide was measured for the fundamental TE mode of specimen 41. This angle was measured by inverse triangulation. The measured value of the radiation angle is  $\phi' = 34.65 \pm 0.05^\circ$  and corresponds to a phase-matching angle  $\phi = 14.39 \pm 0.02^\circ$  within the specimen. Compare this value of  $\phi$  to the value  $\phi = 14.16 \pm 0.03^\circ$  calculated using the measured  $\Delta N$  of Table 5.1 and Equation (5.4). There is a discrepancy of  $0.23 \pm 0.05^\circ$  between these two methods of calculating  $\phi$ . Either the value of  $\Delta N$  must decrease by 0.0023 or the value of  $\phi'$  must decrease by  $0.64^\circ$  in order for these values of  $\phi$  to equal. Both of these changes lie outside the experimental errors. We cannot account for this discrepancy.

We investigate the temporal properties of the polarization coupling using two experiments. The first experiment determines whether there is a turn-on delay between the input of TE light and the observation of TM light. This experiment consists of translating the input fiber parallel to the plane of the waveguide while maintaining coupling to the TE modes. We observe the TM radiation pattern as the input coupling position is translated. We found that the translation of the TM radiation pattern coincides with the movement of the TE input coupling position within a time of less than 1 s. This measurement was limited by the minimum response time of the human eye.

The second experiment investigates the temporal response of the polarization coupling to amplitude-modulated TE light. This experiment consisted of chopping the input-coupled TE light from the HeNe laser while monitoring the TM radiation with a power meter. No time delay greater than 0.45 ms was observed. Time delays less than 0.45 ms could not be measured due to instrument limitations.

The polarization coupling ratio  $\rho$  was measured for specimens, 41, 42, and 53. Values of  $\rho$  are shown in Table 5.2 along with the measured values for the TE input power and the measured values of the TM power in branch A, the length of the specimen, and the value for the compensation factor. The multiple entries in Table 5.2 for specimen 41, which have the same input TE power, correspond to the situations where different groups of waveguide modes were selectively excited by adjusting the input coupling.

No change in the TM radiation was observed when we illuminate the specimens with the white-light source.

When the input fiber source was oriented so that TM polarization was coupled into the waveguides, no TE radiation modes were observed for any of the waveguide specimens.

## 5.5 Discussion

Our experimental results explicitly demonstrate the coupling between TE-polarized guided modes that propagate along the substrate's x-axis and TM-polarized radiation modes in Ti:LiNbO<sub>3</sub> slab waveguides. Summarizing the observed characteristics of this polarization coupling, we found that the power in the TM radiation is linear with the TE input power, the TM onset time is  $< 0.45$  ms, which is less than the  $10 - 1000$  s onset time found in photorefractive processes

[67, 82], the TM radiation angle corresponds closely to the phase matching condition to the TE guided mode, polarization coupling occurs for the fundamental and higher order TE modes, and the coupling ratio decreases with increasing diffusion time.

We do not observe this polarization coupling in  $\text{LiNbO}_3$  slab waveguides formed without titanium in-diffusion but otherwise fabricated using similar procedures. Thus, we conclude that this on-axis polarization coupling is directly or indirectly attributed to titanium in-diffusion. The remainder of this section discusses a mechanism from which this on-axis polarization coupling could originate.

**5.5.1 Polarization coupling through rotation of the principal dielectric axes** A mechanism certain to cause TE and TM polarization coupling would be the rotation of the waveguide region's principal axes relative to the substrate reference axes. In general, these hybrid modes contain all polarization components and, in certain cases, have characteristics similar to the mode coupling we observe. Rotations of the principal axes can come about from the presence of particular lattice strains through the photo-elastic properties of lithium niobate. Strains, in the form of lattice contractions, have been verified and measured in titanium in-diffused lithium niobate [62, 83, 84]. In fact, these strains, in combination with the photo-elastic effect might contribute to the increase in refractive index observed in titanium in-diffused lithium niobate [62, 61]. We consider the possibility that these lattice strains rotate the principal dielectric axes through the photo-elastic effect in the titanium in-diffused region.

The photo-elastic effect has also been called upon to explain hybrid mode propagation in proton-exchanged lithium niobate slab waveguides [84]. Later, this

mechanism was again used to explain hybrid mode propagation in high temperature proton-exchanged lithium niobate slab waveguides [85].

The optical properties of lithium niobate are described by the relative dielectric tensor  $\underline{\epsilon}$ . The relative dielectric tensor for lithium niobate in the substrate's principal axis coordinate system is

$$\underline{\epsilon} = \begin{pmatrix} \epsilon_x & 0 & 0 \\ 0 & \epsilon_y & 0 \\ 0 & 0 & \epsilon_z \end{pmatrix}, \quad (5.6)$$

where the ordinary refractive index is

$$n_o \equiv \sqrt{\epsilon_x} = \sqrt{\epsilon_y} \quad (5.7)$$

and the extraordinary refractive index is

$$n_e \equiv \sqrt{\epsilon_z}. \quad (5.8)$$

Equation (5.6) is the form of the relative dielectric tensor used to solve for slab waveguide modes when the mode propagation directions and the crystal's principle axes coincide. Solutions to the wave equation for this case describe true TE- and TM-polarized modes. For the general case of off-axis mode propagation, or equivalently rotation of the principal dielectric axes, coupling between all six field components takes place. We designate the rotated dielectric tensor as  $\underline{\epsilon}'$ . The fields are coupled through the nonzero off-diagonal elements in  $\underline{\epsilon}'$ . The presence of these off-diagonal elements can be the result of a particular strain field acting through the photo-elastic effect. We will discuss the effects of strains on mode propagation in a slab waveguide and compare theoretical predictions to our experimental results. First, we offer a brief introduction to the nomenclature describing the photo-elastic effect.

Changes to the dielectric tensor  $\underline{\underline{\epsilon}}$  caused by the photo-elastic effect are described through changes to the impermeability tensor  $\underline{\underline{\eta}}$ . The impermeability tensor is defined to be the inverse of the dielectric tensor

$$\underline{\underline{\eta}} \equiv \underline{\underline{\epsilon}}^{-1}. \quad (5.9)$$

The change in the  $i$ th element of the impermeability tensor due to the photo-elastic effect is [86, 87]

$$\Delta\eta_i = \sum_{j=1}^6 p_{ij} S_j; \quad i, j = 1, \dots, 6, \quad (5.10)$$

where the  $p_{ij}$  is an element of the elasto-optic tensor and  $S_j$  is an element of the strain tensor. We are using contracted indices  $(i, j = 1, \dots, 6)$  to identify tensor elements. Each numeral subscript represents a pair of axes in the substrate coordinate system according to:  $1 = xx$ ,  $2 = yy$ ,  $3 = zz$ ,  $4 = yz = zy$ ,  $5 = xz = zx$ , and  $6 = xy = yx$ .

The new impermeability tensor  $\underline{\underline{\eta}}'$  showing the modifications due to the photo-elastic effect is

$$\underline{\underline{\eta}}' = \underline{\underline{\eta}} + \Delta\underline{\underline{\eta}}. \quad (5.11)$$

The new dielectric tensor  $\underline{\underline{\epsilon}}'$  is found by taking the inverse of  $\underline{\underline{\eta}}'$  according to Equation (5.9).

Now we examine the specific photo-elastic induced modifications to  $\underline{\underline{\epsilon}}$  using the elasto-optic tensor for lithium niobate and the lattice strain fields due to titanium in-diffusion. The contracted form of the fourth-rank elasto-optic tensor

for bulk lithium niobate showing the eight independent elements is [88]

$$\underline{\underline{p}} = \begin{pmatrix} p_{11} & p_{12} & p_{13} & p_{14} & 0 & 0 \\ p_{12} & p_{11} & p_{13} & -p_{14} & 0 & 0 \\ p_{31} & p_{31} & p_{33} & 0 & 0 & 0 \\ p_{41} & -p_{41} & 0 & p_{44} & 0 & 0 \\ 0 & 0 & 0 & 0 & p_{44} & p_{41} \\ 0 & 0 & 0 & 0 & p_{14} & \frac{1}{2}(p_{11} - p_{12}) \end{pmatrix} \quad (5.12)$$

where the value of the elements is given in [89]. We assume that using the bulk elasto-optic tensor is appropriate for our discussion of the photo-elastic effect within the titanium in-diffused region. Furthermore, the values for  $p_{ij}$  we use represent the total effect of a strain field on the optical properties of lithium niobate. As discussed in [88], the total effect includes the primary modification due to the photo-elastic effect and a secondary modification due the combination of the piezoelectric and electro-optic effects.

Next, we must determine the elements of strain tensor  $\underline{\underline{S}}$  which describe the strain field present in the titanium in-diffused region. We will have to consider only strains along the principal axes of the crystal since we are dealing with a static strain field. The strain along the crystal's x-axis is  $S_1$ , the strain along the crystal's y-axis is  $S_2$ , and the strain along the crystal's z-axis is  $S_3$ . Thus, in our case, the general form of the strain tensor has nonzero elements only along the

diagonal

$$\underline{\underline{S}} = \begin{pmatrix} S_1 \\ S_2 \\ S_3 \\ 0 \\ 0 \\ 0 \end{pmatrix}. \quad (5.13)$$

Using Equations (5.9) through (5.13), we find the only nonzero off-diagonal element of the rotated dielectric tensor  $\underline{\underline{\epsilon}}'$  is  $\epsilon'_4$ . This element depends on the strain field according to

$$\epsilon'_4 \propto \epsilon_2 \epsilon_3 p_{41} (S_2 - S_1), \quad (5.14)$$

where we take

$$p_{41} = 0.154 \quad (5.15)$$

as in [89]. The proportionality factor in Equation (5.14) is a function of all three strain elements,  $\epsilon_2$ ,  $\epsilon_3$ ,  $p_{12}$ ,  $p_{31}$ ,  $p_{41}$ ,  $p_{11}$ ,  $p_{13}$ , and  $p_{33}$ . From Equation (5.14) we notice the following condition on  $\epsilon'_4$ :

$$\epsilon'_4 = 0 \text{ if } S_1 = S_2 \text{ or if } S_1 = S_2 = 0. \quad (5.16)$$

Next, we discuss the specific strains present in the titanium in-diffused region. Several groups have measured the lattice strain in the titanium in-diffused region on y-cut lithium niobate. A lattice contraction is found in each case. However, there is disagreement regarding the nonzero terms of  $\underline{\underline{S}}$ . We present three examples from the literature which use different strain elements in their analysis of slab waveguides formed by titanium in-diffusion on y-cut lithium niobate. In the first example a nonzero strain  $S_2$  was measured in y-cut slab waveguides [62]. The

strain  $S_1$  was assumed to be equal to  $S_2$  and the strain  $S_3$  was calculated using  $S_2$ . In contrast, the authors of [61] use symmetry arguments to determine the only nonzero strain element would be  $S_2$  in y-cut slab waveguides. In comparison, the third example [84] reports that  $S_2 = 0$  while both  $S_1$  and  $S_3$  are nonzero.

According to Equation (5.16), there will not be any off-diagonal elements in  $\underline{\epsilon}'$  if  $S_1 = S_2$ . Thus, the strain field described in the first example would not couple TE- and TM-polarized modes. However, in the second and third examples there would be off-diagonal terms in  $\underline{\epsilon}'$  corresponding to crystal axis rotation; consequently there would be coupling of the TE and TM polarized modes.

We cannot accurately model the crystal axis rotation caused by the photo-elastic effect without a consensus regarding the strain elements present in the diffused region. However, since we think that the photo-elastic effect is causing the polarization coupling, we will proceed by assuming the only nonzero element of strain is  $S_2$ . We base our assumption on the opinion that the substrate anchors the lattice dimensions that are parallel to the plane of the waveguide. Thus,  $S_1$  and  $S_3$  are 0 due to the influence of the unperturbed substrate lattice spacing. Contrarily, the lattice spacing perpendicular to the plane of the waveguide is free to experience strains resulting from titanium in-diffusion. Next, we calculate the effects on the dielectric tensor from the strain  $S_2$ .

We need to know the relationship between titanium concentration and strain in order to calculate the strain  $S_2$  in the in-diffused region. We found this relationship from the data presented in [62]. We use measurements of strain  $S_2$  and surface titanium concentration from a y-cut, titanium in-diffused lithium niobate specimen that was in-diffused for 10 h at 1000 °C . We find the relationship

between strain  $S_2$  and titanium concentration  $C_s(\text{Ti})$  is

$$S_2 = -9.5 \times 10^{-25} C_s(\text{Ti}) \quad (5.17)$$

where the units of titanium concentration are atoms/cm<sup>3</sup>. We assume the linear relationship of Equation (5.17) holds over the range of titanium concentrations found in our specimens. We find different values for the proportionality constant in Equation (5.17) using the data in [62] for specimens fabricated similarly except with different diffusion temperatures. Values of  $S_2/C_s(\text{Ti})$  are plotted against diffusion temperature in Figure 5.8. We speculate that this variation in  $S_2/C_s(\text{Ti})$  is a result of the titanium ions residing at different lattice sites corresponding to different diffusion temperatures.

The strain within the titanium in-diffused region of waveguide specimen 42 is calculated using Equation (5.17), and the measured titanium concentration is plotted in Figure 5.4. The resulting strain profile is plotted in Figure 5.4. The maximum contractive strain occurs at the surface and has a value of  $-2.2 \times 10^{-3}$ . The magnitude of this maximum contractive strain is greater than the breaking strain ( $2 \times 10^{-4}$ ) resulting from thermal expansion in lithium niobate reported in [90]. In fact, the magnitude of the strain in specimen 42 is greater than the breaking strain until a depth greater than  $2.2 \mu\text{m}$ .

These calculations show that the titanium in-diffused region will consist of different layers each with its principal dielectric axes oriented differently because of the nonuniform strain field. We calculate the rotated dielectric tensor  $\underline{\epsilon}'$  at several depths within the titanium in-diffused region using the strain profile of Figure 5.4. Then, we reduce  $\underline{\epsilon}'$  to its diagonal form to find values of the new principal refractive indices ( $n'_x$ ,  $n'_y$  and  $n'_z$ ) corresponding to new principal dielectric axes ( $x'$ ,  $y'$ ,  $z'$ ). The rotation angles  $\alpha_{x,y,z}$  are defined as the angles

between the substrate principal dielectric axes ( $x$ ,  $y$ , and  $z$  in Figure 5.1) and the corresponding new principal dielectric axes of  $\underline{\epsilon}'$ . We also calculate the difference between the new and the old principal refractive indices  $\Delta n_{x,y,z} = n'_{x,y,z} - n_{x,y,z}$ . The rotation angles and the principal refractive index differences are plotted in Figure 5.9. The new principal axes experience a rotation about the mode propagation axis ( $x$ -axis). The maximum rotation angle is  $\alpha_y = \alpha_z = 1.3^\circ$ . Also, the refractive indices  $n_x$  and  $n_y$  change by different amounts. Thus, the titanium in-diffused region becomes biaxial.

For comparison, a crystal axis rotation of less than  $1^\circ$  was calculated in [84] for proton-exchanged lithium niobate waveguides. In another study [85], a crystal axis rotation of  $10^\circ$  about the  $x$ -axis was used to fit theoretical calculations to measured values of hybrid mode effective indices in proton exchanged slab waveguides in  $x$ -cut lithium niobate.

The waveguide geometry resulting from this depth-dependent rotation of the principal dielectric axes is complex. Traditionally, the titanium in-diffused region is modeled as a region characterized as graded-index, uniaxial anisotropic and uniformly oriented principal axes. However, in the presence of photo-elasticity, the titanium in-diffused region has a depth dependent biaxial anisotropy and a depth dependent principal axes orientation.

We know this waveguide geometry will couple the  $z$ -directed electric field (TE) with the  $y$ -directed electric field (TM). We also know the  $y$ -directed field is not guided and will radiate from the waveguide region. This is so because the phase-matching condition between the TE and TM fields does not simultaneously satisfy the TM waveguide condition. We cannot be more specific about waveguide mode characteristics without solving the electro-magnetic boundary value problem

for this geometry.

We are not aware of any investigations analyzing a waveguide geometry of the same complexity as our waveguide geometry. There have been investigations into the modal properties of waveguides formed from 3 step-index layers, each with own arbitrary anisotropic properties [72]. A multi-layer approach was used in [77] to analyze graded-index waveguides of uniaxial anisotropy. Certainly, an approach combining these two methods would provide the capabilities to analyze the waveguide geometry of interest here.

## 5.6 Summary

We have observed polarization coupling from TE guided modes to TM radiation modes in titanium in-diffused lithium niobate slab waveguides. The characteristics of this polarization coupling are not the same as the polarization coupling that originates from photo-refractive effects. We hypothesize the polarization coupling we observe is the result of the photo-elastic effect. The photo-elastic effect transforms the titanium in-diffused waveguide region into one with a complex geometry. Still, this waveguide geometry is amenable to analysis by numerical techniques.

## 5.7 Acknowledgments

We acknowledge the support of the National Science Foundation under grant number ECS-9015752, the United States Army Research Office under grant number DAAL-03-92-G-0289 and the Office of Naval Research under grant number DOD ONR 14-92-J-1190. We also acknowledge many helpful editorial comments from Dr. Matt Young.

Table 5.1. The difference between the TE mode effective index and the substrate extraordinary index ( $n_e = 2.2028$ ) are tabulated for the  $\text{LiNbO}_3$  slab waveguides. Effective index measurements were made using prism out-coupling. Also listed are the phase-matching angles  $\phi$  calculated using equation (5.4) and the substrate ordinary index  $n_o = 2.2865$ . The effective mode index  $N$  was found by adding the substrate extraordinary index  $n_e = 2.2028$  to the value of  $\Delta N$ . The values for  $n_e$  and  $n_o$  are from [35].

Mode	Specimen 41		Specimen 42		Specimen 53	
	$\Delta N$	$\phi^\circ$	$\Delta N$	$\phi^\circ$	$\Delta N$	$\phi^\circ$
1	0.0142	14.16	0.0127	14.32	0.0025	15.32
	$\pm 0.0003$		$\pm 0.0002$		$\pm 0.0004$	
2	0.0028	15.29	0.0046	15.11	0.0015	15.41
	$\pm 0.0002$		$\pm 0.0002$		$\pm 0.0004$	
3	0.0006	15.49	0.0030	15.27	0.0004	15.51
	$\pm 0.0002$		$\pm 0.0003$		$\pm 0.0004$	
4			0.0014	15.42		
			$\pm 0.0002$			
5			0.0011	15.45		
			$\pm 0.0002$			

Table 5.2. Measured TE-TM coupling characteristics for the  $\text{LiNbO}_3$  slab waveguides.

Specimen	Conversion Ratio $\rho$ , %-cm <sup>-1</sup>	TE Input Power, $\mu\text{W}$	Branch A TM Power, $\mu\text{W}$	Length L, cm	Compensation Factor $\Gamma$	Comments
41	3.2%	83	2.1	1.9	2.4	Fundamental waveguide mode
41	3.2%	47	1.2	1.9	2.4	Fundamental waveguide mode
41	1.2%	83	0.79	1.9	2.4	Higher-order waveguide modes
41	1.2%	47	0.46	1.9	2.4	Higher-order waveguide modes
42	0.8%	63	0.68	2.8	2.2	Input fiber positioned for maximum TM Power
42	0.7%	62	0.56	2.8	2.2	Same as above
42	0.8%	55	0.59	2.8	2.2	Same as above
42	0.7%	40	0.37	2.8	2.2	Same as above
42	0.7%	22	0.20	2.8	2.2	Same as above
42	0.8%	11	0.11	2.8	2.2	Same as above
53	0.07%	63	0.025	1.3	2.2	Same as above

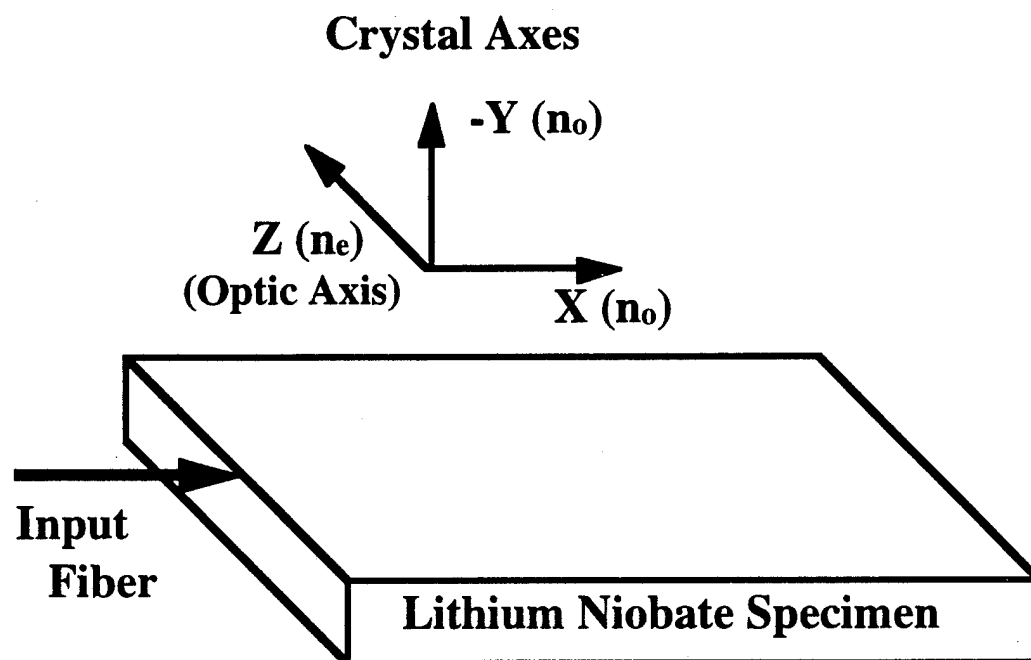


Figure 5.1. The waveguide orientation and mode propagation direction relative to the  $\text{LiNbO}_3$  crystal's axes. The extraordinary index is  $n_e = 2.2028$  and the ordinary index is  $n_o = 2.2865$  at the wavelength  $\lambda = 0.6328 \mu\text{m}$  [35].

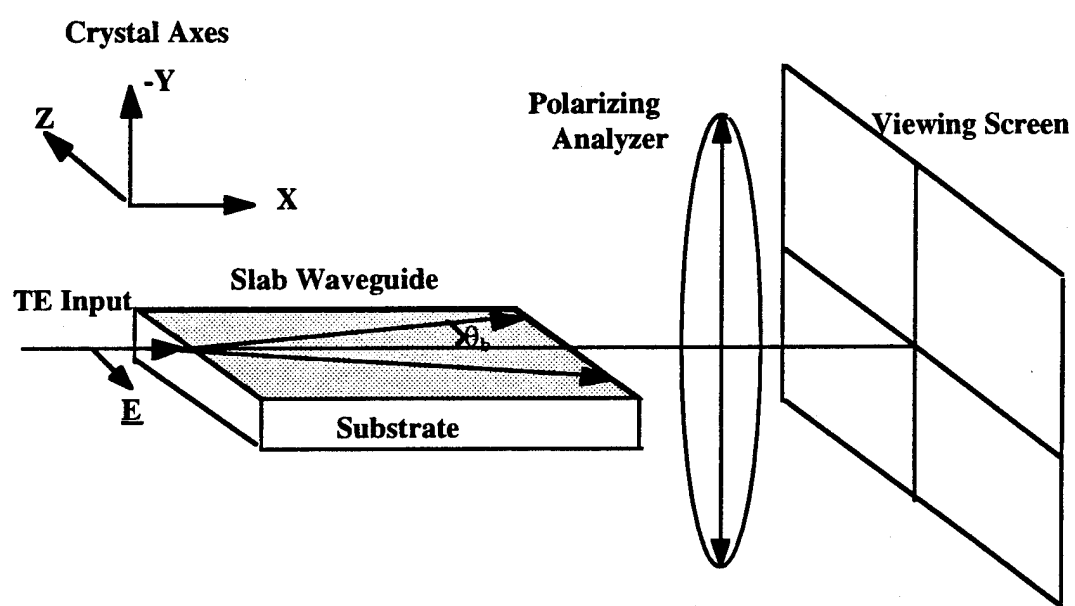


Figure 5.2. The experimental setup used to observe the intensity patterns emerging from the waveguide specimens. The polarization of the emerging radiation is determined using the polarizing analyzer.

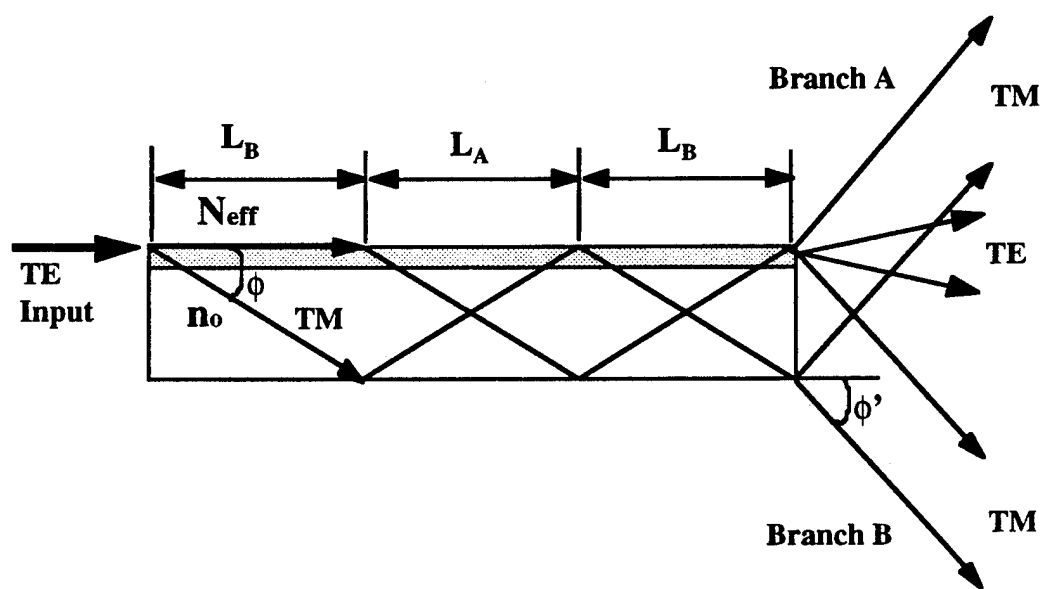


Figure 5.3. Illustration of phase matching between the TE polarized waveguide and the TM radiation mode. The TE mode propagates with effective index  $N$  while the TM mode propagates with refractive index  $n_o$ .

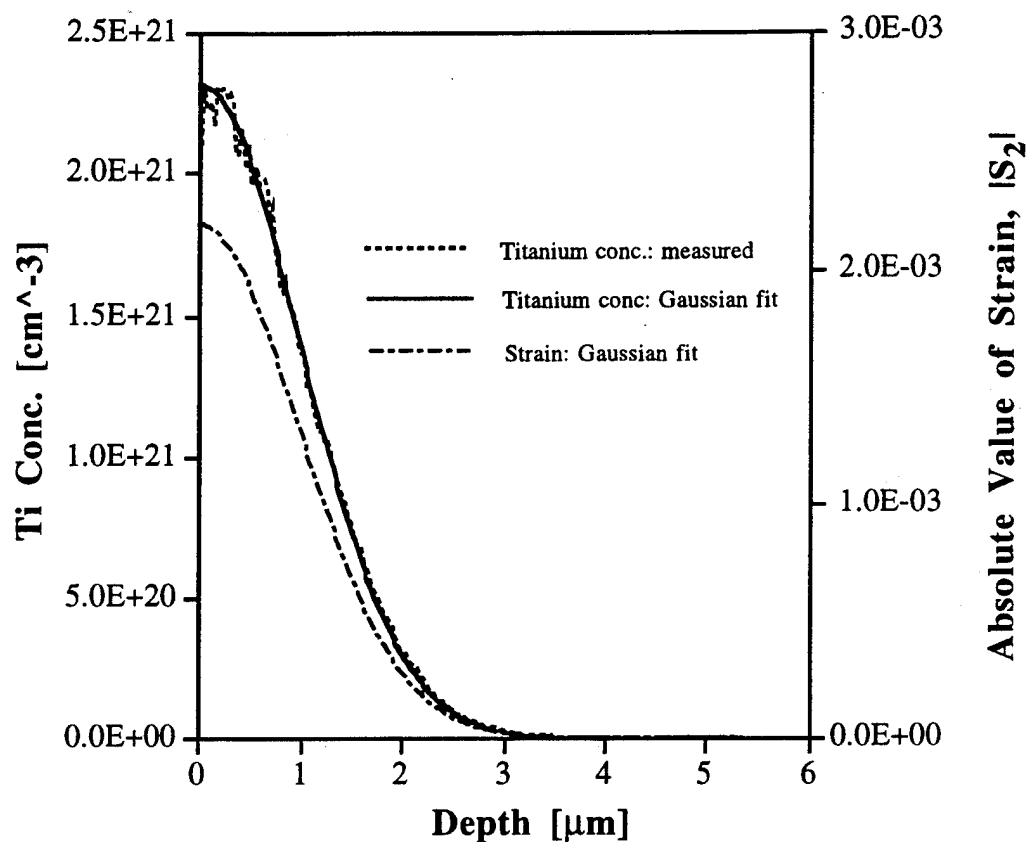


Figure 5.4. Depth dependence of titanium concentration and absolute value of strain within specimen 42 after diffusion. Measured titanium concentration is compared to the Gaussian solution to the diffusion equation. The Gaussian profile was fitted with the following parameter values: the surface concentration  $C_{Ti}(0)$  is  $2.31 \times 10^{21}$  atoms/cm<sup>3</sup> and the  $1/e$  diffusion depth is  $1.4 \mu\text{m}$ . The strain along the crystal's y-axis  $S_y$  is calculated using the Gaussian titanium concentration profile and the linear relationship between strain and titanium concentration calculated from the data in [62].

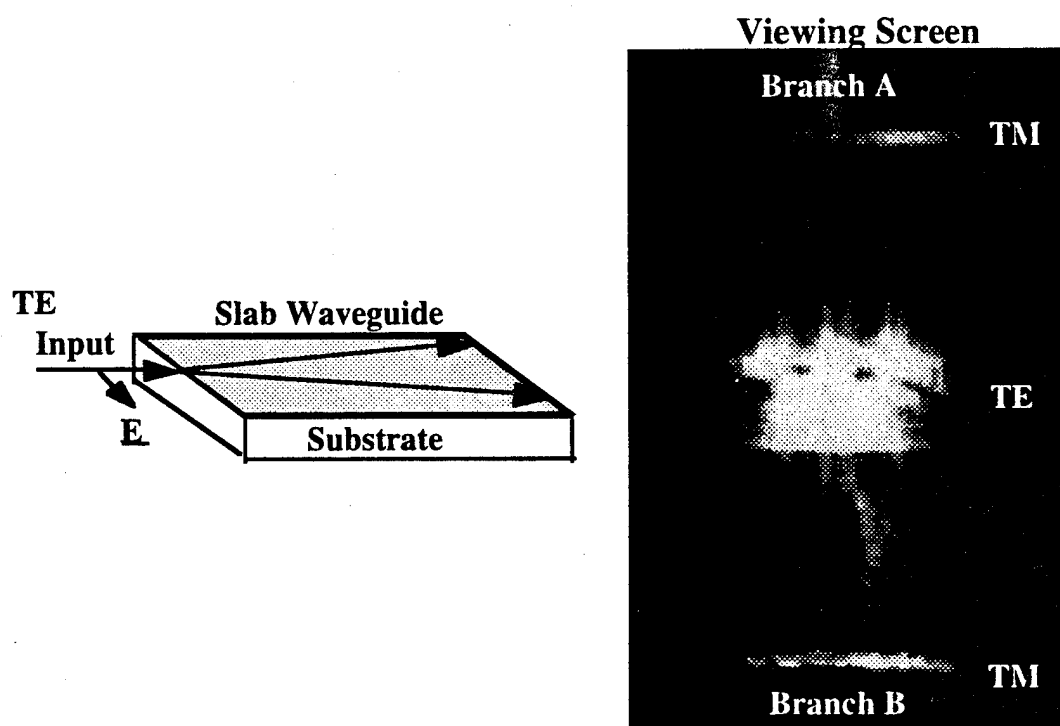


Figure 5.5. Intensity pattern emerging from specimen 41 as seen on the viewing screen. The central region is TE polarized while both the upper and lower regions are TM polarized.

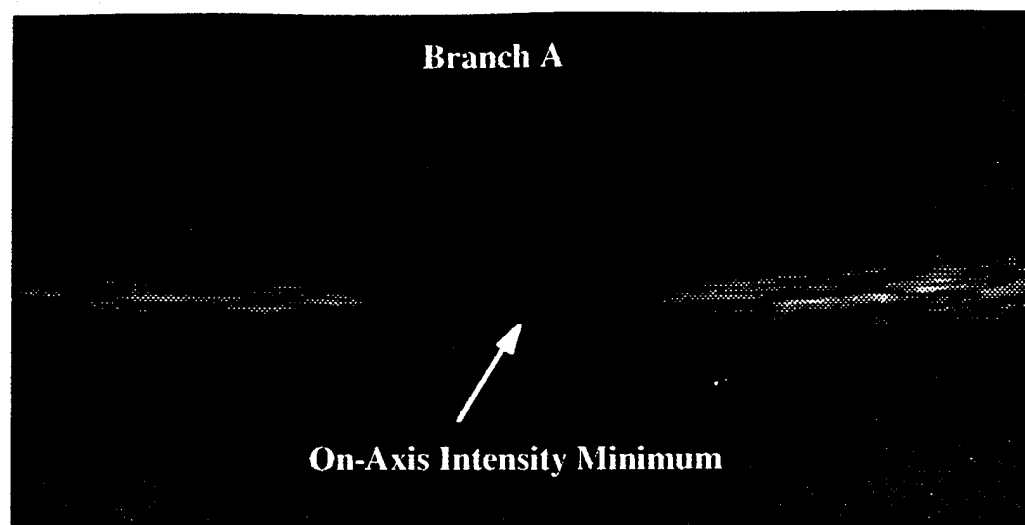


Figure 5.6. Detailed view of branch A radiation from specimen 53. The on-axis intensity minimum is indicated by the arrow.

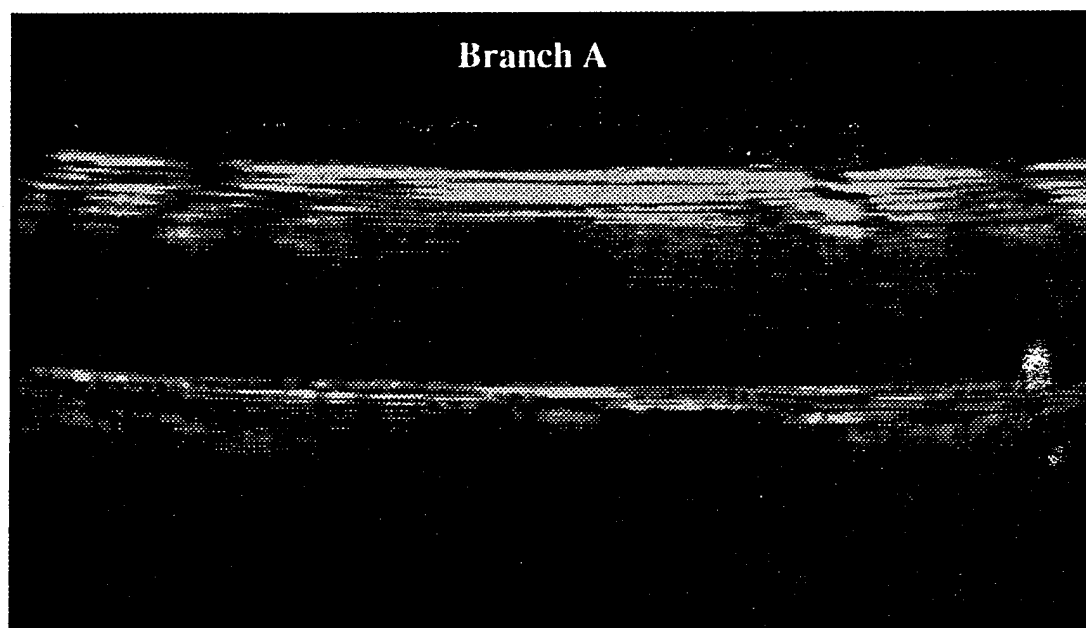


Figure 5.7: Detailed view of branch A radiation from specimen 41.

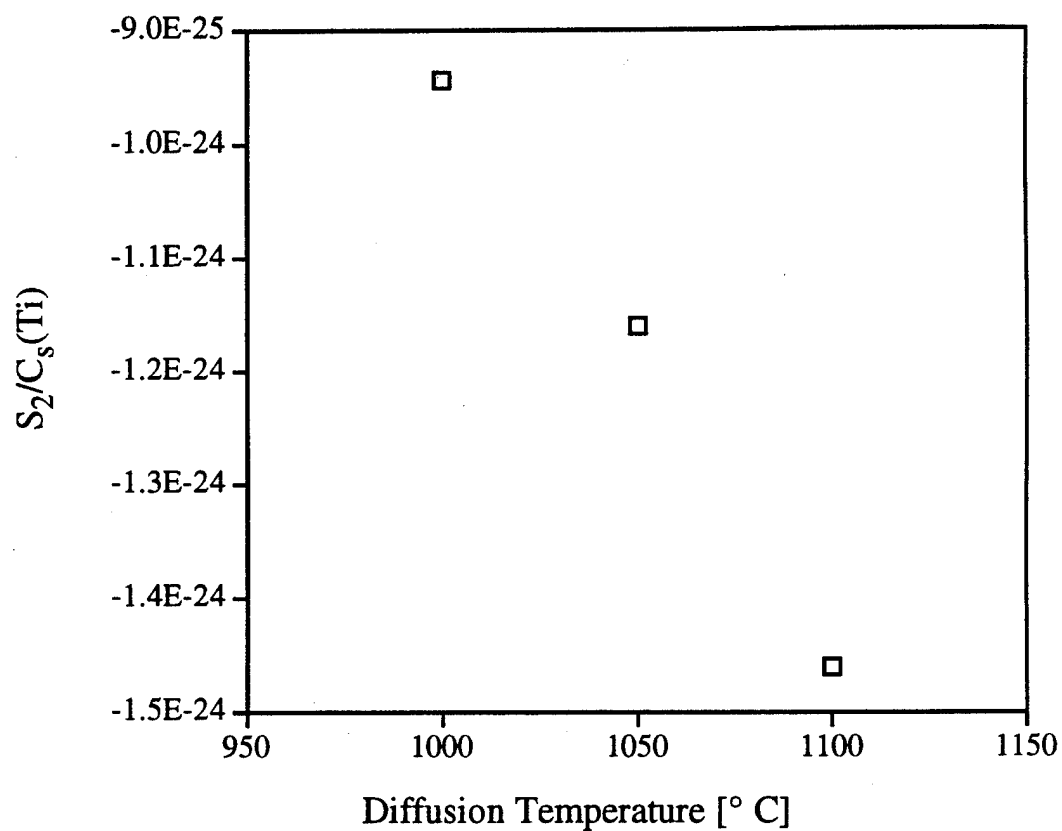


Figure 5.8. Temperature dependence of  $S_2/C_s(\text{Ti})$  from [62] where  $S_2$  is the strain along the  $y$ -axis and  $C_s(\text{Ti})$  is the surface concentration of titanium in atoms/cm<sup>3</sup>.

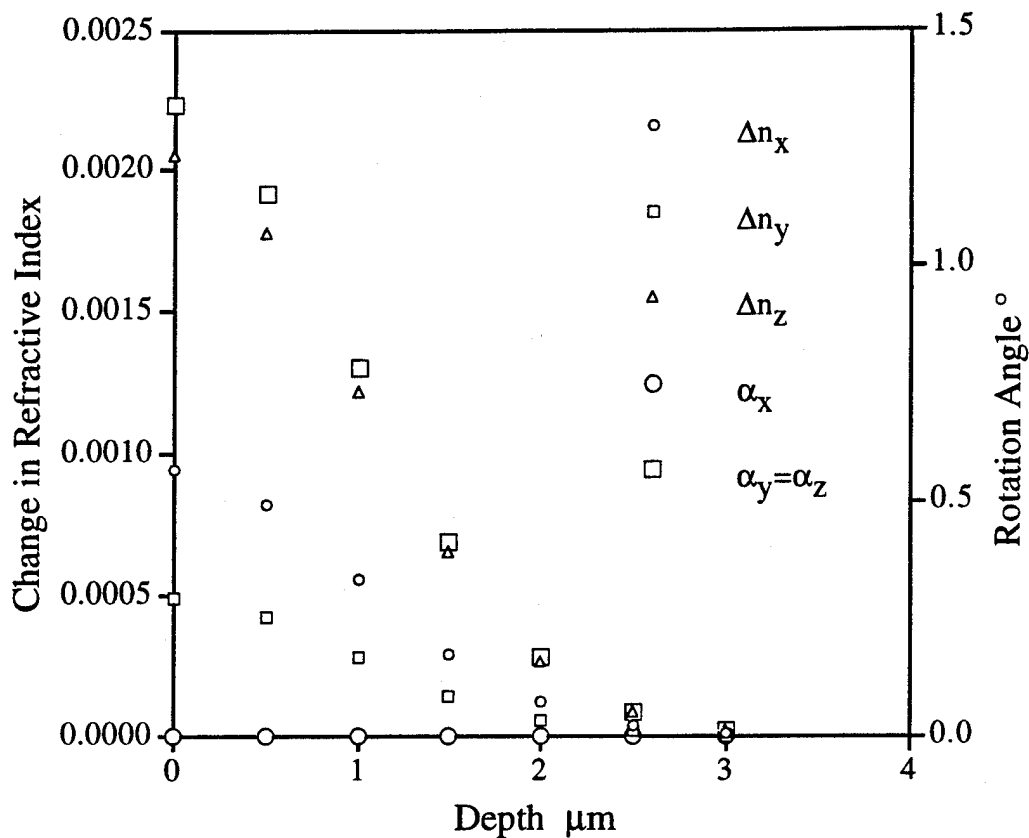


Figure 5.9. Depth dependence of the change in principal refractive index  $\Delta n$  and the principal axes rotation angles  $\alpha$  within specimen 42 after diffusion. The change in refractive index between the principal axes  $x$  and  $x'$  is  $\Delta n_x$ , between principal axes  $y$  and  $y'$  is  $\Delta n_y$  and between principal axes  $z$  and  $z'$  is  $\Delta n_z$ . The rotation angles are found by taking the vector dot product between corresponding principal dielectric axes. The angle between  $x$  and  $x'$  is  $\alpha_x$ , the angle between  $y$  and  $y'$  is  $\alpha_y$  and the angle between  $z$  and  $z'$  is  $\alpha_z$ .

## CHAPTER 6

### CONCLUDING STATEMENTS

The results of my work show that there remain several unexplained and interesting phenomena regarding both optical waveguides in lithium niobate and waveguide metrology.

I have demonstrated that it is not possible to fabricate low loss, single mode planar waveguides using the extraordinary index of refraction in lithium niobate. Further research is necessary to accurately model the changes in lithium niobate's extraordinary index of refraction resulting from diffusion.

I have demonstrated polarization coupling in  $\text{Ti:LiNbO}_3$  waveguides. Mine is the first report of this phenomena to the best of my knowledge. Additional research is needed to identify the mechanisms causing the polarization coupling. Once identified and understood, these mechanisms will allow for the beneficial use of this phenomena. Furthermore, knowledge of these mechanisms may contribute to our understanding of titanium in-diffusion kinetics in lithium niobate.

I have demonstrated that different models, and their experimental verifications are needed before the prism coupler can make highly accurate and precise measurements of effective index. Improving the capability of effective index measurement is of fundamental importance to the fabrication of high performance, and low cost integrated optics.

## BIBLIOGRAPHY

- [1] S. L. Kwiatkowski and A. R. Mickelson, "Nearly cut-off modes caused by diffusion in lithium niobate," **J. Appl. Phys.**, vol. 76, pp. 5877-5885, 1994.
- [2] S. L. Kwiatkowski, D. R. Hjelme, and A. R. Mickelson. "Polarization coupling in y-cut titanium in-diffused lithium niobate planar waveguides,". Submitted to Appl. Optics, 1994.
- [3] S. L. Kwiatkowski and A. R. Mickelson. "Perturbations on effective index of refraction from prism coupling,". Submitted to Appl. Optics, 1995.
- [4] T. Tamir, **Integrated Optics**. Berlin, New York: Springer-Verlag, second ed., 1985.
- [5] H. Osterberg and L. W. Smith, "Transmission of optical energy along surfaces: Part ii, inhomogeneous media," **J. Opt. Soc. Am.**, vol. 54, pp. 1078-1084, 1964.
- [6] P. Tien and R. Ulrich, "Theory of prism-film coupler and thin-film light guides," **J. Opt. Soc. Amer.**, vol. 60, pp. 1325-1337, 1970.
- [7] R. Ulrich, "Theory of the prism-film coupler by plane-wave analysis," **J. Opt. Soc. Amer.**, vol. 60, pp. 1337-1350, 1970.
- [8] J. E. Midwinter, "Evanescent field coupling into a thin-film waveguide," **IEEE J. Quantum Electron.**, vol. 6, pp. 123-130, 1970.
- [9] P. K. Tien, "Light waves in thin films and integrated optics," **Appl. Opt.**, vol. 10, pp. 2395-2413, 1971.
- [10] R. Ulrich, "Optimum excitation of optical surface waves," **J. Opt. Soc. Amer.**, vol. 61, pp. 1467-1477, 1971.
- [11] T. Tamir and H. L. Bertoni, "Lateral displacement of optical beams at multilayered and periodic structures," **J. Opt. Soc. Amer.**, vol. 61, pp. 1397-1413, 1971.
- [12] R. T. Kersten, "The prism-film coupler as a precision instrument part i. accuracy and capabilities of prism couplers as instruments," **Optica Acta**,

- vol. 22, pp. 503-513, 1975.
- [13] J. S. Wei and W. D. Westwood, "A new method for determining thin-film refractive index and thickness using guided optical waves," **Appl. Phys. Lett.**, vol. 32, pp. 819-821, 1978.
  - [14] H. J. W. M. Hoekstra, J. C. van't Spijker, and H. M. M. K. Koerkamp, "Ray picture for prism-film coupling," **J. Opt. Soc. Am. A.**, vol. 10, pp. 2226-2230, 1993.
  - [15] J. D. Swalen, M. Tacke, R. Santo, K. E. Rieckhoff, and K. Fischer, "Spectra of organic molecules in thin films," **Helvetica Chimica Acta**, vol. 61, pp. 960-977, 1978.
  - [16] J. Chilwell and I. Hodgkinson, "Thin-films field-transfer matrix theory of planar multilayer waveguides and reflection from prism-loaded waveguides," **J. Opt. Soc. Am. A**, vol. 1, pp. 742-753, 1984.
  - [17] L. M. Walpita, "Solutions for planar optical waveguide equations by selecting zero elements in a characteristic matrix," **J. Opt. Soc. Am. A**, vol. 2, pp. 595-602, 1985.
  - [18] A. K. Ghatak, K. Thyagarajan, and M. R. Shenoy, "Numerical analysis of planar optical waveguides using matrix approach," **J. Lightwave Technol.**, vol. 5, pp. 660-667, 1987.
  - [19] P. K. Tien, R. Ulrich, and R. J. Martin, "Modes of propagating light waves in thin deposited semiconductor films," **Appl. Phys. Lett.**, vol. 14, pp. 291-294, 1969.
  - [20] R. Ulrich and R. Torge, "Measurement of thin film parameters with a prism coupler," **Appl. Opt.**, vol. 12, pp. 2901-2908, 1973.
  - [21] R. T. Kersten, "The prism-film coupler as a precision instrument part ii. measurements of refractive index and thickness of leaky waveguides," **Optica Acta**, vol. 22, pp. 515-521, 1975.
  - [22] S. Morasca and C. De Bernardi, "High accuracy determination of semiconductor substrate and waveguide refractive index by prism coupling," in **Integrated Optical Circuit Engineering VI**, Vol. 993, SPIE, 1988, pp. 164-166.
  - [23] T. Tamir, **Integrated Optics**. Berlin, New York: Springer-Verlag, second ed., 1985.

- [24] K. S. Chiang, "Construction of refractive-index profiles of planar dielectric waveguides from the distribution of effective indexes," **J. Lightwave Technol.**, vol. 3, pp. 385-391, 1985.
- [25] G. C. Righini and G. Molesini, "Design of optical-waveguide homogenous refracting lenses," **Appl. Optics**, vol. 27, pp. 4193-4199, 1988.
- [26] D. Marcuse, **Theory of Dielectric Optical Waveguides**. New York: Academic Press, first ed., 1974.
- [27] A. R. Mickelson, **Guided Wave Optics**. New York: Van Nostrand Reinhold, first ed., 1992.
- [28] J. W. Goodman, **Introduction to Fourier Optics**. San Francisco: McGraw-Hill, first ed., 1968.
- [29] R. V. Schmidt and I. P. Kaminow, "Metal-diffused optical waveguides in  $\text{LiNbO}_3$  films," **Appl. Phys. Lett.**, vol. 25, pp. 458-460, 1974.
- [30] J. R. Carruthers, I. P. Kaminow, and L. W. Stulz, "Diffusion kinetics and optical waveguiding properties of out-diffused layers in lithium niobate and lithium tantalate," **Appl. Opt.**, vol. 13, pp. 2333-2342, 1974.
- [31] J. Crank, **The Mathematics of Diffusion**. New York: Oxford University Press, second ed., 1986.
- [32] J. Vollmer, J. P. Nisius, P. Hertel, and E. Krätzig, "Refractive index profiles of  $\text{LiNbO}_3\text{:Ti}$  waveguides," **Appl. Phys. A**, vol. 32, pp. 125-127, 1983.
- [33] J. Crank, **The Mathematics of Diffusion**. New York: Oxford University Press, second ed., 1986.
- [34] M. Born and E. Wolf, **Principles of Optics**. Oxford: Pergamon Press, sixth ed., 1980.
- [35] D. F. Nelson and R. M. Mikulyak, "Refractive indices of congruently melting lithium niobate," **J. Appl. Phys.**, vol. 45, pp. 3688-3689, 1974.
- [36] W. L. Bond, "Measurement of the refractive indices of several crystals," **J. Appl. Phys.**, vol. 36, pp. 1674-1677, 1965.
- [37] J. Noda, N. Uchida, S. Saito, T. Saku, and M. Minakata, "Electro-optic amplitude modulation using three-dimensional  $\text{LiNbO}_3$  waveguide fabricated by  $\text{TiO}_2$  diffusion," **Appl. Phys. Lett.**, vol. 27, pp. 19-21, 1975.

- [38] W. K. Burns, P. H. Klein, E. J. West, and L. E. Plew, "Ti diffusion in Ti:LiNbO<sub>3</sub> planar and channel optical waveguides," **J. Appl. Phys.**, vol. 50, pp. 6175-6182, 1979.
- [39] S. Forouhar, G. E. Betts, and W. S. C. Chang, "Effects of water vapor on modes in ti-indiffused LiNbO<sub>3</sub> planar waveguides," **Appl. Phys. Lett.**, vol. 45, pp. 207-209, 1984.
- [40] I. P. Kaminow and J. R. Carruthers, "Optical waveguiding layers in LiNbO<sub>3</sub> and LiTaO<sub>3</sub>," **Appl. Phys. Lett.**, vol. 22, pp. 326-328, 1973.
- [41] M. N. Armenise, C. Canali, M. D. Sario, A. Carnera, P. Mazzolodi, and G. Celotti, "Characterization of (Ti<sub>0.65</sub>Nb<sub>0.35</sub>)O<sub>2</sub> compound as a source for ti diffusion during Ti:LiNbO<sub>3</sub> optical waveguide fabrication," **J. Appl. Phys.**, vol. 54, pp. 62-70, 1983.
- [42] J. L. Jackel, C. E. Rice, and J. Veselka, "Proton exchange for high-index waveguides in LiNbO<sub>3</sub>," **Appl. Phys. Lett.**, vol. 41, pp. 607-608, 1982.
- [43] J. L. Jackel, "Suppression of outdiffusion in titanium diffused LiNbO<sub>3</sub>: A review," **J. Opt. Comm.**, vol. 3, pp. 82-85, 1982.
- [44] C. Canali, C. D. Bernarde, M. D. Sario, A. Loffredo, G. Mazzi, and S. Morasca, "Effects of water vapor on refractive index profiles in Ti:LiNbO<sub>3</sub> planar waveguides," **J. Lightwave Technol.**, vol. 4, pp. 951-954, 1986.
- [45] J. L. Jackel, V. Ramaswamy, and S. P. Lyman, "Elimination of out-diffused surface guiding in titanium- diffused LiNbO<sub>3</sub>," **Appl. Phys. Lett.**, vol. 38, pp. 509-511, 1981.
- [46] A. Rasch, M. Rottschalk, and W. Karthe, "Suppression of outdiffusion in Ti:LiNbO<sub>3</sub>," **J. Opt. Comm.**, vol. 6, pp. 14-17, 1985.
- [47] J. Noda and M. Fukuma, "Phase matching temperature variation of second-harmonic generation in Li out-diffused LiNbO<sub>3</sub> layers," **J. Appl. Phys.**, vol. 51, pp. 1379-1384, 1980.
- [48] V. E. Wood, N. F. Hartman, A. E. Austin, and C. M. Verber, "Stoichiometry dependence of lithium outdiffusion in LiNbO<sub>3</sub>," **J. Appl. Phys.**, vol. 52, pp. 1118-1120, 1981.
- [49] S. T. Vohra, A. R. Mickelson, and S. E. Asher, "Diffusion characteristics and waveguiding properties of proton exchanged and annealed LiNbO<sub>3</sub> waveguides," **J. Appl. Phys.**, vol. 66, pp. 5161-5174, 1989.

- [50] Y. Handa, M. Miyawaki, and S. Ogura, **Guided-wave characteristics and optical damage in  $\text{LiNbO}_3$  waveguides**, Vol. 460. Bellingham, Washington: Proc. Soc. Photo-Opt. Instrum. Engrs., 1984.
- [51] A. L. Dawar and J. C. Joshi, "Fabrication of optical waveguides in y-lithium niobate from dilute melts proton exchange technique," **Optics Comm.**, vol. 73, pp. 199–202, 1989.
- [52] M. Goodwin and C. Stewart, "Proton-exchange optical waveguides in y-cut lithium niobate," **Electron. Lett.**, vol. 19, pp. 223–224, 1983.
- [53] J. Chilwell and I. Hodgkinson, "Thin-films field-transfer matrix theory of planar multilayer waveguides and reflection from prism-loaded waveguides," **J. Opt. Soc. Am. A**, vol. 1, pp. 742–753, 1984.
- [54] J. Crank, **The Mathematics of Diffusion**. New York: Oxford University Press, second ed., 1986.
- [55] H. S. Carslaw and J. C. Jaeger, **Conduction of Heat in Solids**. London: Oxford University Press, second ed., 1956.
- [56] L. Goldberg, **Application of intergrated optics to optical signal processing**. PhD thesis, University of California, San Diego, 1979.
- [57] C. Canali, C. D. Bernarde, M. D. Sario, A. D'Orazio, and S. Morasca, "Step-like refractive-index increase induced in planar  $\text{Ti}:\text{LiNbO}_3$  waveguides diffused in  $\text{o}_2:\text{h}_2\text{o}$  atmosphere," **Appl. Optics**, vol. 27, pp. 3957–3958, 1988.
- [58] S. A. M. Al-Chalabi, B. L. Weiss, K. M. Barfoot, and G. W. Arnold, "Analysis of he-implanted  $\text{LiNbO}_3$  by elastic recoil detection," **J. Appl. Phys**, vol. 63, pp. 1032–1036, 1988.
- [59] R. G. Wilson, S. W. Novak, J. M. Zavada, A. Loni, and R. M. D. L. Rue, "Secondary ion mass spectroscopy depth profiling of proton-exchanged  $\text{LiNbO}_3$  waveguides," **J. Appl. Phys.**, vol. 66, pp. 6055–6058, 1989.
- [60] C. H. Harper, ed., **Handbook of Materials and Processes for Electronics**. New York: McGraw-Hill, first ed., 1970.
- [61] S. Fries, P. Hertel, and H. P. Menzler, "Extraordinary versus ordinary refractive index change in planar  $\text{LiNbO}_3:\text{Ti}$  waveguides," **Phys. Stat. Sol. (a)**, vol. 108, pp. 449–455, 1988.
- [62] K. Sugii, M. Fukuma, and H. Iwasaki, "A study on titanium diffusion into

- LiNbO<sub>3</sub> waveguides by electron probe analysis and X-ray diffraction methods," **J. Mater. Science**, vol. 13, pp. 523-533, 1978.
- [63] P. Skeath, W. T. Elam, W. K. Burns, F. A. Stevie, and T. H. Briggs, "Concentration dependence of the octahedral Ti<sup>4+</sup> center in LiNbO<sub>3</sub> : its effect on refractive indices," **Phys. Rev. Lett.**, vol. 59, pp. 1950-1953, 1987.
  - [64] C. Zaldo, C. Prieto, H. Dexpert, and P. Fessler, "Study of the lattice sites of ti and ni impurities in LiNbO<sub>3</sub> single crystals, by means of x-ray absorption spectroscopy," **J. Phys.: Condens. Matter**, vol. 3, pp. 4135-4144, 1991.
  - [65] Private communication with Steve Novak of Evans East, Inc.
  - [66] R. Dahan, N. Croitoru, and S. Ruschin, "Studies on the relation between the diffusion process and optical properties in ti-diffused planar optical waveguides," **Appl. Opt.**, vol. 30, pp. 4396-4401, 1991.
  - [67] P. G. Kazansky, "Photo-induced conversion of radiation polarization in integrated optics components based on LiNbO<sub>3</sub>," **IEEE J. Quantum Electron.**, vol. 25, pp. 736-741, 1989.
  - [68] R. Chen and W. S. C. Chang, "Anomalous attenuation and depolarization scattering in y-cut LiNbO<sub>3</sub> proton exchanged waveguides," **IEEE J. Quantum Electron.**, vol. 22, pp. 880-881, 1986.
  - [69] D. P. Russo and J. H. Harris, "Wave propagation in anisotropic thin-film optical waveguides," **J. Opt. Soc. Amer.**, vol. 63, pp. 138-145, 1973.
  - [70] M. O. Vassell, "Structure of optical guided modes in planar multilayers of optically anisotropic materials," **J. Opt. Soc. Amer.**, vol. 64, pp. 166-173, 1974.
  - [71] W. K. Burns and J. Warner, "Mode dispersion in uniaxial optical waveguides," **J. Opt. Soc. Amer.**, vol. 64, pp. 441-446, 1974.
  - [72] M. S. Kharusi, "Uniaxial and biaxial anisotropy in thin-film optical waveguides," **J. Opt. Soc. Amer.**, vol. 64, pp. 27-35, 1974.
  - [73] D. Marcuse, "Modes of a symmetric slab optical waveguide in birefringent media-part 1: Optical axis not in plane of slab," **IEEE J. Quantum Electron.**, vol. 14, pp. 736-741, 1978.
  - [74] D. Marcuse, "Modes of a symmetric slab optical waveguide in birefringent

- media-part 2: Slab with coplanar optical axis," **IEEE J. Quantum Electron.**, vol. 15, pp. 92-101, 1979.
- [75] P. Yeh, "Electromagnetic propagation in birefringent layered media," **J. Opt. Soc. Am.**, vol. 69, pp. 742-756, 1979.
  - [76] L. Torner, F. Canal, and J. Hernandez-Marco, "Leaky modes in multilayer uniaxial optical waveguides," **Appl. Opt.**, vol. 29, pp. 2805-2814, 1990.
  - [77] K. Yamanouchi, T. Kamiya, and K. Shibayama, "New leaky surface waves in anisotropic metal-diffused optical waveguides," **IEEE Trans. Microwave Theory Tech.**, vol. 26, pp. 289-304, 1978.
  - [78] S. K. Sheem, W. K. Burns, and A. F. Milton, "Leaky-mode propagation in Ti-diffused LiNbO<sub>3</sub> and LiTaO<sub>3</sub> waveguides," **Optics Letters**, vol. 3, pp. 76-78, 1978.
  - [79] Optical grade lithium niobate wafers were purchased from Crystal Technologies Inc., Palo Alto, California.
  - [80] A. Yariv, **Quantum Electronics**. New York: Wiley, second ed., 1975.
  - [81] SIMS measurements were performed by Steve Novak of Evans East, Plainsboro, New Jersey, USA.
  - [82] D. Kip, R. Fink, T. Bartholomäus, and E. Krätzig, "Coupling of orthogonally polarized waves in LiNbO<sub>3</sub> optical waveguides," **Opt. Comm.**, vol. 95, pp. 33-38, 1993.
  - [83] M. N. Armenise, M. D. Sario, C. Canali, P. Franzosi, J. Singh, R. H. Hutchins, and R. M. D. L. Rue, "In-plane scattering in titanium-diffused LiNbO<sub>3</sub> optical waveguides," **Appl. Phys. Lett.**, vol. 45, pp. 326-328, 1984.
  - [84] V. A. Ganshin and Y. N. Korkishko, "Deformations, stress and birefringence in proton-exchanged lithium niobate waveguides," **J. Opt. Commun.**, vol. 13, pp. 2-7, 1992.
  - [85] S. Chen, P. Baldi, M. P. D. Micheli, D. B. Ostrowsky, A. Leycuras, G. Tararini, and P. Bassi, "Hybrid modes in proton exchanged waveguides realized in LiNbO<sub>3</sub>, and their dependence on fabrication parameters," **Opt. Lett.**, vol. 18, pp. 1314-1316, 1993.
  - [86] T. S. Narasimhamurty, **Photoelastic and Electro-optic properties of crystals**. New York: Plenum Press, first ed., 1981.

- [87] A. Yariv and P. Yeh, **Optical Waves in Crystals**. New York: Wiley, first ed., 1984.
- [88] R. S. Weis and T. K. Gaylord, "Lithium niobate: Summary of physical properties and crystal structure," **Appl. Phys. A**, vol. 37, pp. 191-203, 1985.
- [89] R. J. O'Brien, G. J. Rosasco, and A. Weber, "Brillouin scattering in lithium niobate," **J. Opt. Soc. Am.**, vol. 60, p. 716, 1970.
- [90] J. C. Brice, "The cracking of czochralski-grown crystals," **J. Cryst. Growth**, vol. 42, pp. 427-430, 1977.
- [91] S. T. Vohar, **Diffusion characteristics and waveguiding properties of  $\text{Li}_{1-x}\text{H}_x\text{NbO}_3$  optical waveguide devices**. PhD thesis, University of Colorado, 1989.
- [92] W. Charczenko, **Coupled mode analysis, fabrication, and characterization of microwave intergrated optical devices**. PhD thesis, University of Colorado, 1990.
- [93] D. P. B. III, "Review: Analysis of diffusion in lithium niobate," **J. Mat. Sci.**, vol. 28, pp. 302-315, 1993.
- [94] J. G. Bergman, A. Ashkin, A. A. Ballman, J. M. Dziedzic, H. J. Levinstein, and R. G. Smith, "Curie temperature, birefringence, and phase-matching temperature variations in  $\text{LiNbO}_3$  as a function of melt stoichiometry," **Appl. Phys. Lett.**, vol. 12, pp. 92-94, 1968.
- [95] A. M. Prokhorov and Y. S. Kuz'minov, **Physics and Chemistry of Crystalline Lithium Niobate**. New York: Adam Hilger, 1990.
- [96] K. Nassau, H. J. Levinstein, and G. M. Loiacona, "Ferroelectric lithium niobate. 2. preparation of single domain crystals," **J. Phys. Chem. Solids**, vol. 27, pp. 989-996, 1966.

## APPENDIX A

### QUANTIFICATION OF SECONDARY ION MASS SPECTROSCOPY DATA FROM LITHIUM NIOBATE SPECIMENS

This Appendix discusses the data processing procedures used to quantify secondary ion mass spectroscopy (SIMS) data. In some cases, I have processed the SIMS data presented in this dissertation. In these cases, I have modified the data processing procedure from that which is followed by Evans East. These modifications are noted in Section A.2.4.

SIMS measurements on optical waveguide specimens formed in x-cut lithium niobate substrates will be used to demonstrate the affects of the different data processing procedures. The SIMS measurements were performed by Senior Analyst Steve Novak at Evans East, Inc., Plainsboro, New Jersey.

#### A.1 Introduction to SIMS

The SIMS measurement determines species concentration of a specimen by ion bombardment. The bombarding ion is Cesium ( $\text{Cs}^+$ ) with energy of 6 keV. A crater is formed on the specimen surface as a result of the cesium bombardment. A typical crater cross-section is  $300 \cdot 300 \mu\text{m}^2$ . The detected area of the crater is  $90 \cdot 90 \mu\text{m}^2$ . Thus, the information about species composition is averaged over this detected area.

Cesium is a member of the I A metals, also called the alkali-metals. The alkali-metals are the most reactive metal group. The Cesium ions readily react with the other atomic species in the specimen to form ion pairs. These ion pairs are

detected as counts/s during a measurement cycle. The ion pair count rate, or ion intensity ( $I$  counts/s) is recorded once during each measurement cycle. The total number of measurement cycles is recorded. The ion intensity and measurement cycle are the raw data from a SIMS measurement.

The goal of processing this raw data is to convert the ion intensity into atom density ( $\rho$  ions/cm<sup>3</sup>), and measurement cycles into depth. The conversion of this raw data into the more useful quantities involves subjective calibration steps that are based upon the analyst's experience. This experience includes knowledge of both the specific SIMS instrument, and the specimen's material properties. In addition, the calibration of the two quantities of raw data is not independent. These calibration steps are the source of uncertainty in both the accuracy and precision of SIMS. These uncertainties bring into question both the quantitative and the qualitative value of the measurement.

## A.2 SIMS Calibration Procedures

Evans East's calibration procedure is based on standards and assumptions of material parameters that do not necessarily apply to my specimens. Furthermore, there is an element of data interpretation that enters into the calibration process.

As a result, when I process the raw data, I use a modified version of Evans East's calibration procedure to convert ion intensity into atom density. The modifications I made reflect differences in material properties, data interpretation and calibration standards that exist between my specimens those which form the bases of Evan East's calibration procedure. Furthermore, I have found that it is sometimes necessary to customize the calibration procedures for a specific waveguide specimen because of its particular fabrication history. The remainder of

this Appendix outlines the general calibration procedures used for the specimens presented in this dissertation. Deviations from this general procedure are noted when discussing a particular specimen.

**A.2.1 Depth Calibration** I use the results of the calibration procedure performed by Evans East to convert measurement cycles into depth. The depth of the crater is measured at the end of the SIMS run using a stylus profilometer. This measurement has an uncertainty of  $\pm 10\%$ . Reporting the uncertainty as a percentage of the depth is in contrast to depth uncertainty of  $\pm 10$  nm reported elsewhere [91, 92]. Dividing the crater depth by the total cycles provides the constant factor to convert cycles into depth. The underlying assumption here is that the excavation rate of the crater is constant during the SIMS measurement. This implies that the excavation rate is independent of specimen composition. For example, this assumes that regions of a titanium in-diffused  $\text{LiNbO}_3$  specimen containing high concentrations of titanium erode at the same rate as regions of low titanium concentrations. Similarly, for proton exchanged  $\text{LiNbO}_3$  it assumes that the regions of high proton concentration erode at the same rate as the regions of low proton concentration. This assumption is probably satisfactory for titanium in-diffusion. However, the assumption may not be valid for proton exchange where a distinct phase boundary exists between the hydrogen rich layer and the substrate.

**A.2.2 Atom Density Calibration** The next part of the calibration is to convert ion intensity ( $I$  counts/s) into atom density ( $\rho$  ions/cm<sup>3</sup>). There are two steps to this calibration. The first step is to normalize the raw data to remove any variations that can be attributed to instrument drift. I use the same procedures followed by Evans East for this normalization step.

The normalization is accomplished using the measure of an ionic species of the specimen that is thought to maintain a uniform concentration throughout the specimen during the fabrication procedures. The leading candidate for calibration species, or matrix element in lithium niobate is oxygen. The oxygen sublattice is believed to remain intact during the processes of titanium in-diffusion, and proton exchange [93, 65]. The oxygen concentration is measured by monitoring the Cesium-oxygen ion intensity  $I_{CsO+}$ . The raw data of the other species is normalized by dividing their ion intensity by the matrix ion intensity,  $I_{matrix} \equiv I_{CsO+}$ . This normalization can either be done on a point-by-point (cycle-by-cycle) basis, or by finding an average value of  $I_{matrix}$ . Deciding which normalization to use is subjective and based on experience. This decision requires examining the raw ion intensity data for features or patterns that suggests one normalization is better than the other.

The second step to the calibration procedure is to convert the normalized ion intensity into atom density. This calibration step requires finding a relative sensitivity factor (RSF) for each ion species.

We combine these two steps to write the relationship between ion intensity and atom density as

$$\rho = \frac{I_{ion}}{I_{matrix}} \text{RSF} \frac{\text{atoms}}{\text{cm}^3}. \quad (\text{A.1})$$

Finding the RSF for a particular ion species requires using either standards, or a priori knowledge of the atom density. For example, when measuring the density changes in a constituent ion species such as lithium, niobium, or oxygen in  $\text{LiNbO}_3$ , one can assume that, at sufficient depth, the constituent atom concentration should approach that of an unprocessed  $\text{LiNbO}_3$  substrate. Thus, the RSF is found using the calculated atom density  $\rho_{calc.}$  in the substrate, and

the normalized ion intensity measured in the substrate  $I_{sub}$  in Equation (A.1). Solving Equation (A.1) for the RSF yields

$$RSF = \frac{\rho_{calc.}}{\left(\frac{I_{ion}}{I_{matrix}}\right)} \frac{\text{atoms}}{\text{cm}^3}. \quad (\text{A.2})$$

**A.2.3 Stoichiometry of Lithium Niobate** In order to calculate  $\rho_{calc.}$  we need to know the measure of the elements, or the stoichiometry of the lithium niobate substrate.

The empirical formula commonly used for lithium niobate is  $\text{LiNbO}_3$ , where the subscripts denote the mole ratio of each element. This formula describes the mole ratio for stoichiometric lithium niobate. However, lithium niobate can exist in different phases. These other phases of lithium niobate have been grown and their properties studied [35, 94, 95]. There, the lithium-to-niobium mole ratios range from  $0.80 < \text{Li/Nb} < 1.20$ .

I am using optical grade, congruent lithium niobate from Crystal Technology, Palo Alto, CA, USA. These lithium niobate crystals are grown from a melt using the Czochralski technique. The crystal is of congruent composition when the stoichiometry of the melt and of the crystal are the same. This property allows for the growth of uniform, stress free crystals. The congruent phase is achieved by adjusting the mole percentage of  $\text{Li}_2\text{O}$  according to

$$\frac{[\text{Li}_2\text{O}]}{[\text{Li}_2\text{O} + \text{Nb}_2\text{O}_5]} = 0.4838 \pm 0.0001. \quad (\text{A.3})$$

In comparison, the stoichiometric phase is described by the mole fraction of  $\text{Li}_2\text{O}$  according to

$$\frac{[\text{Li}_2\text{O}]}{[\text{Li}_2\text{O} + \text{Nb}_2\text{O}_5]} = 0.500 \quad (\text{A.4})$$

In my opinion, Equation (A.3) does not clearly, or directly convey information regarding the relative atomic ratios in the congruent phase. I have not

found a procedure for determining the chemical formula for the congruent phase using Equation (A.3) that was either adequately explained, or easily defended. However, I have been given instructions [65] on how to use Equation (A.3) to determine the chemical formula for congruent lithium niobate, and thus the atomic ratios.

The subscript for lithium in chemical formula for the congruent phase of lithium niobate is found by dividing the right hand side of Equation (A.3) by the right hand side of Equation (A.4). The subscript for niobium is found by subtracting this ratio from 2. It is assumed that the amount of oxygen in the congruent phase is the same as that in the stoichiometric phase. The chemical formula for the congruent phase resulting from these steps is



We calculate the lithium-to-niobium mole ratio for congruent lithium niobate from Equation (A.5) to be

$$\frac{\text{Li}}{\text{Nb}} = 0.937. \quad (\text{A.6})$$

In contrast, the mole ratio of lithium-to-niobium is  $\text{Li}/\text{Nb} = 1$  for the stoichiometric phase. Thus, there are about 6% less lithium atoms per cubic centimeter in congruent lithium niobate than in stoichiometric lithium niobate.

The density of the constituent atoms is calculated using the formula weight, and the density of  $\text{LiNbO}_3$ . The formula weight of stoichiometric lithium niobate is 147.84 g/mole. In comparison, the formula weight of congruent lithium niobate is 150.63 g/mole, where I have used the atomic proportions indicated in Equation (A.5).

Unfortunately, I can not locate a value for the mass density of congruent lithium niobate. The reported mass densities of lithium niobate include 4.612

g/cm<sup>3</sup> [95], 4.628 g/cm<sup>3</sup> [88], and 4.64 g/cm<sup>3</sup> [96]. Only in [95] is it specifically stated that the density is for stoichiometric lithium niobate. Crystal Technologies quotes the density reported in [96]. However, we cannot assume this is the density of the congruent phase because [96] does not specify the stoichiometry. Furthermore, it is also stated in [95] that the density of the crystal increases (by approximately 0.2% for an unspecified Li/Nb ratio) and the unit cell size increases as the lithium-to-niobium ratio becomes less than 1 (which is the case for congruent lithium niobate).

We cannot determine the atom densities in congruent lithium niobate without knowledge of the mass density. However, we can make a reasonable approximation by assuming the mass density of congruent phase is the same as that for the stoichiometric phase, that is  $\rho_m = 4.612 \text{ g/cm}^3$ . The atom density is found by dividing the mass density by the formula weight, and multiplying by the number of formula units per mole to yield

$$\rho_{Li} = 1.78 \cdot 10^{22} \frac{\text{atoms}}{\text{cm}^3} \quad (\text{A.7})$$

for the lithium atom density, and

$$\rho_{Nb} = 1.90 \cdot 10^{22} \frac{\text{atoms}}{\text{cm}^3} \quad (\text{A.8})$$

for the niobium atom density in congruent lithium niobate.

**A.2.4 Calibration of Titanium Concentration** This is the calibration step I have modified to reflect my interpretations of the SIMS data. First, the procedure followed by Evans East is outlined, then the procedure I use is presented.

Evans East uses a calibration standard to determine the RSF for titanium. This calibration standard is an titanium-ion implanted lithium niobate

substrate obtained from AT&T. The amount of implanted titanium per square centimeter  $S$  was determined during the implantation process to be

$$S_{im} = 1.4 \cdot 10^{14} \frac{\text{atoms}}{\text{cm}^2}. \quad (\text{A.9})$$

SIMS measurements are made on the calibration standard under conditions intended to be the same as those that were in place for the specimens under test. Figure A.1 shows the raw intensity data from the calibration standard plotted versus depth. This data was acquired to calibrate the x-cut lithium niobate specimens discussed in Chapter 4.

The calibration step begins by normalizing the raw intensity data using the matrix ion intensity  $I_{CsO}$ . Next, this normalized curve is integrated with respect to depth yielding  $A$ . Dividing  $S_{im}$  by  $A$  yields the RSF for titanium.

Evans East chooses to ignore the raw intensity data near the surface from 0 to 0.37 nm when calculating  $A$ . They interpret this surface layer as a measurement artifact. Including this surface layer would decrease their RSF for titanium by 30%.

I also observe a surface layer in x-cut titanium in-diffused lithium niobate specimens. The raw titanium intensity from these x-cut specimens is shown in Figure A.2. Here, we see indications of surface layer that produces higher titanium intensity. I interpret the data in Figure A.2 to indicate a residual titanium-compound layer on the surface of these specimens. Thus, I believe the surface layers on the x-cut specimens should be included in the calibration of titanium density.

Others have reported a residual surface layer of titanium compound on titanium in-diffused specimens [38, 41, 66]. However, there is disagreement in the reported composition of the surface layer.

There is another disadvantage to using a calibration standard in addition to the uncertainty raised by the surface layer. This is the assumption that the conditions present during the measurement of the calibration standard applies to all of the specimens under test. For example, only one titanium RSF is obtained from the calibration standard and it is used for all of the x-cut titanium profiles shown in Figure A.2. Using only one RSF will not yield correct results when specimen-to-specimen variations exist. Furthermore, the normalization procedure discussed above will not compensate for these inter-specimen variations. Table A.1 lists the normalized lithium intensity for the x-cut specimens. These are average values taken from regions representing the unperturbed substrate. Thus, if identical conditions were present during the SIMS measurement then the normalized lithium intensities would be the same for each x-cut specimen. Since this is not case for one of the constituent species (lithium) then we cannot assume identical conditions existed for the titanium measurement. Thus, each specimen requires a unique RSF.

I am using a different titanium calibration procedure that overcomes these concerns. First, I calculate the number of titanium atoms per square centimeter  $S_{ev}$  using the thickness  $\tau$  of the evaporated titanium, the mass of a titanium atom  $m_{Ti} = 7.95 \cdot 10^{-23}$  g, and the mass density of titanium metal  $\rho_{m,Ti} = 4.51$  g/cm<sup>3</sup> (for 99.5% pure Ti [60]) according to

$$\begin{aligned} S_{ev} &= \frac{\rho_{m,Ti}}{m_{Ti}} \tau \\ &= 5.67 \cdot 10^{22} \tau \end{aligned} \quad (A.10)$$

Next, I integrate the raw titanium intensity curve of each specimen with respect to depth yielding  $A_s$ . Then, I calculate a titanium relative sensitivity

factor for each specimen  $RSF_s$  according to

$$RSF_s = \frac{S_{ev}}{A_s}. \quad (A.11)$$

The results of using this calibration procedure are shown in Figure A.3. Notice the equal titanium concentrations for each specimen just below the surface layer. This is not the case when the SIMS data was processed by Evans East as seen in Figure A.4. An accurate measurement of the titanium concentration just below the surface layer is important for determining titanium diffusion kinetics.

Even though using a different RSF for each specimen accounts for inter-specimen variations, it does not in general yield quantitatively accurate results when two different materials are present in a specimen. This situation may require a different RSF for each material.

One final comment regarding processing the SIMS data in Figure A.3 is that I omitted the matrix normalization step. I did not normalize the titanium intensity using the CsO intensity because we cannot assume the oxygen concentration of the surface layer is the same as that in lithium niobate. The proper way to normalize SIMS data when two different material are present is to use two different matrix intensities.

Table A.1. The variability of the averaged normalized lithium intensity. The average is taken over measurement cycles representative of the unperturbed lithium niobate substrate.

Specimen	Averaged Normalized	Standard Deviation
	Intensity	
	$I_{\text{CsLi}}/I_{\text{CsO}}$	
x2	5.70	0.05
x3	3.89	0.05
x4	5.09	0.03

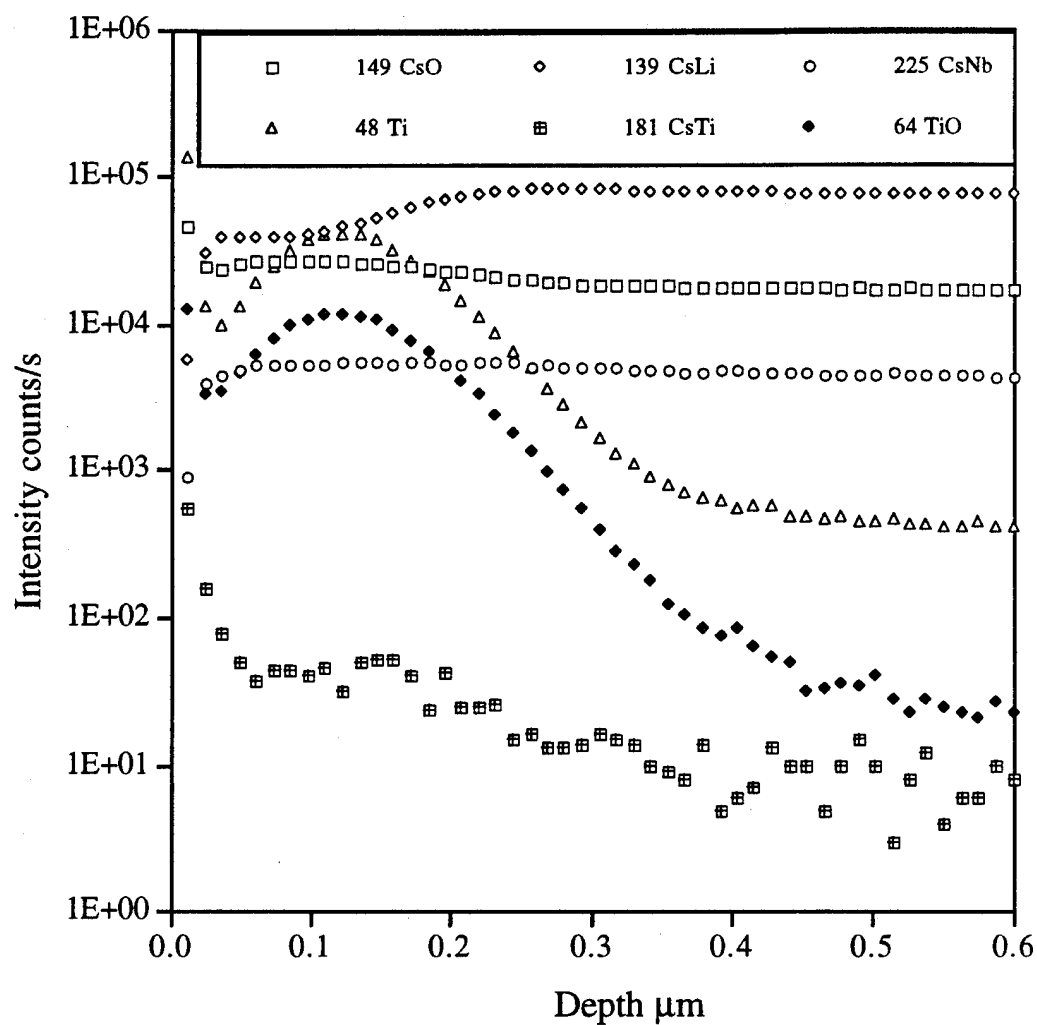


Figure A.1. Raw intensity data from SIMS measurements of the implanted titanium standard. Data is from Evans East file 41785\_10.

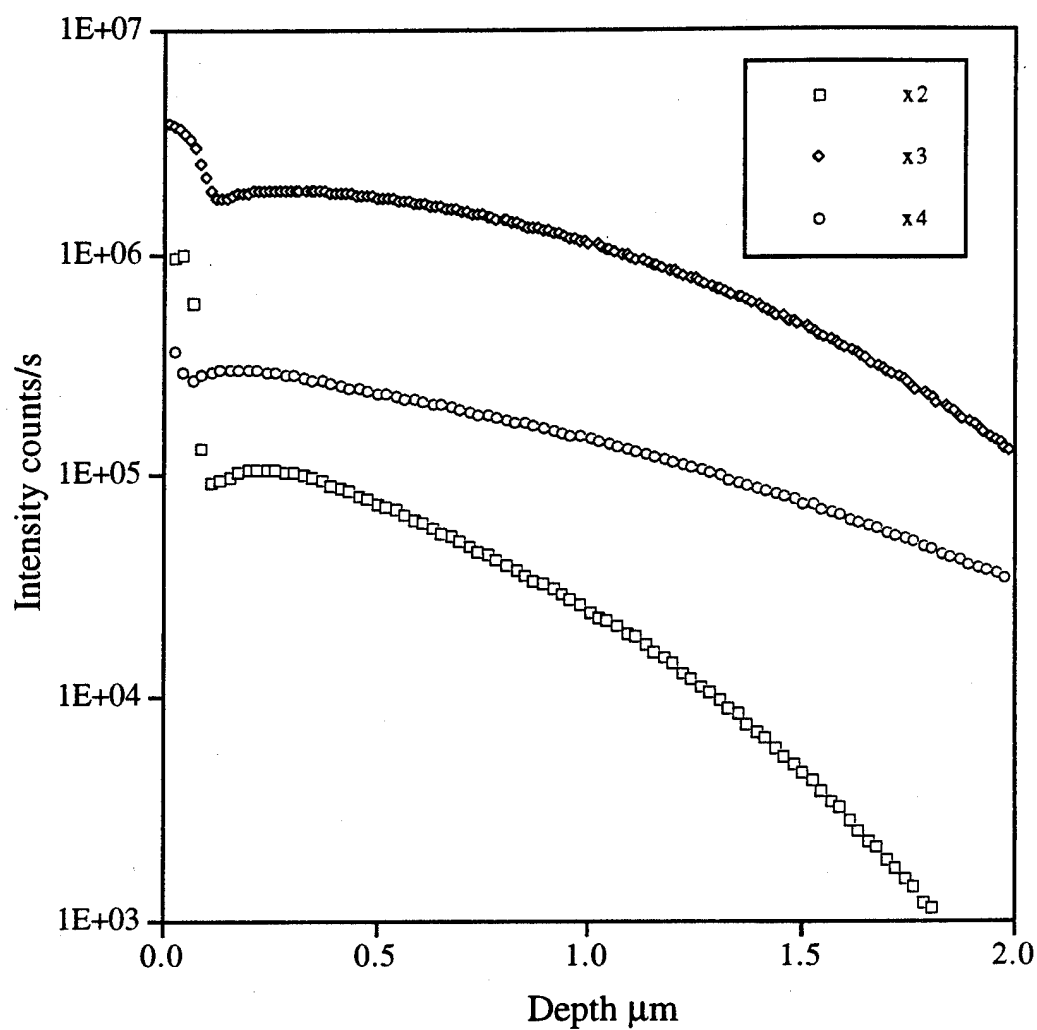


Figure A.2. Raw titanium intensity  $I_{Ti}$  from SIMS measurements of x-cut titanium in-diffused lithium niobate specimens. The in-diffusion time was 1 h for specimen x2, 2 h for specimen x3, and 4 h for x4. The in-diffusion temperature was 950 °C .

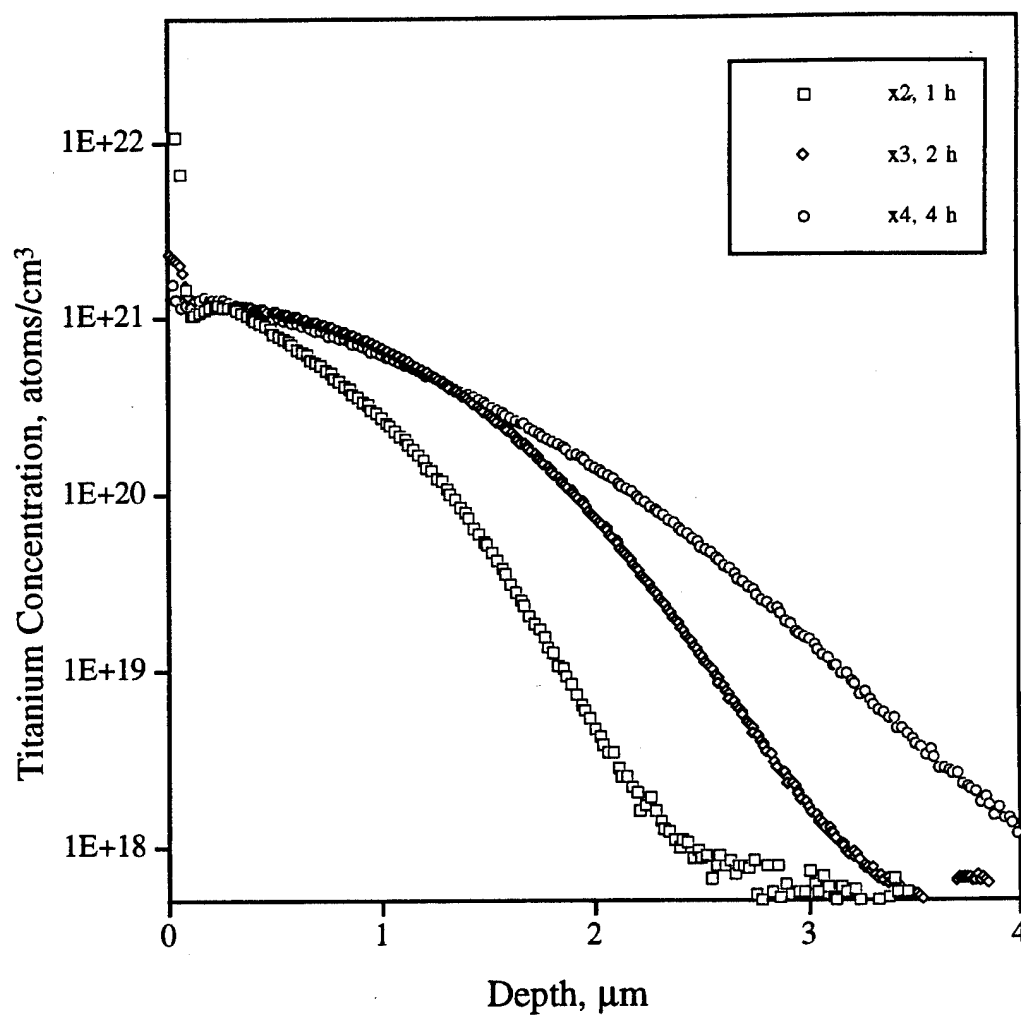


Figure A.3. Titanium densities for the x-cut specimens calibrated using my procedure discussed in Section A.2.4. The in-diffusion time was 1 h for specimen x2, 2 h for specimen x3, and 4 h for x4. The in-diffusion temperature was 950 °C .

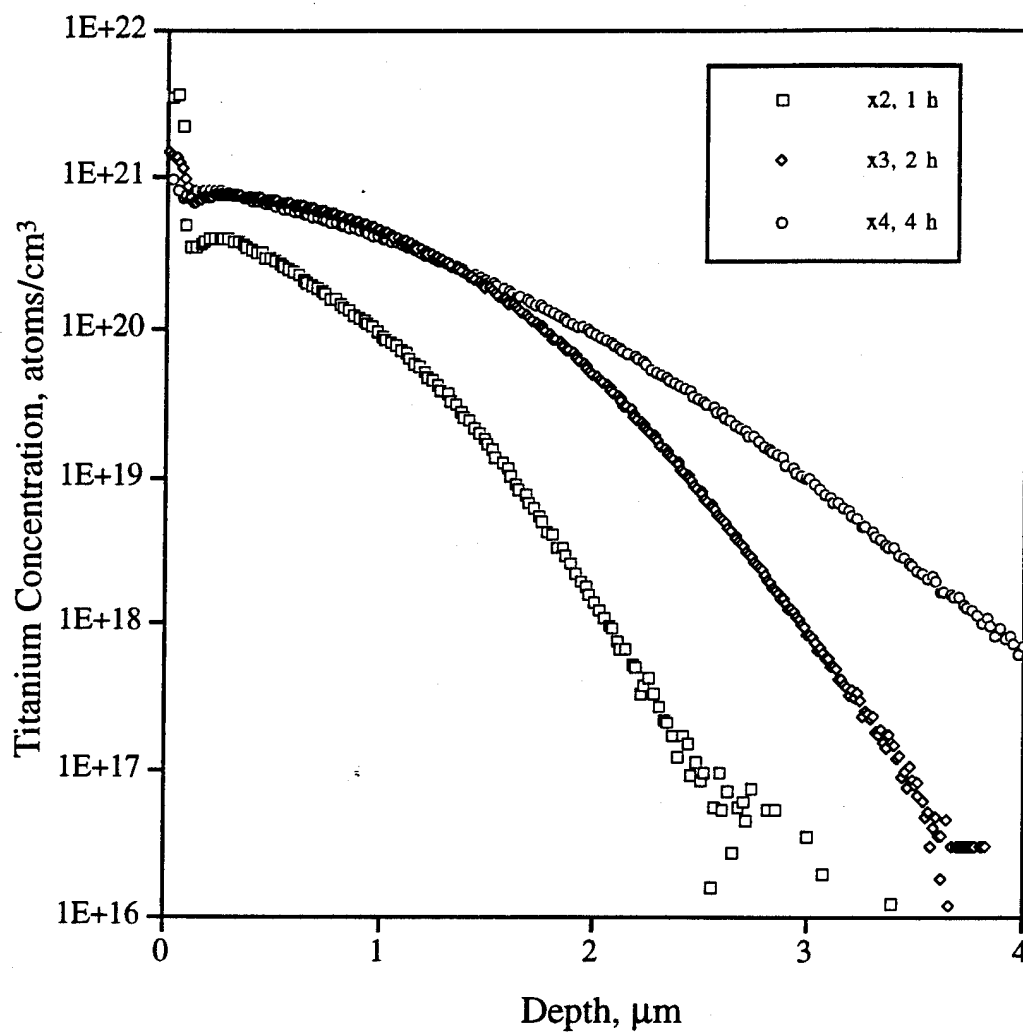


Figure A.4. Titanium densities for the x-cut specimens calibrated by Evans East. The in-diffusion time was 1 h for specimen x2, 2 h for specimen x3, and 4 h for x4. The in-diffusion temperature was 950 °C .